Simulations and Tests for the High-Energy-Telescope on Solar Orbiter

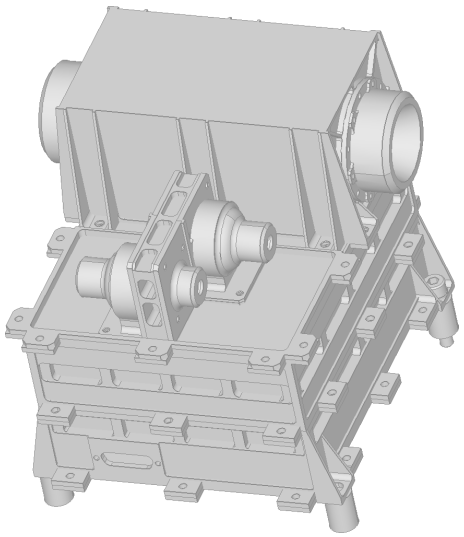

Dissertation
zur Erlangung des Doktorgrades
der Mathematisch-Naturwissenschaftlichen Fakultät
der Christian-Albrechts-Universität zu Kiel
vorgelegt von

Jan Tammen

Kiel, 2016

Erster Gutachter:	Prof. Dr. R.F. Wimmer-Schweingruber
Zweiter Gutachter:	Prof. Dr. S. Wolf
Tag der mündlichen Prüfung:	26. April 2016
Zum Druck genehmigt:	17. Mai 2016

gez. Prof. Dr. W. J. Duschl, Dekan

Zusammenfassung

Solar Orbiter ist eine Raumsonde der Europäischen Raumfahrtagentur (ESA), deren Ziel insbesondere die Untersuchung der Quellen des Sonnenwindes, des solaren Dynamos und von Beschleunigungsmechanismen und -orten für hochenergetische solare Teilchen ist. Die Sonde hat zu diesem Zweck eine Vielzahl verschiedener wissenschaftlicher Instrumente an Bord und kombiniert diese mit einer bisher einzigartigen Umlaufbahn. Solar Orbiter wird einen minimalen Abstand zur Sonne von 0.3 Astronomischen Einheiten (AU) haben und damit der Sonne ähnlich nahe kommen, wie einst die Helios Missionen. Die Umlaufbahn wird außerdem im Laufe der sieben Jahre dauernden Untersuchungen durch Gravitationsmanöver an Erde und Venus zu größeren geographischen Breiten verlegt, so dass auch die Pole der Sonne mit Hilfe von Fernerkundungsinstrumenten untersucht werden können. Neben verschiedenen bildgebenden Messinstrumenten besitzt Solar Orbiter auch in-situ Instrumente, die den Sonnenwind, das solare Magnetfeld, elektromagnetische Wellen sowie die energetischen Sonnenteilchen untersuchen.

Der *Energetic Particle Detector* (EPD), zu dem auch das *High Energy Telescope* (HET) gehört, übernimmt hierbei die Messung der energetischen Teilchen der Sonne. Das HET mißt dabei die besonders hochenergetischen Teilchen: Elektronen von 0.3 bis 15 MeV, Protonen und Heliumkerne von 7 MeV/nuc bis 100 MeV/nuc und schwerere Ionen ab etwa 20 MeV/nuc bis zu 300 MeV/nuc – abhängig vom Typ. Ein besonderes Augenmerk liegt auf der Unterscheidung von ^{3}He und ^{4}He, die noch bis zu einem Isotopenverhältnis von 1:100 nachgewiesen werden sollen, um besonders ^{3}He reiche Sonneneruptionen zu identifizieren.

Die vorliegende Dissertation beschäftigt sich mit verschiedenen Aspekten, die während der Entwicklung von HET und darüber hinaus bei der späteren Datenanalyse eine wichtige Rolle spielen. Zum einen wurde durch ein selbst entwickeltes Modell die voraussichtliche Strahlungsdosis von HET während der siebenjährigen Mission analysiert. Mithilfe dieses Modells konnte gezeigt werden, dass die Wahl strahlungsharter, elektronischer Bauteile ausreicht um einen – zumindest strahlungsbedingten – Ausfall zu verhindern, so dass auf zusätzliche Masse in Form von Abschirmung verzichtet werden konnte. Die Ergebnisse dieser Analyse wurden in Form eines internen, technischen Berichts bei der ESA veröffentlicht und während einer Designüberprüfung des Instruments (*Critical Design Review, CDR*) durch die ESA geprüft. Der Überprüfungsprozess des Instruments wurde – nicht zuletzt auch aufgrund dieser Analyse – im Jahr 2014 erfolgreich bestanden.

Da die Unterscheidung von ^{3}He und ^{4}He ein wesentlicher Bestandteil von HET ist, wurde das Verhalten des Instruments in Bezug auf diese Eigenschaft hin untersucht. Die verschiedenen Rauschquellen entlang des Signalpfades wurden analysiert und durch geeignete Modelle nachgebildet, u.a. durch Raytracing Monte-Carlo Simulationen für die Lichtausbreitung im Szintillator. Diese Modelle wurden dann auf Simulationsergebnisse mit dem GEANT Toolkit angewandt und somit die zu erwartende Antwort des HET Sensors in Bezug auf die Isotopentrennung von ^{3}He und ^{4}He berechnet. Es konnte dadurch festgestellt werden, wie die Auswerteelektronik dimensioniert werden musste, um die Heliumisotope bei einer relativen Häufigkeit von 1 % noch trennen zu können. Die Ergebnisse flossen daraufhin in die Entwicklung des Sensors ein und werden während der Entwicklung der Software für die Ausleseelektronik, die aktuell im Gang ist, benötigt.

Der HET Sensor verfügt über einen BGO ($Bi_4Ge_3O_{12}$) Szintillationskristall über den die

Gesamtenergie einfallender Teilchen gemessen wird. Dieser Kristall hat jedoch eine nichtlineare Lichtantwort, die sowohl von der Teilchensorte als auch von der Energie abhängt. Da für die spätere Auswertung der Messdaten die genaue Kenntnis über die vorkommenden Nichtlinearitäten notwendig ist, wurden hierfür im Rahmen der Dissertation bereits umfangreiche Voruntersuchungen durchgeführt. Es wurde mit hochenergetischen Ionen am *Heavy Ion Medical Accelerator in Chiba* (HIMAC) die Lichtantwort des Kristalls vermessen und diese mit Simulationsrechnungen mit dem GEANT Toolkit verglichen. Aus dem Vergleich von Simulation und Experiment konnte ein Vorhersagemodell für die Lichtantwort des BGO für den – für HET wichtigen – Energiebereich entwickelt werden. Die Methoden und das Modell wurden bereits vorab in der Zeitschrift "*Nuclear Instruments and Methods in Physics Research Section B: Beam Interactions with Materials and Atoms*", Volume 360 (2015) auf den Seiten 129-138 veröffentlicht. Das entwickelte Modell konnte außerdem durch weitere Messungen am HIMAC erfolgreich verifiziert werden und zeigte gute Übereinstimmung der experimentellen mit den vorhergesagten Daten.

Abstract

Solar Orbiter is a space probe from the European Space Agency (ESA). It's aim is to discover the sources of solar wind and of the solar dynamo. It will also investigate acceleration mechanisms for energetic particles near the sun. The spacecraft has for this reason a variety of scientific instruments on board and combines them with a unique orbit. Solar Orbiter will have a minimal distance of 0.3 AU and be as close to the sun as the Helios missions. The orbit will be altered with gravity assisted maneuvers at Earth and Venus during the seven years of mission. These maneuvers will increase the heliographic latitude such that the solar poles can be observed by remote sensing instruments. In addition there are also in-situ Instruments which analyse the solar wind, the solar magnetic field, electromagnetic waves as well as energetic particles.

The Energetic Particle Detector (EPD), to which also the High Energy Telescope (HET) belongs, measures those energetic particles accelerated at the Sun. HET measures the high energetic part of those particles: Electrons from 0.3 to 15 MeV, protons and helium Ions from 7 to 100 MeV/nuc and heavier ions from 20 MeV up to 300 MeV/nuc – depending on the ion type. For HET the separation of ^{3}He and ^{4}He is of special interest which shall be detected down to an isotope ratio of 1:100 to identify ^{3}He rich solar eruptions.

This thesis investigates certain aspects which are important during the development of HET as well as thereafter during the data analysis. At first a model was developed which estimates the radiation dose on HET during the seven years of mission. With this model it could be shown that the use of radiation hard electronical parts is sufficient to prevent the instrument from failing due to ionising radiation. Additional mass in form of shielding could therefor be saved and the results were published as internal technical report for the ESA. The report was checked during the Critical Design Review (CDR) process at ESA and the review process was passed successfully in 2014.

As the separation of ^{3}He and ^{4}He is a vital task for HET the capabilities in respect to this have been investigated. The different origins for noise along the signal path were analysed and modeled. Those models then have been applied to simulated data from the GEANT toolkit and the expected sensor response of HET in respect to the separation of ^{3}He and ^{4}He has been calculated. The readout electronic has been dimensioned due to this analysis to separate helium isotopes with an abundance of 1 %. Also the development of the readout software which is currently ongoing was driven by those results.

The HET sensor contains a BGO ($Bi_4Ge_3O_{12}$) scintillation crystal which is used to measure the total energy of incident particles. This type of crystal has certain non-linearities in light yield which depend on particle type as well as energy. For the latter data analysis detailed knowledge about these non-linearities is vital and thus a comprehensive study has been carried out. The light yield of BGO has been analysed with different types of light to heavy ions at the Heavy Ion Medical Accelerator in Chiba (HIMAC). From the comparison of those measurements with simulations calculated with the GEANT toolkit a prediction model for the light yield of BGO could be derived. The model as well as the method were published in "*Nuclear Instruments and Methods in Physics Research Section B: Beam Interactions with Materials and Atoms*", volume 360 (2015) on the pages 129-138. The model could also successfully be verified with additional measurements at HIMAC and showed good agreement of the experimental data with the predicted values.

Contents

List of Figures

List of Tables

Acronyms

1 Introduction

Solar Orbiter is the next ESA mission dedicated to solar and heliospheric physics. In this thesis fundamental research is performed for the development of the High Energy Telescope (HET) sensor which is a particle detector onboard Solar Orbiter. HET will measure high energetic electrons, protons and ions up to iron from roughly 10 MeV/nuc to 100 MeV/nuc for ions. This thesis covers a small part of the development work of HET and is divided in three parts. At first the radiative dose which is expected during the mission is estimated and from this point possible implications for the need of shielding and the use of radiation hard integrated circuits are analysed. Thereafter a theoretical analysis of the isotope separation capabilities of ^{3}He and ^{4}He is performed. This separation capability is a key requirement for the latter scientific work which will be conducted with HET. Since the measuring principle of HET includes the used of a scintillating BGO ($Bi_4Ge_3O_{12}$) crystal the last part characterises non-linearities in the energy-to-light conversion of BGO. A model which can be used to correct the measured data for those non-linearities is developed and verified.

The following section (1.1) will give a short introduction into the current status of heliospheric physics and present how Solar Orbiter and especially the HET will enhance our current understanding of solar and heliospheric physics. The section thereafter (1.2) will introduce the Solar Orbiter spacecraft in detail with a focus on the HET instrument.

1.1 Heliospheric physics

During the last decades the knowledge about our close-by universe has increased constantly and until now it is the only part of space which is accessible to us by in-situ measurements. Because of this the near Earth space plays a major role as laboratory for mechanisms and processes involved in astrophysical and plasma phenomena which we cannot reproduce in any laboratory on Earth. Previous missions like Helios, Ulysses, SOHO, STEREO and many others not mentioned here have increased the current understanding of the solar system. Nevertheless all of those missions had a very focused field of study embedded in its particular solar and heliospheric research at that time. Today we have reached a point at which we have a good understanding of single phenomena on large scales. On the contrary the interconnections and interactions between them as well as the driving mechanisms at smaller scales are still partly unknown. Today the main question driving the heliospheric research is [1]:

How does the Sun create and control the heliosphere?

This comprehensive problem seems to be a giant task for current and future space scientists. It can be split up in four separate but interconnected questions of modern solar physics which are the scientific questions of ESA's long term space program "*Cosmic Vision 2015-2025*" [1]:

1. How and where do the solar wind plasma and magnetic field originate in the corona?
2. How do solar transients drive heliospheric variability?
3. How do solar eruptions produce energetic particle radiation that fills the heliosphere?
4. How does the solar dynamo work and drive connections between the Sun and the heliosphere?

A detailed treatment of these four questions would go beyond the scope of this thesis, thus only their main background shall be introduced briefly on the following pages. Some important parameters of Solar Orbiter which characterise key points of the mission will be mentioned here without going into details about the spacecraft itself. This is done to emphasize the unique capabilities of the Solar Orbiter mission and to explain how these key points will help to answer the open scientific questions. The spacecraft itself is then later introduced in more detail in section 1.2. Even though some questions will be explained with the help of exemplary processes or phenomena it shall be mentioned that this does not mean a claim for completeness. Also the four questions are addressed in a different order than presented before.

How and where do the solar wind plasma and magnetic field originate in the corona?
The solar wind fills and influences the whole heliosphere. It consists of mainly electrons and protons but also contains heavier, charged ions. It continuously streams outwards radially from the Sun at speeds in the range from $300\,\mathrm{km\,s^{-1}}$ to $\approx 750\,\mathrm{km\,s^{-1}}$ [2, 3]. Since the plasma can be considered to have a huge conductivity the interplanetary magnetic field is "frozen" into it. Hence the field is carried radially outwards from the sun. This movement in combination with the solar rotation $\Omega = 1.642 \times 10^{-4} \circ \mathrm{s^{-1}}$ leads to a magnetic field in the form of an Archimedean spiral [4] which is called the "*Parker spiral*" [5]. The curvature of this spiral depends on the out-flowing gas velocity $\vec{v}$. This velocity dependence has a large influence on the heliospheric magnetic field structure. Figure 1.1 shows the resulting magnetic field for two different solar wind speeds of $300\,\mathrm{km\,s^{-1}}$ and $600\,\mathrm{km\,s^{-1}}$ exemplary. The out-flowing solar wind interacts with the magnetospheres and atmospheres of the planets it passes in our solar system. This leads to deformed magnetospheres and partly to atmospheric erosion in absence of a protective planar magnetic field [6].

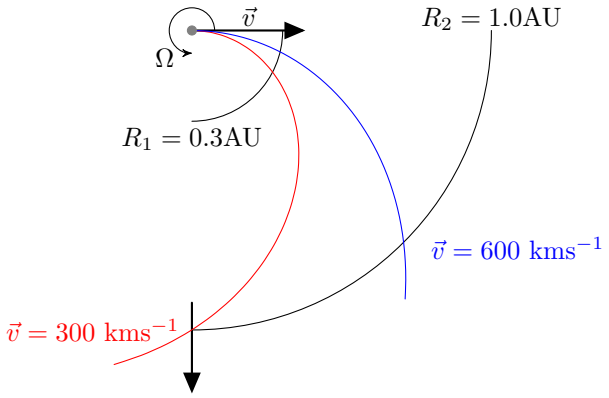

Figure 1.1: Schematic view of the solar wind expansion in the ecliptic for two different flow speeds starting at the same location on the Sun which is indicated as grey circle in the upper left. According to [4].

As it is already indicated in figure 1.1 the solar wind can be divided into two types and their most obvious difference is the velocity. The two wind types are therefore denoted as "*slow*" and "*fast*" solar wind. While the slow solar wind expands at 300 to 500 km s^{-1} the fast one spreads out with ≈ 750 km s^{-1} [2]. In addition to the different expansion speeds the fast and slow solar wind have different compositions and mass fluxes as well as different temperatures [2, 7]. The differences between both wind types arise from their individual origins which are reasonably well understood at large scales. It was found that the fast solar wind originates from coronal holes [8] which are located across the Sun's less active surface areas especially the polar coronal holes [3]. In these areas the magnetic field lines of the solar magnetic field are open and reach into interplanetary space [4] along which the fast solar wind expands in open space. In contrast to that, the slow solar wind originates from areas at the Sun's more active surface [2]. In these areas the magnetic field lines are closed and form large loops in which the plasma is enclosed. Since the plasma cannot escape from these closed loops the reconnection process of magnetic field lines is supposed to play an important role for the sources of the slow solar wind. Nevertheless the exact sources are unknown and currently under investigation [9].

To identify the sources of the slow solar wind on smaller scales it is necessary to determine the solar wind parameters and correlate them with remote-sensing observations of the structure of photosphere and corona where possible candidate source regions are located. Figure 1.2 shows the evolution of small scale structures flowing in the solar wind observed with the STEREO Heliospheric Imager (HI) instrument [10] from a distance of 1 AU. The HI is a wide-angle visible light imager with two cameras HI-1 and HI-2. The plot is composed by stacking together the central lines of differential images of HI-1 (elongation $< 18°$) and HI-2 (elongation $> 18°$) of STEREO-A at consecutive times [11]. The central line in this case represent the view in the ecliptic and is denoted with elongation. The elongation is a measure for the radial distance to the Sun and the moving small-scale structures are visible as diagonal lines from the bottom axis upwards. The different slopes of these lines denote different propagation velocities. Collisions and overlaps of structures with different speeds can be observed. This blurs the structures and information about their exact origins. Solar Orbiter will be as close to the Sun as 0.3 AU. This radial distance corresponds to an elongation of 16.7° in the time-elongation plot and is indicated by the red solid line. It can be seen that at such a close distance the small structures can be separated much more clearly and undisturbed. This will enable measurements of the unevolved

small-scale structures in the solar wind with Solar Orbiter.

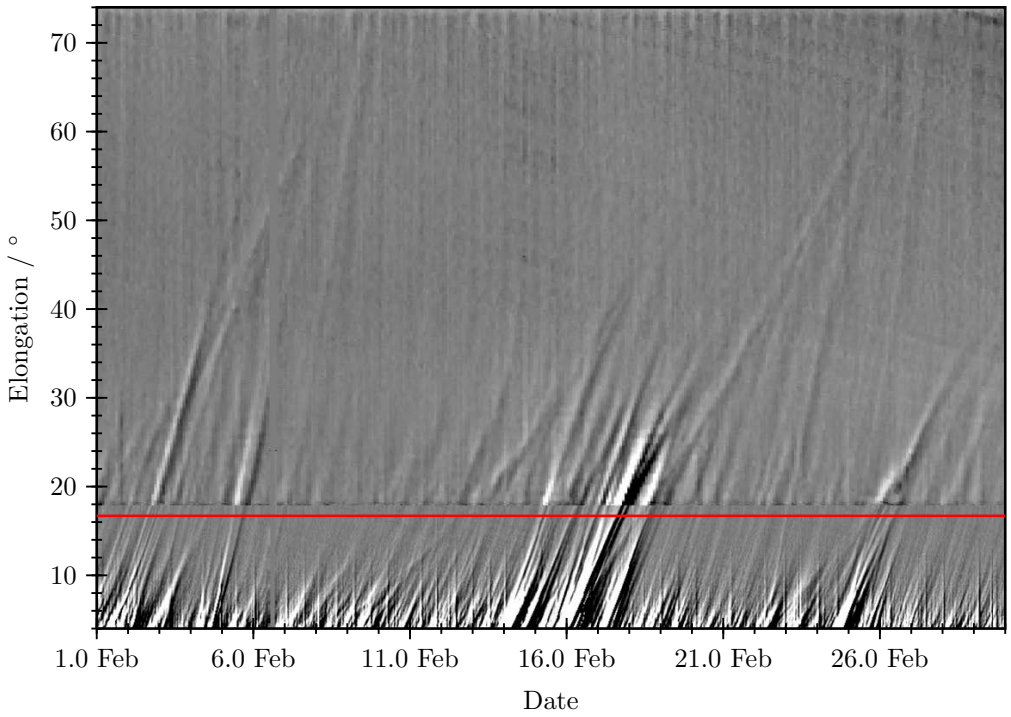

Figure 1.2: Time-elongation plot constructed from observations with STEREO-A Heliospheric Imager instrument. The evolution of small scale structures can be seen as diagonal lines with their slopes corresponding to different propagation velocities. The red line indicates the closest distance of Solar Orbiter to the Sun. For more information see text. Figure according to [1, 12].

How does the solar dynamo work and drive connections between the Sun and the heliosphere?

The solar dynamo produces the Sun's magnetic field which connects the interior with the interplanetary space. It is dominated by an 11-year activity cycle of the Sun which modulates the heliosphere. The magnetic field is created by complex 3-dimensional mass flows in the convection zone of the Sun. It is wound up along the equator due to differential rotation. This produces a torodial magnetic field which is transported to the poles by meridional flows [13]. Since the direction and speed of mass flow drives the solar dynamo an accurate determination of these parameters is needed to fully understand the process. Until today there were no remote observations of the Sun's polar regions performed but these observations are important for the understanding of mass flows in this region. Solar Orbiter will have orbits which will reach out of the ecliptic and will then be able to perform exactly the necessary measurements at high solar latitudes. As a result the directions and velocities of the meridional flows will be precisely determined and subduction zones will be identified. Solar Orbiter will also act as a measurement device for helioseismic observations in combination with Earth bound observations. This enables the investigation of volumes lying deep in the convection zone for a comprehensive understanding of the solar dynamo.

How do solar transients drive heliospheric variability?
The heliosphere is filled with the solar wind plasma which carries the magnetic field outwards (see figure 1.1) and energetic charged particles which propagate along the magnetic field lines. Transients like Coronal Mass Ejections (CMEs), flares and shock waves constantly influence this appearance on short time scales. One of the largest and most important transients regarding these short term variation are the CMEs [14]. A CME denotes the rise of a huge amount of gas within a magnetically closed volume from the lower corona into the open space [15]. It belongs to the most energetic activities of our Sun with energies of 1×10^{25} J and the ejection speeds vary from $100\,\mathrm{km\,s^{-1}}$ up to more than $2000\,\mathrm{km\,s^{-1}}$ [16, 14, 17]. These impressively large events have an influence on the structure of the heliospheric magnetic field. They also may reach the Earth's magnetosphere and may cause geomagnetic storms which lead to aurorae in the upper atmosphere. The geomagnetic storms may affect power grids since they can induct large currents there. Hence the prediction of geomagnetic storms will become even more important in the near future and the understanding of the formation and propagation of those structures in the heliosphere is the key to a working 'space weather' prediction system protecting the Earth's infrastructure.

The effects of CMEs on the Earth are partially understood but the much more important questions why they erupt and how they evolve upon passage through the heliosphere are still unanswered. CMEs originate from regions with a highly-sheared magnetic field, wound up due to the differential rotation of the Sun as it was described earlier. Current models predict CME structures like a twisted flux rope [18] and today's knowledge about CME structures was greatly improved when multi-spacecraft observations with the two STEREO spacecraft became possible [19]. Furthermore current measurements are only performed inside the ecliptic providing no information about the 3-dimensional structure of CMEs. Solar Orbiter will not only measure plasma and magnetic field parameters near the Sun and therefore provide data for CME structures very close to it's primordial structure. The spacecraft is also equipped with a complete suite of remote sensing instruments and will measure magnetic fields on the Sun with unique precision. Additional observations with spectrograph, X-ray imaging and coronagraph can be used to identify the processes which transfer the stored magnetic energy into kinetic energy. Solar Orbiter will also have orbits reaching out of the ecliptic to provide more information about the out-of-ecliptic structure of CMEs. It will also act as additional observation point in the inner heliosphere and it will improve the capabilities of multi-spacecraft observations. With this information about the early structure and the evolution of CMEs from the Sun to a distance of 1 AU can be investigated with the help of Solar Orbiter.

How do solar eruptions produce energetic particle radiation that fills the heliosphere?
The heliosphere is filled with a variety of energetic particles belonging to many different sources. The Sun itself is one of the most powerful and temporarily variable source of energetic particles producing so called Solar Energetic Particles (SEPs). These highly energetic particles may hit the Earth and, depending on their energy, penetrate the Earth's magnetosphere, sometimes even through the whole atmosphere such that they and their secondary particles can be detected at ground level. SEPs can introduce radiation damage in spacecraft electronics, they can disturb communication systems or other electronic devices. They also may cause additional radiation dose to human beings, especially to airborne personnel and astronauts.

In current theory there are two mechanisms in the solar system which accelerate electrons and ions to such large energies (up to $\approx$ GeV) [20]. The first is the acceleration at shock fronts, e.g. in front of CMEs. If those CMEs are fast enough they can drive shock fronts [21, 22] which can act as particle accelerators inside the heliosphere [23]. CME driven shocks accelerate particles on time scales of minutes and longer and can convert up to 10 % of it's energy into energetic

particles [17]. Those shocks are often extended over a large spatial range.

Another possible mechanism of particle acceleration are solar flares. In this case magnetic fields are reconnected close to the Sun and magnetic energy is released. Since these fields are changing over time they create strong electric fields which accelerate charged particles reaching theoretically up to 10 GeV within several seconds [22]. These two acceleration mechanisms were assigned to two types of SEPs events, the gradual and the impulsive ones [20] (see also figure 2.1 therein). The terms "gradual" and "impulsive" in this case describe the temporal profiles of electron and proton intensities, distinguished in impulsive and long-duration [20].

Gradual events typically last from hours to even days and are associated with shock driven particle acceleration over large angular ranges for example at CME shock fronts. CME observations show that only few CMEs can be associated with energetic particle events [14] suggesting a more complex process which is currently not fully understood. It is very likely that especially for CMEs driven shocks starting conditions are important to generate energetic particles such as shock geometry and seed populations [24, 25].

In contrast to that the impulsive type of SEPs events happens on shorter timescales than the gradual ones. Those events do also have a narrower spread of $\lesssim 30°$ [26]. They show a significantly enhanced ratio of ^{3}He to ^{4}He and increased electron intensities. Those events are related to flares. During reconnection of the magnetic field, the electrons and ions which are trapped in magnetic loops are accelerated in sunwards and anti-sunwards directions. Especially the accelerated electrons then produce X-ray signatures due to collision and deceleration. The fraction of particles which manages to escape along open field lines into the interplanetary space has a different ion composition and isotope abundance in respect to the typical solar wind composition. In the solar wind the ^{3}He to ^{4}He ratio is about 1:2300 [27, 28] whereas it can be enhanced in impulsive events. Solar energetic particle events with ^{3}He to ^{4}He ratios of more than 1 % are called ^{3}He-rich events. The ratio can even be much larger increased by a factor of 1×10^3 to 1×10^4 with abundance ratios of unity or even more than unity.

Apart from the acceleration of SEPs, its transport through the heliosphere is still a topic of ongoing research. The propagation through the interplanetary magnetic field is described by the focused transport model [29, 4]:

$$\frac{\partial f}{\partial t} + \underbrace{\mu v \frac{\partial f}{\partial z}}_{\text{Convection}} + \underbrace{v \frac{1-\mu^2}{2L} \frac{\partial f}{\partial \mu}}_{\text{Focusing}} - \underbrace{\frac{\partial}{\partial \mu}\left(D \frac{\partial f}{\partial \mu}\right)}_{\text{Diffusion}} = Q(z, \mu, t) \tag{1.1}$$

with f being the phase-space density of charged particles in a field-aligned transport, v the particle speed, $\mu = \cos(\theta)$ the cosine of the particle's pitch angle[1], D the pitch angle diffusion coefficient and L is the so called focusing length which is a function of the magnetic field B [4]:

$$L = -\frac{B}{\frac{\partial B}{\partial z}} \tag{1.2}$$

This model describes the evolution of the particles' phase-space density $f(z, v, \mu, t)$ which consists of three main parts. The *convection* term describes the propagation of particles with velocity v along the magnetic field line, described by the z-direction in this model. Since this equation is restricted to field-aligned transport, the z direction always coincides with the magnetic field direction. The *focusing* term describes the reduction of the particles' pitch angle when moving into regions with weaker magnetic fields $B(z)$. Figure 1.3 shows a sketch of this focusing effect where a particle traverses from high (left side) to low (right side) magnetic field strengths. Upon

[1] The pitch angle describes the angle between the particle's velocity vector and the magnetic field vector.

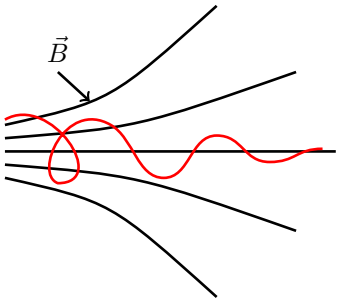

Figure 1.3: Sketch of the focusing of charged particles in a diverging magnetic field. The red line indicates the trajectory of a particle moving along the central field line. After [29].

passage to lower B-fields the particle's pitch angle is reduced. The last *diffusion* term describes the scattering of pitch angles with the diffusion coefficient D as parameter. From this equation one can see that there are two competing processes, the focusing and the diffusion. Depending on the relative strength of these both processes the particles arrive at 1 AU either in a very narrow, beam-like distribution when the focusing dominates or in a much more isotropic distribution in the diffusion case. In the focusing case the intensity-time profile is similar to that at the time of injection and only broadened due to different velocities and therefore different propagation times. In the diffusion dominated case the particles' path lengths are less predictable but in general the temporal information will get blurred. In this case the shape of a flare-like delta injection of particles at $t = 0$ might look like a gradual event after arriving at 1 AU (similar to figure 3 in [30]).

Recent multi-spacecraft observations with STEREO showed that the simple picture of gradual and impulsive events has to be modified. There were ^{3}He-rich and electron-rich events observed which showed a wide-spread of up to 136° for ^{3}He-rich [31] and up to 360° for electron-rich events [32, 33]. It is therefore possible that SEP measurements at 1 AU are composed of a mixture of acceleration processes [25]. The focused transport also is limited to field-line aligned transport of particles but there might also be a non-negligible amount of particle transport perpendicular to magnetic field for SEPs [34, 35, 36].

Solar Orbiter and especially the High Energy Telescope (HET) will measure those energetic particles very close to the Sun. It will combine those measurements with imaging instruments, X-ray spectrometer and coronagraph measurements which allows a complete characterisation of the particles' starting conditions. With those measurements it will be able to investigate the acceleration mechanisms and their exact origins at the Sun to a much greater extent than currently possible. The HET will also resolve ^{3}He-rich events down to a ratio of 1 % which allows a characterisation of the events seen. Due to it's close proximity the particles' temporal, spatial and energetic characteristics are similar to those at injection time. The close vicinity to the Sun also increases the count statistics obtainable in a given time frame. This is especially interesting since current research indicates that there are events with smaller intensities, called micro-flares. Those events are candidates for coronal heating processes but cannot be observed at Earth distance due to the background signal. Solar Orbiter will enable us to observe those micro-flares and HET in this case will be able to acquire data in the high-energy regime to reveal the micro-flares' contribution to the coronal heating process.

Finding solutions to those four questions will bring us in a much better position to understand how the Sun creates and controls the heliosphere. On this basis we will then be able to do prediction for space weather which directly influences people and instruments at Earth. ESA's Solar Orbiter mission is designed in such a way that it can address all four questions with a carefully selected set of instruments. Not only that Solar Orbiter will perform revolutionizing unique measurements but they will be even more striking in combination with Earth bound observations at 1 AU. Solar Orbiter will then provide well defined starting conditions for particle transport mechanisms through interplanetary space. The instruments on board Solar Orbiter will be much more advanced than those on present space missions. Hence Solar Orbiter will be able to reach time resolutions of 1 s which to the current day is unique for such a suite of instruments. Solar Orbiter's capabilities will also benefit from NASA's planned Solar Probe Plus mission which will go even closer to the Sun [37] enabling observations from two spacecraft within 0.3 AU. The HET will contribute to all these scientific goals by measuring the part of the SEPs which occur at high energies and therefore plays an important role in the instrument suite of Solar Orbiter. As some measurement capabilities of Solar Orbiter have already been mentioned it's scientific payload will be introduced in the next section in more detail.

1.2 Solar Orbiter

As noted above, Solar Orbiter is the first mission to be launched with ESA's "*Cosmic Vision 2015-2025*" plan. Solar Orbiter's main objective is to investigate the properties of energetic particles and fields close to the Sun and combine those measurements with high resolution, remote sensing observations from the solar atmosphere [38, 39]. The mission was selected in October 2011 to be the program's first medium class mission [40]. Currently the official launch date is in October 2018 and the mission will have a three years cruise phase after which a nominal science phase of four years will follow. An optional, extended science phase is also baselined for 3 additional years. Solar Orbiter will be the first spacecraft since the Helios mission in 1974/76 to study the Sun from as close as 0.3 AU and will combine those measurements with high-latitude (up to 35° above the ecliptic) observations enabling studies of the solar poles like they were performed by the Ulysses mission (launched in 1990). But in contrast to Ulysses the Solar Orbiter spacecraft will have remote sensing instruments on board for those observations and combine them with the in-situ experiments. Both missions, Helios and Ulysses, were very special in respect to their scientific objectives and they both had a large impact on our view on the solar system. Helios' unique feature was that it's distance to the Sun was one of the lowest ever reached by a spacecraft ($\approx$ 0.29 AU) [41]. It's scientific payload contained mainly experiments for plasma and radio wave analysis, magnetometers and energetic particle detection instruments. The close distance to the Sun could be used to investigate particle populations and propagation very close to their source which is much less disturbed than at 1 AU. Ulysses on the other hand had a minimal distance of 1 AU but it's unique specialisation was that it's highly inclined orbit with inclinations of about 80° enabled the investigation of polar coronal holes and the solar wind originating from those. Like Helios, Ulysses also had magnetometers, solar wind plasma experiments, radio wave instruments and energetic particle instruments on board but no imaging instruments [42].

In contrast to the two other missions, Solar Orbiter will contain remote sensing units in addition to radio-wave and plasma experiments together with magnetometers and energetic particle instruments and will have a significantly improved temporal resolution of up to 1 s[2]. Another important point for scientific investigation will be that the Solar Orbiter orbit is designed in such

[2]Helios had a minimum time resolution of 4 s for in-situ energetic particle instruments

a way that it's orbit will contain parts in which the spacecraft's rotation is close to the Sun's rotation period enabling scientists to observe points of interest in the Sun's atmosphere over a longer time period than before at distances well below 1 AU. Solar Orbiter will also have inclined orbits which enables us to observe polar coronal holes with the complete instrument suite of scientific instruments. It will therefore be designed and equipped with a variety of instruments enabling it to perform measurements necessary to find answers to all of the four central questions mentioned in the previous section (1.1) and combine the best features of Helios (short distance to the Sun), Ulysses (highly inclined orbit) and STEREO (imaging instruments) to a highly versatile and powerful scientific system which will be even more powerful if combined with observations at 1 AU from STEREO, SOHO or other observatories at Earth and the planned Solar Probe Plus mission.

Figure 1.4 shows a drawing of the Solar Orbiter satellite with instruments attached to it. The positions of both HET sensor heads are marked by red arrows with their four viewing directions shown as blue arrows. Since Solar Orbiter will have orbits close to the sun it needs a heat shield pointing in direction of the Sun to maintain an appropriate temperature level on the spacecraft. This heat-shield can be seen in that figure as a large, rectangular panel pointing to the right side. The solar panels are omitted in the image but they will be attached to the left and right side on the spacecraft body. From the top part of the spacecraft body a boom runs away to the left side. On this boom there are two magnetometers which will measure the magnetic field. On the bottom of the spacecraft there is an antenna to communicate with Earth. The instruments on board Solar Orbiter are listed in table 1.1 for the remote sensing instruments and in table 1.2 for the in-situ instruments with the responsible principal investigator (PI). The instruments with their locations are also labelled in figure 1.4. The set of all those different instruments will allow to link solar wind structures back to their source regions at the Sun and in combination with the sun-close and high-latitude orbit and a unprecedented time resolution to perform research in a regime which has not been accessible before. Since this thesis deals with the High Energy Telescope (HET) which is one sensor of the Energetic Particle Detector (EPD) the next section will give more detailed information about the EPD and the section thereafter will focus on the EPT/HET sensor.

Instrument	Principal Investigator (PI)	PI Institution	Collaborating countries
Extreme Ultraviolet Imager (EUI)	Pierre Rochus	Centre Spatial de Liège	Belgium, United Kingdom, France, Germany, Switzerland
Coronagraph (METIS)	Ester Antonucci	INAF- Astronomical Observatory of Turin	Italy, Germany, Czech Republic
Polarimetric and Helioseismic Imager (PHI)	Sami K. Solanki	Max-Planck-Institut für Sonnensystemforschung	Germany, Spain, France
Heliospheric Imager (SoloHI)	Russell A. Howard	US Naval Research Laboratory	USA
Spectral Imaging of the Coronal Environment (SPICE)	-	European-led facility instrument	-
X-ray Spectrometer/Telescope (STIX)	Säm Krucker	FHNW	Switzerland, Poland, Germany, Czech Republic, France

Table 1.1: Remote-sensing instrument list on board Solar Orbiter with responsible principal investigator, PI institution and collaborating countries [43, 44].

Instrument	Principal Investigator	PI Institution	Collaborating countries
Energetic Particle Detector (EPD)	**Javier Rodriguez-Pacheco**	**University of Alcala**	**Spain, Germany, USA, ESA**
Magnetometer (MAG)	Tim Horbury	ICSTM	United Kingdom
Radio and Plasma Waves (RPW)	Milan Maksimovic	LESIA, Observatoire de Paris	France, Sweden, Czech Republic, Austria
Solar Wind Plasma Analyser (SWA)	Christopher Owen	Mullard Space Science Laboratory	United Kingdom, Italy, France, USA

Table 1.2: In-situ instrument list on board Solar Orbiter with responsible principal investigator, PI institution and collaborating countries [43, 44].

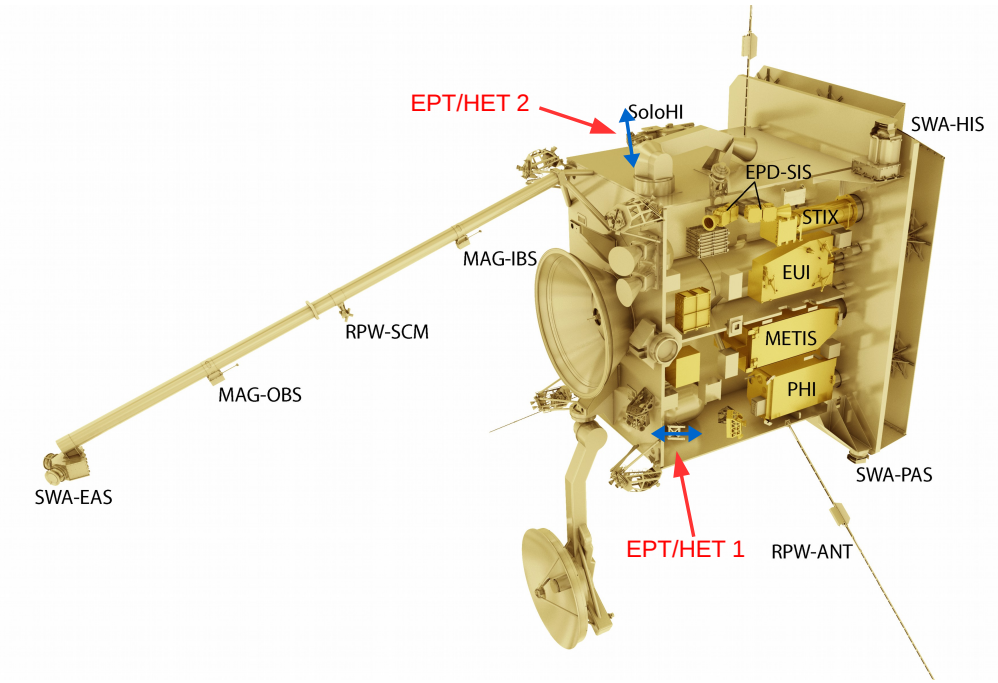

Figure 1.4: CAD drawing of the Solar Orbiter spacecraft with positions of both EPT/HET sensors indicated with red arrows. Also the viewing directions (forward/backward for EPT/HET 1, north/south for EPT/HET 2) are shown with blue arrows. Several other instruments according to tables 1.1 and 1.2 are also shown and labeled. The heat-shield on the right side is directed at the Sun while the solar panels are omitted here. From [45].

1.2.1 Energetic Particle Detector (EPD)

The EPD is a suite of instruments all designed to measure energetic particles. It consists of four individual sensors with different individual energy measurement ranges:

- Suprathermal Electrons and Protons (STEP)
- Suprathermal Ions Spectrograph (SIS)
- Electron Proton Telescope (EPT)
- **High Energy Telescope (HET)**

The University of Kiel is involved in the development of all of those sensors and three of them are completely built in house (STEP, EPT and HET). In addition to the four sensors the EPD suite has a common Instrument Control Unit (ICU) which contains the Central Data Processing Unit (CDPU) and the power supply for the sensors. The ICU is responsible for the communication between the sensors and the spacecraft and for the power distribution within EPD. Figure 1.5 shows a sketch of the structure of the whole EPD suite. For STEP and SIS there is only one unit per sensor and for EPT and HET there are two units per sensor looking along two different directions.

Each sensor is specially designed to measure in a well defined energy range as plotted in figure 1.6. STEP will measure protons from roughly 3 to 100 keV and electrons from 2 to 100 keV. EPT will then cover the energy range from 0.02 to 15 MeV for protons and from 20 to 400 keV for electrons and to some extent also measure helium ions with the capability to resolve ^{3}He and ^{4}He isotopes in this energy range [47]. SIS will then provide data for ions in a range from 30 keV/nuc up to 10 MeV/nuc depending on the ion species. HET will then cover the complete high energy range for electrons, protons and ions from several MeV/nuc up to several hundreds MeV/nuc, also depending on the exact ion type. Figure 1.6 also shows the coverage of individual ion species. The complete energy range is covered especially for electrons and protons as well as for light ions like ^{3}He and ^{4}He but there is a gap for heavier ions between SIS and HET.

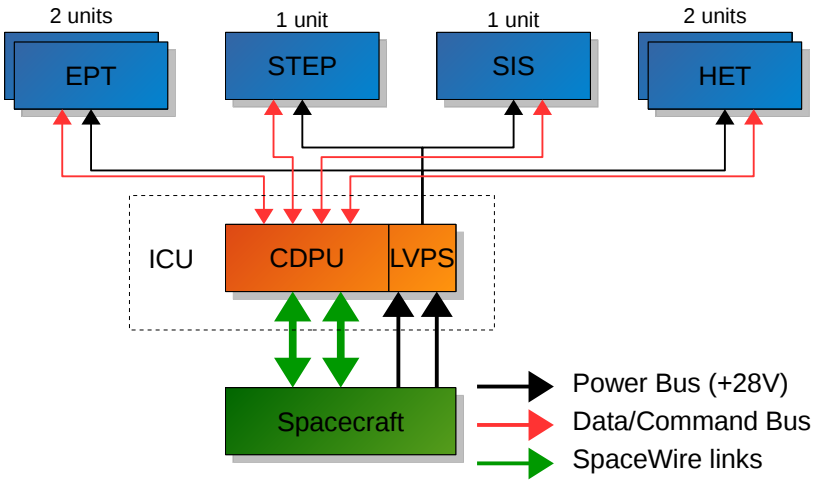

Figure 1.5: Sketch of Energetic Particle Detector (EPD) structure. Black lines indicate the 28 V power lines running through the low voltage power supply. Red lines indicate the data and command bus. After [46].

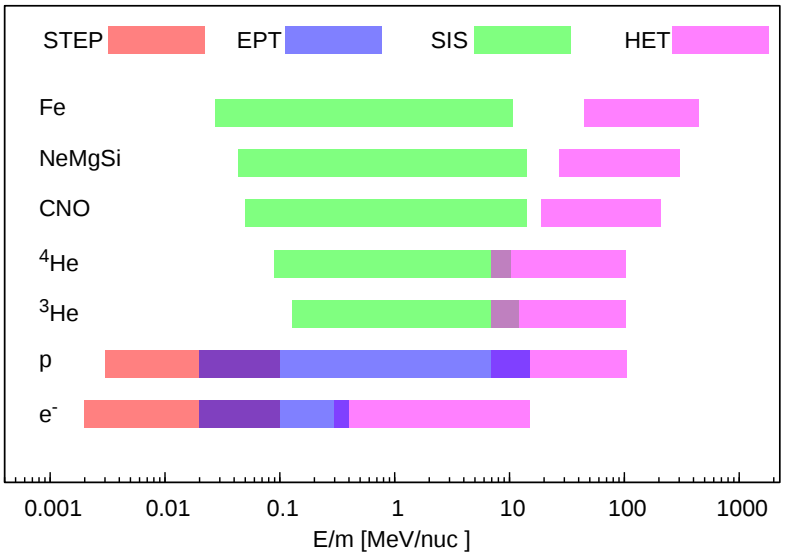

Figure 1.6: Energetic Particle Detector (EPD) energy coverage for each of the four individual sensors STEP, SIS, EPT and HET [48].

1.2.2 EPT/HET

EPT and HET share a common electronics box and therefore they are described both in this section although the focus will still be on the HET sensor which will be explained in more detail. As mentioned in section 1.2.1 there are two units of EPT/HET instruments located on the spacecraft. Both are mechanically identical and their only difference is the viewing direction. One EPT/HET looks along the nominal Parker spiral within the ecliptic (see section 1.1) and the other's viewing direction is perpendicular to that in north/south direction. The viewing directions are shown in figure 1.7 together with magnetic field measurements from Helios-1. The color code indicates along which direction the magnetic field is oriented most of the time. As charged particles perform a gyrating movement along the magnetic field lines, the red areas denote the direction in which particles from the Sun and from the opposite direction are expected to be found. Hence the orientation of sunwards and anti-sunwards looking particle detection telescopes is preferred to look along this axis as it is done for STEP, EPT and HET. The position at $(0, 0)$ in this coordinate system points directly at the center of the Sun's photosphere.

Both sensor heads are positioned on the spacecraft body and are protected by the satellite's heat shield. Figure 1.4 shows a CAD view of the Solar Orbiter spacecraft with the positions of both instruments indicated by red arrows as well as their viewing directions with blue arrows. The heat shield is located at the very right side of the spacecraft and points in the direction of the Sun.

The EPT/HET sensor heads are designed in such a way, that they have a free field-of-view in two directions per unit (forward/backward and north/south). The EPT/HET instrument is shown as a CAD drawing in figure 1.8. The instrument consists of an electronics box on top of which the two sensor heads of EPT and HET are installed and has a size of about $15 \times 15 \times 15\,\mathrm{cm}^3$. The design of the HET sensor head [49] has some heritage from the Mars Science Laboratory (MSL) Radiation Assessment Detector (RAD) [50] which is currently measuring energetic particles on the martian surface on-board the Curiosity rover. It consists of a scintillating BGO crystal which acts as a calorimeter and it has several silicon tracking detectors

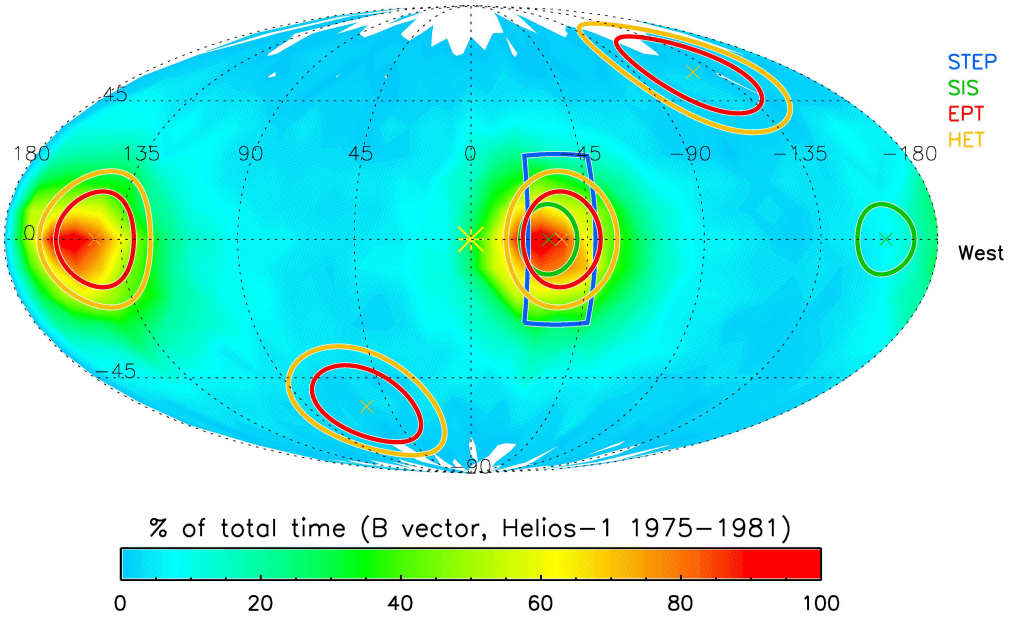

Figure 1.7: Field of views for STEP (blue), SIS (green), EPT (red) and HET (yellow) in the spacecraft coordinate frame and Mollweide projection. The underlying heatmap shows coverage of magnetic field vector measured with Helios-1 [48].

which allow to distinguish between particles entering from the forward or backward direction. The instrument uses coincidences between tracking detectors and the calorimeter to identify ions by the $\frac{\mathrm{d}E}{\mathrm{d}x}$ vs. E_{total} method [51, 52] and those coincidences in combination with segmented silicon detectors can be used to lower the count rate during high flux events.

In this thesis the radiation hardness of the EPT/HET instrument will be analysed since this is one key point of possible failures of the mission. In addition to that the expected instrument's response will be investigated and modeled with respect to it's measurement capabilities to validate that HET will comply with the scientific requirements. As the instrument uses a BGO scintillating crystal fundamental research is performed to identify scintillation non-linearities in the light output [53]. This is performed concerning later data analysis during the mission and the time thereafter.

A more detailed description on the inner parts of the EPT/HET sensor including the electronics and the measurement principle can be found in section 3 (page 41). There are also the various models described which were built and used for data acquisition of this thesis.

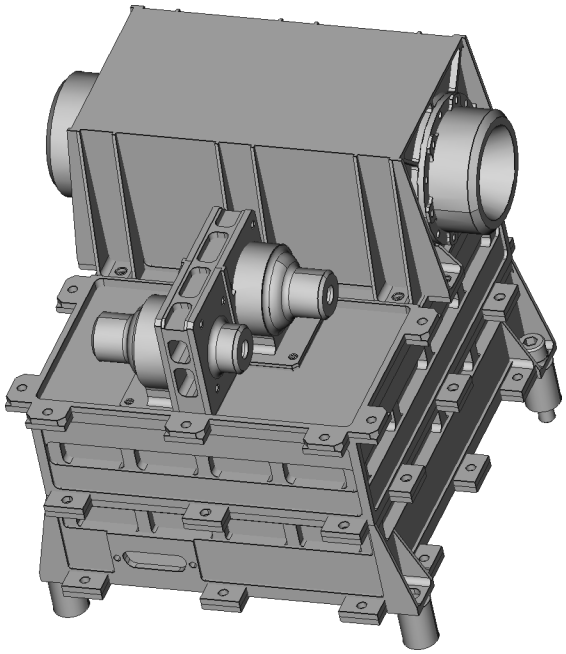

Figure 1.8: CAD top view of EPT/HET instrument [54]. Visible is the electronics box and the two sensor heads on top of it. The smaller sensor head consisting of two barrels in the front belongs to EPT and the bigger rectangular one in the background is the sensor head of HET.

2 Particle matter interaction and particle detection

This chapter focuses on particle matter interaction and how these interactions can be used to detect particles. At first the Bethe formula is presented which describes the deceleration of fast ions when passing through a target of a given material (section 2.1). Afterwards, in section 2.2, two types of detectors are introduced which can be used to transform the energy deposition of particles into a measurable signal starting with the solid state detectors and afterwards explaining scintillators. In the last section (2.3) Geometry and Tracking (GEANT) will be introduced which is a toolkit for the simulation of particle-matter interaction and transport through a given geometry.

2.1 Bethe Formula

Charged particles passing through matter cause interactions with the traversed material. For fast ions moving through such a material these interactions are mainly due to inelastic collisions with the host material's electrons. The mean energy deposition for ions per path length can be described by the relativistic Bethe formula [55]:

$$-\left\langle \frac{\mathrm{d}E}{\mathrm{d}x} \right\rangle = \frac{4\pi n Z^2}{m_e c^2 \beta^2} \cdot \left(\frac{e^2}{4\pi\epsilon_0} \right)^2 \cdot \left[\ln\left(\frac{2 m_e c^2 \beta^2}{I \cdot (1-\beta^2)} \right) - \beta^2 \right] \tag{2.1}$$

where Z is the primary particle's charge number, n describes the host material's electron density, $\beta = \frac{v}{c}$ where v denotes the particle's velocity and I is the material's mean excitation potential which can be found in literature for various materials and compounds [56, 57]. Electrons need a slightly different treatment due to other radiative losses and due to the fact that they have the same masses as the orbital electrons. Incident primary electrons are also indistinguishable from electrons of the target material which has also to be taken into account [55]. The value of $dEdX$ is also called the Linear Energy Transfer (LET). Equation 2.1 is valid as long as the particle's velocity is too large to perform a charge exchange with the target material [55]. Also for higher, relativistic energies there are additional corrections necessary. Figure 2.1 shows the solution of equation 2.1 for protons and helium ions impacting on a silicon target in the energy range of 0.1 to 100 MeV/nuc. At low energies the value of $\frac{\mathrm{d}E}{\mathrm{d}x}$ bends down towards lower values. This is the energy region in which charge transfer between the energetic particle and the target material is happening and the results become unphysical without any additional correction.

The LET ($\frac{\mathrm{d}E}{\mathrm{d}x}$) of an 100 MeV/nuc proton passing though a silicon target calculated with equation 2.1 is plotted in figure 2.2. There the energy loss is shown as a function of depth inside the target. The increasing value of $\frac{\mathrm{d}E}{\mathrm{d}x}$ with decreasing energy E leads to the formation of a "*Bragg peak*" at the end of the particle's trajectory where the LET reaches it's maximum and the particle has lost all it's energy (around $x = 41\,\mathrm{mm}$).

The particles' interaction with the target will decelerate them since $\frac{\mathrm{d}E}{\mathrm{d}x} < 0$ and the energy is transferred to excitations and ionisations in the material. These excitations can then be utilised in combination with special target materials to measure a particle's energy deposition inside a

detector. Two widely used detector types are the Solid State Detectors (SSDs) and scintillators which are introduced in the next section.

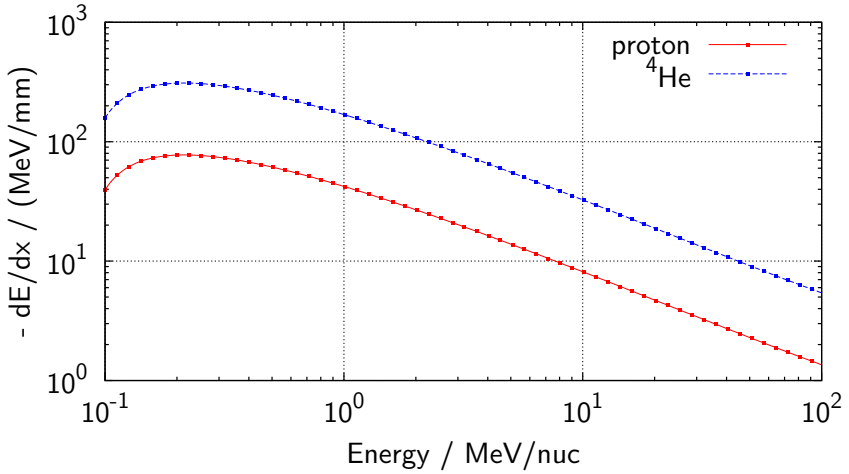

Figure 2.1: Plot of the Bethe formula (equation 2.1) with protons (red) and helium (blue) when passing through a silicon target without any additional corrections. The function is not valid in the lower energy range where a decrease of $\frac{\mathrm{d}E}{\mathrm{d}x}$ can be seen.

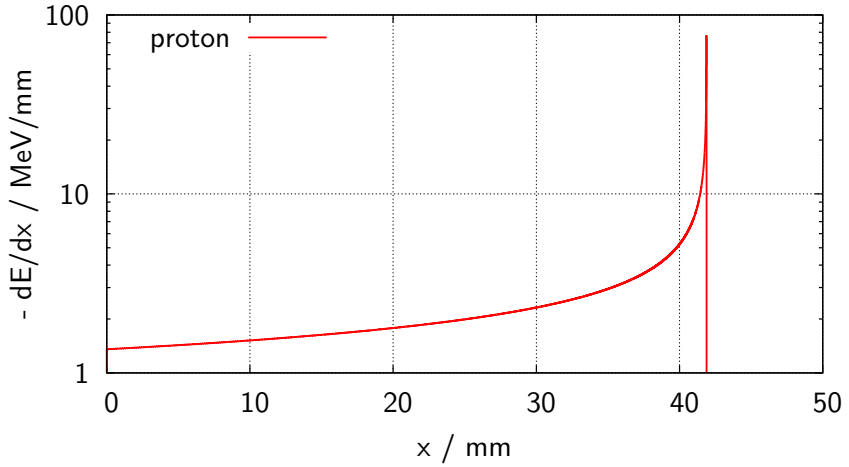

Figure 2.2: LET of 100 MeV protons passing though a silicon target as a function of the penetration depth x with the Brag peak around 41 mm.

2.2 Particle detectors

To these days the two most important particle detectors are Solid State Detectors (SSDs) and scintillators. A combination of both detector types will be used in HET on Solar Orbiter hence both of these types are described here on the basis of the used detectors starting with silicon SSDs and followed by BGO and BSO scintillation crystal.

2.2.1 Solid State Detector (SSD)

SSDs are detectors based on semiconductors in which electrons are excited from the valence band to the conduction band to form electron-hole pairs by transfer of energy from the incident particle. Today there are three main types of semiconductors which are used for particle detection [55]:

- **Silicon (Si)**
- Germanium (Ge)
- Gallium arsenide (GaAs)

The choice of the semiconducting material for a special application depends on the exact purpose since each has it's own field of applications. Silicon is the material which can be produced in the purest quality nowadays and is relatively cheap compared to the other two. Germanium has the smallest bad gap which is as low as 0.7 eV so that it is used in applications where high energy resolution is necessary. Gallium arsenide detectors have a very good resistance against radiation-damage-induced changes in detector parameters and are used in cases where radiation hardness is vital [58]. All detector types require several eV for the creation of a single electron-hole pair [59]. In the case of HET silicon detectors are used which have a mean energy of 3.6 eV for the creation of an e-h pair at room temperature. Based on this mean energy the number of pairs produced by an incident particle can be estimated. For energies of some keV this results in a few thousands of electrons. The number of thermally excited charge carriers at room temperature can be estimated as $n_{\mathrm{Si}} = 1 \times 10^{10}\,\mathrm{cm}^{-3}$ [60]. In typical detector applications (300 µm thickness, $\approx 1\,\mathrm{cm}^2$ surface) this corresponds to $3 \times 10^8\,\mathrm{cm}^{-3}$ free charge carriers which is orders of magnitudes higher than the measurement signal strength. As a result the measurement signal would be completely hidden in the thermally created noise. To overcome this problem the semiconductor detectors are reversely biased creating a depletion region inside the detector where no free charge carriers are present except for those created due to ionising radiation. It is desired to have a depletion region which extends over the complete thickness of the detector as only energy depositions in the depletion region can be detected. The required voltage to extend the depletion region over the whole detector is given by [61]

$$U_{\mathrm{Bias}} \approx \frac{z^2 \cdot eN_D}{2\epsilon\epsilon_0} \tag{2.2}$$

where z is the thickness of the detector, ϵ and ϵ_0 denote the relative and vacuum permittivity and N_D is the donator dopant concentration which typically varies from 1×10^{12} to $1 \times 10^{14}\,\mathrm{cm}^{-3}$ for silicon detectors. For a given detector thickness of 300 µm the depletion voltage is then in the order of 70 V but strongly depends on the actual dopant concentration.

The electric field $\vec{E}$ which is created by the bias voltage also accelerates the charge carriers to velocities as high as $1 \times 10^7\,\mathrm{cm\,s}^{-1}$ [62] resulting in very short collection times in the order of nanoseconds [63] due to the very high carrier mobility in the semiconducting material. This is another positive property of SSDs as it enables radiation detection with very short coincidence intervals and at high count rates.

2.2.2 Scintillators

Scintillation materials emit light after absorption of ionising radiation as for instance by electrons, γ-rays or ions. In most applications the scintillators are solid but there are also liquid or gaseous ones. All scintillators have in common that the energy deposited inside the material due to the incident particle leads to electronic excitation of the materials' electrons which then relaxes under emission of photons. Scintillators can be separated into organic and inorganic scintillators where the latter one can be further differentiated into doped and intrinsic scintillators. The scintillation principle is similar for all those types and will be described for the inorganic, intrinsic ones since both scintillation materials ($Bi_4Ge_3O_{12}$ and $Bi_4Si_3O_{12}$) investigated here belong to this category.

The process of scintillation can be divided into four regimes, each dominated by different processes on timescales varying from sub femto-second to several nanoseconds as they can be seen in figure 2.3. In the first part (I) and on the shortest timescales from 1×10^{-16} s to 1×10^{-14} s the excitation of the primary particle, in this case a γ-ray, takes place and excites electrons from core and/or valence bands into high energy states in the conduction bands creating the same amount of holes in the lower energy bands. The electrons (e in figure 2.3) may undergo inelastic electron-electron scattering ($e \rightarrow e+e+h$) increasing the number of charge carriers while relaxing to the lower edge of the conduction band. The holes (h) on the other hand also tend to relax into higher lying bands via auger processes also creating more charge carriers ($h \rightarrow h+h+e$).

During the second step the electrons and holes thermalise to the band edges creating a charge carrier population at the lower edge of the conduction band (electrons) as well as at the higher edge of the valence band (holes). This thermalisation occurs on timescales of up to picoseconds [65]. During thermalisation the charge carriers may interact with the host lattice creating

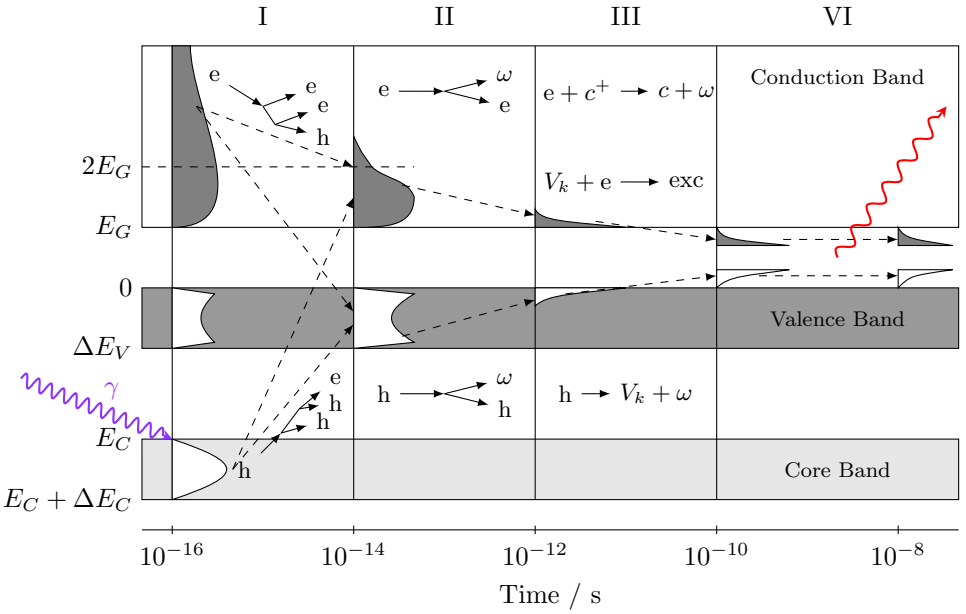

Figure 2.3: Scheme of relaxation of electronic excitations in an insulating material. E_C denote the core band edge, ΔE_C and ΔE_V the core and valence band heights and E_G the band gap between valence and conduction band. See text for further information. After [64]

additional phonons, denoted as ω ($e/h \rightarrow e/h + \omega$).

In the third step the excitations are at least partly locally bound. The holes might become "*self-trapped*" and form local vacancy centers ($h \rightarrow V_k + \omega$)[66, 67]. The electrons can then recombine with these localised holes and form self-trapped excitons ($V_k + e \rightarrow exc$) located at intermediate energy level within the band gap. Electrons and holes also might be captured by traps ($c^{\pm}$) dissipating their energy non-radiatively in the form of phonons ($e/h + c^{\pm} \rightarrow c^0 + \omega$).

In the last step (IV) the remaining excited charge carriers recombine either non-radiatively or radiatively under emission of the characteristic spectrum of the scintillation material. The emissions typically occur on timescales of a few to several hundred nanoseconds and the resulting light flashes can be detected by photo-diodes or photo-multiplier tubes which are attached to the scintillation crystal.

The parameters which are important for particle detection differ strongly when comparing scintillators with solid state detectors making them suitable for different detection applications. Table 2.1 shows a list with typical ranges for the most important parameters. The main advantage of scintillators is that they can be fabricated in bigger sizes and that their density is larger compared to solid state detectors. This makes it possible to build small detectors having a large stopping power without any energy gaps in the desired measuring range. On the other hand solid state detectors are vital whenever a high energy resolution is necessary. On the detection signal timescales the scintillators show a much larger spread than solid state detectors making a careful design of the instrument necessary to meet requirements for coincidences and count rates.

In the next section the two investigated scintillation materials ($Bi_4Ge_3O_{12}$ and $Bi_4Si_3O_{12}$) are presented and similarities and differences are pointed out.

2.2.2.1 Bismuth Germanate (BGO) and Bismuth Silicate (BSO)

BGO ($Bi_4Ge_3O_{12}$) and BSO ($Bi_4Si_3O_{12}$) are two scintillation materials which are very similar as they share the same crystalline structure [68]. Their only difference is that BSO has silicon atoms at those lattice points where the BGO has germanium atoms. As germanium and silicon are both elements of the carbon group they differ in the size occupied by the different atoms leading to slightly modified inter-atom distances [69] but keeping the overall lattice symmetry. As both crystals show only few variation in the lattice constants the same can be seen for the electronic structure where the main contributions around the band gap are due to bismuth and oxygen atoms [68, 69] resulting into very similar optical parameters. Table 2.2 lists several structural parameters for both BGO and BSO. The most structural and optical parameters are very similar to each other as for example the peak emission/absorption wavelength and the refractive index which can be ascribed to the previous mentioned similarities in the band structure. On the other hand the replacement of the heavy germanium atoms with lighter silicon atoms can clearly be seen in the density difference between both crystals. The usage of BGO is widely spread and it became a very common scintillator for various applications such as positron emission tomography. BSO is used not very often since it's light yield is five times lower than that of BGO. This is a big

	SSD	**Scintillator**
Thickness	$\leq$1 mm (Si)	$\gtrsim$cm
Energy resolution	<1 %	$\approx$10 %
Signal timescale	$\approx$10 ns	2 to 1000 ns
Density / g cm^{-1}	2.3 (Si), 5.3 (Ge)	$\approx$1 (plastic) – 8.3 ($PbWO_4$)

Table 2.1: Comparison of scintillators and solid state detectors by selected parameters which are important for particle detection.

Property	BSO	BGO
Stoichiometric formula	$Bi_4Si_3O_{12}$	$Bi_4Ge_3O_{12}$
Density / $g\,cm^{-3}$	6.8	7.13
Radiation length / cm	1.15	1.12
Peak emission / nm	480	480
Peak excitation / nm	285	295
Light yield (LY)/ photons/MeV	2000	10 600
d(LY)/dT / %K	−2	−1.5
Decay constants / ns	2.4 (6 %)	5.2 (2 %)
	26 (12 %)	45 (9 %)
	99 (82 %)	279 (89 %)
Radiation hardness / rad	1×10^5 to 1×10^6	1×10^4 to 1×10^5
Refractive index	2.06	2.15
Cleavage	None	None
Hygroscopicity	No	No
Melting Point / °C	1030	1050
Hardness / Mohs	5	5

Table 2.2: Properties of BSO and BGO, from [70, 71].

disadvantage affecting energy resolution and detection thresholds which is in most applications not compensated by it's advantages of the faster decay constants or radiation hardness in respect to BGO.

2.3 Simulating Particle-Matter interaction with Geometry and Tracking (GEANT) 4

Geometry and Tracking (GEANT) 4 is a toolkit for simulating particle trajectories in matter and electromagnetic fields [72]. It is the third successor of the first GEANT version which was released in 1974 [73] and it is developed by the GEANT 4 collaboration at the Conseil Européen por la Recherche Nucléair (CERN). GEANT 4 is written entirely object oriented in C++ and the source code is available free of charge. The most recent version available at the beginning of this thesis was *9.3 patch 02* and it was developed further till version *10.1 patch 02* which was released in December 2014. Over the duration of this thesis it was always the most recent version of GEANT 4 used and consistency checks were performed to ensure comparability between different versions. It should be mentioned that the most changes in GEANT were due to performance improvements (switching from single threaded to multi threaded, faster and resource saving algorithms, refined scientific datasets or bug-fixes) and did not change the physics models behind the simulation. However, the consistency of the simulations was also checked within our experiments and is described in detail in chapter 4 (page 83).

GEANT 4 simulates physical interaction of particles by means of Monte Carlo methods. Those methods are often used to solve complex problems and mathematical equations with the help of stochastic and are used in a wide variety of applications in scientific research nowadays [74, 75, 76]. In the case of GEANT the track of the particle is not simulated in one calculation, including all possible physical interactions, but rather is split up into many small steps which are calculated separately with only one physical process involved per step. If the physical interaction is then chosen from a list of all possible interactions weighted by their cross-sections the calculation

results will produce physically correct results. In order to achieve good results with this method one has to pay attention to three important points:

1. The number of simulated particles should be large.
2. The maximum step length needs to be short compared to the target's dimensions.
3. The possible physical interactions of the particle with the target needs to be known.

The first two points are necessary since the quality of Monte Carlo simulations is based on the law of large numbers. This means that the significance of simulation results increases the more particles are observed to behave in a certain way during the simulation. The same is true in respect with the step length. The shorter those steps are the more physical interactions are calculated increasing the statistics for each individual process. To achieve those two points is very simple and one is only limited by the available computation power. In this case GEANT provides a set of possible commands with which the user can set up the program according the needs, allowing him to chose the number of involved primary particles and to adjust the minimal step length. A proper selection for the step limitation is necessary since too large values lead to results of bad quality because the particles' passage through matter is then approximated by only few physical interactions whereas too small values might increase the calculation time unnecessarily. Due to the fact that the simulations performed within this thesis are also made for 300 µm thick silicon detectors and thin foils the maximum step length was reduced from 1 mm (default value) to several nm for those applications in the specific areas.

In contrast to the first two points the third is of much greater importance. GEANT allows the user to apply any combination of physical interactions to any particle even if this combination is completely unphysical. It is even possible to have particles without any physical interaction if one only needs geometrical calculations for example. Each tracked particle is assigned a list of possible physical interactions it may undergo, called the "*physics list*". The processes on this list can either be selected individually by the user or a predefined reference physics list can be used which are provided by the GEANT team [77]. Those reference lists are routinely validated [78] and updated with each release [79] and provide a fast and reliable solution to selecting the interactions for each particle.

Figure 2.4 sketches the principle behind GEANT when running a simulation with N particles. At the very beginning of the simulations the physics list and the simulation geometry consisting of the material properties as well as the dimensions of each object will be created. Those two things (marked as yellow parts in figure 2.4) will remain unchanged until the complete calculations for all N particles will be finished. After this initialisation process the first primary particle will be created with the desired starting energy E_j, position $\vec{x_j}$, direction $\vec{\hat{v}_j}$ with $j = 1$ and particle type (e.g. γ-ray, electron or ion). The transport of the particle is then calculated step wise taking into account the simulation geometry and the physical processes until the particle has lost all it's energy. For particles which aren't stable the simulation is continued by randomly sampling decay products according to radioactive decay datasets and tracking them as well until they reach stable states and their energy is zero. At the beginning of each step the particles' possible interactions are determined according to particle type and energy and then for each of those interactions a "*Physical Interaction Length (PIL)*" is calculated. The PIL indicates how likely an interaction will happen during the step and in this calculation the distance (or time for particles at rest) since the last interaction of the same type is accounted for. As mentioned above only one process is calculated per step and the winning process is the one with the lowest PIL for this particular step. This leads to processes with high cross-sections to have small PILs and to be in favor most of the time but also to decreasing PILs of processes with small cross-sections until their PIL is low enough to win against all other processes. The PIL is sampled randomly

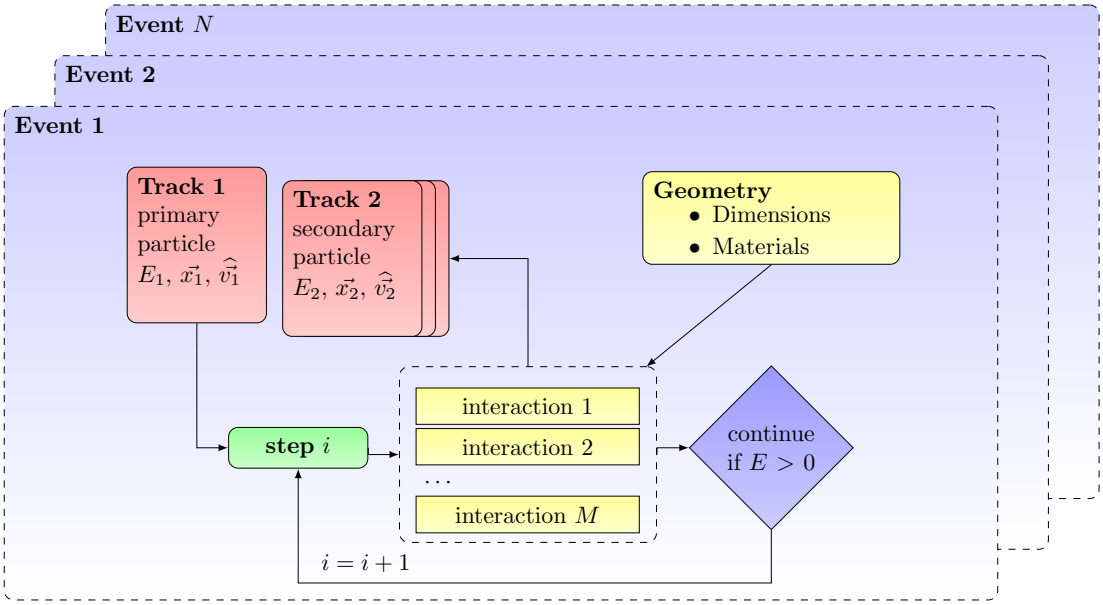

Figure 2.4: Scheme of GEANT simulation.

from the physical cross-section distribution of each interaction process. This implies that each particle step and therefore each complete track is unique and differs from each other track since there are several thousands or even orders of magnitude more of steps in each track, depending on the complexity of the simulation geometry. If secondary particles are produced due to an interaction with the material along one of those steps, those are put on the stack of tracks to be simulated with the secondary particle creation parameters (particle type, E_j, $\vec{x_j}$, $\hat{\vec{v_j}}$ with $j > 1$). It is obvious that the selection of available physical processes for each particle, specifically the "*physics list*", is vital for correct results. Although it is possible to select each process manually there are several reference physics list which are preconstructed by the CERN team and can be used as a starting point. Each of these physics lists has a certain energy range and application in which it should be used. The reference physics list used for the simulations in this thesis is the "*QGSP_BERT*" list. It is the physics list most recommended for high energy physics and it is used by the ATLAS experiment at CERN. It uses the Bertini cascade for hadrons of energy below 10 GeV and the Quark Gluon String (QGS) model for high energies (> 20 GeV). The exact description of each individual physical process included in GEANT would go beyond the scope of this thesis and is therefore omitted here since they are described elsewhere [81] by the developers of GEANT including information about their implementations. Nevertheless the quality of the simulations should be addressed here by comparing the results of a simple experiment with a simulated result. Figure 2.5 shows the comparison of measured ^{207}Bi decays (red line) and results performed by simulating the experiment with GEANT (blue line) together with the appropriate decay scheme behind the spectrum (right side of figure 2.5). The spectrum was acquired with a silicon solid state detector as it will be used in HET, specifically an HET-B detector. Shown is the histogramed data obtained in the central segment with circular shape and a diameter of 8 mm. The source was positioned approximately 1 cm below the detector and both were positioned horizontally during the experiment. ^{207}Bi in it's ground state decays only by electron capture (ϵ) where an electron of the inner shells is captured by a proton resulting in a neutron with the emission of an electron neutrino $p^+ + e^- \rightarrow n + \nu_e$ [80, 82]. The resulting

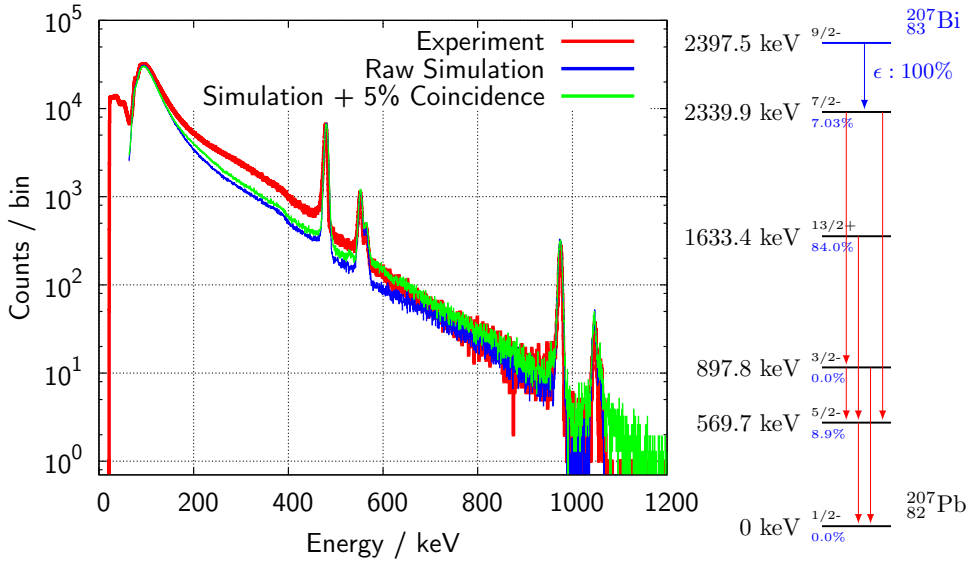

Figure 2.5: Left: Comparison of experimental (blue) and simulated (red) spectra of a ^{207}Bi decay. Right: decay scheme of $^{207}_{83}$Bi to $^{207}_{82}$Pb, from [80].

decay product is an excited lead nucleus $^{207}_{82}$Pb which relaxes under the emission of specific γ lines indicated as red arrows in the decay scheme of figure 2.5. The most probable decay (84 %) ends in the 1.6334 MeV level of lead followed by two consecutive de-excitations with energy differences of 1063.7 keV and 569.7 keV. These γ-rays can furthermore interact with shell electrons and lead to the emission of those. The emitted electrons are mono-energetic and have energies of 975.7 keV, 1047.8 keV and 1059.8 keV [80] for the first transition and 481.7 keV, 553.8 keV and 565.8 keV [80] for the second transition. The three different energies correspond to interactions with K, L or M shell electrons of lead with binding energies of 88 keV, 15.9 keV and 3.9 keV respectively [83]. The emitted electrons can be seen in the spectra at the corresponding energies with a single peak (481.7 keV, 975.7 keV) followed by a double peak structure at higher energies (553.8 keV/565.8 keV and 1047.8 keV/1059.8 keV). It can furthermore be seen that the overall shape of the simulation is in very good agreement with the experiment but that there are also some minor differences. These differences can be explained by several simplifications made in the simulation:

1. low energetic X-ray lines have not been simulated
2. electronics readout system has not been modeled
3. coincidences of multiple decays have not been taken into account
4. no cosmic muons have been simulated
5. geometry has only been approximated and greatly simplified

The effects of the first point can be seen very clearly at energies below 63 keV. In the experiment (red line, figure 2.5) are several peaks visible which originate from low energy X-ray lines present in the decay of ^{207}Bi. These lines were excluded during the simulation of the radioactive decay due to calculation time and this has obviously a large impact on the spectrum at this energy range. The effects of the second and third point are estimated by simply adding the energy deposit in two consecutive events with a certain probability, in this case 5 %, and is plotted in figure 2.5 as green line. This largely simplified model already reduces the differences between

experimental and simulated data as one can see in the energy range between 550 keV and 1 MeV where the raw simulation data lies below those of the experiment while the "corrected" data is in good agreement. Regarding the fourth point, the detector was stored horizontally during the measurement so that it's area was exposed to cosmic muons which where not simulated here. The cosmic muons are expected to have a contribution to the Minimum Ionizing Particles (MIPs) peak around 100 keV with a declining tail towards higher energies which might be the reason for the difference in the energy range from 200 keV to 500 keV. Finally the different geometries in experiment and simulation might also have a non-negligible effect on the instrument. In this case nothing except for a simple cylindrical plate of bare silicon detector and the air gap has been simulated. The real experiment however was much more complicated as for example the radioactive material is milled in a special foil which is held by an aluminum frame and the detector for example has a thin surface coating which is also not accounted for in the simulation. Also the distance and the position of the radioactive source might differ slightly in the experiment from those values used in the calculation. Especially the missing additional materials in adjacent parts of the setup suppresses the signal contribution of scattered electrons which would increase the background signal.

In the literature there are examples in which much more effort is put into the design of the detector and source which then leads to a very good agreement of experiment and calculation but with much higher calculation costs [84, 85]. All in all it can be seen that the exact adaption of an experiment into a simulation can become very difficult not only because one has to take into account the exact geometry but also the readout system. It is also possible that minor artifacts are created which have to be identified and discussed after the simulation. Nevertheless it can also be seen that a very simple simulation, consisting only of one single plate of silicon an an air gap represents the experiment already very well. This implies that the underlying simulation code of GEANT produces results which are physically correct and that GEANT is suitable be used for the simulation of instrument responses.

3 The High Energy Telescope (HET)

In this chapter the High Energy Telescope instrument as well as two of the intermediate development stages are introduced. In the first section (3.1) three models which were used for data acquisition in this thesis are described in detail. Those models can be separated in so-called "demonstration models" and in more advanced "official" models which are build in agreement with the European Space Agency (ESA) according to a development schedule. The first type of model is built with commercial off-the-shelf components to keep cost and complexity as low as possible and include all major parts necessary for the particle detection such as scintillators, detectors, preamplifiers and the digitisation electronic. They are built to demonstrate and test the basic principle of measurement and to identify possible challenges for future developments.

With the knowledge gained through these already working demonstration models a variety of official instruments are produced:

- Structural and Thermal Model (STM), consisting of a flight-like case and a flight-like mass distribution inside the model. This is used to test mechanical stability as well as thermal behaviour in extreme, space-like conditions.

- Proto Qualification Model (PQM) which consists of flight like housing and detector parts but still contains non-flight electronic circuits. The PQM is used to develop software and circuits in an environment which is as close to flight as possible. It will furthermore be tested in respect to thermal, structural and electromagnetic interference.

- Flight Model (FM) / Flight Spare (FS), identical instruments. There will be two FMs which will be the final instruments mounted on the spacecraft while the FS will stay on earth and act as a replacement part in case one of the FMs breaks during integration. The FMs will also be tested like the PQM but to lower test levels.

After the introduction of the three used models, in section 3.2 the measurement principle will be explained and how the analog signals coming from one detector are processed until they arrive at some point where the experimenter has access to them.

After the capabilities of the instrument have been presented the second to last section is about dimensioning of the Front End Electronic within the limits of the readout electronics. One key requirement for the HET will be to distinguish between ^{3}He and ^{4}He down to a ratio of several percent. In this section (3.3) the separation of ions and the separation of ^{3}He and ^{4}He will be analysed with the data gathered with one of the demonstration models.

In the last section (3.4) the radiative environment over the time of the mission will be analysed. Since the instrument will be in a rough radiative environment for several years without any possibility to access it this sets high requirements at the radiation hardness of every part of the instrument. The dose will be estimated by combining GEANT simulations with space radiation models to estimate total dose and radiation effects inside the instrument electronics as well as radiation damage in the detectors.

3.1 Versions of HET

Three different models were used to acquire the data evaluated in this thesis. These models are introduced and described in detail in the following subsections. Two of them are demonstration models and the third is the previously mentioned PQM. All models have the same measurement principle and therefore the readout electronics are described in a separate section (3.2) following this one. Despite the fact that the demonstration models were built prior to the PQM the latter will be explained first. This is done to explain all features and capabilities of the final flight instrument as a self-contained system. The demonstration models are then described on the basis of the PQM highlighting and the differences and shortly evaluating their impact on the system development.

3.1.1 HET Proto Qualification Model (PQM)

The HET Proto Qualification Model consists of most of the structural and electronical parts which will be used in the final Flight Model (FM). Figure 3.1 shows the assembled PQM from two different viewing directions and has a size of about $20 \times 20 \times 20$ cm^3. The basis of the instrument is the electronics box containing the low power voltage supply and the readout and data processing electronics. As already mentioned earlier the electronics is shared by both HET and EPT telescopes of Solar Orbiter. The two sensor heads for HET and EPT are located on top of this box. The HET sensor head is built up in an aluminum box extending over the full length of the instrument and half of it's width (top right half of figure 3.1a and top left half of figure 3.1b). The HET sensor head has one conoidal opening at each end covered with a thin two layered foil with one layer of aluminum and one layer of Kapton.

Figure 3.2 shows a sketch of the parts involved in detecting energetic particles. The central element is one hexagonal scintillating[1] crystal made of $Bi_4Ge_3O_{12}$(BGO, marked as C in figure 3.2). The thickness of the crystal in viewing direction is 2 cm and the edges also have the same length. From the position of the crystal the telescope is built symmetrically along the detection axis. Directly in front of the crystal with a distance of about 2 mm there is a circular, segmented silicon solid state detector[2] (B1 and B2 in figure 3.2) with a thickness of 300 µm. The three segments have diameters of 8 mm (inner), 17.4 mm (middle) and 36.5 mm (outer). In front of the B detectors with a distance of 44 mm there are two smaller solid state detectors (A1 and A2

[1] The detection principle of a scintillator is explained in section 2.2.2 on page 34.
[2] The functionality of a SSD is explained elsewhere in section 2.2.1 on page 33.

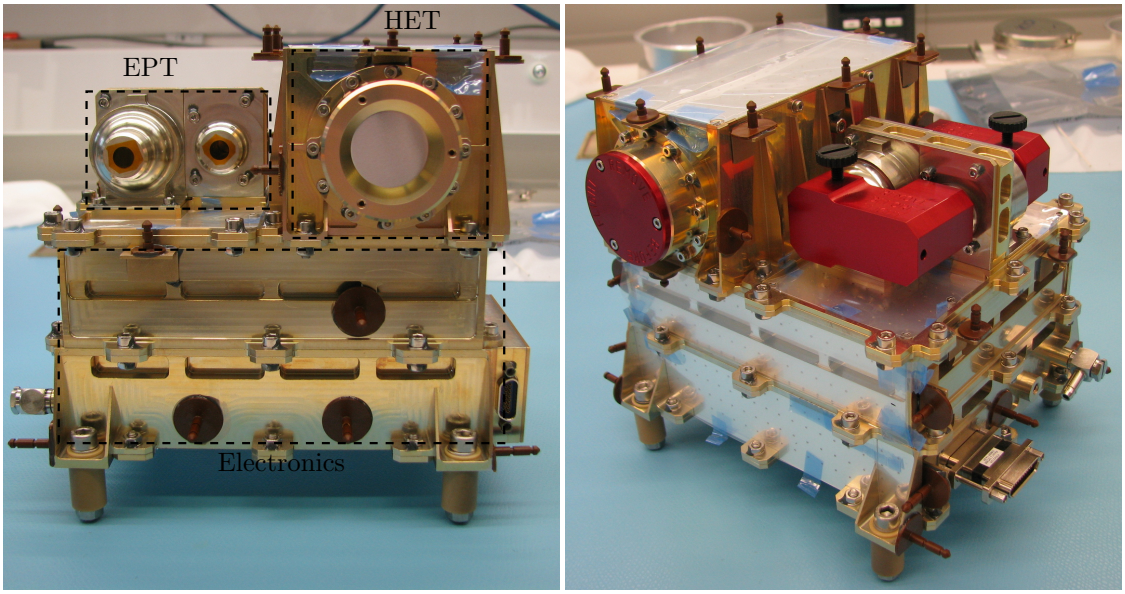

(a) Front view of HET/EPT PQM. HET sensor head is on the right side and the entrance window is clearly visible with its aluminum foil. Below the two sensor heads there is the common electronics box.

(b) Inclined view from above on HET/EPT PQM. The HET sensor is in the background and all entrance windows are covered with red aluminum protection lids, so-called red-tag items.

Figure 3.1: Front and inclined view of HET/EPT PQM.

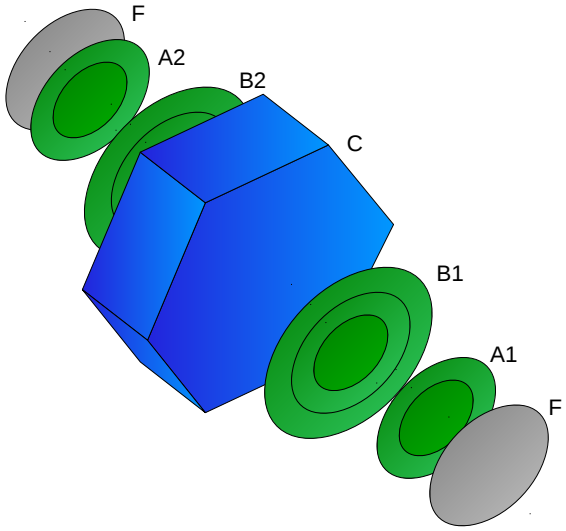

Figure 3.2: Isometric schematic view of HET (not to scale) to indicate the shapes of detectors and crystal. Labeled are both front silicon detectors (A1, A2; in green), the second silicon detectors (B1, B2, green), the BGO crystal (C, blue) and the two entrance window foils (F, grey).

in figure 3.2) having two segments which have the same diameter and thickness as the two inner segments of the B detectors. Both openings are covered by a thin foil (F in figure 3.2) consisting of one outside aluminum layer and one inner kapton layer. The aluminum layer has a thickness of 1 mil (25.4 µm) whereas the kapton has a thickness of 2 mil. Since particles need a minimum energy to penetrate the foil it introduces a lower threshold for particle energy to enter the first detector. For electrons this limit is at $\approx$ 150 keV and for protons at $\approx$ 2.5 MeV. The silicon detector segments are connected via golden bond wires to a detector holder and from there a coaxial wire for each segment runs down into the electronics box.

The scintillation light is captured by two Hamamatsu photo-diodes glued on two opposing sides of the hexagonal crystal with Dow Corning DC93-500 space grade, transparent glue. The crystal is furthermore wrapped in two layers of nitrocellulose filter sheets (Millipore Corporation, 0.45 µm pore size, 140 µm thickness) and two layers of white Polytetrafluoroethylene (PTFE) tape. The Millipore paper is highly porous and has therefore only a very limited contact area with the crystal surface. The small contact area and the high refractive index of BGO ($n = 2.15$ [86]) ensures that the scintillation light will undergo total reflection as one can see in the angular dependent reflectivity function of a BGO to air boundary in figure 3.3a. The figure shows the reflectance of visible light at BGO's peak emission wavelength leaving the crystal into a medium with a refractive index of $n = 1$ (air / vacuum). The curves are calculated from the Fresnel equations in combination with Snell's law giving the reflectance for s-polarised (R_s) and

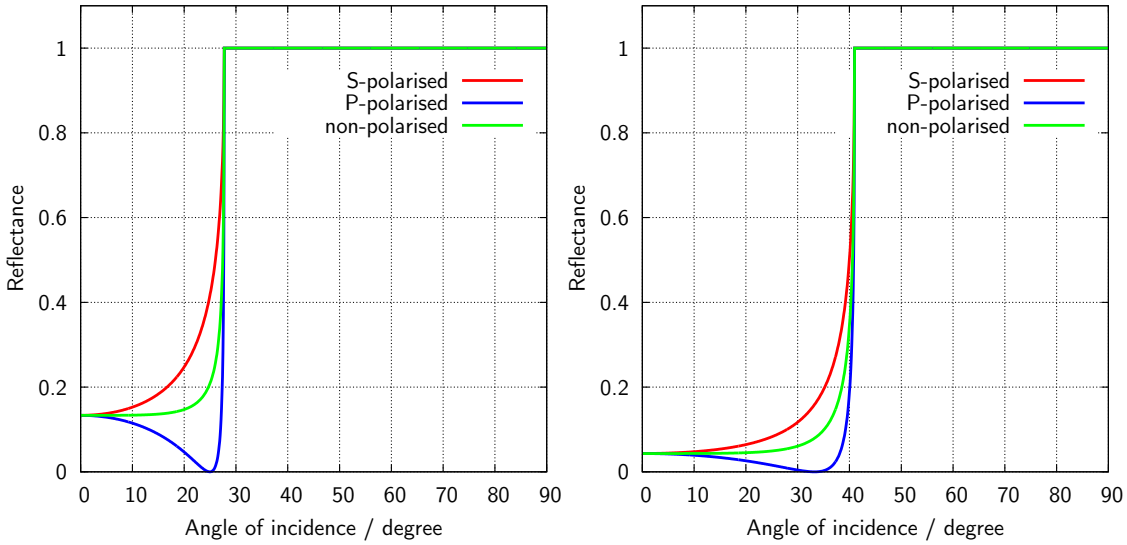

(a) BGO-air boundary layer with $n_{\text{air}} = 1$

(b) BGO-Dow Corning 93-500 boundary layer with $n_{\text{DC}} = 1.41$

Figure 3.3: Angle of reflectance for light leaving BGO into a medium with different refractive indices n for polarised and non-polarised light. Calculated from equations 3.1 and 3.2 with the denoted refractive indices. Unpolarised light is calculated from the mean value of both functions.

p-polarised (R_p) light [87]:

$$R_s = \left| \frac{n_1 \cos(\theta) - n_2 \sqrt{1 - \left(\frac{n_1}{n_2} \sin(\theta)\right)^2}}{n_1 \cos(\theta) + n_2 \sqrt{1 - \left(\frac{n_1}{n_2} \sin(\theta)\right)^2}} \right|^2 \tag{3.1}$$

$$R_p = \left| \frac{n_1 \sqrt{1 - \left(\frac{n_1}{n_2} \sin(\theta)\right)^2} - n_2 \cos(\theta)}{n_1 \sqrt{1 - \left(\frac{n_1}{n_2} \sin(\theta)\right)^2} + n_2 \cos(\theta)} \right|^2 \tag{3.2}$$

θ is then the incident angle of the light and the n_i denote the refractive indices of both media forming the boundary layer.

One can see that the light will be totally reflected back into the crystal for all angles above 27°. The remaining fraction of light leaving the crystal will then be reflected back to the crystal by the white wrapping of nitrocellulose paper and PTFE. At the locations where the photo-diodes are glued to the crystal surface it is desired to reduce the amount of reflected light back into the crystal to increase the light intensity at the photo-diodes. The glue has thus not only the purpose of holding the photo-diodes in place but furthermore is an important part in the optical path of the scintillation photons. The whole active area of the photo-diode is covered with this glue to have a homogeneous boundary layer between BGO and the silicon of the diode without any air gaps inbetween. The refractive index of the glue needs to be as close to the value of BGO for a good optical coupling. The Dow Corning DC93-500 glue has a refractive index of

$n_{\mathrm{DC}} = 1.41$ in it's cured state [88]. This refractive index shifts the angle of total reflexion by 13° in respect to the BGO-air boundary layer to a value of 40° as one can see in figure 3.3b. To reduce the remaining angular dependence of the outcoupled scintillation light the surface positions where the diodes are attached to are ground prior to the gluing process. The optical parameters introduced here are used later in section 3.3.2 in a ray-tracing calculation to estimate the instruments response on incident particles.

With this setup the sensor head is able to detect energetic particles impacting from two directions. For particles stopping inside the crystal it can distinguish between forward and backward particles when using the opposite B detector as anti-coincidence. With two units of HET on-board Solar Orbiter this leads to a total of four different, perpendicular viewing directions. This setup offers the possibility to correct count rates for backward particles as well as estimating the anisotropy of the radiation field.

Figure 3.4 shows a more detailed sketch of the cross section of the HET sensor head with two possible particle trajectories. The first trajectory is plotted as solid black line and passes both central segments of the A1 and B1 detectors. In this case the detector segment diameters are chosen such that the particle will also pass though one of the inner segments of the opposite B detector (in this case B2). The second trajectory shows the out-most possible trajectory. It is limited by the collimator and particles following this trajectory will pass through one of the segments in A (here A1) as well as one of the two inner segments of B (here B1). Those particles will then also pass through the outermost segment of the opposite B detector (B2 in this example). Since the instrument is built up symmetrically the same considerations are true for the other viewing direction. The geometry implies that a particle hitting both silicon detector and the crystal with no signal in the opposite B detector can be considered as a particle which lost all of its energy inside the two tracking detectors and crystal:

$$E_{\mathrm{total}} = E_{\mathrm{A1}} + E_{\mathrm{B1}} + E_{\mathrm{BGO}} \tag{3.3}$$

It should be mentioned that these examples are valid for particles along geometric trajectories and that the real path may be affected by physical interactions like scattering or fragmentation and that secondary particles moving in a different direction than the primary particle may also be created. Nevertheless, most of the ions follow their geometric trajectory so that the principle of the measurement is only affected by a small fraction passing the detectors close to their borders.

The segmentation of the front detector is useful in times when the instrument sees high particle fluxes when the mean time between two consecutive hits approaches the order of the shaping time constant, which will be explained later in the electronics section 3.2. Under these circumstances the output signal of the electronics might drift towards the supply voltage preventing the instrument from performing any further measurements with the affected detector channel. The segmentation provides a very simple way to continue measurements also during high flux events since the single detector count rate in any detector is proportional to it's area. With a detector separated in multiple segments of different areas the instrument can continue measuring at fluxes when the larger segments already show saturation effects while preserving the possibility of high statistics during low flux times. In the HET PQM the ratio of both detector segment areas is ≈ 3.7.

The telescope geometry of the instrument has also another positive attribute. Since the tracking detectors are thin compared to the scintillating crystal they can be used to estimate the LET of a penetrating particle. In this case the LET can be estimated by

$$\mathrm{LET} = \frac{\mathrm{d}E}{\mathrm{d}x} \approx \frac{\Delta E}{d\cos(\varphi)} \tag{3.4}$$

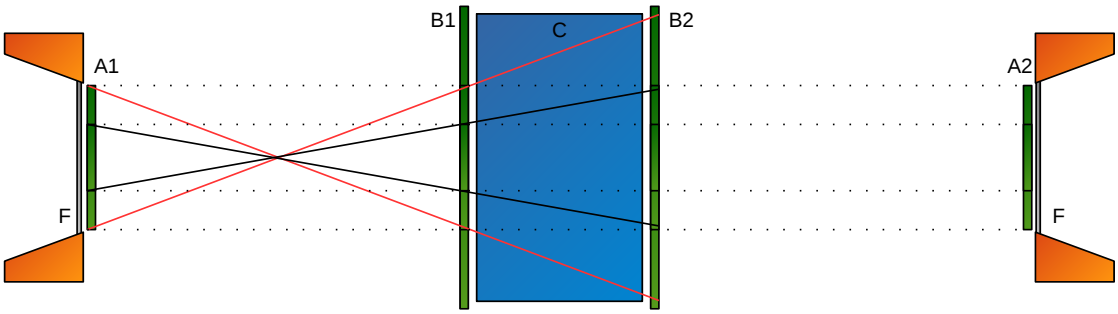

Figure 3.4: Schematic side view of HET sensor head with correct length and angular ratios except for the silicon detector thickness. The collimator is indicated as orange trapeze below and above the foil (F, grey). Two possible particle trajectories are shown: The first (black solid lines) is passing though both central segments and stopping in the middle segment of B2. The second one (red solid lines) passes the outer segment of A1 and the middle one of B1 and stops in the outer (anti-coincidence) segment of the B2 detector.

where ΔE is the energy deposited in a thin detector, d is the detector thickness and φ is the angle under which the particle passes the detector. The angle φ can not be determined for an individual particle depositing an energy ΔE in the silicon detector so that the energy have to be corrected with an average angle $\bar{\varphi}$ resulting in an LET of:

$$\frac{\mathrm{d}E}{\mathrm{d}x} \approx \frac{\Delta E}{d\cos(\bar{\varphi})} \tag{3.5}$$

One now has values for E_{total} (equation 3.3) and an estimated value for $\frac{\mathrm{d}E}{\mathrm{d}x}$ (equation 3.5) and with those the particle identification with the ΔE versus E_{total} technique can be performed for stopping ions [51, 52, 89, 90, 91, 92]. The identification technique is based on an approximation of the Bethe formula (equation 2.1) giving the relation

$$E_{\mathrm{total}} \cdot \Delta E \propto AZ^2 \tag{3.6}$$

between the total energy E_{total} of a particle and the energy deposited in a thin detector ΔE. Figure 3.5 shows this product for experimental data as a function of $\frac{E}{\Delta E}$ in combination with a histogram of the data projected to the y-axis. The data-points shown there are those of He, C, O, Si and Fe and indicate the basic principle of the ion separation technique (details on experimental setup are explained later in section 4.1). The data is projected along the dashed black line to the y-axis and the resulting histogram is shown at the left side of the image. The trend of the data points with an increasing slope in this plot can be explained with the Bethe formula (equation 2.1). The slightly tilted distribution of the data points which can especially be seen at the helium data points in the lower right corner is caused by energy straggling in the tracking detector. E denotes the total energy which is fixed for a monoenergetic beam like it was used here. However, the value of dE can vary due to energy straggling in the silicon detector [93] resulting into a slightly tilted distribution. The rotation of the tilted distribution depends on the ratio between E and $\mathrm{d}E$. According to the Bethe formula particles with lower energy produce larger energy values in a thin detector. This leads to different tilt angles of the individual monoenergetic distributions. The histogram on the left side of figure 3.5 shows several peaks with those labeled which are originating from the primary particles. It can furthermore be seen,

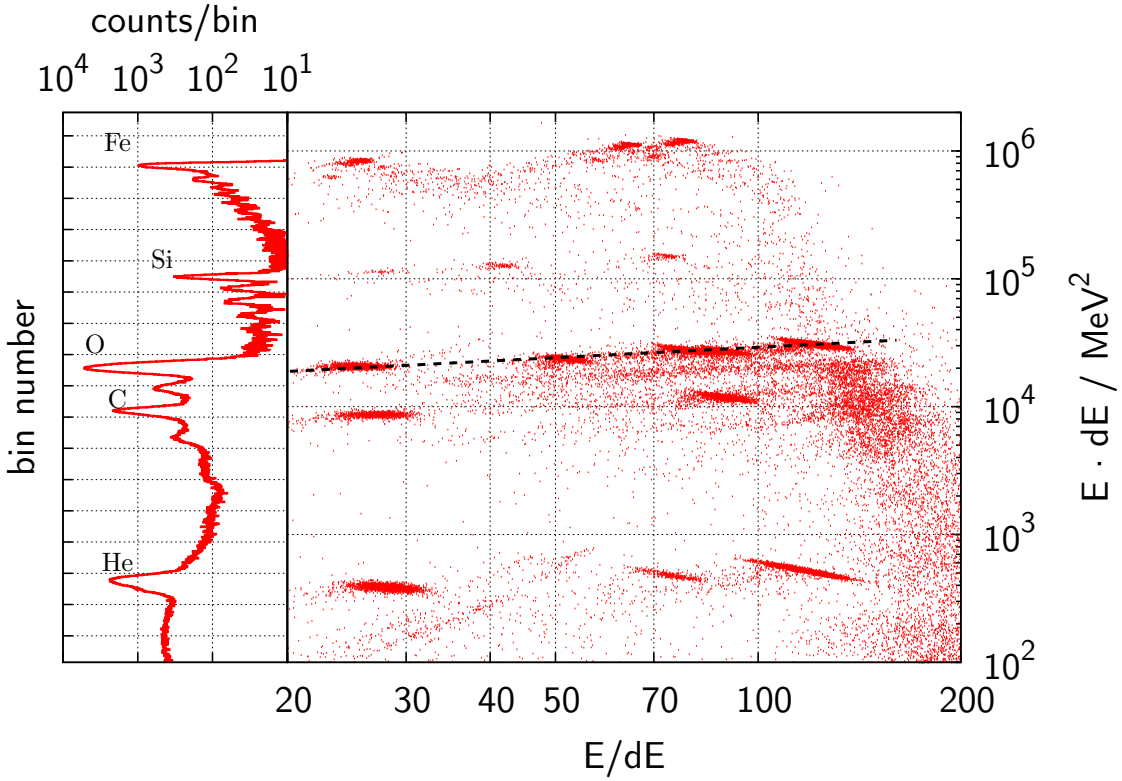

Figure 3.5: Particle identification with the ΔE vs. E_{total} technique.

especially for silicon and iron, that each primary peak has a tail towards ions with lower values of $E \cdot \mathrm{d}E \propto AZ^2$ (equation 3.6). Those peaks are produced by fragmentation of the primary particles inside the polyethylen absorber before they reach the first tracking detector.

The particle identification shortly described here has been further investigated with respect to the ^{3}He /^{4}He separation capabilities of HET which is presented later in section 3.3.3 whereas the following sections will introduce the demonstration models which were used for experiments.

3.1.2 HET Demonstration Model (BGO)

The HET demonstration model (BGO) was built in 2013 together with Shrinivasrao R. Kulkarni. It was built to demonstrate the proposed measuring principle with the E_{total} vs. ΔE method as described in the previous section (3.1.1). Figure 3.6 shows a CAD drawing of the cross section though the sensor head of the demonstration model. The model contains a scintillating crystal (C in figure 3.6) and two silicon tracking detectors (A/B) in front of it. The model is built in telescope geometry with two tracking detectors like the HET PQM with the difference that the silicon detectors have other diameters than those used in the PQM. The silicon tracking detectors A and B are identical and were originally manufactured for the EPT on the STEREO spacecraft. The crystal geometry, wrapping and readout system is identical with that used in the PQM. It is a hexagonal shaped BGO crystal with two Hamamatsu photo-diodes attached to it and finally wrapped in Millipore nitrocellulose paper and PTFE tape. The demonstration model only has one viewing direction in contrast to the final model and therefore a simple Hamamatsu

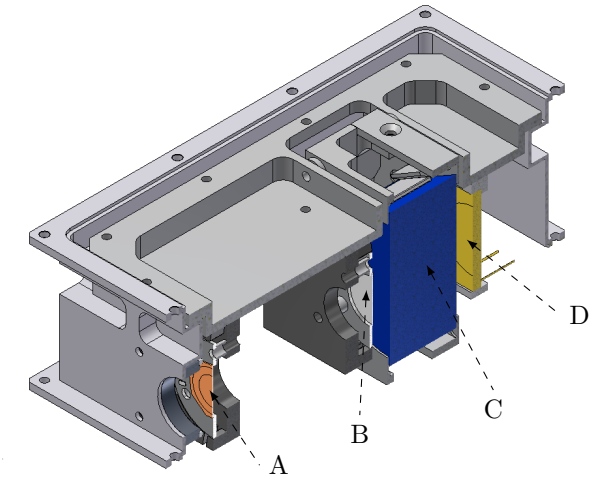

Figure 3.6: HET demonstration model section drawing with BGO (C) crystal. The front tracking silicon detector (A) and the anti-coincidence detector (D) behind the BGO crystal. Second tracking detector (B) is barely visible and points in direction of the scintillator. It has the same dimensions as the first detector. First and second detector mounts are also visible (dark grey). The foil covering the entrance window is omitted in this CAD view. According to [54].

photo-diode has been used as anti-coincidence detector behind the crystal (D). Pictures of the assembled model can be seen in figures 3.7a and 3.7b on the left side. The readout electronic is in principle also identical with that of the PQM but it uses only commercial available electronic parts and is described in section 3.2.

3.1.3 HET Demonstration Model (BSO/LSO)

The HET demonstration model (BSO/LSO) has been developed and built during this thesis. The assembly was performed in cooperation with Robert Elftmann who analysed the LSO scintillator during his master thesis [94]. On the right side of figure 3.7 the second demonstration model can be seen. Just like the previously mentioned HET demonstration model with BGO crystal it is composed of three modular boxes. The upper two contain mainly the detectors, scintillators and the preamplifiers while in the lower part the readout electronics and power supplies are placed. Figure 3.8 shows a CAD drawing of the upper part of this demonstration model with left out walls in the top area where the detectors are located. One can see the placements of each detector and scintillator within the topmost box but the detector holders and other structural parts except for the outer housing are omitted for clarity. The two scintillators are drawn in yellow (LSO, $3 \times 1 \times 1.5\text{cm}^3$) and blue (BSO, $2 \times 2 \times 2\text{cm}^3$) and in-between one can see the Hamamatsu PIN diodes (S3590-19) acting as tracking detectors. The same type of diodes are used as scintillator readout for both scintillators. It should be mentioned that the two tracking diodes on the right side (directly before and behind the BSO crystal) were turned by 180° during assembly so that their sensitive areas (red) show in the direction of the entrance window at the BSO side. Both entrance windows are covered with 50 µm thick aluminum foil. The model was designed in such a way that switching between the two crystals during measurement can be achieved by just turning the instrument without any changes inside the instrument. In contrast

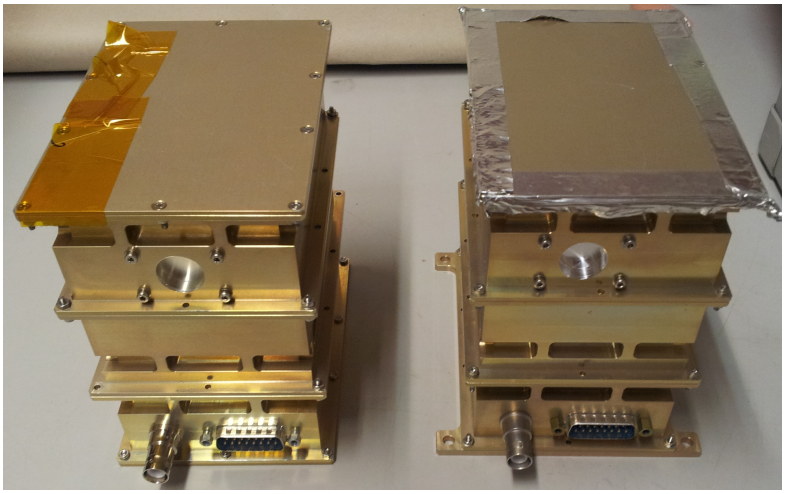

(a) Front view of both HET demonstration models.

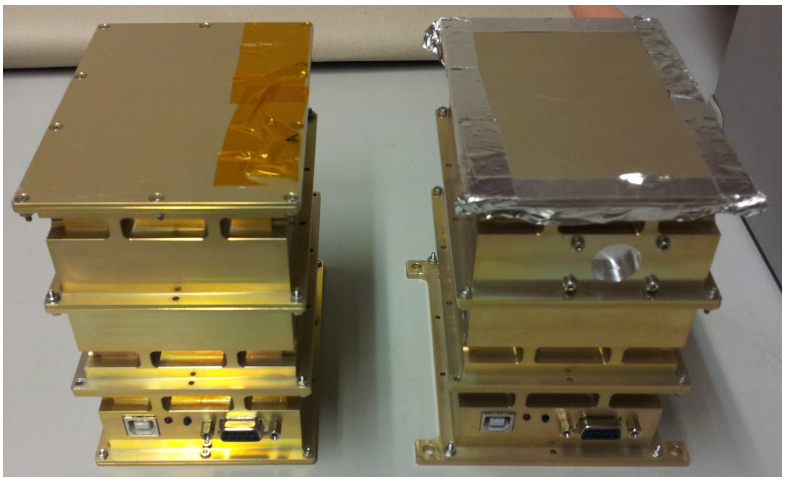

(b) Back view of both HET demonstration models.

Figure 3.7: Images of the two HET demonstration models. The instrument on the left side is the HET demonstration model with BGO and on the right side the one with BSO/LSO scintillating crystals. The second one has one entrance window on each side.

to the demonstration model with BGO crystal the preamplifiers in this model are not on a single Printed Circuit Board (PCB) below the detectors but soldered directly to the pins of each diode. Figure 3.9 shows a picture of one single photo-diode with its aluminum holder frame. The pins of each diode are kinked so that the connected preamplifier board with a dimension of about $1 \times 2\,\mathrm{cm}^2$ is not located in the beam path of the particles. It also ensures that the signal wires are as short as possible to avoid noise. The preamplifiers are then connected to the readout electronics with a ribbon cable terminated with a 10-pole connector which is located underneath the detectors. The readout system is also identical with that of the other demonstration model and is explained in the next section.

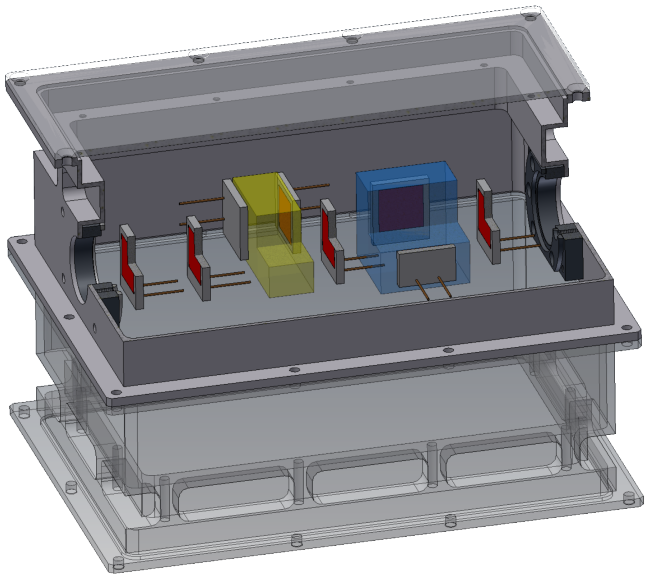

Figure 3.8: HET demonstration model section drawing with BSO (blue) and LSO (yellow) crystals. Photo-diodes with their sensitive area (red) and connection wires (orange) are visible but their mounts as well as the entrance foils are omitted. The lower (transparent) box contains the readout electronics (not shown here) [95].

Figure 3.9: Single tracking photo-diode for the HET demonstration model (BSO/LSO). The diode has an active area of 1×1 cm^2 and can be seen in the lower left part of the image as black square. Above the diode there is a preamplifier with an area of $\approx 2 \times 1$ cm^2 soldered directly to the kinked pins of the diode.

3.2 HET readout electronics and data acquisition

The HET readout system is called Iras REadout chip for Nuclear Applications (IRENA) and was developed within our workgroup [96]. The central element is a Field Programmable Gate Array (FPGA) which controls the Analog-to-Digital-Converters (ADCs) used to digitise the signal and preprocesses the incoming data by checking trigger conditions. The analog signal path before the digitisation is sketched in figure 3.10. Every silicon detector as well as every photo-diode for crystal readout is biased by a filtered high voltage of $-70\,\mathrm{V}$ (V_{bias}). This bias voltage ensures that the detectors with a thickness of 300 µm are fully depleted (see section 2.2.1). The detector is then connected to a Charge Sensitive Preamplifier (CSA) converting the resulting current pulses to voltage steps. Behind the CSA there is a shaper with a shaping time of 2 µs. The shaper has two outputs with gains of unity and 16.

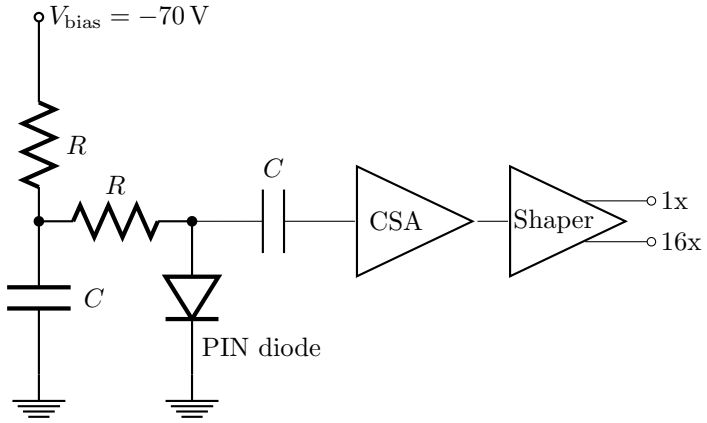

Figure 3.10: Schematics of the silicon detector and photo-diode readout. The PIN diode denotes the detector/photo-diode.

The two outputs are connected to individual ADCs which are controlled by the FPGA. Due to this setup there are two channels (corresponding to two ADCs) per detector. All ADCs are read out simultaneously at a frequency of 3 MHz in the case of the demonstration models and 12 bit resolution by the FPGA. The flight models are later clocked at a slightly lower frequency of 1 MHz. For each channel the FPGA stores the last 64 acquired data points in a ring buffer and after an acquisition has been completed it calculates two values A and B from a subset of 16 of those 64 values according to:

$$\begin{aligned} A &= \sum_{i=0}^{15} a_i s_i \\ B &= \sum_{i=0}^{15} b_i s_i \end{aligned} \tag{3.7}$$

where a_i and b_i are coefficients and s_i are the digitised 12 bit values. The subset of the 16 values is chosen in such a way that they follow the expected curve of the shaper output. Figure 3.11 shows some part of the ring buffer with a shaped detector signal. The filled squares denote those 16 points s_i while the others, not used in the current correlation are plotted as crosses. On the next clock signal the data points would be shifted to the left in respect to the positions

of the s_i positions and the next ADC value of this channel will be appended at the end of the sample list. Then the new correlation is calculated.

The coefficients a_i are chosen in such a way that they follow the expected form of the shaper output signal and the b_i are chosen according to the expected derivative of the shaper output as shown in figure 3.11. This continuous correlation reaches a maximal value for A when the shaper output has reached it's maximum. The B parameter then acts as a phase parameter with which the A value can be corrected for effects that happen due to a discretisation by the ADC clock.

In addition the coefficients are normalised such that:

$$\sum_{i=0}^{15} a_i = \sum_{i=0}^{15} b_i = 0 \tag{3.8}$$

This ensures that the resulting A and B values are independent of an offset in the baseline which happens when the detector is hit by different particles within a time Δt that is on the order of the shaping constant (2 µs).

Figure 3.12 shows the principle with a simple Gaussian signal. The previous described algorithm has been applied to two different Gaussian functions centered at $t_0 = \pm 10$ and $\sigma_t = 1$ with offsets of 0 ($t_0 = -10$, green solid line) and -0.5 ($t_0 = 10$, red solid line). The set of coefficients for a_i and b_i has been calculated from a Gaussian with $t_0 = 0$ and the same σ_t value. As one can see in that plot (figure 3.12) the resulting signals (red dashed lines for A and blue dashed lines for B parameters) are identical and the phase parameter in the vicinity of the maximum of A can be used to determine how close one is in respect to the real maximum value of A.

After all A and B values for each channel have been calculated the FPGA checks whether a predefined trigger threshold (individually set for each channel) has been exceeded and it is checked whether the current A value is higher than the one determined in the last step. This is performed as long as a peak is detected. A peak is indicated by a lower A value than in the previous clock which means that the curve reached it's maximum in the last clock cycle. This is the case in figure 3.11 at sample number 13 (s_7). At this time the FPGA triggers the event processing logic which receives all A values from the clock cycle where the triggering A value had it's maximum. When particles pass through multiple detectors there will be only one readout procedure since this is triggered on a per-event basis. The data send to the trigger logic contains the following information:

- a trigger bit-mask indicating which detector channel has exceeded its trigger threshold
- a 3-tuple of integers for each channel containing
  - a "Pulse Age (PA)" value
  - the resulting A-value of correlation
  - the resulting B-value of correlation

The PA is an integer calculated during trigger evaluation and can be used to identify special cases of invalid triggers. The generation of the PA value is only mentioned for completeness of the evaluation process and is described in detail in [97]. The A_i values are then proportional to the pulse heights of the shaped signals which are again proportional to the energy deposited inside the detector. These pulse height values can now be used to identify particle type (equation 3.6) and calculate energy spectra of those species. The B_i values are proportional to the phase of the pulse in respect to the digitising clock. Those B_i values can be used for small energy corrections in the order of $< 1\,\%$ which occur due to the discretisation of the clocked ADCs. The resulting dataset is then sent to a connected PC in the case of the demonstration models or will be evaluated by another FPGA in the final flight version which histograms the raw data according to the needs and communicates with the Instrument Control Unit (ICU).

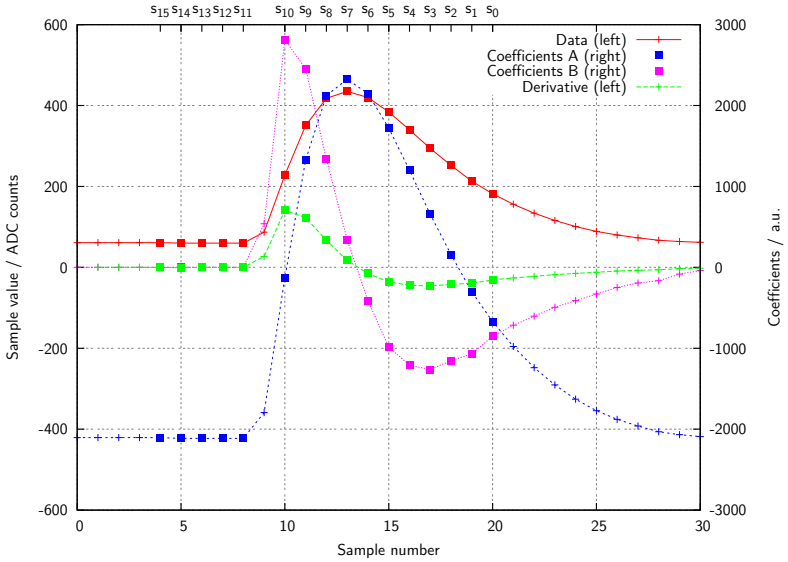

Figure 3.11: Digitised shaper output for one channel (red) with its derivative (green) and the coefficients A (blue) and B (magenta). The 16 data points from the ring buffer denoted as s_0-s_{15} (plotted as solid squares) are used for the calculation of the coefficients according to equation 3.7. From [96].

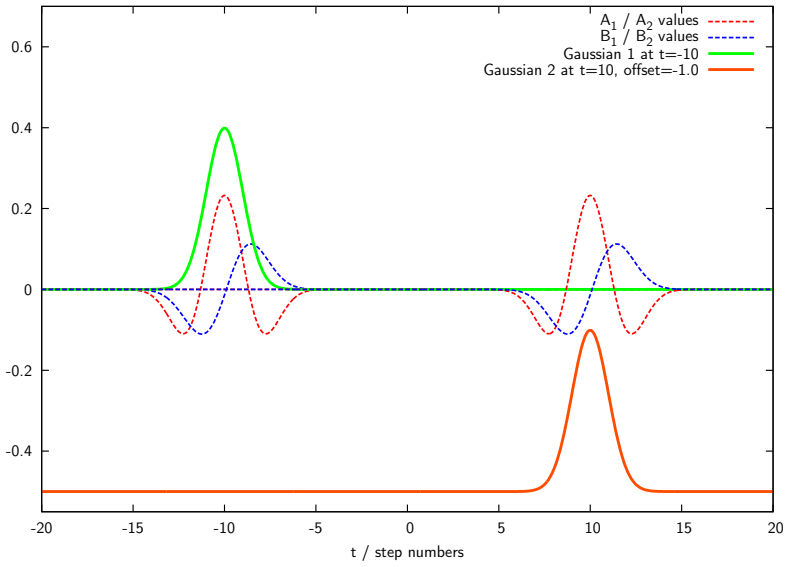

Figure 3.12: Example for the peak detection algorithm inside the FPGA. Plotted are the resulting values for A (red dashed lines) and B (blue dashed lines) calculated with equation 3.7 for two Gaussian with $t_0 = \pm 10$ and $\sigma_t = 1$ with offsets of 0 (green solid line) and -0.5 (red solid line).

3.3 Dimensioning of Front End Electronic (FEE) for BGO scintillation crystal

To comply with the scientific requirements of HET the dimensioning of the Front End Electronic (FEE) for the BGO crystal is very important. The instrument is not only required to cleanly separate different ion species but even more challenging is the separation of isotopes, especially ^{3}He and ^{4}He which is of great interest for heliospheric physics. In the next two sections the sources for fluctuations of the measured signal are analysed. At first the electronic noise is quantified by measurements made with the HET demonstration model (BGO) and thereafter the influence of the light collection efficiency within the scintillating crystal are estimated by a Monte Carlo ray-tracing simulation.

In the third section GEANT simulations are performed for the HET sensor and are combined with both models developed before. With these simulations the instrument's response to ^{3}He and ^{4}He ions is estimated and necessary implications for the FEE are discussed.

3.3.1 Noise estimation of readout electronics

The noise of HET's readout electronics is estimated with the HET demonstration model (BGO). The model was kept in upright position so that the telescope was looking upwards for about 4 weeks while measuring secondary muons of the cosmic radiation created at high altitudes within the earth's atmosphere [98]. The instrument was measuring without any coincidence conditions and all channels were read out simultaneously whenever at least one detection channel was triggered. Figure 3.13 shows a histogram of the calibrated data collected with the inner segment of the A detector (red). The coincidence of the front detector's inner segment with the scintillation crystal is also shown (blue). The plot shows three characteristic features:

1. the muon peak around 100 keV, marked with (M)
2. the trigger threshold at roughly 40 keV, marked with (T)
3. the noise peak at 0 keV

The muon peak (M) is caused by cosmic muons depositing energy in the detector while passing it. The red histogram shows the measured data with no coincidences so that the muons' incident angle can vary from 0 to 90° with respect to the detector normal. The muons can therefore have track lengths inside the detector which are as short as the detector thickness or as long as the detector's diameter. It is even possible that muons only pass through one of the corners having an even shorter track length inside the detector than the thickness. The resulting muon peak can be seen in figure 3.13 as a broad peak (M) with a maximum at around 100 keV. The blue histogram shows now only those events in which a muon also penetrates the crystal which significantly reduces the acceptance angle with the same binning as the red diagram. Due to the restrictions on the acceptance angle the counts per bin are less than in the former case. Also the mean path length inside the detector is reduced to the restrictions on the acceptance angle, excluding the most extreme angles (e.g. 90°). Since the LET of the cosmic muons is approximately constant upon passage through the detector the deposited energy is proportional to the traversed track length. This can be seen in figure 3.13 where the maximum of the blue curve is shifted towards lower energys in respect to the muon peak in the red curve. The blue curve then roughly represents the energy distribution which is deposited by relativistic muons upon perpendicular passage through a 300 µm thick silicon detector.

The next feature is the trigger threshold which corresponds to the signal's pulse height to be be exceeded to issue a trigger signal for this specific channel. It is marked in figure 3.13 as (T)

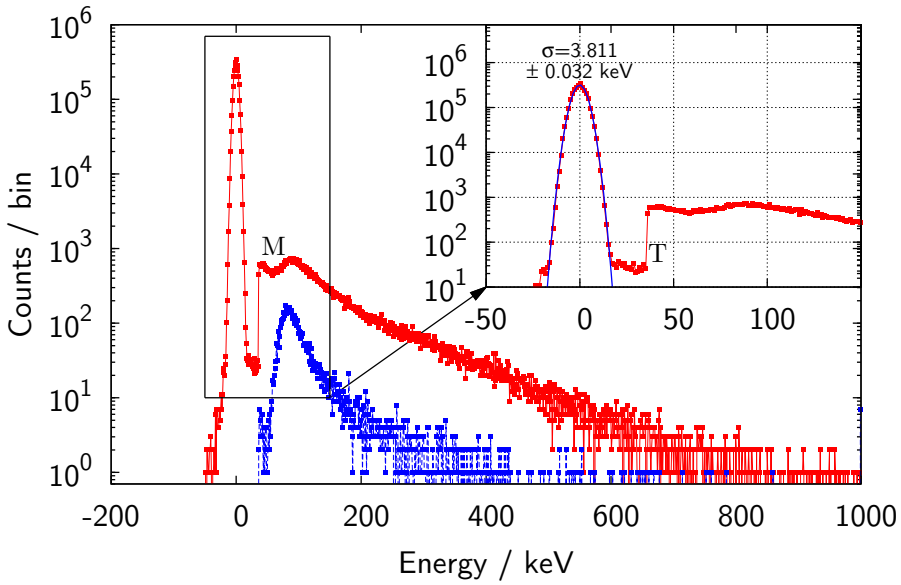

Figure 3.13: Muon data acquired with the inner segment of A-detector of HET demonstration model (BGO, red data points). The muon peak is located around 100 keV, marked as (M), and the trigger threshold is marked as (T). The inset shows the enlarged noise peak with a Gaussian fit and the corresponding σ value of the fit. The blue curve shows the same data-set with a coincidence of the silicon detector and the scintillation crystal.

in the inset. At the point of the threshold the count rate in the spectrum increases by more than one magnitude. This happens because as soon as one channel detects a signal which is higher than it's threshold all channels are digitised and stored as one event. In this case all events in bins above the threshold issued a trigger in the inner A detector and activated the readout process for all channels. On the contrary the noise peak is composed of those events which did **not** trigger the specific detector (in this case inner segment of A) but any combination of other detectors. In this case the signal should be 0 keV but since the readout electronics has a certain amount of noise a slight variation is expected to happen which will result in a broadening around 0 keV. Most electronic noise sources do have an amplitude characteristic of a Gaussian distribution and this effect is clearly visible at the noise peak of the inset of figure 3.13. A Gaussian peak was fitted to the measured data and it can be seen that it represents the measured data perfectly around 0 keV with a σ value of 3.811 ± 0.032 keV. This shows that the assumption of normal distributed noise is a very good approximation for the electronics.

Figure 3.14 shows the same data but this time for one of the photo-diodes attached to the BGO crystal. All three features explained above can also be found here at different energies and are marked with the same labels, (M) for the muon peak at 18 MeV and (T) for the trigger threshold at 2.5 MeV. The blue curve shows the data of the crystal signal in coincidence with the inner segment of the first and second tracking detector. The binning is identical with the data of the red curve but it is multiplied by a factor of 100 for a better comparison. Due to the additional coincidence condition with the inner segment of the second tracking detector the sum of the counts is less. The muon peak in this case is again shifted towards lower energies as for the same reasons as in the case of the silicon detector.

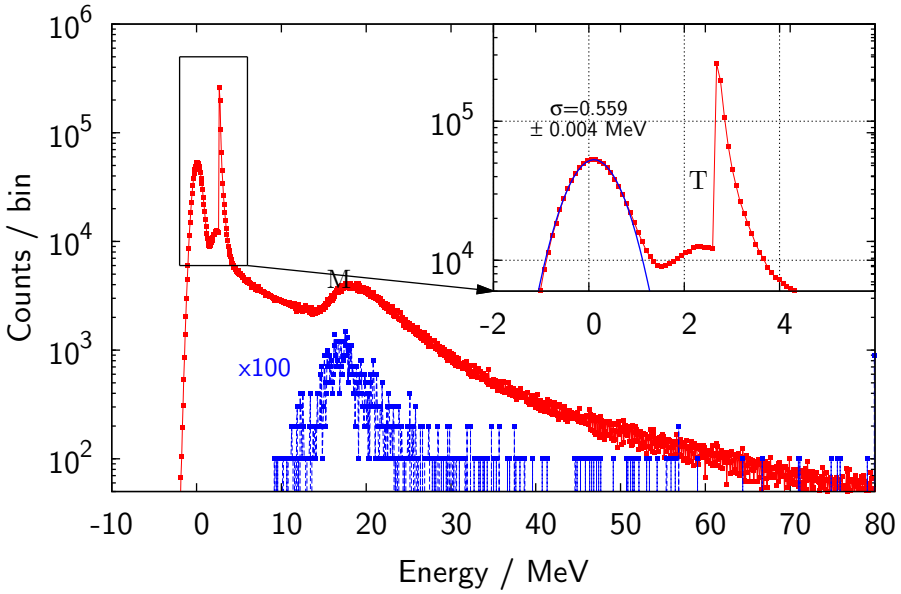

Figure 3.14: Muon data acquired with one diode of the BGO crystal of HET demonstration model (BGO). The muon peak is located around 18 MeV, marked as (M), and the trigger threshold is marked as (T). The inset shows the enlarged noise peak with a Gaussian fit and the corresponding σ value of the fit.

It can also be seen that the electronics noise is again represented by a normal distribution but with a higher σ value of 0.559 ± 0.004 MeV due to different gains and therefore different calibration factors compared to the silicon detectors. In addition to the three features there is another peak in the gap between the noise peak and the trigger threshold between 1.5 to 2.5 MeV with a maximum at around 2.3 MeV. This peak might originate from isotope traces within bismuth since many isotopes of bismuth show γ lines at around 2.3 MeV according to [80]. It is also possible that any kind of impurities during crystal production might be the reason for this peak since only very small activities of radioactive material inside scintillation crystals can cause this kind of effect [94].

The calibrated noise levels are determined here since this value is important for the latter usage in the following sections. An additional estimation can explain the difference between both noise levels given by:

$$\frac{\sigma_{\mathrm{BGO}}}{\sigma_{\mathrm{Si}}} = \frac{559\,\mathrm{keV}}{3.811\,\mathrm{keV}} = 146.7 \tag{3.9}$$

This value can be explained by the different gains in the charge sensitive preamplifiers (see figure 3.10). The crystal channels have a feedback capacitance of 1 pF (C_{BGO}) while the silicon detector has 3.3 pF (C_{Si}) resulting in a factor of 3.3 in gain. Additionally the conversion factor from photodiode to an LSO crystal has been calculated as $\nu_{\mathrm{Si/LSO}} = 18.6$ [94] and the relative light yields of BGO (L_{BGO}) and LSO (L_{LSO}) are 7.3 and 16.6 [99]. Combining those numbers gives a factor of

$$\nu_{\mathrm{Si/LSO}} \cdot \frac{L_{\mathrm{LSO}}}{L_{\mathrm{BGO}}} \cdot \frac{C_{\mathrm{Si}}}{C_{\mathrm{BGO}}} = 18.6 \cdot \frac{16.6}{7.3} \cdot \frac{3.3\,\mathrm{pF}}{1\,\mathrm{pF}} = 139.6 \tag{3.10}$$

which is very close to the calculated value from the noise levels. A slight difference is also not uncommon since the capacitors in the amplifiers typically have tolerances in the order of a few percent which is in the order of the differences observed here.

As a conclusion the noise of HET's readout electronics is expected to be $\approx 4\,\mathrm{keV}$ for the silicon detectors and $\approx 0.56\,\mathrm{MeV}$ for the crystal channel. A preliminary analysis of noise levels in the PQM showed that they are expected to be not larger as with the demonstration model analysed here. This indicates that the described noise models can be well applied to the latter flight hardware.

3.3.2 Scintillation light propagation inside BGO

The light propagation inside the crystal introduces another source for fluctuations of the measured signal. To estimate the influence on the signal a ray-tracing Monte Carlo simulation was used. For each ray starting at a given point $\vec{p}_0 = (x, y, z)$ inside the crystal a random starting direction was generated by creating three Gaussian random variables $r_1 \dots r_3$. The random direction $\vec{d}$ is then given by [100]:

$$\vec{d} = \frac{1}{\sqrt{r_1^2 + r_2^2 + r_3^2}} \cdot \begin{pmatrix} r_1 \\ r_2 \\ r_3 \end{pmatrix} \tag{3.11}$$

The crystal consists of six surfaces for the hexagonal sides and two for the front faces as one can see in figure 3.17. All eight surfaces are defined by an offset point $\vec{s}_i$ and a surface normal vector $\vec{n}_i$ with $i = 1 \dots 8$. The distance λ_i to the point of intersection for a ray with the i-th surface is calculated according to:

$$\lambda_i = \frac{\vec{n}_i \cdot \vec{s}_i - \vec{p} \cdot \vec{n}_i}{\vec{n}_i \cdot \vec{d}} \tag{3.12}$$

The closest intersection point $\vec{p}_1$ of the ray with one of the surfaces is then

$$\vec{p_1} = \vec{p}_0 + \lambda_{\min} \cdot \vec{d} \tag{3.13}$$

with $\lambda_{\min} = \min(\lambda_1, \dots, \lambda_8)$. The angle θ between surface normal of i-th surface $\vec{n}_i$ and ray direction $\vec{d}$ can be calculated from the normalised scalar product

$$\theta = \cos^{-1}\left(\frac{\vec{n}_i \cdot \vec{d}}{|\vec{n}_i||\vec{d}|}\right) \tag{3.14}$$

At the point $\vec{p}_1$ the reflectivity $R(\theta)$ for inside-out direction which is plotted in figure 3.15 is compared against a uniform random number u in the interval $[0, 1)$. If u is less or equal to $R(\theta)$ the ray is considered to be reflected mirror-like back into the crystal. In this case the raytracing is continued with the new ray direction inside the crystal. If u is greater than $R(\theta)$ the ray is considered to leave the BGO crystal. In the latter case the ray is reflected diffusely at the nitrocellulose filter paper/PTFE tape wrapping. An angle θ' for re-entry of the ray is calculated with a probability

$$P(\theta') \propto \cos(\theta') \tag{3.15}$$

which corresponds to a diffuse Lambertian reflectance and is continued until another random uniform number u' is larger than the reflectivity $R(\theta')$ in outside-in direction (figure 3.15, upper

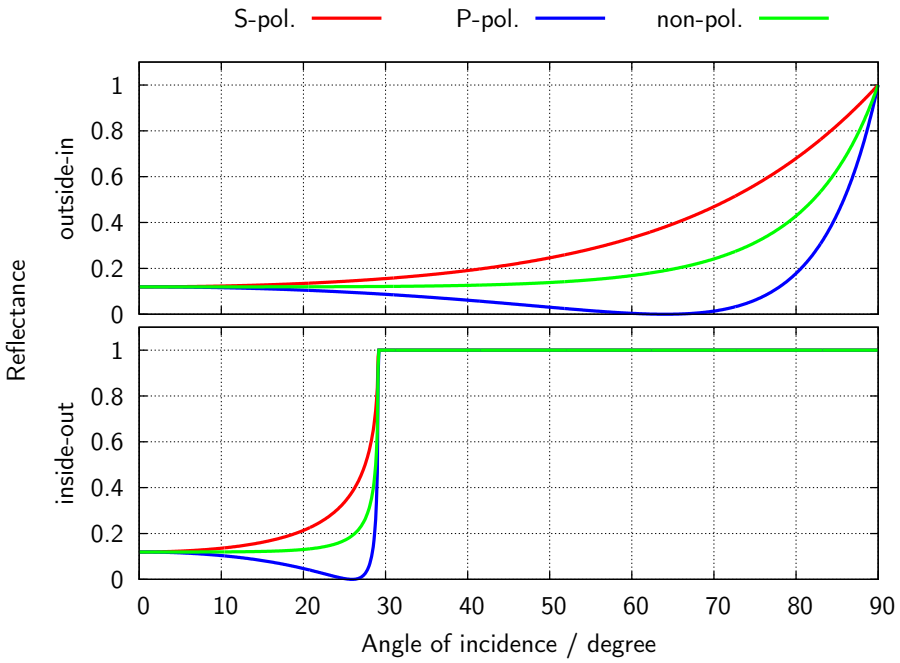

Figure 3.15: Reflectance of light entering (upper diagram) or leaving (lower diagram) BGO into a medium with refractive index $n \approx 1$ as a function of the incident angle and for P-, S- and unpolarised light (according to [101, 102]).

part). For each such reflection of any single ray a variable N_{R} is incremented to count the total number of reflections at the crystal wrapping. The value of N_{R} is later used in equation 3.17 to calculate the absorption inside the wrapping. When a (θ', u') combination is found in which the ray again enters the crystal, the final direction inside the crystal is then determined by Snell's law

$$\frac{\sin(\theta')}{\sin(\theta)} = \frac{n_{\mathrm{BGO}}}{n_{\mathrm{air/vacuum}}} \tag{3.16}$$

in combination with a random uniform angle φ in $[0, 2\pi)$ lying in the plane of the crystal surface. The ray-tracing is then continued from the point $\vec{p}_1$ (equation 3.13) in direction of (θ, φ) with respect to the surface normal $\vec{n}_i$ of the reflection plane. This is continued until one intersection point is at the position where one of the diodes is glued at the crystal surface. It is assumed that the light at that point will leave the crystal since this area was ground with sandpaper prior to gluing the diodes as described earlier in section 3.1.1. After a ray reached this position the light intensity of the current ray is calculated as

$$I = I_0 \cdot \exp(-L/\sigma) \cdot (1-\epsilon)^{N_{\mathrm{R}}} \tag{3.17}$$

where $I_0 = 1$ is the intensity of the ray at the very beginning, ϵ is the absorption of light in the nitrocellulose filter / PTFE layer, σ is the absorption length of light in BGO and L is the total track length inside the crystal with

$$L = \sum_{i=1} |\vec{p}_i - \vec{p}_{i-1}| \tag{3.18}$$

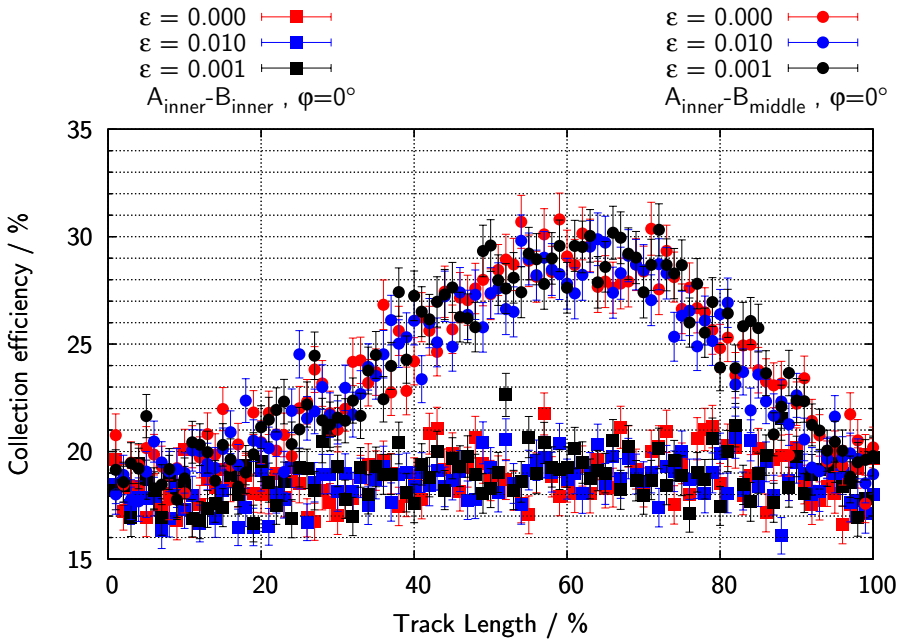

Figure 3.16: Light collection efficiency for two tracks with $\varphi = 0°$ and two coincidence conditions (A_{inner}-B_{inner}, squares / A_{inner}-B_{middle}, circles) for different values of ϵ from 0 to 1 %. Since the two compared tracks are of different length, they are normalised to relative track lengths here.

The value for σ has been chosen to be 24.5 cm according to datasheets from crystal manufacturers [103]. The value for ϵ has been assumed to be 0.001 which sounds reasonable since PTFE is an almost perfect diffuse reflector in the visible light regime and both materials appear as bright white surfaces. Simulations with an ϵ value of 0.01 and no absorption ($\epsilon = 0$) showed that the difference is negligible compared to the estimated error-bars as one can see in figure 3.16. In this figure the light collection efficiencies for two distinct tracks have been plotted as a function of the track length. The two selected tracks have the same angle φ. An angle of $\varphi = 0°$ means that the track will point in the direction of one of the photo diodes as shown in figure 3.17. The two tracks denote the outermost trajectories of the two different coincidence conditions between the A_{inner}-B_{inner} and the A_{inner}-B_{middle} detector segments. Since these two tracks have different track length inside the crystal they are normalised to relative track lengths on the x-axis, shown as percentage values.

The ray-tracing procedure is performed $N = 1000$ times at each step of the ion track. The steps used in this section are defined by the linear trajectories which are divided equally in single steps. In the next section where the model is applied to simulation data the steps will be defined by the GEANT4 results as defined in section 2.3. The resulting light collection efficiency at a certain step is then the sum of all intensities $I_{j,1/2}$ for the j-th ray and photo diode 1 or 2 as calculated with equation 3.17. The corresponding standard deviation is then given by $\sigma_{1/2}$. The total intensity for the individual photo diode in one step is then

$$I_{\text{total},1/2} = \frac{1}{N} \sum_{j=1}^{N} I_{j,1/2} \pm \frac{\sigma_{1/2}}{\sqrt{N}} \tag{3.19}$$

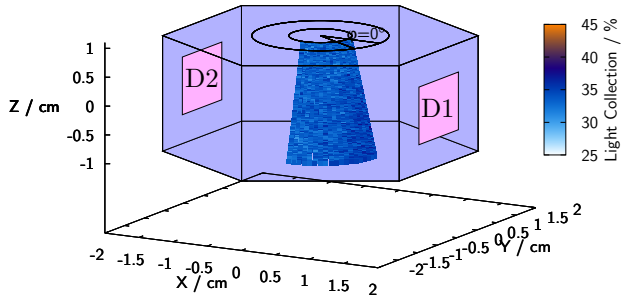

(a) A_{inner}-B_{inner} coincidence

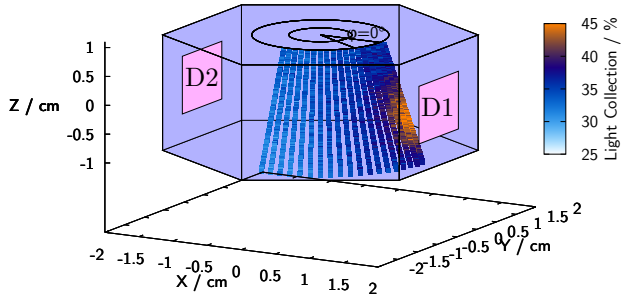

(b) A_{inner}-B_{middle} coincidence

Figure 3.17: Summed light collection inside BGO along selected tracks with angles between $\varphi = 0 - 90°$for two different coincidence conditions. Diode active areas are shown as pink areas and size of the B detector segments are indicated as black circles on top of the crystal.

Figure 3.17 shows the results of the ray-tracing simulation for selected tracks inside the crystal. The plotted light collection intensity I is the sum of both photo diode's average light intensities I_1 and I_2 as calculated by equation 3.19. The selected tracks correspond to the outermost possible tracks of particles passing through both inner segments of the A and B tracking detectors (figure 3.17a) and of particles passing through the inner segment of A and the middle segment of the B (figure 3.17b). Due to the symmetry of the crystal/diode system only one quadrant of the crystal has been calculated. The φ angle represents the angle between the track's projection onto the front surface and the connection line between both diode centers (equal to the x-axis). From the two plots it is very obvious that the inner-inner coincidence shows a very homogeneous light collection efficiency regardless of the φ angle whereas for the inner-middle coincidence the light collection shows enhancements for tracks closer to one of the diodes. Figure 3.18 shows the same data but in contrast to figure 3.17 it is plotted for each diode (D1, D2) separately. The diodes are named as in figure 3.17, the one closest to the track with $\varphi = 0°$ is D1.

From the results of the ray-tracing one can see that the light collection efficiency for the coincidence of the inner segments of both tracking detectors is equal regardless of the track direction inside the crystal. For track passing through the inner segment of the first and the middle segment in the second detector the signal ratio of both detectors varies by a factor of 2 depending on position inside the crystal. The ratio is worst for particles passing along tracks in direction of one of the photo-diodes. It shall be noted that this effect diminishes very fast for increasing angle between track's projection and diode normal and that the ratio between both

diodes for φ above 30° are already close to unity. Figure 3.19 shows the anisotropy of both diodes' signals as a function of φ. In this case the data of coincidence A_{inner} and B_{middle} is plotted. The location on the track is at 60 % of the total track length since the ratio of D1 to D2 reaches a maximum there (see figure 3.17b). It can be seen that the diode which is closer to the track receives an increased signal for angles below 20° while the signal at the opposing diode is decreased. At around 30° the difference between both diodes is negligible compared to the statistical errors. There is also an overall trend in the summed signal visible which shows a decrease of the total intensity as a function of the angle φ. It shall be mentioned here that the selected track for figure 3.19 is a trajectory with a very extreme extend and that the implications of the model results will be discussed in detail in the next section. There the ray-tracing model will be applied to simulated data and it is combined with other models and assumptions to analyse the ion separation capabilities of HET and to identify the requirements for the Front End Electronic (FEE).

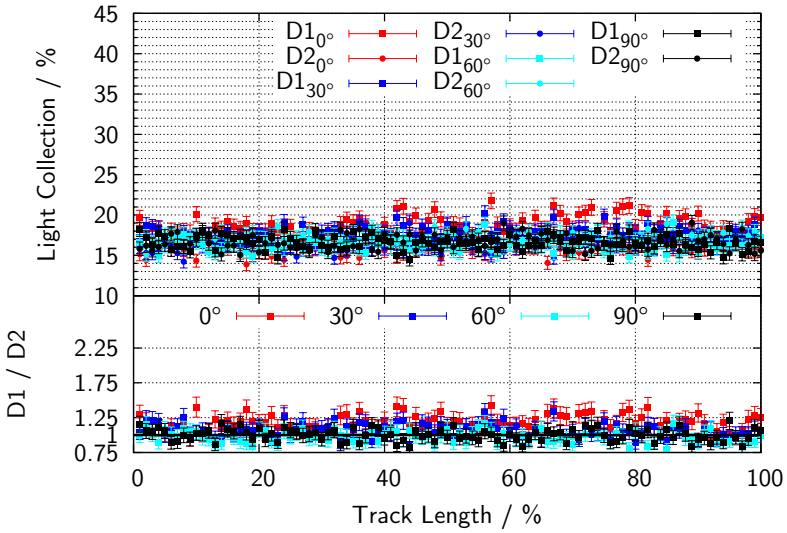

(a) A_{inner}-B_{inner} coincidence.

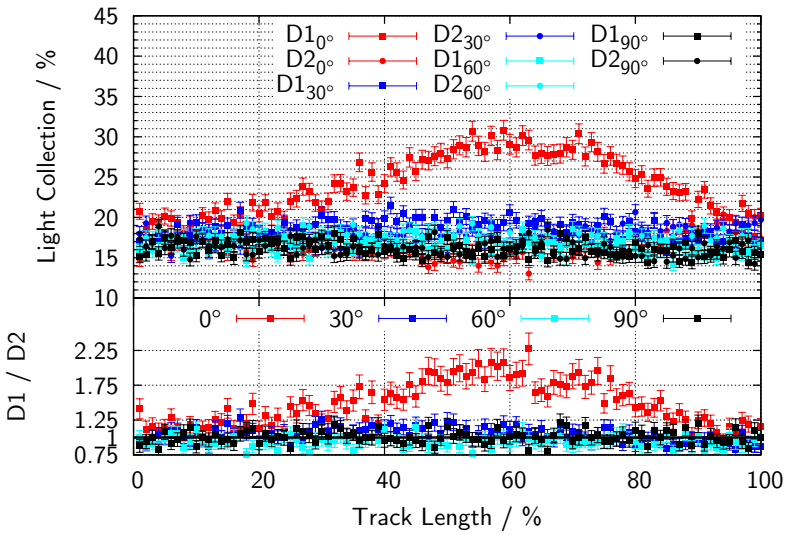

(b) A_{inner}-B_{middle} coincidence.

Figure 3.18: Light collection rate of diodes D1 (squares) and D2 (circles) as a function of the track length for selected tracks with different angles of φ between 0 degree and 90° and two difference coincidence conditions (upper part of each plot). The lower parts show the ratio of D1 and D2.

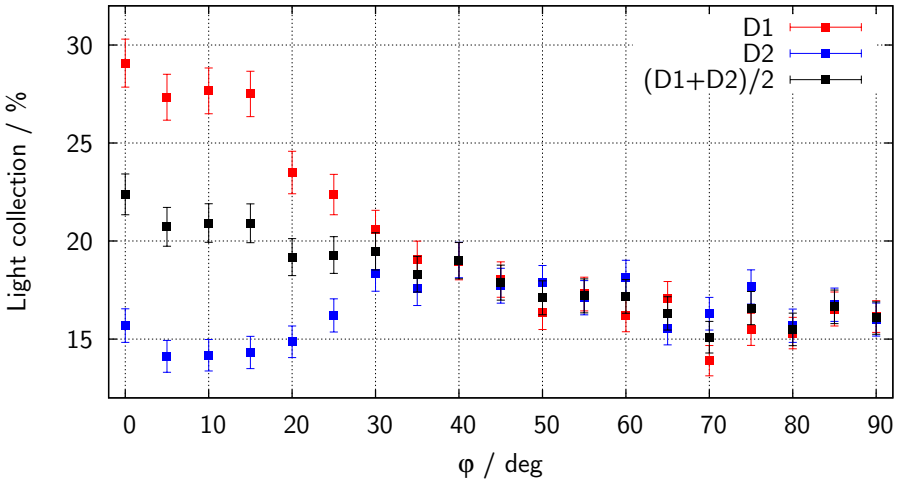

Figure 3.19: Light collection efficiency as a function of φ angle at that point of track where the D_1 signal is close to its maximum (at 60 % of track length).

3.3.3 Isotope separation of ^{3}He and ^{4}He

The separation of ions is one important task for HET but even more challenging is the separation of isotopes. As the separation of ^{3}He and ^{4}He is an important requirement for HET on Solar Orbiter (see chapter 1) the requirements on HET's FEE for the separation of those two ions will be identified within this section. The analysis is performed by combining GEANT simulations with the ray-tracing and noise models described in the previous sections.

For the simulations GEANT version 4.9 and a simplified model of HET was used. The simplified model can be seen in figure 3.20. It consists of all important parts for the particle detection process such as entrance windows foils, silicon detectors and the crystal and the crystal's PTFE and nitrocellulose filter wrapping. It also contains simplified versions of the main structural parts such as the housing (grey parts in figure 3.20), crystal holder structure (yellow part in the center of 3.20) and the electronics boards (rectangular, multi-coloured parts in the lower part of figure 3.20. As a particle source the area of the collimator opening was chosen. This neglects effects of particles passing through the housing but since only particles passing through a coincidence of A and B-detector and the crystal are considered this is a good approximation of the expected data. The particles' starting angular distribution was a cosine-law which is the resulting flux through a plane when being within an isotropic radiation field. The input energy spectrum has been taken from the CREME 2009 model [104, 105] as it is plotted in figure 3.21. For both isotopes the ^{4}He energy spectrum was taken since the CREME 2009 does not provide any data except for the most common isotopes. The simulations were carried out in multiple stages. At first the energy depositions of ^{3}He and ^{4}He inside the detectors were calculated and the particles' tracks inside the scintillator crystal were saved for latter analysis.

Figure 3.22 shows the results of the first stage of the analysis split up into the four possible coincidence conditions between $\mathrm{A_{inner}/A_{outer}}$ and $\mathrm{B_{inner}/B_{middle}}$. The product of total energy E_{total} and the energy deposited inside the first silicon detector $\mathrm{d}E$ is plotted as a function of $E_{\mathrm{total}}/\mathrm{d}E$ as it was described earlier in section 3.1.1 for the particle identification. The energy is binned logarithmically with 16 steps per order of magnitude in a binary system resulting in 16

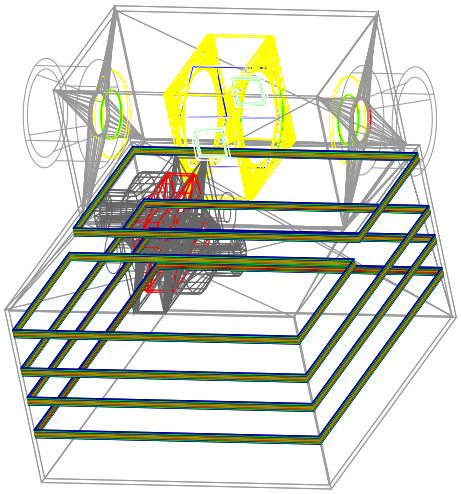

Figure 3.20: GEANT4 wire-frame model of HET. The main parts which can be seen are the aluminum housing (grey), BGO scintillator (blue) surrounded by crystal holder (yellow), the EPT magnet system (red) and the electronics boards consisting of multiple layers of different materials (various colors).

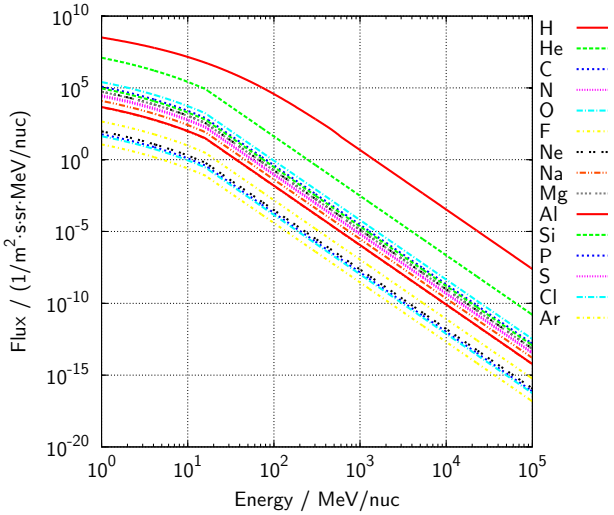

Figure 3.21: Solar energetic particle flux spectra according to CREME [104, 105] from the most recent version of 2009.

steps per factor of two. The data points of ^{4}He are in the upper and the ones of ^{3}He in the lower branch. The separation of ^{4}He and ^{3}He is caused by the relation given in equation 3.6 (page 47). The difference in mass number A of the two isotopes can be utilised to separate the two isotopes even if they share the same charge Z as in this case. The plot shows three areas denoted with (I), (II) and (III) where the data has slightly different slopes. Each region corresponds to a different total energy for the incident particles. In region (I) the particles' energy is $\lesssim 12\,\mathrm{MeV/nuc}$, in (II) $\lesssim 30\,\mathrm{MeV/nuc}$ and in (III) $\gtrsim 30\,\mathrm{MeV/nuc}$ up to the maximal detectable enery for stopping ions at around $100\,\mathrm{MeV/nuc}$. The three regions are indicated by a separation function between the two isotope distributions which is plotted as a black solid line in figure 3.22. The functions are modeled as power functions with exponent l:

$$E \cdot \mathrm{d}E = \left(\frac{\mathrm{d}E}{\mathrm{d}x}\right)^{l} \cdot C_{\mathrm{offset}} \tag{3.20}$$

The boundaries of the three regions are definded as cuts on the x-axis ($E/\frac{\mathrm{d}E}{\mathrm{d}x}$ axis). The exponents of l in the three regions have been found by fitting equation 3.20 to the data points of ^{4}He. The position of the separation function has then been shifted downwards by multipliing C_{offset} with 0.85. The resulting exponent parameters in the different regions of the separation function are then:

$$I: \quad E/dE < 2 \quad l = 0.378 \pm 0.003 \tag{3.21}$$

$$II: \quad 2 <= E/dE < 5.5 \quad l = 0.051 \pm 0.001 \tag{3.22}$$

$$III: \quad 5.5 <= E/dE \quad l = 0.104 \pm 0.001 \tag{3.23}$$

The data will later be stored in the same kind of double logarithmic histogram in the FPGA [97]. Also the summation along linear curves is forseen to be performed by the FPGA on those histograms such that this rather complex looking scheme can be implemented easily in the final data processing logic. In contrast to figure 3.5 the simulated data is shifted to higher values on both axes. In figure 3.5 the ^{4}He data points are located around $600\,\mathrm{MeV}^2$ while they are at

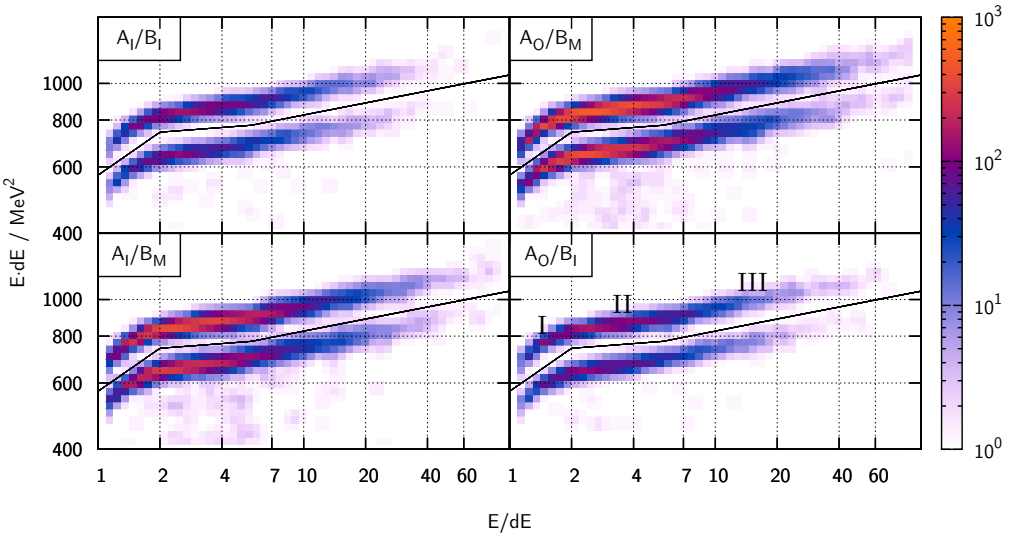

Figure 3.22: Raw simulation results for the separation of ^{3}He and ^{4}He without any additional effects for the four possible coincidences with the two innermost segments of A and B.

800 MeV^2 in this plot on the y-axis ($E \cdot \mathrm{d}E$-axis). This shift can be explained by the quenching which will be addressed in a later chapter. It should only be mentioned here that the quenching affects the total energy E by lowering the value with by certain factor. This factor leads to the previously mentioned shift between experiment and simulation since both data are stored in a double logarithmic histogram. Hence the quenching will affect the offsets of the exponential functions C_{offset} and the boundaries of the three regions but not the slopes l which are important for the ion separation.

The second stage of the analysis estimates the effects which are expected due to the different light collection efficiencies at various locations inside the crystal (see section 3.3.2). As described in section 2.3 a particle track in GEANT consists of many small steps. Each of these steps is characterised by a starting point $\vec{s}$, an end point $\vec{e}$ and an energy loss ΔE along this step. The total energy loss inside the crystal is then given by:

$$E_{\mathrm{BGO}} = \sum_i \Delta E_i \tag{3.24}$$

For each step along this track the ray-tracing is performed for the central point $\vec{c}_i = \vec{s}_i + (\vec{e}_i - \vec{s}_i)/2$ with a number of 1000 rays as described in the previous section (3.3.2) resulting in a light collection value $l_i(\vec{c}_i)$ for each point along the track. The value of 1000 rays per step was chosen since BGO produces 6300 to 6900 photons per MeV [106] and the energy deposition along one step is typically in the order of several hundred keV. Therefore the counting statistic should be well represented by the ray-tracing model. To increase calculation speed it is checked first if the ray-tracing has been performed for any point within a radius of 500 µm around $\vec{c}_i$ and if this is the case the l_i value of the closest of these points is selected as collection efficiency. The distance of 500 µm is approximately twice the distance between two adjacent data points in figure 3.18 and the difference between those two points is usually smaller than the estimated uncertainties indicated by the error bars. With the light collection efficiency estimated by the ray-tracing model, a value for the detected energy, $E_{\mathrm{BGO,\ ray\text{-}traced}}$, can be calculated by summing up the

individual energy losses at each step of the track weightend by the local light collection efficiency $l_i(\vec{c}_i)$:

$$E_{\text{BGO, raytraced}} = \frac{1}{\bar{l}} \cdot \sum_i \Delta E_i \cdot l_i(\vec{c}_i) \tag{3.25}$$

ΔE_i is the energy loss along the i-th step of the track and $\bar{l}$ denotes the light collection efficiency averaged over the complete crystal and has a value of 0.3486 ± 0.0002. It is necessary to correct the value with $\bar{l}$ since the data is already in units of energy. If the correction with $\bar{l}$ would not be applied here, the energy deposition in the crystal would be reduced by the light collection efficiency leading to unphysical results. Figure 3.23 shows the results of the second stage of analysis. It shows the same data as in figure 3.22 with the ray-tracing model applied. It can

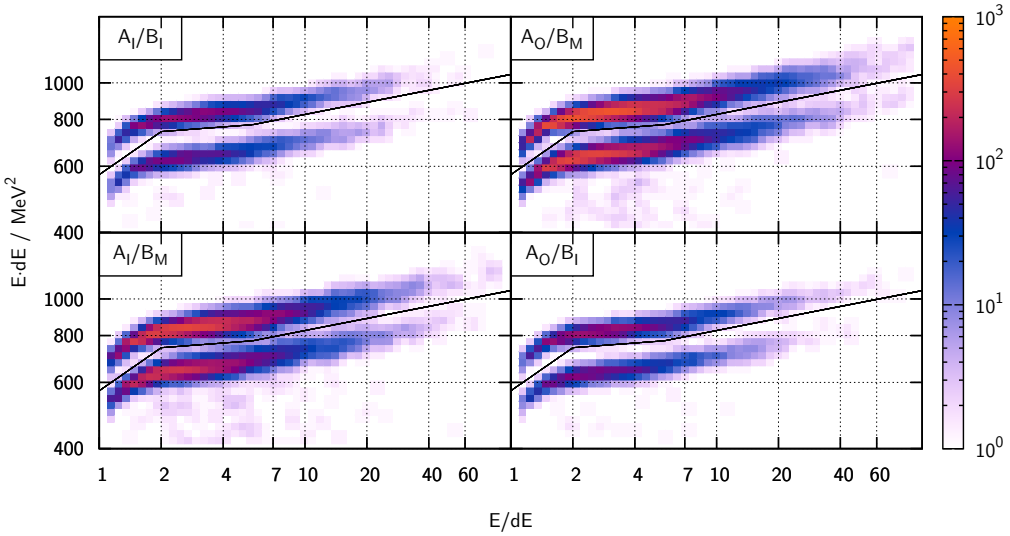

Figure 3.23: Simulation results for the separation of ^{3}He and ^{4}He with additional effects due to ray-tracing model for the four possible coincidences with the two innermost segments of A and B.

be seen that the distributions of the two ions got slightly broader. This effect is maximal for the coincidence of the outer segment of A and the middle segment of B and minimal for the coincidence of both inner segments. This behaviour is in good agreement with the results of the previous section (see figure 3.17) where tracks close to one diode show enhanced light collection rates while tracks passing through the center of the crystal have very homogeneous light collection efficiencies. If one compares the broadening of the particle distribution with the results from the bare raytracing simulation (see section 3.3.2) one can see that the very large increase in light collection efficiency for extrem trajectories is negligible. The effect vanishes due to the averaging over many possible trajectories with different legths and leads only to a slightly broader distribution as previouly mentioned.

In the third step of the analysis the electronical noise is added to the simulated data in addition to the ray-tracing effects. As already mentioned in section 3.3.1 the noise can be assumed as normal distributed noise with a σ of 3.8 keV for the silicon detectors and 0.56 MeV for the crystal channel. This corresponds to a Full Width Half Maximum (FWHM) of 9 keV for the silicon detectors and 1.32 MeV for the crystal. The noise is simply added to the data by generating

normal distributed random numbers with the denoted σ/FWHM values and is then added on top of the simulated data after performing the ray-tracing. The resulting data is plotted in figure 3.24 again separated into the four possible coincidence conditions. The electronics noise has a

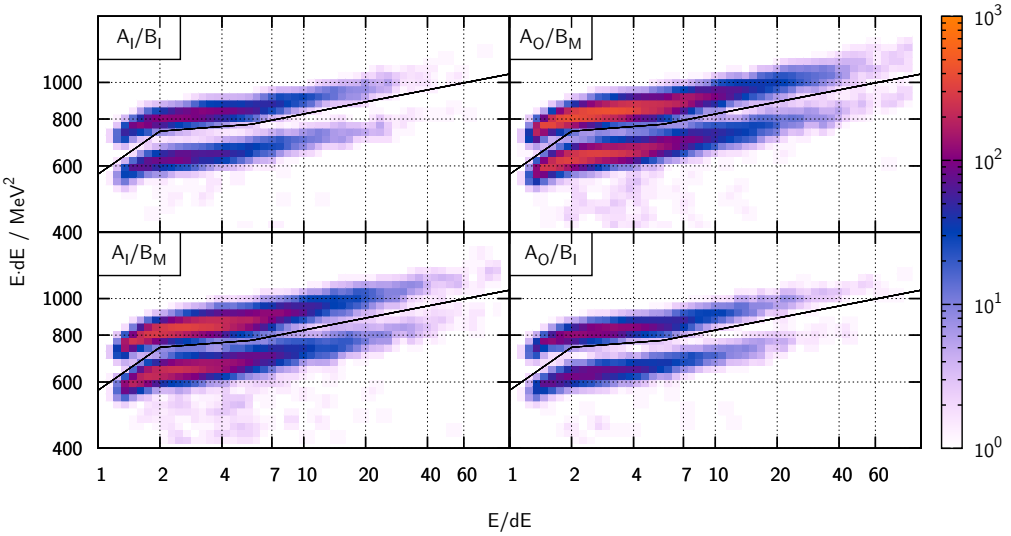

Figure 3.24: Simulation results for the separation of ^{3}He and ^{4}He with additional effects due to ray-tracing model and simulated electronical noise for the four possible coincidences with the two innermost segments of A and B.

much larger effects on the data-point spreading than the light propagation inside the crystal. The data points of ^{3}He and ^{4}He can still be well separated according to their positions in the diagram since the number of data points of each species are almost equal. To further analyse the data a projection to the $E \cdot \mathrm{d}E$-axis (y-axis) is calculated for each coincidence condition. The bins of the intensity plot (figure 3.24) are summed up along the x-direction ($\frac{E}{\mathrm{d}E}$ direction) in such a way that the bin containing the separation function (black, solid line) in each slice is identified as bin zero. The resulting histogram shows the distribution of ^{3}He (blue line) and ^{4}He (red line) relative to the separation function in number of bins and it is plotted in figure 3.25. It can be seen that the distance between the two maxima of ^{3}He and ^{4}He is as small as 6 bins and that the total amount of ^{3}He is less than the amount of ^{4}He. This is caused by the fact that both ions were simulated with the same $\frac{E}{m}$ flux from the spectrum in figure 3.21. This reduces the total energy for the ^{3}He ions by 25 % while having the same charge Z resulting in an increased stopping power and therefore reducing the number of ^{3}He hits in the simulation.

Until now the shown plots were made from simulation results performed with the same number of particles for both isotopes but the expected ratios of ^{3}He and ^{4}He ions will be significantly lower than 1 for most ^{3}He rich events as mentioned in the introduction (see chapter 1). To evaluate the separation capabilities at ratios as small as 1 %, the data for the ^{3}He ions was scaled down by a factor of 100. The separation was then evaluated for each of the previously defined regions (I), (II) and (III) (as denoted in figure 3.22). The scaled down data is again projected relative to the separation function. Figure 3.26 shows the basic principle how the following plots are created to illustrate the large relative difference. In this figure the ratio of ^{3}He (blue line) to ^{4}He (red line) is 1 %. On the left side both isotope peaks are completely visible in a logarithmc plot while on the right side only the red shaded part is shown, this time in a linear scale. This type of plot is chosen for the following images since differences indicated by errorbars can much

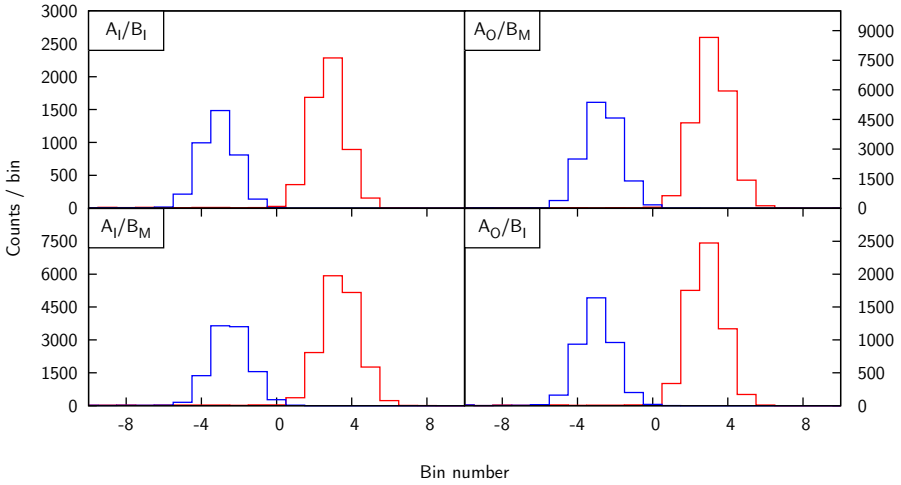

Figure 3.25: Projection of the ^{3}He (blue lines) and ^{4}He (red lines) data. The histograms are calculated as distance to the separation function 3.23 in number of bins.

easier be seen and compared in the region of the low count rates where the ^{3}He peak is located. In the closeup view the ^{4}He peak is only visible as a steep increasing edge followed by another edge at higher bin numbers.

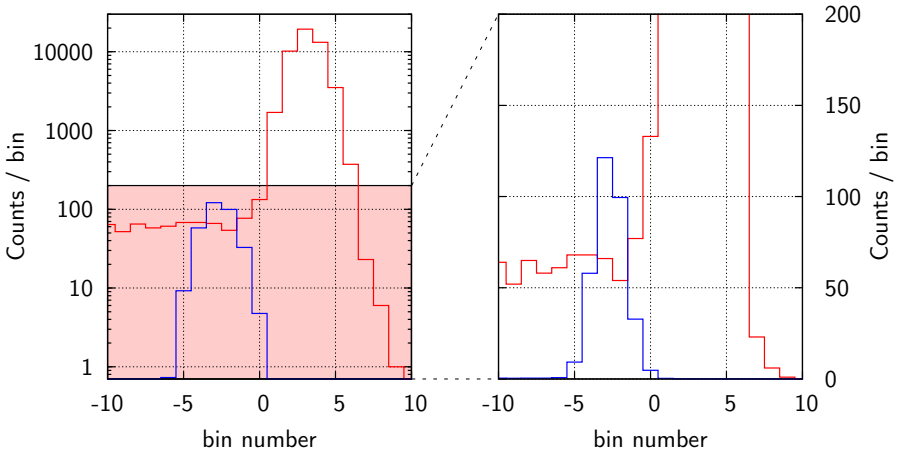

Figure 3.26: Logarithmic plot of the ^{3}He and ^{4}He peaks with a ratio of 1 % (left side). The right plot shows a zoomed version of the red shaded area in a linear scale to better indicate the count rate differences in the bins near the ^{3}He peak.

The histograms for each region and the four different coincidence conditions with a ratio of 1 % are plotted in figure 3.27 (a)–(c). The error-bars shown there are calculated by simple poissonian error with $\sigma_i = \sqrt{c_i}$ where c_i are the counts in the corresponding i-th bin. The projection of ^{3}He data (blue lines) results in a narrow peak with just a few ten counts per coincidence. There is also a contamination background due to ^{4}He ions (red lines) which are detected in the bins where the ^{3}He ions are located. The contamination is independent of the coincidence condition but shows large differences between regions (I) and (II) and the region (III). The first two regions

show a good separation of the ^{3}He signal from the background whereas in region (III) the signal vanishes in the limb of the broad neighboring peak. One reason for the weak signal in region (III) is the counting statistics. The count rate of the input spectrum (see figure 3.21) can be appoximated by two power laws with different exponents of which the one with the stronger decrease dominates the spectrum in region (III). This effect is amplified by the fact that both isotopes were calculated using the same $\frac{E}{m}$ spectra. This leads to an earlier (in terms of energy) start of the steeper decrese for ^{3}He ions than for ^{4}He . A short estimation on the basis of the derived count rates of regions (II) and (III) show that a factor of 3 in the integration time could resolve this problem. At this point it should be mentioned that the graphs show individual counts for ^{3}He and ^{4}He while in the final version the signal would be the sum of both graphs which would result in a more prominent ^{3}He peak but the separation of counts per isotope at this points facilitates the estimation of good or bad ion separation. Good separation in this case means that the difference between counts of the ^{3}He and ^{4}He is larger than at least 2 σ_i of the corresponding bin.

To increase the statistics to obtain a better signal-to-noise ratio the regions (I) and (II) are again combined together while excluding region (III). This histogram is plotted in figure 3.27 (d).

The simulation was performed with a fixed amount of particles $N = 1 \times 10^8$ and this number can be transformed into a measurement time t a real measurement would have taken under the assumption of a spectrum as shown in figure 3.21. To calculate the time t one needs first to integrate the input flux over the used energy range, half of the solid angle sphere (Ω) and the source area (A). Under the assumption of an isotropic flux F and with a radial source surface with a radius of 15.4 mm covering the complete entrance window the value of the resulting integral is:

$$C = \int_{\Omega/2} \int_A \int_0^{10^5 \frac{\mathrm{MeV}}{\mathrm{nuc}}} F \mathrm{d}E \mathrm{d}\Omega \mathrm{d}A = 7.9584 \times 10^5 \,\mathrm{s}^{-1} \tag{3.26}$$

With the value of C and the number of simulated particles N this simulation would then represent a measurement with the duration of:

$$t = \frac{N}{C} = \frac{1 \times 10^8}{7.9584 \times 10^5 \,\mathrm{s}^{-1}} = 125.65\,\mathrm{s} \approx 2\,\mathrm{min} \tag{3.27}$$

Since the 5 minutes peak spectrum from the CREME 2009 model was taken as input the time of two minutes would apply to large solar events whereas for small events the time to achieve the same statistics would then be on the order of some ten minutes.

The influence of a larger abundance than 1 % is plotted in figure 3.28. There the separation between both isotopes is simulated with abundances of 2 % (a) and 3 % (b) and the projections of regions (I) and (II) is plotted there. The ^{3}He signal (blue lines) can be clearly separated from the ^{4}He background (red lines) for all coincidence conditions. This shows that the 1 % ratio of ^{3}He to ^{4}He is indeed the lower limit the instrument will be able to resolve and that ratios above 1 % are clearly resolved.

Since the noise of the instrument has the largest effect on the broadening of the signal (see difference of figures 3.23 and 3.24) and thereby also a large effect on the separation of ^{3}He (blue lines) and ^{4}He (red lines) an estimation on higher noise levels is also performed. Two scenarios with increased noise are calculated where the noise was set to values twice as high as determined in section 3.3.1 ($\sigma_{\mathrm{ssd}} = 7.6\,\mathrm{keV}$, $\sigma_{\mathrm{BGO}} = 1.12\,\mathrm{MeV}$). Also ^{3}He abundances of 1 % and 2 % were taken into account. The results of these calculations are shown in figure 3.29 (a) for the 1 % abundance and in (b) for 2 %. The coincidence between the $\mathrm{A_{outer}}$ and $\mathrm{B_{middle}}$ segments shows the highest statistics of all the four possible coincidences resulting in a signal which is well

distinguishable from the ^{4}He background. In the three other coincidence situations the count-rates of ^{3}He are similar to those of ^{4}He ions contaminating the bins of ^{3}He which is slightly worse than in the case of normal noise levels as plotted in figure 3.27 (d). This implies that the separation is still possible under high noise situations but requires larger integration times to get a more accurate value for the ^{3}He abundance.

The combination of all four coincidence segments provides very simple mean to increase the overall statistics. Figure 3.30 shows the combined data from regions (I) and (II) with all four coincidences and a 1 σ instrument noise. The sum of both ion species is shown with a solid black line indicating the expected measured signal since in the real experiment ^{3}He and ^{4}He events are not distinguishable immediately. The counts in bins below bin number -6 almost entirely contain counts triggered by ^{4}He ions and show a rather flat distribution up to the ^{4}He main peak. This can be utilised to estimate the background contamination for a latter correction of measurement if one extrapolates the count rates of the left sided bins -10 to -6 towards higher bins where the ^{3}He signal is expected to be. Also at higher noise levels of twice the expected noise the separation remains possible as one can see in figure 3.31 which also shows the combined histograms of regions (I) and (II) for all coincidence segments. In this case also the background estimation with the help of the left-sided bins seems to be a promising method.

As a summary one can see that there is always a certain amount of ^{4}He contaminating the ^{3}He signal but one should be able to estimate the background signal with the help neighboring bins. The resolution of the isotope ratio of ^{3}He and ^{4}He can be performed down to a ratio of $\sim 1\,\%$ and if one combines the statistics of all coincidences also with degrading electronics and hence increasing noise the resolution should be possible for HET. It can also be seen that the chosen binning scheme with a logarithmic binning with 16 steps per octave is suitable to resolve ^{3}He and ^{4}He. Due to this analysis the binning scheme has been implemented as described in the FPGA logic for the flight software.

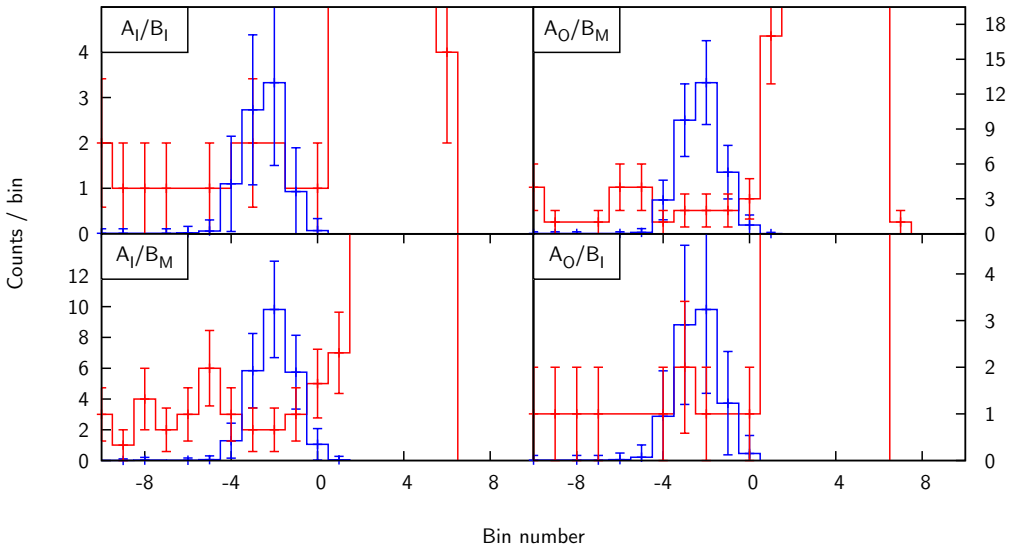

(a) Histogram of data in region (I).

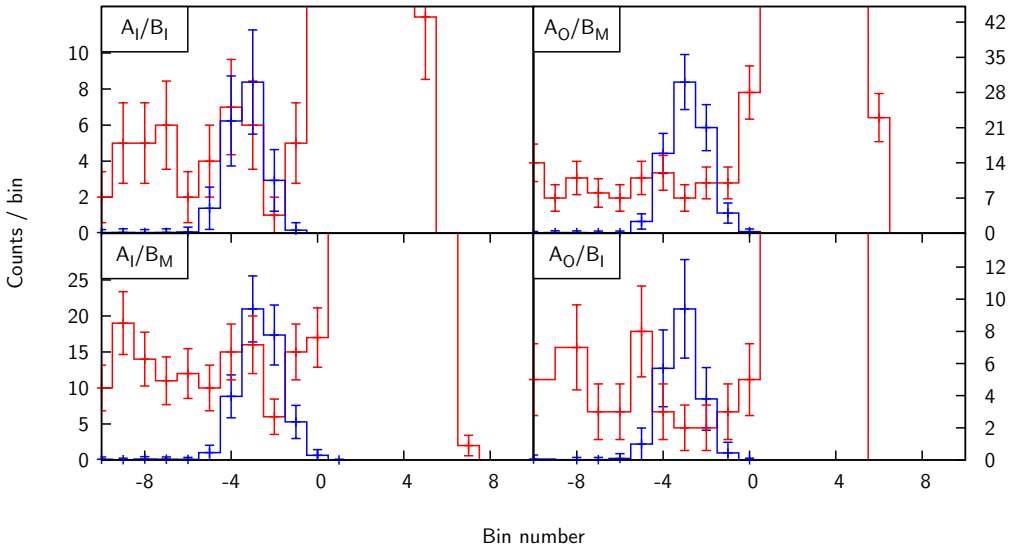

(b) Histogram of data in region (II).

Figure 3.27: Histograms of data projected to to the y-axis with bins relative to the separation function for the different regions (see equation 3.23) and a 1 % ratio of ^{3}He / ^{4}He . Negative bin values denote bins below the function, positive above. The data of ^{3}He is plotted in blue and ^{4}He data in red solid lines. *(continued on next page)*

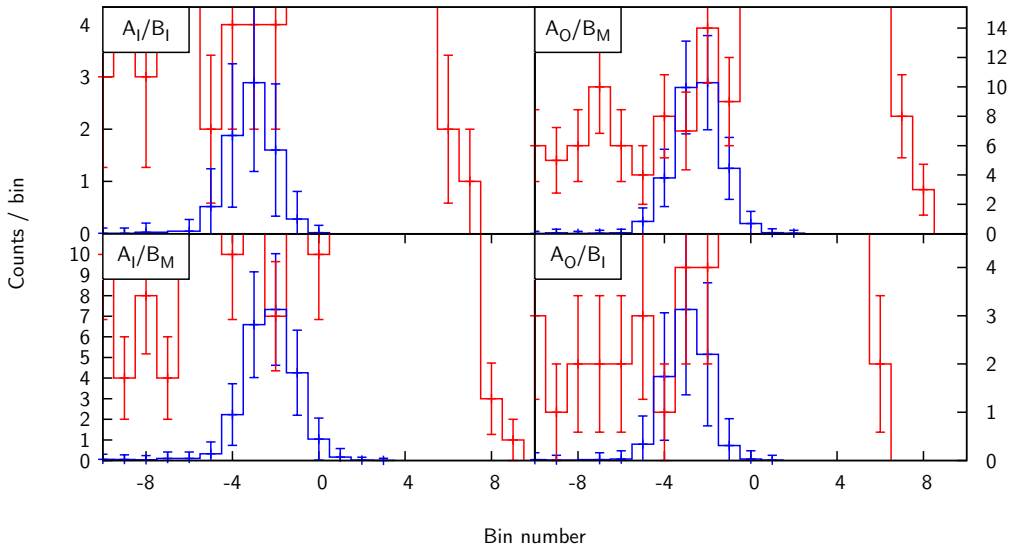

(c) Histogram of data in region (III).

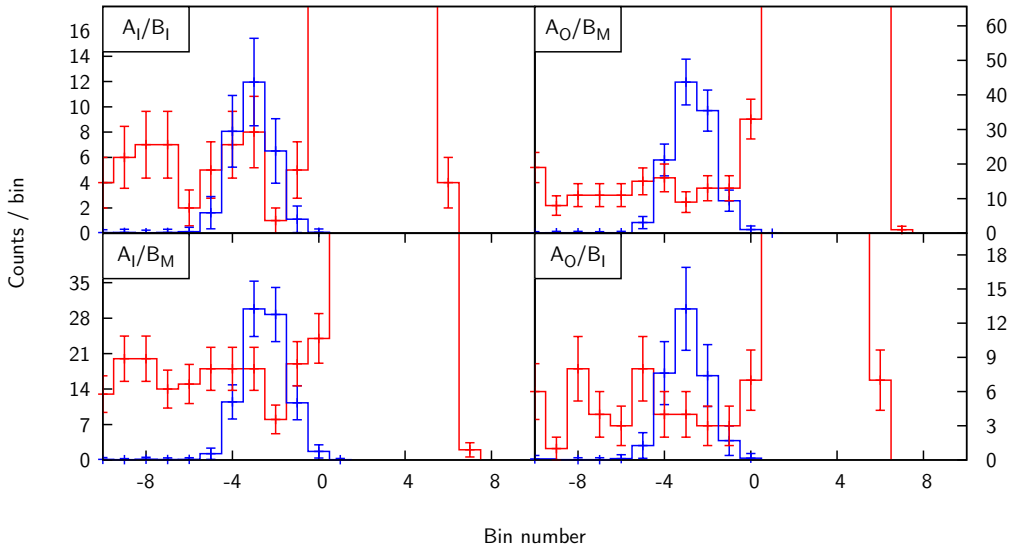

(d) Histogram of combined data in region (I) and (II).

Figure 3.27: *(continued)* Histograms of data projected to to the y-axis with bins relative to the separation function for the different regions (see equation 3.23). Negative bin values denote bins below the function, positive above. The data of ^{3}He is plotted in blue and ^{4}He data in red solid lines.

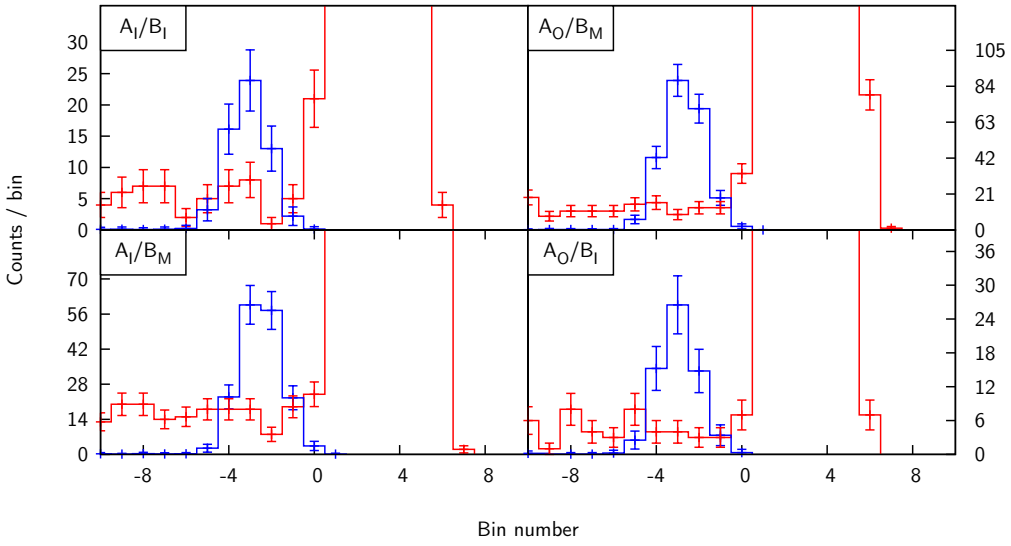

(a) ^{3}He abundance of 2 %.

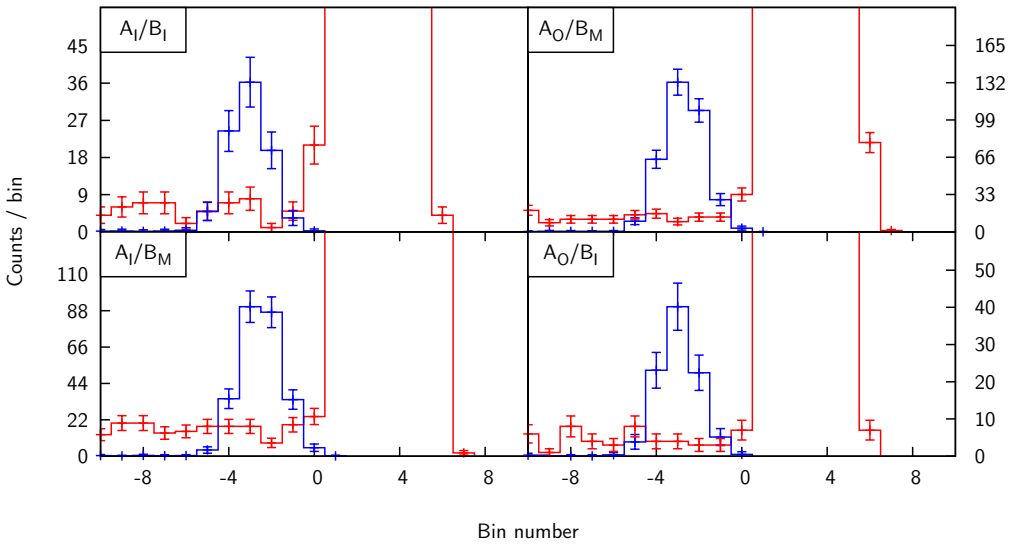

(b) ^{3}He abundance of 3 %.

Figure 3.28: Histograms of data projected to to the y-axis with bins relative to the separation function for regions (I) and (II) and abundances larger than 1 % as denoted under each sub-image. ^{3}He is plotted in blue and ^{4}He in red lines.

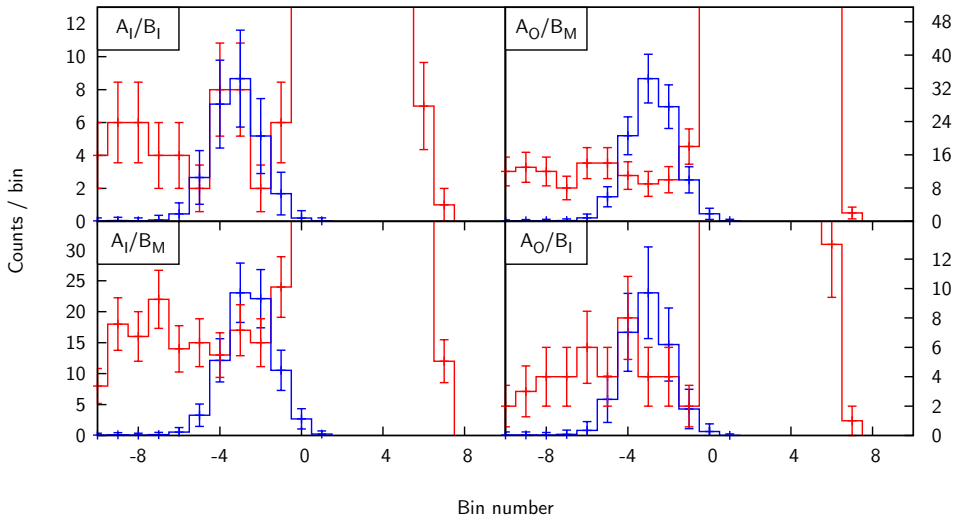

(a) 2σ noise level and ^{3}He abundance of 1 %.

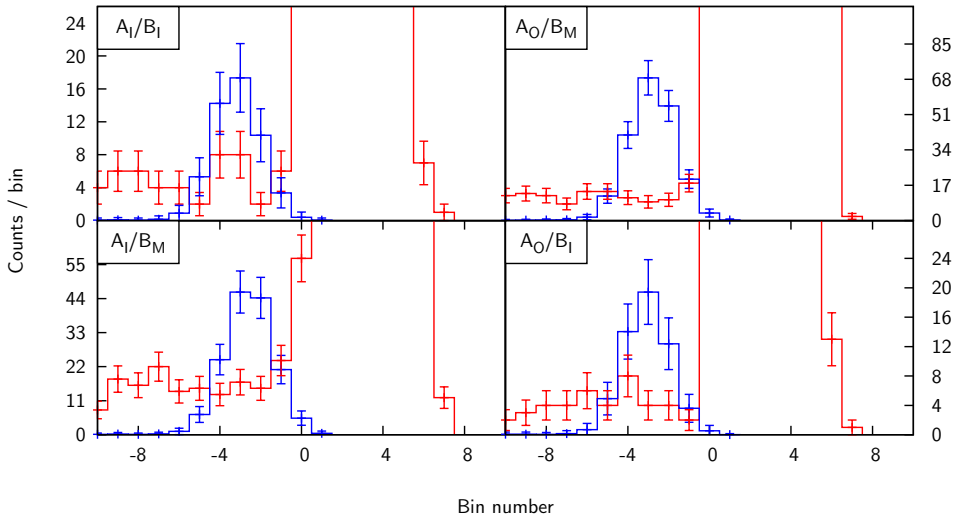

(b) 2σ noise level and ^{3}He abundance of 2 %.

Figure 3.29: Histograms of data projected to to the y-axis with bins relative to the separation function for the combination of regions (I) and (II). The instrument noise (σ) is doubled in respect to the noise as determined in section 3.3.1. Two different abundances of ^{3}He (blue lines) are simulated in this case as denoted under each sub-image (^{4}He data is plotted in red lines).

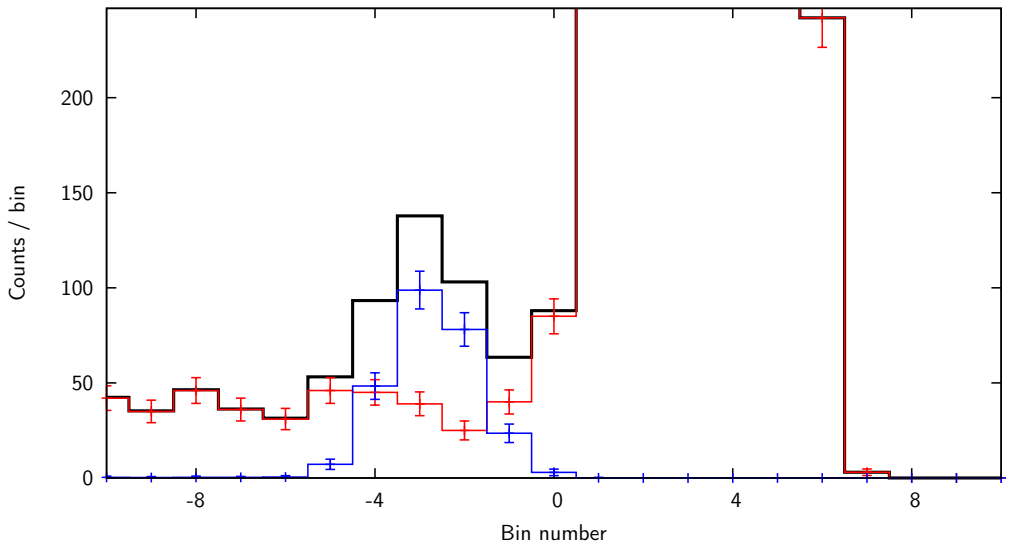

Figure 3.30: Combined histogram of regions (I) and (II) for all coincidence segments, 1 σ noise and 1 % ^{3}He abundance. ^{3}He is plotted in blue and ^{4}He in red lines. The solid black line represents the sum of ^{3}He and ^{4}He histograms.

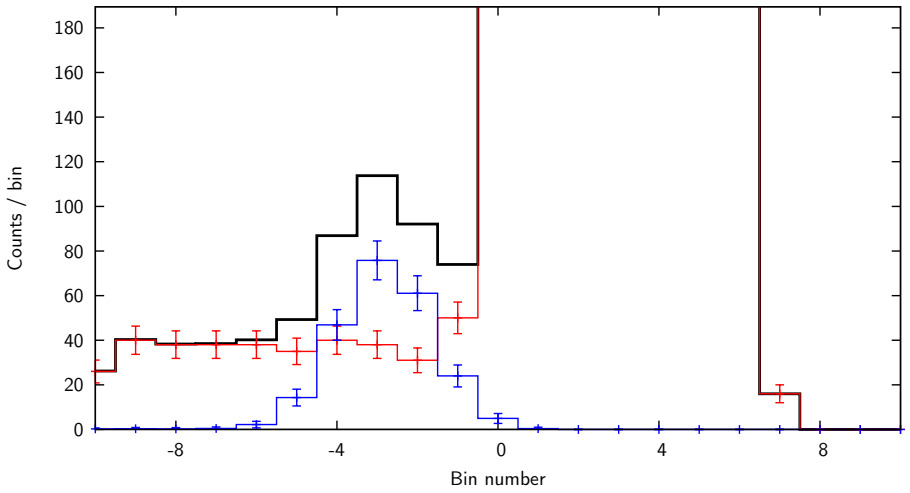

(a) 1 % ^{3}He abundance

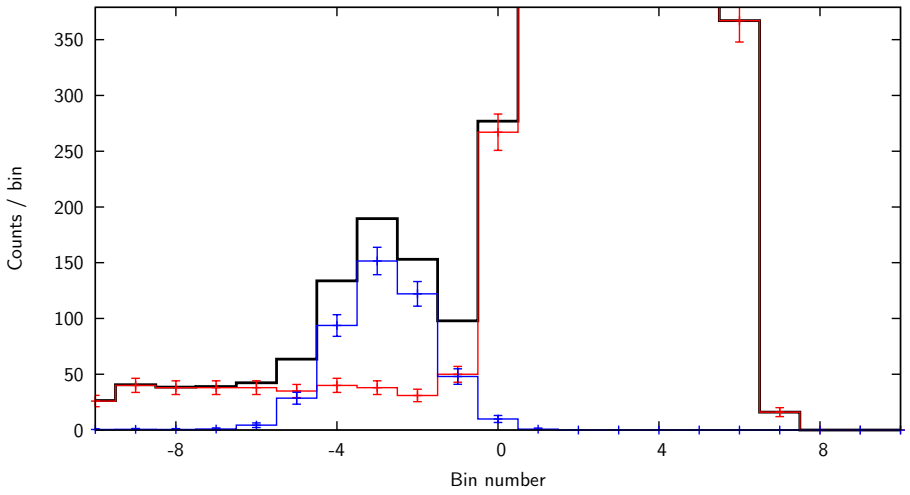

(b) 2 % ^{3}He abundance

Figure 3.31: Combined histogram of regions (I) and (II) for all coincidence segments and 2 σ noise. ^{3}He is plotted in blue and ^{4}He in red lines. The solid black line represents the sum of ^{3}He and ^{4}He histograms.

3.4 Modeling the radiation environment

During the engineering process of HET/EPT the assessment of potential effects due to the space environment is necessary since this may have an impact on various decisions throughout the instrument development. The Solar Orbiter Environmental Specification [107] provides a general description on possible problems due to space environment which are:

- Solar and Planetary electromagnetic radiation
- Plasma
- **Energetic particle radiation**
- Particulates
- Molecular and particulate contamination

This section focuses on the energetic particle radiation which HET/EPT will be exposed to during the mission. Unlike on earth's surface the Solar Orbiter spacecraft does not have any atmosphere or magnetosphere which protects the spacecraft from radiation when traveling through the interplanetary space. This makes it necessary to increase the radiation resistance of the instrument in a way that the possibility of failures due to radiation damage is minimised. The HET instrument will be attached on the outside of Solar Orbiter as described in section 1.2.2 and will therefore be exposed to the open space without any shielding except for the aluminum casing which is as thin as some mm.

Radiation damages in matter is not only dangerous for living organisms but it can also influence technical parts, especially electronic components. Damages can be caused either by lattice displacement damages or by ionisation due to primary or secondary particles and/or photons or a mix thereof. Displacement damages describe defects of the crystalline lattice of the host material mainly caused by neutrons or ions. They can be categorised in vacancies and interstitials. In the first case atoms of the host lattice are kicked out of their equilibrium position leaving an unoccupied lattice position. The latter case a primary or secondary ion occupys an intermediate position between the regular lattice points (ion implantation). Both lattice defects disturb the periodicity of the crystalline structure at that position and will have an influence on the electrical properties of the material especially for active elements made of semiconductors.

The most sensitive part in the instrument susceptible to these kinds of radiation damages are the integrated circuits used in electronics. Lattice defects such as interstitials or vacancies may introduce traps inside semiconductor junctions and therefore affect the movement of charge carriers altering the circuit parameters. Additional traps inside a pn-junction of a bipolar transistor may for example result in a reduced gain parameter influencing the signal amplification. In the case of Metal–Oxide–Semiconductor Field-Effect Transistors (MOSFETs) the gate is electrically insulated from the source-drain channel by an insulator (often SiO_2) and charged particles created by ionising radiation inside this insulation layer may cause parasitic fields or, at higher concentrations, increase the conductivity resulting in worse switching parameters or even in an insulator breakthrough destroying the electric system.

Figure 3.32 shows an example of radiation induced damages to an integrated circuit. The test device was a VIRENA chip and it was performed at the Universitätsklinikum Schleswig-Holstein in Kiel. The chip was irradiated by X-rays produced in a 6 MeV linear electron accelerator for cancer therapy. The input current (I_{CC}, red dots) is taken as a proxy for the circuit performance under the effect of ionising radiation. The acquired dose of the chip is shown in figure 3.32 as solid, blue line. The supply current starts to increase after acquiring a dose of ≈ 320 Gy. After an additional dose of 200 Gy the input current has increased by 50 % in respect to the starting value. Additional tests during the irradiation process showed that the chip started to decrease it's performance at ≈ 320 Gy and stopped being functional after the complete dose of 500 Gy.

This simple example shows that ionising radiation may cause severe problems in an instrument. The test also shows that the probability of radiation damages depends basically on the absorbed dose since this is a statistical process and electronics parts may be optimised for radiation hardness by special production procedures. In contrast to the tests shown in figure 3.32 radiation hard integrated circuits can withstand doses of 100 krad to several Mrad [108, 109] which is equivalent to 1 kGy. This is a factor of at least 3 higher than the dose where the first effects of radiation damage occur in figure 3.32.

Since the direct measurement of the radiation induced damage can barely be accomplished the manufacturers provide values for the Total Ionising Dose (TID) an electronic part can withstand without failure. In addition to the TID also LET limits are provided which denote ionisation threshold needed by particles to induce so called Single Event Effects (SEEs). The two most important SEEs are the Single Event Latchup (SEL) and Single Event Upset (SEU). The first one (SEL) denotes effects by ionising particles which create a conducting path between the supply voltages of a transistor and cause a short circuit which may destroy the part. The second one (SEU) may be created by smaller ionisation densities (smaller LETs) and can be seen as "bit-flips" in memory cells. The radiation hard RTAX[3] FPGA series is for example immune to SEU up to LET values of 37 MeV cm^2 mg^{-1} and immune to SEL up to an LET of 117 MeV cm^2 mg^{-1} [109].

The radiation doses are estimated by combining GEANT simulations of a reduced HET/EPT model with SEP and Galactic Cosmic Ray (GCR) spectra [104]. Those doses are afterwards weighted with intensities from other models [110] and corrected for orbital distances in cruise and science phase from [107]. The calculations were performed as conservatively as possible using worst case approximations if necessary. As an example the aluminum hull of the instrument has been taken as box of constant thickness d. In the real model this thickness is larger at various position which include structural stiffener and other mounting structures while the bare wall thickness is indeed equal to d. The model then returns probabilities up to which a certain dose per year will not be exceeded for the cruise and science phases. These probabilities can then be combined with the limits on TID and SEE threshold given in the datasheets of the electronic

[3]Solar Orbiter will contain RTAX 2000 FPGAs.

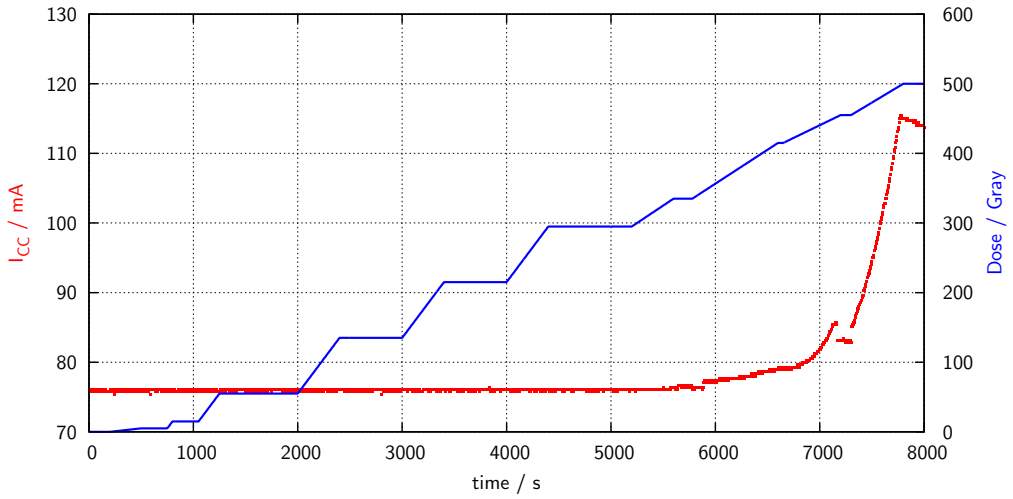

Figure 3.32: Radiation hardness tests on a VIRENA integrated circuit performed with X-rays from a 6 MeV linear accelerator at the Universitätsklinikum Schleswig-Holstein.

parts which will be used in the FMs of HET/EPT. The combination of these limits with the model is used to estimate the probability of failures in the HET/EPT electronics and silicon detectors. The results were published as report for Solar Orbiter [111] which can be found in the appendix A.2 on page 112. The report addresses all issues raised by the radiative environment expected during the mission duration and is is structured as follows:

- Introduction, data sources, simulation setup and parameters
- dose due to GCRs in
  - electronics parts
  - silicon detectors
- dose due to SEPs in
  - electronics parts
  - silicon detectors
- non-ionizing dose in silicon detectors
- dose due to solar electrons
- estimation of probability for SEEs
- probability model for total dose

Figure 3.33 shows the report's main result regarding the TID of electronic parts on different positions, denoted as "*board #i*". It describes the probability of not exceeding a certain dose inside a specific electronic board for the duration of three years of cruise phase and four years of science phase. The probability at which a TID level of 100 krad is exceeded is marked with a vertical, dashed line and occurs approximately at around 93 %. The model is limited to statements below probabilities of ≈93.2 %. This limit occurs because the model combines annual mean doses which are given at probabilities of 99 %. For a duration of seven years (three years of cruise and four years of science) the maximal attainable confidence is therefore $(99\,\%)^7 \approx 93.2\,\%$.

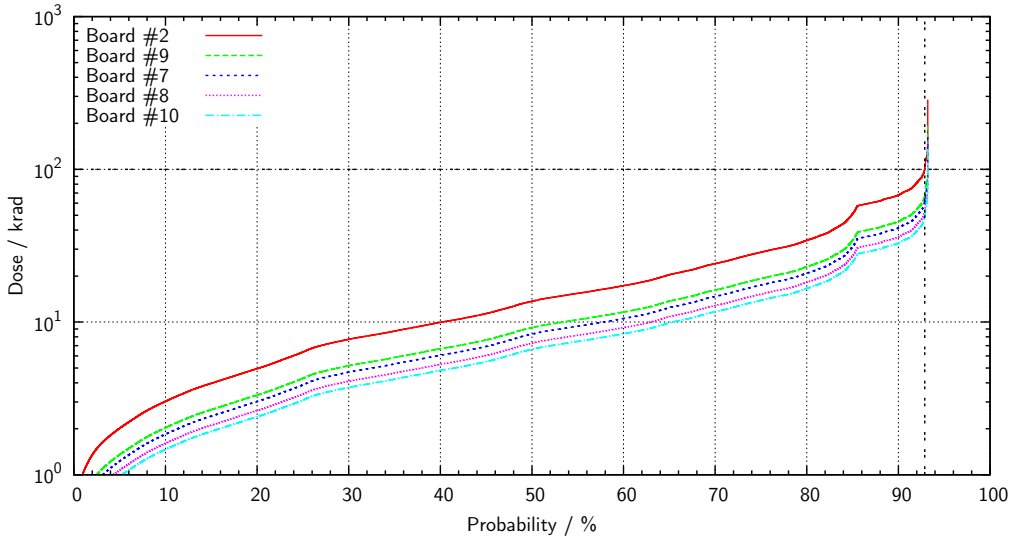

Figure 3.33: Probability of not exceeding a certain dose inside different electronic boards of HET/EPT over the duration of the whole Solar Orbiter mission, from [111]

The results of this report had direct influence on the design of HET/EPT as it could be shown that the used electronic parts are sufficient radiation hard to not fail over the course of the mission. The report was also a requirement for the instrument's Critical Design Review (CDR) which was successfully passed in 2014.

4 Scintillation non-linearity

In this chapter the term **scintillation non-linearity** is at first introduced and then an analysis for $Bi_4Ge_3O_{12}$(BGO) and $Bi_4Si_3O_{12}$(BSO) scintillation crystals is presented which was published recently in *Nuclear Instruments and Methods in Physics Research Section B 360 (2015) 129–138* [53]. The publication can also be found in the appendix A.3 starting from page 147. In this publication a model is developed which can be used to correct for scintillation non-linearity in both of the two crystal types investigated and thereafter the model will be successfully validated against an additional dataset which has been recorded after the model development to test its prediction qualities.

Scintillation non-linearity is basically a property of scintillators causing a non-linear energy-to-light conversion [112, 113]. It was discovered in organic scintillators in 1950 [114, 115] and is nowadays also known to exist in organic (i.e., anthracene, naphthalene [114, 115, 116, 117]) as well as in inorganic scintillators regardless if their scintillation property is intrinsic or because of dopants (i.e. BGO, CsI(Tl), GSO(Ce), LSO(Ce) [117, 118, 119, 120, 99]). Although the effect exists in many scintillators, it's importance depends on the exact material. As discovered by Birks, the specific light output $\frac{\mathrm{d}L}{\mathrm{d}x}$ depends on the ionisation density $\frac{\mathrm{d}E}{\mathrm{d}x}$ along the track of the incident particle [116]

$$\frac{\mathrm{d}L}{\mathrm{d}x} = \frac{S \cdot \frac{\mathrm{d}E}{\mathrm{d}x}}{1 + kB \cdot \frac{\mathrm{d}E}{\mathrm{d}x}} \tag{4.1}$$

where S is the scintillation factor and kB the "Birks"-constant indicating the extent of the non-linearity. This relationship can be found by simply assuming that an electron-hole pair created by ionising excitation has the possibility p_R for radiative or p_N for non-radiative recombination with $p_\mathrm{R} + p_\mathrm{N} = 1$. If the number of created electron-hole pairs $N_\text{e-h}$ is taken to be linear with the energy deposition along the path

$$\frac{\mathrm{d}N_\text{e-h}}{\mathrm{d}x} = S' \cdot \frac{\mathrm{d}E}{\mathrm{d}x} \tag{4.2}$$

this leads to the number of emitted photons Y per path length:

$$\frac{\mathrm{d}Y}{\mathrm{d}x} = \frac{\mathrm{d}N_\text{e-h}}{\mathrm{d}x} \cdot \frac{p_\mathrm{R}}{p_\mathrm{R} + p_\mathrm{N}} = \frac{S' \cdot \frac{\mathrm{d}E}{\mathrm{d}x}}{1 + \frac{p_\mathrm{N}}{p_\mathrm{R}}} \tag{4.3}$$

In the Birks model the probability of non-radiative recombination is set to be proportional to the number of defects along the particles' track created by the particle itself which is set to be linear with the excitation density $\frac{\mathrm{d}E}{\mathrm{d}x}$:

$$p_\mathrm{N} = C \cdot \frac{\mathrm{d}E}{\mathrm{d}x} \tag{4.4}$$

Combining equations 4.3 with 4.4 and including the mean energy of an electron-hole pair into the constant S' leads then to the Birks formula (equation 4.1) where C and p_R are encapsulated in the Birks constant kB. As the Linear Energy Transfer (LET) of particles is a function

of the particles' energy (Bethe-Bloch equation 2.1 on page 31) the energy-to-light conversion factor varies upon passage through the scintillator which is especially true for the Bragg-peak where the ionisation density of particles is increased significantly (see figure 2.2 on page 32). In addition to that the LET not only depends on the energy of the particle but also on its mass and charge resulting in different non-linearities for different ions and energies. This might lead to problems when using scintillators as calorimeter for the detection of energetic particles where a non-linearity in the detection crystal will affect the measurement results and may lead to inconsistent results. Especially for space-borne instruments like HET/EPT on Solar Orbiter the performance of scintillators needs to be well known as post-calibration runs are nearly impossible on spacecrafts.

As already mentioned in section 3.1 a BGO crystal will be used as scintillator in HET thus fundamental knowledge of this type of crystal is necessary for a successful scientific mission. In addition to BGO also the recently developed BSO crystal [70] has been investigated in parallel. For BGO there are already studies which evaluate the scintillation non-linearity but most of them are dealing with electrons and/or γ-rays [117] or with light ions [121, 122, 99, 120] and only few with heavy ions [123]. Most of these studies are also limited to energies of $<$20 MeV/nuc which is considered too low if compared with the proposed energy coverage of HET ranging from 10 to 100 MeV/nuc. In addition to that all studies are also limited to stopping particles whereas the model proposed in the following sections will include also penetrating particles which is completely new to the current day. For the BSO crystal there are currently even no publications known to the author which investigate and quantify the scintillation non-linearity.

The model is developed by comparing measurements with GEANT 4 Monte-Carlo simulations which were used to calculate the theoretical energy deposition. The experimental data was acquired at the Heavy Ion Medical Accelerator in Chiba (HIMAC) in Japan with the PQM as well as with the two demonstration models described earlier (see section 3.1). In the next section (4.1) the experimental setup at HIMAC is explained in detail and thereafter (section 4.2) the GEANT 4 simulations are introduced. Then the data processing and filtering scheme of the measured data are explained (4.3) followed by the introduction to the developed model (4.4). In the last section (4.5) the model will be validated with separate measurements and the prediction qualities are estimated.

4.1 Experimental setup

The measurements were performed at the HIMAC "*physics beam-line*" (see figure 1 in [124] for illustration). The ions provided were mono-energetic and table 4.1 lists all ion types with its initial energy E_0 in combination with the instrument used to acquire the data and the date of the beam-time. The initial particle energy was reduced by placing Polyethylene (PE) absorbers of varying thickness in front of the instrument. This enables us to measure the instrument's response for basically any energy below E_0 with the drawback of a slightly broader energy distribution of the particles which is also taken into account in the reference simulations so that this can be excluded to have a negative impact on the results. Table 4.1 also denotes which instrument was used to acquire the datapoints in a specific measurement campaign[1]. These instruments were already described in section 3.1 together with the readout electronics in section 3.2 so that only a reference to these information shall be given here.

[1] Currently (January 2016) the data is stored in `/data/etph/solo/data/` sorted according to the differnt HIMAC runs. More information about data storage can be found in the appendix A.4 on page 158.

Ion	**E_0 / MeV/nuc**	**Date**	**Instrument**
H	160	Jun 2014	HETDM (BGO)
	160	Jun 2015	PQM
He	100	Feb 2011	HETDM (BGO)
	230	Jun 2013	HETDM (BGO), HETDM (BSO)
	230	Jan 2014	HETDM (BGO), HETDM (BSO)
	230	Jun 2014	HETDM (BGO)
C	400	Feb 2011	HETDM (BGO)
	400	Jan 2014	HETDM (BGO), HETDM (BSO)
	400	Jun 2014	HETDM (BGO)
	400	Jun 2015	PQM
O	400	Feb 2011	HETDM (BGO)
	400	May 2011	HETDM (BGO)
	400	Jun 2013	HETDM (BGO), HETDM (BSO)
	430	Jun 2015	PQM
Ne	600	Jan 2014	HETDM (BGO), HETDM (BSO)
Si	600	May 2011	HETDM (BGO)
Ar	800	Jan 2014	HETDM (BGO), HETDM (BSO)
	650	Jun 2015	PQM
Fe	500	May 2011	HETDM (BGO)
	500	Jan 2014	HETDM (BGO), HETDM (BSO)

Table 4.1: HIMAC measurement campaigns separated by ion species.

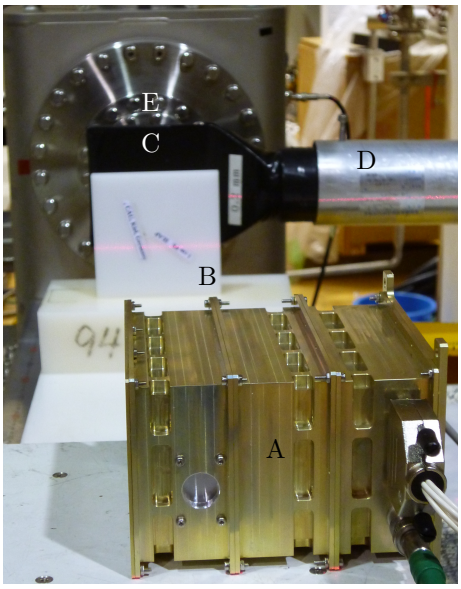

Figure 4.1: Image of the experimental setup at HIMAC showing the HET demonstration model (BSO) (A), absorber plate (B), beam monitor scintillator (C) where a photo-multiplier tube (D) is attached to and the beam exit infrastructure (E).

Figure 4.1 shows a typical experimental setup with the HET demonstration model (BSO) in the front marked as (A). The white square (B) is a polyethylene absorber which is positioned behind a scintillator (C) wrapped in black foil which is attached to a photo-multiplier tube (D). This beam monitor was present in all experiments with varying thickness depending on the ion type and was used by the accelerator operators to check the beam intensity during the measurements. The beam monitoring scintillator was available with two different dimensions ($w \times h \times d$)

- $100 \times 100 \times 0.2\,\mathrm{mm}^3$
- $100 \times 100 \times 3\,\mathrm{mm}^3$

and the thickness was chosen to be 3 mm for helium and lighter ions and 0.2 mm for all ions heavier than helium. In the background of the figure the end of the beam-line can be seen (E) which is a steel vacuum chamber with a foil-covered output window. The output window itself is not visible as it is entirely covered by the beam monitoring scintillator. The density of the PE absorber was calculated from the dimensions and mass of one block, measured with a caliper and weighed with a high precision scale, resulting in $\rho_{\mathrm{PE}} = 0.959 \pm 0.003\,\mathrm{g\,cm^{-3}}$. The instrument was aligned by a vertical and a horizontal line laser of which the latter one is visible on the surface of the white absorber and the photo-multiplier tube. The instrument was then connected via USB to a PC with the corresponding readout software as well as to two power supplies providing several DC voltages for the electronics in the range of -6 to 6 V and a high-voltage supply with -70 V for the detector bias voltage. The distance between beam exit window and the instrument were approximately 80 cm in air. Figure 4.2 [53] shows a not to scale side view sketch of the experimental setup at HIMAC with the HET demonstration model (BGO). The beam monitoring scintillator is marked as (A) and the PE absorber as (B). The instrument's parts located in the beam path, specifically the collimator and entrance foil (C), silicon tracking detectors (D), BGO crystal with readout diodes (E) as well as the anti-coincidence diode (F), are also shown as well as two particle trajectories for one stopping (solid line) and one penetrating particle (dashed line). The term "stopping" and "penetrating" particles will be used repeatedly hereafter.

The instrument was aligned to be parallel to the beam path once in the beginning of the measurement and thereafter only changes on the combination of absorber plates were performed. Ion exposure time was around 15 minutes with a spill rate of one per three seconds and an intensity between 500 to 1000 particles/spill resulting in several hundred thousand primary particles per measurement. The photo of a fluorescent screen positioned in the beam is shown in figure 4.3 with a spacing of the grid of 1 cm. The shape of the beam profile is not very homogeneous but shows a well collimated beam with an extent less than $1\,\mathrm{cm}^2$. All components which were physically present during these measurements and which affect the particles' passage to the detectors

were later included in the reference simulations which are described in the next section.

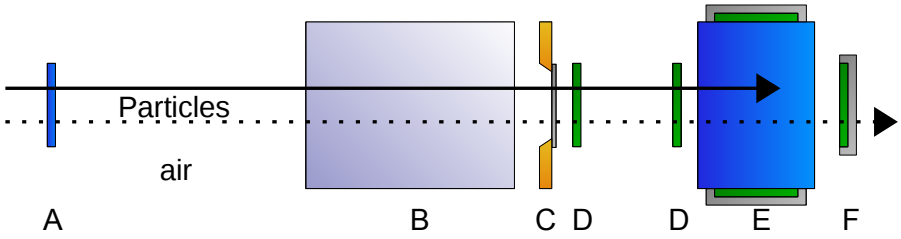

Figure 4.2: Sketch of the experimental setup at HIMAC using the HET demonstration model (BGO). The labeled components are: (A) HIMAC beam monitoring scintillator, (B) PE absorber, (C) entrance window covered with Al foil, (D) tracking detectors, (E) BGO crystal and (F) anti-coincidence detector (photo-diode). From [53] used under CC BY-NC-ND 4.0 [125].

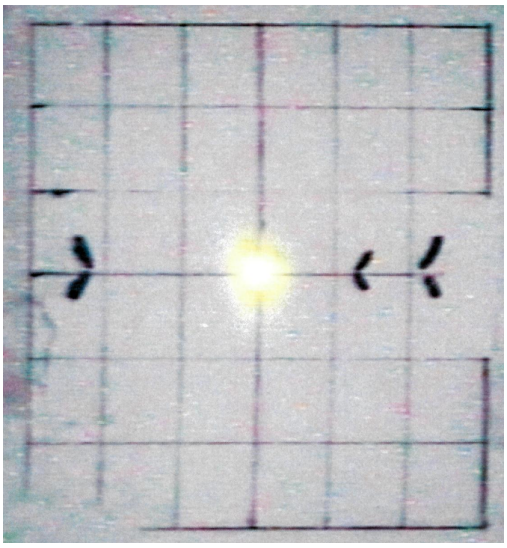

Figure 4.3: Photo of a fluorescence screen showing the beam profile of 230 MeV/nuc helium ion beam at HIMAC. The grid has a spacing of 1 cm and the beam profile can be seen as bright quadratic area in the center.

4.2 Simulations with GEANT 4

The reference calculations were performed with GEANT 4 which was introduced in section 2.3. The experiment was modeled to adopt the experimental setup as exactly as possible. All components which will be penetrated by the incoming particles were modeled with correct thicknesses and positions. As already mentioned in the previous section the beam monitor was the first component in the beam path and was available in two different thicknesses. A sketch of the monitor's profile is shown in figure 4.4 and it consists of a core made of EJ-212 scintillation material [126] wrapped in three different foils. The scintillator thicknesses d_1 was 0.2 mm/3 mm depending on the ions currently accelerated. It was wrapped in $d_2 = 1000\,\text{Å}$ thick aluminum foil and the two outer layers consist of $d_3 = 10\,\mu\text{m}$ thick Mylar shield and an outer layer made of polyvinyl chloride with $d_4 = 0.1\,\text{mm}$. According to the datasheet of EJ-212 scintillation material it was modeled as polyvinyl-toluene based scintillator with the following densities for protons and carbon ions

- $\rho_\text{H} = 5.23 \times 10^{22}\,\text{cm}^{-3}$
- $\rho_\text{C} = 4.74 \times 10^{22}\,\text{cm}^{-3}$

resulting in a total density of $\rho_\text{EJ-212} = 1.03\,\text{g}\,\text{cm}^{-3}$. The scintillator thickness in the simulation was chosen to match the appropriate value during the experiment.

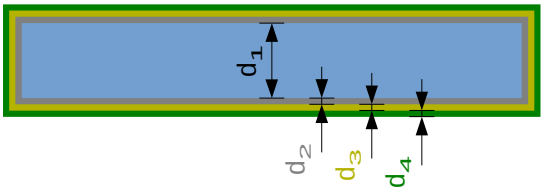

Figure 4.4: Sketch of the HIMAC beam monitoring scintillator. The scintillator (blue) is made of EJ-212 [126] and is wrapped in three different foils of aluminum (grey), Mylar (yellow) and polyvinyl chloride (green).

The next component in the beam path of the simulation is the PE absorber. In the experiments the absorber was composed of several blocks with varying thicknesses to achieve the desired total thickness but in the simulations the absorber was modeled as one single block of PE. As the surfaces of the individual blocks were smooth and all blocks were put together as close as possible without any air gap this is a reasonable approximation of the experiment. The thinnest absorbers were also glued together using simple adhesive tape around their edges. Even in the case of a small air gap this should only affect beam broadening and not the resulting energy behind the absorber. The density ρ_PE of the PE block was set to $0.96\,\text{g}\,\text{cm}^{-3}$ in accordance with the measured value of $\rho_\text{PE} = 0.959 \pm 0.003\,\text{g}\,\text{cm}^{-3}$. The next part in the beam path is then one of the three instruments (PQM, demonstration model (BGO/BSO)) as described in section 3.1. Each instrument has been modeled individually by reconstructing all parts which were located in the beam path and with the parts' exact dimensions and distances. The particle beam was simulated using a $1 \times 1\,\text{cm}^2$ source area which approximates the experimental beam profile as shown in figure 4.3. Differences of the experimental and simulated beam profiles are negligible and only result in different intensities which can be adopted for by simulating more primary particles. The space surrounding the previous described components was assumed to be filled with dry air consisting of

- 78 % nitrogen

- 21 % oxygen
- 1 % argon

with a density of $1.293\,\mathrm{kg\,m^{-3}}$. The main simulation results were the total energy deposition in each individual detector as this value can be compared to the value obtained in the experiment. The simulation data was post-processed in the same manner as the calibrated and filtered experimental data as it is described in the next section.

4.3 Data processing and filtering

All models used for data acquisition were development models and they only provide raw data which has to be processed and filtered prior to a scientific analysis. For the data filtering the digitised data tuples as described in section 3.2 (page 53) were used containing a trigger mask, Pulse Age (PA), pulse height and phase values. As a first step the bit-masks of the trigger logic were evaluated and events which did not have a bit-mask indicating triggers in inner segments of both front silicon detectors and the scintillation crystal were discarded. For the HET demonstration model (BSO) which did not have any segmented tracking detectors the coincidence condition was set to triggers in both tracking diodes. In the same filtering step all events with Pulse Age (PA) values of 1 or less were also rejected. Those events with lower pulse ages are mainly caused by one event which triggers the instrument at two consecutive readout clocks producing two events instead of one for one single incident particle. After this very first filtering procedure for each detector the best matching gain channel is chosen. The high gain channel is chosen as long as the signal was well below the saturation limit of the electronics saturation. All proton and helium and some carbon measurements fall into the high gain category. For all other ion types the signals of the high gain channels are ignored and only the low gain channels are evaluated. After this gain selection the anti-coincidence signal was checked manually for ions with energies around the energy of barely stopping ions of the same kind. It was confirmed that particles which will penetrate through the crystal and raise a trigger in the anti-coincidence detector do this in both datasets, the experiment as well as the simulation. The same was checked for particles which barely stop inside the scintillator. These checks verified that the simulations and experiments were consistent with each other in respect to the total stopping power. After consistency of experiment and simulations has been validated the data was binned in a two-dimensional histogram with the energy deposition of the crystal as x-axis and the energy deposition of the tracking detector as y-axis as shown in figure 4.5 [53] where a comparison of simulated (left) and experimental (right) data is depicted. The image is composed of several measurements/simulations with different absorber thicknesses of polyethylene. Each peak in the picture corresponds to a fixed PE thickness of which in total 7 are used in this plot and which are located at $E_{\mathrm{Si}} > 8\,\mathrm{MeV}$. On the right side where the experimental data is shown, two of those peaks are overlapping and forming a broad peak second from the right. There are also some peaks with lower intensities visible which originate from fragmentation of the primary ion inside the absorber creating boron and lighter ions down to protons. Since the intensity map is in logarithmic scale those fragments are rarer by at least one order of magnitude. The image shows a good agreement between experiment and simulation since the overall structure looks similar. At this point it shall be noted that the y-axes have the same scale but that the scales of the x-axes are different by a factor of $\approx 50\,\%$. This means that the energy depositions for the silicon tracking detectors are equal in experiment and simulation as the energy positions on the y-axis are the same. In contrast to the silicon detectors, the signal in the calibrated crystal shows $\approx 50\,\%$ less energy than one would expect from the simulations. This "*missing energy*" can be assigned to the scintillation non-linearity as introduced earlier in section 4.

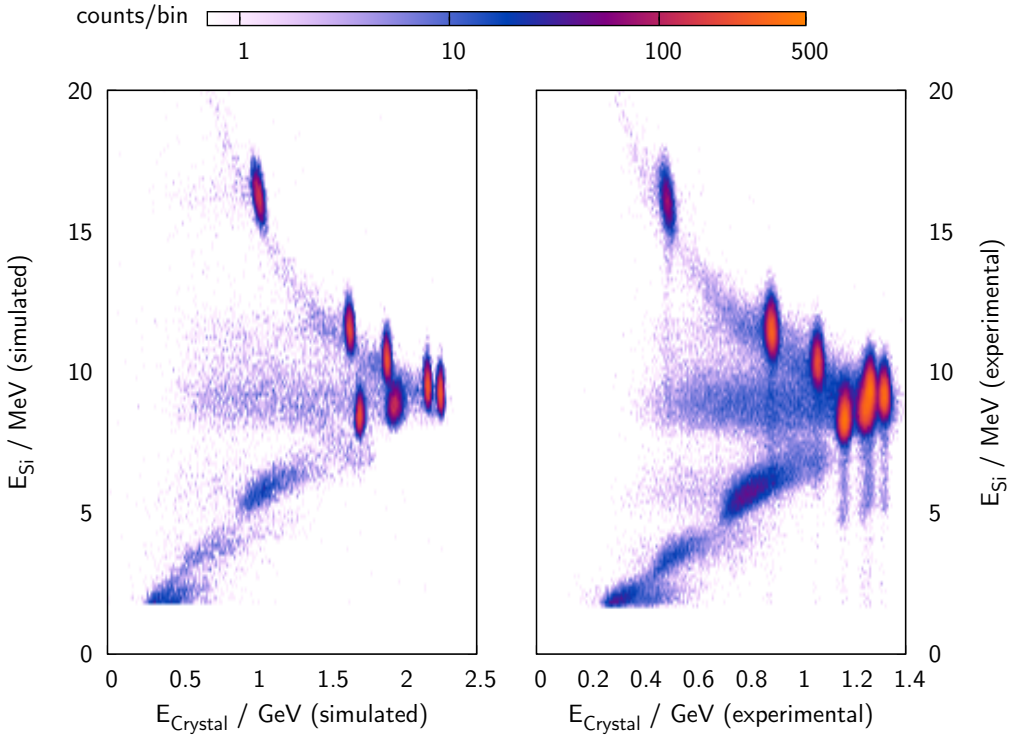

Figure 4.5: Intensity map of simulated (left) and experimental (right) data for BGO crystal and carbon ions with various absorber thicknesses. The plot shows the energy deposition in the first tracking detector E_{Si} as a function of the energy deposition in the scintillation crystal E_{Crystal}. From [53] used under CC BY-NC-ND 4.0 [125].

In figure 4.5 the datapoints of each starting energy are accumulated within one peak with more than 100 counts/bin. For the data analysis those peaks are then fitted with a rotated, two-dimensional Gaussian function

$$g(x,y) = A \cdot \exp\left[-\left(\frac{(x-x_0)\cdot\cos(\varphi) - (y-y_0)\cdot\sin(\varphi)}{\sigma_x} \right)^2 - \left(\frac{(x-x_0)\cdot\sin(\varphi) - (y-y_0)\cdot\cos(\varphi)}{\sigma_y} \right)^2 \right] \tag{4.5}$$

where A, x_0, y_0, σ_x, σ_y and φ were the fit parameters. The resulting values for x_0 and y_0 then represent the center of the peak distribution in units of energy and those values are calculated for each starting energy from both the simulation and experimental dataset. Those tuples of experimental and simulated energy positions can then be used for further analysis as for instance the calibration and the modeling of scintillation non-linearity which will be introduced in the next section.

4.4 Model for quenching prediction

The model for quenching prediction in BGO and BSO crystals will be explained briefly in this section. A more detailed description of the model and the derivation of it can be found in *Nuclear Instruments and Methods in Physics Research Section B 360 (2015) 129–138* [53] which can also be found in the appendix A.3 starting from page 147.

The model is derived from the comparison of experimental, calibrated datapoints with simulated values using GEANT 4 and the energy deposits in the scintillation crystals were compared. Figure 4.6 shows such a comparison for neon ions with an initial energy of 600 MeV for several absorber thicknesses. The plot shows the fitted peak positions obtained from a 2-dimensional histogram as shown in figure 4.5 for simulated and experimental, calibrated values. The measured energy depositions in the scintillators are plotted as a function of the corresponding simulated energies. The mismatch between simulated and experimental values which was mentioned already earlier when describing figure 4.5 and can be seen in this plot as well. If measured and calculated values would be identical the points would be located on the black, dashed line, representing the identity function $y(x) = x$. The energy difference is caused by the scintillation non-linearity as described in section 4 and is as high as 50 %. The dashed line represents the fit of an analytic

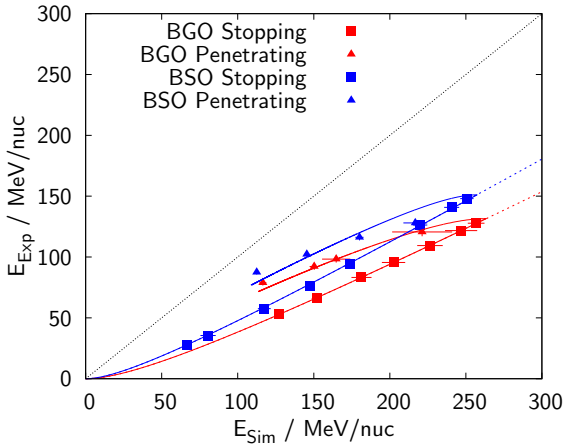

Figure 4.6: Light yield of neon with fits of analytic light curve (equation 4.6) to stopping particles (dashed line). Numerical solution of equation 4.6 including penetrating particles in 2 cm of crystal material (solid line). Particles without quenching are expected to lie on the diagonal black dotted line. From [53] used under CC BY-NC-ND 4.0 [125].

solution of the light yield L which is the integral of equation 4.1 over the path length [53]

$$\begin{aligned} L(E, A, Z) &= \int dL = \int_0^{x_{\max}} \mathrm{d}x \frac{S\frac{\mathrm{d}E}{\mathrm{d}x}}{1 + KB \cdot \frac{\mathrm{d}E}{\mathrm{d}x}} \\ &= f_1 \cdot \left(E - f_2 \cdot AZ^2 \cdot \log\left(\frac{E + f_2 \cdot AZ^2}{f_2 \cdot AZ^2} \right) \right) \end{aligned} \tag{4.6}$$

in which A and Z represent the particle's mass and charge number and E the particle's energy. The best fit with f_1 and f_2 as variable parameters to the datapoints of stopping ions (squares) is shown as dashed line for BGO (red) and BSO (blue) in figure 4.6 together with a numerical solution of the integral (equation 4.6) which also includes penetrating particles (triangles). The

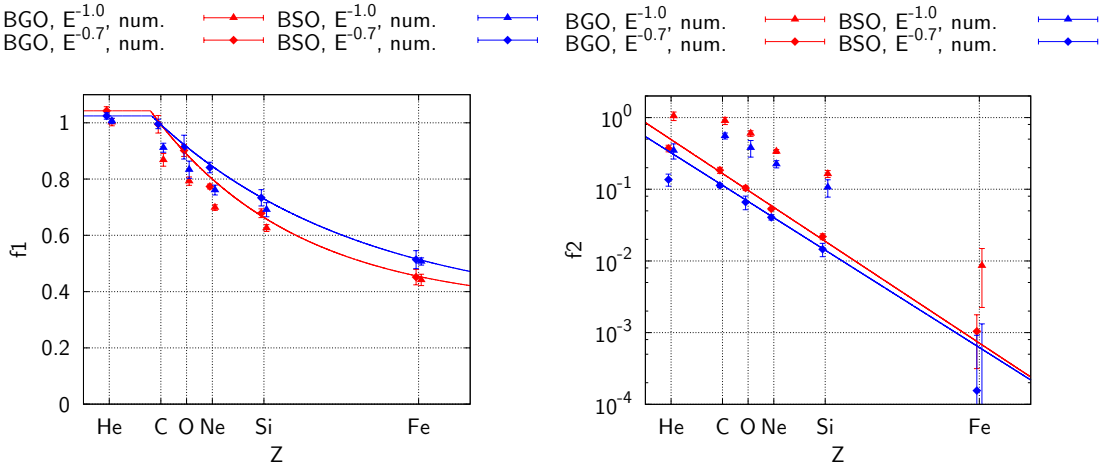

(a) f_1 parameter obtained through fits to all datapoints of stopping and penetrating ions for numerical evaluation with different exponents of -1 (triangles) and -0.7 (diamonds). Solid lines represent model function 4.9 with best fit to the individual points.

(b) f_2 parameter obtained through fits to all datapoints of stopping and penetrating ions for numerical evaluation with different exponents of -1 (triangles) and -0.7 (diamonds). Solid lines represent model function 4.10 with best fit to the individual points.

Figure 4.7: Fit results for the model functions 4.9 and 4.10 to the individual parameters f_1 and f_2 for BGO (red) and BSO (blue).. From [53] used under CC BY-NC-ND 4.0 [125].

LET in this case is approximated as

$$\frac{\mathrm{d}E}{\mathrm{d}x} \approx \frac{C \cdot AZ^2}{E} \tag{4.7}$$

which is commonly used in literature [119]. This approximation already describes the behavior of the datapoints well and allows the analytic solution. Nevertheless it was found that $\frac{\mathrm{d}E}{\mathrm{d}x}$ is better approximated by a slightly different formula with [53]

$$\frac{\mathrm{d}E}{\mathrm{d}x} \approx \frac{C \cdot AZ^2}{E^\alpha} \tag{4.8}$$

with $\alpha = 0.7$. The resulting parameters for f_1 and f_2 which were obtained with numerical integration of equation 4.6 in conjunction with equation 4.8 and fitted to all datapoints of one ion species are shown in figure 4.7. There the fit results for different exponents of α (0.7, 1.0) for BGO (red) and BSO (blue) are shown. It can be seen that the difference due to different assumptions on α is rather small for f_1 but has a large impact on the f_2 parameter which is about one order of magnitude smaller when using $\alpha = 0.7$ than 1.0.

The prediction model is based on the value of $\alpha = 0.7$ and it is shown as solid line in the plot for BGO (red) as well as for BSO (blue). The model functions are given by [53]

$$f_1(Z) = \min(I_1, A_1 \cdot \exp(-\lambda_1 \cdot Z + O_1)) \tag{4.9}$$

and

$$f_2(Z) = I_2 \cdot \exp(-\lambda_2 \cdot Z). \tag{4.10}$$

	BGO	BSO
I_1	1.043 ± 0.121	1.024 ± 0.052
A_1	1.109 ± 0.077	0.978 ± 0.014
λ_1	0.089 ± 0.021	0.062 ± 0.004
O_1	0.344 ± 0.071	0.321 ± 0.026
I_2	0.851 ± 0.203	0.543 ± 0.034
λ_2	0.272 ± 0.024	0.261 ± 0.008

Table 4.2: Fit results for equations 4.9 and 4.10 to the data of figures 4.7a and 4.7b.

with the resulting parameters I_1, I_2, A_1, λ_1, λ_2 and O_1 given in table 4.2. The model was developed to predict quenching factors for ions up to iron with energies up to 100 MeV/nuc in BGO and BSO scintillation crystals. It might also be used to predict non-linearities for ions with higher energies and ions with higher masses and charges but this has not been tested up to now due to lack of datapoints. In the next section the model will be validated with additional argon ions to test the prediction qualities. Those are also quantified and compared to the raw, uncorrected data of HET.

4.5 Validation of proposed model with argon ions

Additional measurements were performed at HIMAC with argon ions in June 2015 to validate the proposed model. These ions are perfectly suited to test the model since the atomic number of argon ($Z_{\mathrm{Ar}} = 18$) is between silicon ($Z_{\mathrm{Si}} = 14$) and iron ($Z_{\mathrm{Fe}} = 26$) which were used among others to develop the model. The primary energy of the accelerated argon ions was 650 MeV/nuc and during the measurement campaign also data for protons (160 MeV/nuc), carbon (400 MeV/nuc) and oxygen ions (430 MeV/nuc) were acquired. The argon data was obtained with the HET/EPT PQM as described in section 3.1.1 and the experimental setup was the same as described earlier (see section 4.1). The data was also processed in the same manner as described earlier in section 4.3.

Prior to the analysis of argon data the individual calibrations of the different measurement campaigns were compared. This was done on the basis of carbon and oxygen measurements since data for both ions has been taken in previous HIMAC runs. They are now used to validate the calibration of the most recent measurement campaign. Figure 4.8 shows all carbon (a) and oxygen (b) datapoints. The color indicates whether the data point has been taken in the validation run in June 2015 (red) or during a previous run (blue). Particles penetrating the scintillation crystal are plotted as triangles and those which stop inside the crystal were marked as squares. The plot shows clearly that the datapoints are in very good agreement within the estimated uncertainties concluding that the individual calibrations are consistent with each other. It is therefore expected that variations between model and experimental data due to calibration differences can be neglected.

Now that the calibration has been validated and possible issues due to differences in calibration could be excluded, the model's prediction for argon ions were calculated and were compared with the measured data. This comparison is shown in figure 4.9 where the datapoints are plotted as red squares (stopping ions) and triangles (penetrating ions) and the model's prediction is shown as dashed line. In addition to the model there is also a best fit to the argon data plotted as solid line. It represents the best numerical fit as described in the previous section with an exponent of $\alpha = 0.7$ (see equation 4.8 on page 92). The aim of the model is to derive the theoretical energy deposit, in this case represented by the simulated energy E_{sim}, from a given experimental deposit

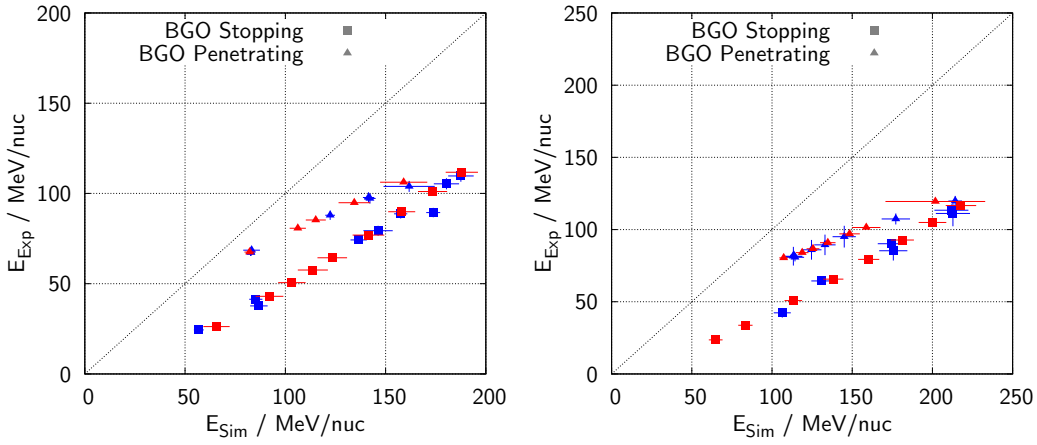

(a) Carbon (b) Oxygen

Figure 4.8: Comparison of old (blue) with most recent (red) calibrated HIMAC data for carbon (left) and oxygen (right) indicating the quality of calibration.

in a calibrated calorimeter:

$$f(E_{\text{exp}}) \longmapsto E_{\text{sim}} \tag{4.11}$$

This is the inverse function of the light yield curves as shown in figure 4.9 for argon ions. The accuracy can be estimated by comparing the difference between model predicted values and the best individual fit for a specific ion species, in this case the argon data. Figure 4.10 shows the deviations from the model with respect to the best individual fit for stopping (solid red line) and penetrating (solid blue line) particles. It also shows the deviation from the best individual fit in respect to the identity function as dashed line. The latter one would be the energy difference between measurement and the actual energy deposition without any correction. The differences represent the trend of the scintillation non-linearities as they are largest for low energy, stopping particles, decreasing for higher energetic particles down to a minimum for strongly penetrating particles. This behavior is consistent with theory since the mean value of $\frac{\mathrm{d}E}{\mathrm{d}x}$ decreases in the same manner which is the main driver for those non-linearities (see equation 4.1). The solid lines represent the percentile deviation between the model predictions for argon and the best individual fit of the light-yield function to the datapoints. It can be seen that the deviations have been reduced to a great extent. The predictions for penetrating particles now is in the range from -10 to $10\,\%$ which was previously in the range from $-40\,\%$ up to $-60\,\%$. Also the predictions for stopping particles has shifted from a range of $-80\,\%$ to $-60\,\%$ down to -20 to $-5\,\%$. The model was able to reduce the overall error of the energy determination from more than $50\,\%$ of the actual energy down to an uncertainty of $10\,\%$ in most of the detection range which is a significant improvement for the precision of particle detecion of HET. It should again be mentioned here that the accuracy of the model has been tested at an ion species which has not been used for the development of the model and that the prediction qualities for important ions like helium, carbon and oxygen are even better.

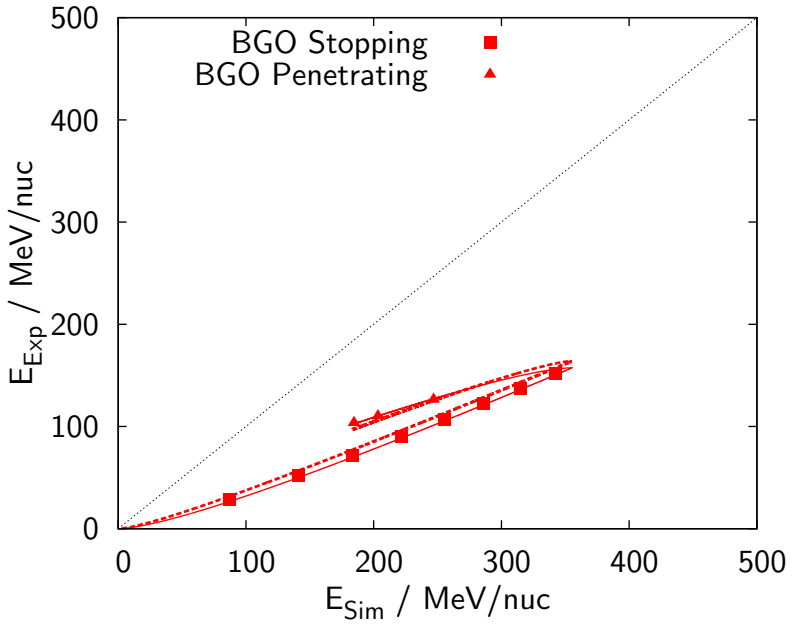

Figure 4.9: Argon experimental data from HIMAC run in June 2015 with best individual fit (solid line) and model function (dashed line).

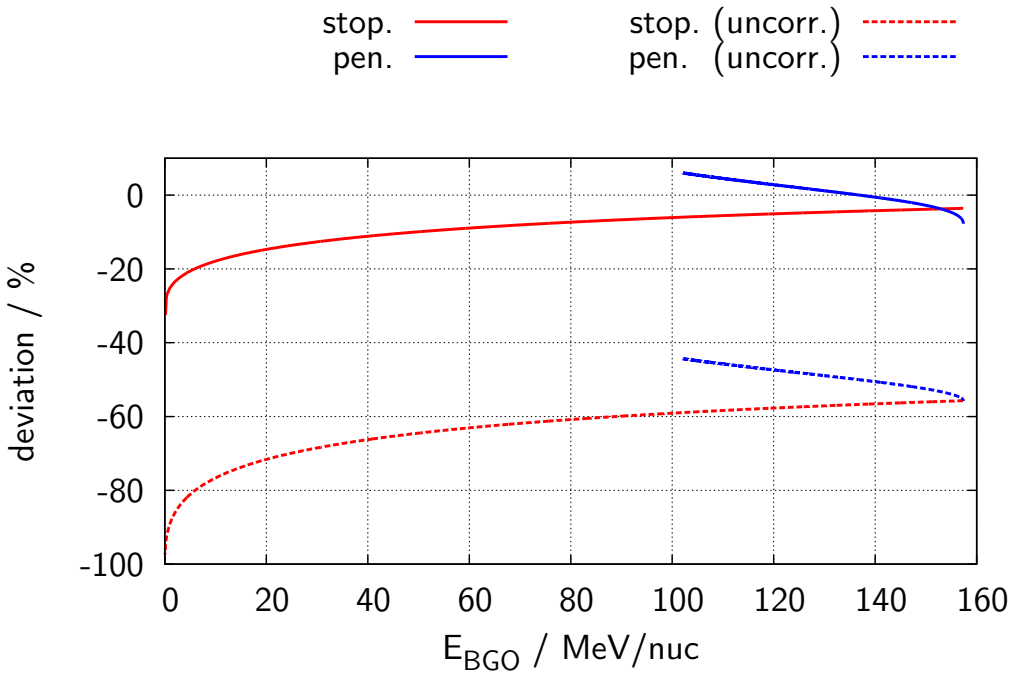

Figure 4.10: Deviations between measured, uncorrected and actual energy deposition of argon ions in BGO (dashed line) and the corrected values using the model predictions (solid line). The deviation are separated into penetrating (blue lines) and stopping particles (red lines).

5 Discussion and conclusions

More than 40 years after the launch of the Helios spacecraft Solar Orbiter will provide an unique insight into heliospheric physics very close to our sun. It will help to develop a much more detailed understanding on the processes taking place at our sun which influence the nearby space and our earth's environment. The HET instrument is part of this complex system and will address the scientific questions by measuring energetic particles created at the sun in the high-energy range of several tens of MeV and above. In this thesis several key points of the HET sensor were analysed in respect to it's influence on the mission.

During the early stages of the instrument development the radiation hardness is one aspect for a successful mission. Without sufficient resistance to ionising radiation the instrument might suffer severe damage which would lead to early failures soon after launch. Since the accurate determination of the radiative environment in the heliosphere is currently not possible, a model for the prediction of Total Ionising Dose (TID) and Single Event Effects (SEEs) was developed from which combines GEANT 4 simulations with existing models for the prediction of particle fluxes and spectra. With this model failure probabilities could be estimated under worst case assumptions and lower limits for the required radiation hardness of the electronic components could be derived to minimise and/or exclude these failure sources. With these results the appropriate electronic components were selected and it was shown that no additional shielding would be necessary. This saves mass and significantly lowers the engineering complexity of HET. Additionally the calculation of the expected ionising dose for the instrument's electronic was one important step during the critical design review process (CDR) for the instrument by the ESA. Since the prediction of "Space Weather" is not possible nowadays this radiation estimation is based on worst case approximations derived from known parameters and empirical studies of the heliosphere and the energetic particles within. The proton fluence model which has been included in the radiation dose estimation is based on data obtained during solar cycles 20 to 22 [110] corresponding to $\approx$ 30 years of data. The estimated probabilities in this case strongly depend on those events observed within this interval observed at Earth. In this dataset events like the "Carrington" event [127] or the solar eruptive event in July 2012 [128] are not included. Those events belong to the largest observed events to the current day and occur on timescales of many decades to centuries [127]. The "Carrington" event was estimated to have at least four times the solar proton fluence than comparable large events recorded during the solar cycles 20 to 22 in August 1972 [127]. Such large events directly hitting the spacecraft would definitely cause larger doses than predicted by the model. Nevertheless since the August 1972 event is included in the statistical analysis and since such large events only occur very rarely the deviations from model predictions are expected to be negligible. On the other hand the model only estimates the probabilities which implies that there is no guarantee that the instrument will not suffer from radiation damage over the duration of the mission. The results of the radiation analysis were published as official report[1] as requested by ESA for the CDR. This report has been accepted during the review process and lead to a successful passing of the CDR in 2014.

A next step in the design process of HET was to dimension the digital readout logic in such a way that the scientific requirements were met. One of these requirements is the separation of ^{3}He and ^{4}He down to a ratio of 1 %. This ensures that ^{3}He -rich solar events can be identified

[1] Latest version: SO-EPD-KIE-RP-0061 iss1 rev5 EPT- HET radiation analysis report

to disentangle the different possible acceleration mechanisms for energetic particles at the Sun. To estimate the ^{3}He and ^{4}He separation capabilities of HET the different noise sources in the instrument were identified and a model has been developed to simulate the instrument's response. For this simulation the light propagation inside the scintillating BGO crystal and the noise of the readout electronics have been investigated, modeled and adopted to simulated ^{3}He and ^{4}He signatures. There were also some data processing procedures found which can later be used with experimental data to increase the intensity of ^{3}He signatures. The simulations of the isotope separation capabilities of ^{3}He and ^{4}He are performed on the basis of the planned data processing electronic and it was taken care that the procedures can be implemented later in the readout electronic without any further constraints. Those SEP signatures were derived for a prototype event with a fixed spectrum. Since each SEP event is unique, especially in respect to it's energy and temporal profile, deviations from simulation and real data can be expected. The analysis is based on the separation of ^{3}He and ^{4}He in three different regions which correspond to three different energy ranges (see page 66). Hence possible deviations from the reference energy spectrum can be compensated for by analysing each of those regions separately with different weighting. In addition to the differences in energy individual SEP events might also differ in intensity from the simulated one. Since the method is based on a statistical analysis of the two isotope populations, this will directly influence the necessary integration time to determine the ^{3}He to ^{4}He ratio of a specific event. For small events a blurred temporal profile of the ^{3}He to ^{4}He ratio is expected while it will be sharpened for events which are larger than the one used for the simulation. Especially at this point it would be very helpful to test the separation capabilities with real, experimental data with the PQM. Since ^{4}He is already rare on Earth the same is true at an even greater extend for ^{3}He. This means that not only the acquisition of ^{3}He is difficult but also the experience of particle accelerator operators with this rare material is very small. In addition to that the HET would then need ^{3}He with energies $> 10\,\mathrm{MeV/nuc}$ which reduces the number of possible acceleration sites even further. Under these circumstances the simulation of the instrument's response is currently the only feasible solution. Furthermore preliminary analysis of recent HIMAC runs in January 2016 showed that the fragmentation of ^{4}He in polyethylene absorber produces a small fraction of ^{3}He isotopes in the order of $\approx$1 to 0.1 %. This fraction of ^{3}He was successfully detected with the PQM of HET and could be separated from the dominating ^{4}He signature. This data is currently subject of analysis and it indicates that the theoretical analysis of the separation capabilities is of good quality. As a result this means that the resolution of ^{3}He and ^{4}He is possible with HET down to a ratio of 1 % during ^{3}He -rich SEP events at integration times in the order of several minutes which satisfies the scientific requirements for HET on Solar Orbiter.

The last issue addressed in this thesis with regards to the later scientific work are the non-linearities of the BGO and BSO scintillation material. To the current day only few publication about these non-linearities in BGO are available which solely focus on stopping, light ions and mainly on lower energies than HET will measure. In addition to that all available publications deal only with distinct ions and no interpolations between those are performed. For BSO this is in fact the first analysis of it's non-linearities know to the author. Since the later data analysis of HET data requires an accurate correction of non-linear energy-to-light conversion ratios in the scintillation crystal a model was developed which has exactly these capabilities. The model was developed to describe both light and heavy ions with one set of parameters and the model parameters have been determined for BGO as well as BSO. In both cases Helium ions have to be treated in a slightly different manner in order to achieve good agreement with the experiment. For Helium the corrected energy values can still be calculated but the set of input parameters slightly differ from that of the other ions. This mismatch of the model for Helium results also in the fact that there were only a few selected ion types available as datapoints. The model

would certainly benefit from additional datapoints with ions in-between Helium and Carbon which would allow a more detailed analysis of the crystal's behavior in this region. Despite the incomplete ion coverage with which the model has been developed it could be shown with additional Argon datapoints that the model successfully predicts scintillation non-linearities for ions with which it has not been calibrated before. It was tested against additional Argon data which has not been used during the model development to evaluate the prediction qualities. The prediction qualities could be estimated to be in the order of $\pm 10\,\%$ depending on the initial energy. This can be considered as good value since the uncorrected energy differences can be as large as $40\,\%$ for carbon and more than $50\,\%$ for iron. The model furthermore successfully predicts non-linearities not only for stopping but also for penetrating ions. To the current day there are no other models known to the author which are capable to predict those for penetrating ion in BGO/BSO. In addition to that the model is a contribution to fundamental research since investigations about scintillators and heavy ions in this energy range are very rare and performed in a much more simplified way. This lead to a publication of the newly developed methods on basis of GEANT4 simulations and the results in *Nuclear Instruments and Methods in Physics Research Section B* [53].

5.1 Outlook

Measurements with the PQM model which closely resembles the flight model showed that the HET is a combination of a very potent and versatile particle detector with a compact and lightweight design. It's dual telescope layout for example makes a good pitch angle coverage possible easily. Since the overall dimensions of the instrument are very small a full coverage of the pitch angles with HET can be obtained by using three of these instruments along linear independent viewing directions. It would even be possible with some design changes of the sensor head to extend the two viewing direction to four in a cross-shaped geometry with one cubic scintillating crystal acting as calorimeter for all those viewing directions. Another possible development stage could include anti-coincidences surrounding the central calorimeter crystal. It should be investigated if the already present readout photo diodes are useable for this purpose. One would then gain another detection channel for neutral particles like neutrons or γ-rays. Especially for γ-ray detection the BGO crystal would be very suitable due to it's large density. It should also be mentioned here that the full capabilities of HET are, at least to some extend, limited by the available data bandwidth on the spacecraft. Future space missions would clearly benefit from increased communication bandwidth.

From the instrument development point of view all structural and electronic parts of HET have reached their final flight like status. The development is now focusing on the software while the flight models are built. The level 3 trigger logic is currently developed by the author and this will be subject to tests with current HIMAC data as well as future measurement campaigns at HIMAC. The level 3 trigger will implement important findings from this theses as from the ^{3}He and ^{4}He separation.

Since all the electronic of HET is already embedded inside the instrument it is possible to reuse the system for future space mission with only a few changes in the communication system with the spacecraft. From the data acquisition point of view the electronic is already very versatile. The HET level 3 trigger allows for in-flight reconfiguration and the change of any data product. This flexibility is very important for later in-flight calibrations and can be useful if for examples parts experiences unexpected degradation during the mission. It is also possible that there will be completely new insights in heliospheric physics which require an adjustment of the scientific data products.

As the launch of Solar Orbiter is currently scheduled to 2018 there will be no real data available prior to this date. After launch the developed model for the correction of the non-linearities will aid those scientists who analyse the data of HET and will then be of great importance for correction of the particles' energy. It would furthermore be desirable to obtain more data for ions to refine the model and reduce the prediction accuracy of $\pm 10\,\%$ down to lower values. As already mentioned earlier it is difficult to obtain particle accelerator beam times for specific ions which is especially true for ^{3}He ions. It is therefore encouraging that for the next HIMAC measuring campaign there might be Nitrogen available in an energy range of several hundreds MeV/nuc. Since Nitrogen is in-between Carbon and Oxygen and since there are already many datapoints available with those ions this is also a good possibility to estimate prediction qualities for lighter ions in the same manner as with Argon. In addition to that the Argon data points used in the determination of the model prediction quality will also be included in a future refinement of the model and will be an additional data point inbetween Silicon an Iron.

Bibliography

[1] ESA, Solar Orbiter Definition Study Report (Red Book), ESA/SRE (July). doi:10.1088/1742-6596/271/1/011004.

[2] R. W. Ebert, D.J. McComas, H.A. Elliott, R.J. Forsyth, J.T. Gosling, Bulk properties of the slow and fast solar wind and interplanetary coronal mass ejections measured by ulysses: Three polar orbits of observations, Journal of Geophysical Research 114 (2009) 1–17.

[3] J. L. Phillips, S. J. Bame, A. Barnes, et al., Ulysses solar wind plasma observations from pole to pole, Geophysical Research Letters 22 (23) (1995) 3301–3304. doi:10.1029/95GL03094.
URL http://dx.doi.org/10.1029/95GL03094

[4] R. Schwenn, E. Marsch, Physics of the Inner Heliosphere: Large-scale phenomena, Physics and chemistry in space, Springer-Verlag, 1991.
URL https://books.google.de/books?id=Xm3vAAAAMAAJ

[5] E.N. Parker, Dynamics of the Interplanetary Gas and Magnetic Fields, Astrophysical Journal 128 (1958) 664–676. doi:10.1086/146579.

[6] R. Lundin, S. Barabash, H. Andersson, et al., Solar wind-induced atmospheric erosion at mars: First results from aspera-3 on mars express, Science 305 (5692) (2004) 1933–1936. arXiv:http://www.sciencemag.org/content/305/5692/1933.full.pdf, doi:10.1126/science.1101860.
URL http://www.sciencemag.org/content/305/5692/1933.abstract

[7] U. Feldman, E. Landi, Schwadron, On the sources of fast and slow solar wind, Journal of Geophysical Research: Space Physics 110 (A7) (2005) 1–12, a07109. doi:10.1029/2004JA010918.
URL http://dx.doi.org/10.1029/2004JA010918

[8] A. Krieger, A. Timothy, E. Roelof, A coronal hole and its identification as the source of a high velocity solar wind stream, Solar Physics 29 (2) (1973) 505–525. doi:10.1007/BF00150828.
URL http://dx.doi.org/10.1007/BF00150828

[9] T. Peleikis, M. Kruse, L. Berger, C. Drews, R. F. Wimmer-Schweingruber, Investigation of Solar Wind Source Regions Using Ulysses Composition Data and a PFSS Model, Proc 14th Int. Solar Wind Conf.

[10] C. J. Eyles, R. A. Harrison, C. J. Davis, et al., The heliospheric imagers onboard the stereo mission, Solar Physics 254 (2) (2008) 387–445. doi:10.1007/s11207-008-9299-0.
URL http://dx.doi.org/10.1007/s11207-008-9299-0

[11] J. A. Davies, R. A. Harrison, A. P. Rouillard, et al., A synoptic view of solar transient evolution in the inner heliosphere using the Heliospheric Imagers on STEREO, Geophysical Research Letters 36 (2), l02102. doi:10.1029/2008GL036182.
URL http://dx.doi.org/10.1029/2008GL036182

[12] J. Davies, Rutherford Appleton Laboratory, UK.

[13] M. Dikpati, P. A. Gilman, Global solar dynamo models: Simulations and predictions, Journal of Astrophysics and Astronomy 29 (1) (2008) 29–39. doi:10.1007/s12036-008-0004-3.
URL http://dx.doi.org/10.1007/s12036-008-0004-3

[14] N. Gopalswamy, Coronal mass ejections of solar cycle 23, Journal of Astrophysics and Astronomy 27 (2) (2006) 243–254. doi:10.1007/BF02702527.
URL http://dx.doi.org/10.1007/BF02702527

[15] H. Hudson, J.-L. Bougeret, J. Burkepile, Coronal mass ejections: Overview of observations, Space Science Reviews 123 (1-3) (2006) 13–30. doi:10.1007/s11214-006-9009-x.
URL http://dx.doi.org/10.1007/s11214-006-9009-x

[16] V. Yurchyshyn, S. Yashiro, V. Abramenko, H. Wang, N. Gopalswamy, Statistical distributions of speeds of coronal mass ejections, The Astrophysical Journal 619 (1) (2005) 599.
URL http://stacks.iop.org/0004-637X/619/i=1/a=599

[17] A. G. Emslie, H. Kucharek, B. R. Dennis, et al., Energy partition in two solar flare/cme events, Journal of Geophysical Research: Space Physics 109 (A10), a10104. doi:10.1029/2004JA010571.
URL http://dx.doi.org/10.1029/2004JA010571

[18] T. Amari, J. F. Luciani, Z. Mikic, J. Linker, A twisted flux rope model for coronal mass ejections and two-ribbon flares, The Astrophysical Journal Letters 529 (1) (2000) L49.
URL http://stacks.iop.org/1538-4357/529/i=1/a=L49

[19] X. Zhao, X. Feng, C. Xiang, et al., Multi-spacecraft Observations of the 2008 January 2 CME in the Inner Heliosphere, The Astrophysical Journal 714 (2010) 1133–1141. doi:10.1088/0004-637X/714/2/1133.

[20] D. V. Reames, Particle acceleration at the Sun and in the heliosphere, Space Science Reviews 90 (3) (1999) 413–491. doi:10.1023/A:1005105831781.
URL http://dx.doi.org/10.1023/A:1005105831781

[21] T. Zurbuchen, I. Richardson, In-situ solar wind and magnetic field signatures of interplanetary coronal mass ejections, in: Coronal Mass Ejections, Vol. 21 of Space Sciences Series of ISSI, Springer New York, 2006, pp. 31–43. doi:10.1007/978-0-387-45088-9_3.
URL http://dx.doi.org/10.1007/978-0-387-45088-9_3

[22] J. Giacalone, J. Kóta, Acceleration of solar-energetic particles by shocks, Space Science Reviews 124 (1) (2006) 277–288. doi:10.1007/s11214-006-9110-1.
URL http://dx.doi.org/10.1007/s11214-006-9110-1

[23] A. R. Bell, The acceleration of cosmic rays in shock fronts – i, Monthly Notices of the Royal Astronomical Society 182 (2) (1978) 147–156. arXiv:http://mnras.oxfordjournals.org/content/182/2/147.full.pdf+html, doi:10.1093/mnras/182.2.147.
URL http://mnras.oxfordjournals.org/content/182/2/147.abstract

[24] F. Allegrini, M. I. Desai, G. M. Mason, H. Kucharek, E. Möbius, Evidence for mass-per-charge-dependent acceleration of a multiple-component seed population by cme-driven interplanetary shocks near 1 au, The Astrophysical Journal 682 (1) (2008) 690.
URL http://stacks.iop.org/0004-637X/682/i=1/a=690

[25] L.-G. Ding, G. Li, G.-M. Le, B. Gu, X.-X. Cao, Seed population in large solar energetic particle events and the twin-cme scenario, The Astrophysical Journal 812 (2) (2015) 171.
URL http://stacks.iop.org/0004-637X/812/i=2/a=171

[26] Y.-M. Wang, M. Pick, G. M. Mason, Coronal holes, jets, and the origin of 3he-rich particle events, The Astrophysical Journal 639 (1) (2006) 495.
URL http://stacks.iop.org/0004-637X/639/i=1/a=495

[27] R. Bodmer, P. Bochsler, J. Geiss, R. von Steiger, Solar wind helium isotopic composition from SWICS/ULYSSES, Space Science Reviews 72 (1995) 61–64.

[28] J. Geiss, G. Gloeckler, Abundances of deuterium and helium-3 in the protosolar cloud, Space Science Reviews 84 (1998) 239–250.

[29] R. E. C., Propagation of solar cosmic rays in the interplanetary magnetic field, in: Ch VII of Lectures in High Energy Astrophysics ed H. Ogelman and J. R. Wayland, NASA SP-199, 1969.

[30] G. Wibberenz, H. V. Cane, Multi-spacecraft observations of solar flare particles in the inner heliosphere, The Astrophysical Journal 650 (2) (2006) 1199.
URL http://stacks.iop.org/0004-637X/650/i=2/a=1199

[31] M. E. Wiedenbeck, G. M. Mason, C. M. S. Cohen, et al., Observations of solar energetic particles from 3he-rich events over a wide range of heliographic longitude, The Astrophysical Journal 762 (1) (2013) 54.
URL http://stacks.iop.org/0004-637X/762/i=1/a=54

[32] N. Dresing, R. Gómez-Herrero, A. Klassen, et al., The Large Longitudinal Spread of Solar Energetic Particles During the 17 January 2010 Solar Event, Solar Physics 281 (1) (2012) 281–300. doi:10.1007/s11207-012-0049-y.
URL http://dx.doi.org/10.1007/s11207-012-0049-y

[33] N. Dresing, R. Gómez-Herrero, B. Heber, et al., Statistical survey of widely spread out solar electron events observed with STEREO and ACE with special attention to anisotropies, Astron. Astropy. 567 (2014) A27. doi:{10.1051/0004-6361/201423789}.
URL http://dx.doi.org/10.1051/0004-6361/201423789

[34] S. Dalla, A. Balogh, S. Krucker, et al., Properties of high heliolatitude solar energetic particle events and constraints on models of acceleration and propagation, Geophysical Research Letters 30 (19), 8035. doi:10.1029/2003GL017139.
URL http://dx.doi.org/10.1029/2003GL017139

[35] M. Zhang, J. R. Jokipii, R. B. McKibben, Perpendicular transport of solar energetic particles in heliospheric magnetic fields, The Astrophysical Journal 595 (1) (2003) 493.
URL http://stacks.iop.org/0004-637X/595/i=1/a=493

[36] M. S. Marsh, S. Dalla, J. Kelly, T. Laitinen, Drift-induced perpendicular transport of solar energetic particles, The Astrophysical Journal 774 (1) (2013) 4.
URL http://stacks.iop.org/0004-637X/774/i=1/a=4

[37] Solar Probe Plus Report of the Science and Technology Definition Team, http://solarprobe.jhuapl.edu/mission/docs/SolarProbePlus2008.pdf (2008).

[38] E. Marsch, R. Harrison, O. Pace, et al., Solar Orbiter, a High-Resolution Mission to the Sun and Inner Heliosphere, Proceedings of "Solar Encounter: The First Solar Orbiter Workshop" (2001) XI–XXVI.

[39] E. Marsch, R. Marsden, R. Harrison, R. Wimmer-Schweingruber, B. Fleck, Solar Orbiter—mission profile, main goals and present status, Advances in Space Research 36 (8) (2005) 1360–1366. doi:10.1016/j.asr.2004.11.012.
URL http://linkinghub.elsevier.com/retrieve/pii/S0273117704008701

[40] European Space Agency, Dark and bright: Esa chooses next two science missions, Press Release, http://sci.esa.int/cosmic-vision/49385-dark-and-bright-esa-chooses-next-two-science-missions/ (October 2011).

[41] H. Porsche, Helios Mission - Mission Objectives, Mission Verification, Selected Results, in: Proc. Alphach Summer School, 1981, pp. 43–50.

[42] Ulysses Fact Sheet, http://esamultimedia.esa.int/docs/ulysses/Ulysses_fact_sheet.pdf (2016).

[43] Filippo Marliani, Experiment Interface Document - Part A issue 5 revision 0 (2015).

[44] ESA Science and Technology - Instruments - Webpage, visited 14.01.2016, http://sci.esa.int/solar-orbiter/51217-instruments/ (2016).

[45] European Space Agency, Satellite: Solar Orbiter (2015).
URL http://sci.esa.int/solar-orbiter/50760-payload-accommodation-onboard-solar-orbiter-annotated/

[46] M. Prieto, Solar Orbiter Energetic Particle Detector Experiment Interface Document Part B (2015).

[47] Sebastian Boden, S.R. Kulkarni, Jan Steinhagen, et al., Distinguishing 3He and 4He with the Electron Proton Telescope (EPT) on Solar Orbiter, AGU 2015 Poster presentation (2015).

[48] R. Wimmer-Schweingruber, Personal Correspondance (2014).

[49] A. Posner, D. Hassler, D. McComas, et al., A high energy telescope for the Solar Orbiter, Advances in Space Research 36 (8) (2005) 1426–1431. doi:10.1016/j.asr.2004.11.040.
URL http://linkinghub.elsevier.com/retrieve/pii/S027311770400883X

[50] D. M. Hassler, C. Zeitlin, R. F. Wimmer-Schweingruber, et al., The Radiation Assessment Detector (RAD) investigation, Space Science Reviews 170 (1-4) (2012) 503–558. doi:10.1007/s11214-012-9913-1.

[51] M. Hauschild, Progress in dE/dx techniques used for particle identification, Nuclear Instruments and Methods in Physics Research Section A: Accelerators, Spectrometers, Detectors and Associated Equipment 379 (3) (1996) 436–441. doi:10.1016/0168-9002(96)00607-9.
URL http://linkinghub.elsevier.com/retrieve/pii/0168900296006079

[52] C. Martin, E. Bronchalo, J. Medina, A new identification method for energetic ion ΔE-E telescopes, Nuclear Instruments and Methods in Physics Research Section A: Accelerators, Spectrometers, Detectors and Associated Equipment 582 (2) (2007) 581–591. doi:10.1016/j.nima.2007.08.236.
URL http://linkinghub.elsevier.com/retrieve/pii/S0168900207018864

[53] J. Tammen, R. Elftmann, S. Kulkarni, S. Böttcher, R. Wimmer-Schweingruber, Quenching comparison of BGO and BSO for heavy ions, Nuclear Instruments and Methods in Physics Research Section B: Beam Interactions with Materials and Atoms 360 (2015) 129 – 138. doi:http://dx.doi.org/10.1016/j.nimb.2015.07.127.
URL http://www.sciencedirect.com/science/article/pii/S0168583X15007168

[54] L. Seimetz, Personal Correspondance (2013).

[55] G. E. Knoll, Radiation Detection and Measurement.

[56] C. Tschalär, H. Bichsel, Mean excitation potential of light compounds, Phys. Rev. 175 (1968) 476–478. doi:10.1103/PhysRev.175.476.
URL http://link.aps.org/doi/10.1103/PhysRev.175.476

[57] W. K. Chu, D. Powerd, Calculation of mean excitation energy for all elements, Physics Letters A 40 (1) (1972) 23–24. doi:http://dx.doi.org/10.1016/0375-9601(72)90181-8.
URL http://www.sciencedirect.com/science/article/pii/0375960172901818

[58] Valery Chmill, Radiation Tests of Semiconductor Detectors (2006).

[59] R. C. Alig, S. Bloom, Electron-hole-pair creation energies in semiconductors, Phys. Rev. Lett. 35 (1975) 1522–1525. doi:10.1103/PhysRevLett.35.1522.
URL http://link.aps.org/doi/10.1103/PhysRevLett.35.1522

[60] F. J. Morin, J. P. Maita, Electrical properties of silicon containing arsenic and boron, Phys. Rev. 96 (1954) 28–35. doi:10.1103/PhysRev.96.28.
URL http://link.aps.org/doi/10.1103/PhysRev.96.28

[61] N. C. MacDonald, T. E. Everhart, Direct measurement of the depletion layer width variation vs applied bias for a p-n junction, Applied Physics Letters 7 (10) (1965) 267–269. doi:http://dx.doi.org/10.1063/1.1754252.
URL http://scitation.aip.org/content/aip/journal/apl/7/10/10.1063/1.1754252

[62] S. M. Sze, Physics of Semiconductor Devices, 1st Edition, Wiley, 1969.

[63] W. Seibt, K. Sundström, P. Tove, Charge collection in silicon detectors for strongly ionizing particles, Nuclear Instruments and Methods 113 (3) (1973) 317 – 324. doi:http://dx.doi.org/10.1016/0029-554X(73)90496-5.
URL http://www.sciencedirect.com/science/article/pii/0029554X73904965

[64] C. Pedrini, Scintillation Mechanisms and Limiting Factors on Each Step of Relaxation of Electronic Excitations, Physics of the Solid State 47 (8) (2005) 1406–1411.

[65] J. Faure, J. Mauchain, E. Papalazarou, et al., Direct observation of electron thermalization and electron-phonon coupling in photoexcited bismuth, Phys. Rev. B 88 (2013) 075120. doi:10.1103/PhysRevB.88.075120.
URL http://link.aps.org/doi/10.1103/PhysRevB.88.075120

[66] K. Michaelian, A. Menchaca-Rocha, E. Belmont-Moreno, Scintillation response of nuclear particle detectors, Nuclear Instruments and Methods in Physics Research A 356 (1995) 297–303.

[67] M. N. Kabler, R. T. Williams, Vacancy-interstitial pair production via electron-hole recombination in halide crystals, Phys. Rev. B 18 (1978) 1948–1960. doi:10.1103/PhysRevB.18.1948.
URL http://link.aps.org/doi/10.1103/PhysRevB.18.1948

[68] M. Lalic, S. Souza, The first-principles study of electronic and optical properties of BGO and BSO scintillators, Optical Materials 30 (7) (2008) 1189–1192. doi:10.1016/j.optmat.2007.05.046.
URL http://linkinghub.elsevier.com/retrieve/pii/S0925346707001917

[69] A. F. Lima, S. O. Souza, M. V. Lalic, Electronic structure and optical absorption of the Bi4Ge3O12 and the Bi4Si3O12 scintillators in ultraviolet region: An ab initio study, Journal of Applied Physics 106 (1) (2009) 013715. doi:10.1063/1.3160291.
URL http://link.aip.org/link/JAPIAU/v106/i1/p013715/s1&Agg=doi

[70] M. Ishii, K. Harada, Y. Hirose, et al., Development of BSO (Bi4Si3O12) crystal for radiation detector, Optical Materials 19 (2002) 201–212.

[71] E. Sakai, Recent measurements on scintillator-photodetector systems, Nuclear Science, IEEE Transactions on 34 (1) (1987) 418–422. doi:10.1109/TNS.1987.4337375.

[72] S. Agostinelli, J. Allison, K. Amako, et al., Geant4—a simulation toolkit, Nuclear Instruments and Methods in Physics Research Section A: Accelerators, Spectrometers, Detectors and Associated Equipment 506 (3) (2003) 250–303. doi:10.1016/S0168-9002(03)01368-8.
URL http://linkinghub.elsevier.com/retrieve/pii/S0168900203013688

[73] R. Brun, R. Hagelberg, M. Hansroul, J. C. Lassalle, Simulation program for particle physics experiments, GEANT : user guide and reference manual, CERN Data Handling Division (1978) 1–73.
URL https://cds.cern.ch/record/118715

[74] A. Ausmees, M. Elango, A. Kikas, J. Pruulmann, Monte Carlo Simulation of Electron–Phonon Scattering in the XUV-Induced Electron Emission of NaCl, Physica Status Solidi (B) 137 (2) (1986) 495–500. doi:10.1002/pssb.2221370211.
URL http://doi.wiley.com/10.1002/pssb.2221370211

[75] R. A. Glukhov, A. N. Vasilev, Monte-Carlo simulation of the creation of excited regions in insulators by a photon, Radiation Effects and Defects in Solids: Incorporationg Plasma Science and Plasma Technology 135 (1-4) (1995) 315–319.

[76] J. Greenwood, The correct and incorrect generation of a cosine distribution of scattered particles for Monte-Carlo modelling of vacuum systems v 67 (2002) 217–222.

[77] J. Apostolakis, G. Folger, V. Grichine, et al., Geant4 physics lists for hep, in: Nuclear Science Symposium Conference Record, 2008. NSS '08. IEEE, 2008, pp. 833–836. doi:10.1109/NSSMIC.2008.4774655.

[78] F. Gianotti, GEANT4 hadronic physics validation with LHC test-beam data: first conclusions. CERN-LCGAPP-2004-10.
URL http://lcgapp.cern.ch/project/mgmt/doc.html

[79] D. Wright, S. Incerti, A short guide to choosing physics lists, GEANT4.94 (2013).
URL http://geant4.in2p3.fr/IMG/pdf_PhysicsLists.pdf

[80] R. Kinsey, et. al., The NUDAT/PCNUDAT Program for Nuclear Data, 9th Symposium of Capture Gamma-Ray Spectoscropy and Related Topics.

[81] GEANT 4 Collaboration, Physics Reference Manual, Version: geant4 10.1 (2014).
URL http://geant4.web.cern.ch/geant4/UserDocumentation/UsersGuides/PhysicsReferenceManual/fo/PhysicsReferenceManual.pdf

[82] D. E. Alburger, A. W. Sunyar, Decay of bi^{207}, Phys. Rev. 99 (1955) 695–702. doi:10.1103/PhysRev.99.695.
URL http://link.aps.org/doi/10.1103/PhysRev.99.695

[83] J. A. Bearden, A. F. Burr, Reevaluation of x-ray atomic energy levels, Rev. Mod. Phys. 39 (1967) 125–142. doi:10.1103/RevModPhys.39.125.
URL http://link.aps.org/doi/10.1103/RevModPhys.39.125

[84] S. Hauf, M. Kuster, M. Batic, et al., Validation of geant4-based radioactive decay simulation, Nuclear Science, IEEE Transactions on 60 (4) (2013) 2984–2997. doi:10.1109/TNS.2013.2271047.

[85] S. Hauf, M. Kuster, M. Pia, et al., Progress and validation of geant4 based radioactive decay simulation using the examples of simbol-x and ixo, in: Nuclear Science Symposium Conference Record (NSS/MIC), 2009 IEEE, 2009, pp. 2060–2065. doi:10.1109/NSSMIC.2009.5402112.

[86] N. Akchurin, F. Bedeschi, A. Cardini, et al., A comparison of BGO and BSO crystals used in the dual-readout mode, Nuclear Instruments and Methods in Physics Research Section A: Accelerators, Spectrometers, Detectors and Associated Equipment 640 (1) (2011) 91–98. doi:10.1016/j.nima.2011.03.013.
URL http://linkinghub.elsevier.com/retrieve/pii/S0168900211005468

[87] J. Peatross, M. Ware, Physics of Light and Optics, Brigham Young University, 2008.

[88] Dow Corning, Dow Corning 93-500 space-grade Encapsulant Datasheet (2016).
URL http://corysimon.github.io/articles/uniformdistn-on-sphere/

[89] G. W. Butler, A. M. Poskanzer, D. A. Landis, Identification of nuclear fragments by a combined time-of-flight, ΔE-E technique, Nuclear Instruments and Methods 89 (1970) 189–198. doi:http://dx.doi.org/10.1016/0029-554X(70)90822-0.
URL http://www.sciencedirect.com/science/article/pii/0029554X70908220

[90] W. Allison, P. Wright, The Physics of Charged Particle Identification : The solution of practical problems for dE / dx detectors, Oxford Nuclear Physics 1–42.

[91] A. Seamster, R. Green, R. Korteling, Silicon detector ΔE, E particle identification: a theoretically based analysis algorithm and remarks on the fundamental limits to the resolution of particle type by ΔE, E measurements, Nuclear Instruments and Methods 145 (3) (1977) 583–591. doi:10.1016/0029-554X(77)90590-0.
URL http://linkinghub.elsevier.com/retrieve/pii/0029554X77905900

[92] S. Carboni, S. Barlini, L. Bardelli, et al., Particle identification using the technique and pulse shape discrimination with the silicon detectors of the FAZIA project, Nuclear Instruments and Methods in Physics Research Section A: Accelerators, Spectrometers, Detectors and Associated Equipment 664 (1) (2012) 251–263. doi:http://dx.doi.org/10.1016/j.nima.2011.10.061.
URL http://www.sciencedirect.com/science/article/pii/S0168900211020134

[93] H. Bichsel, Straggling in thin silicon detectors, Reviews of Modern Physics 60 (1988) 663–699.

[94] R. Elftmann, J. Tammen, S. R. Kulkarni, et al., Characterization of an LSO scintillator for space applications, Journal of Physics: Conference Series 632 (1) (2015) 12006.
URL http://stacks.iop.org/1742-6596/632/i=1/a=012006

[95] S. Kolbe, Personal Correspondance (2013).

[96] Stephan I. Böttcher, Analysis of a 207 Bi spectrum measured with a Hamamatsu photo diode, a tsh310 based preamp, and the heti irena, Internal document (June 2011).

[97] Böttcher, S., FlyRENA documentation (2015).

[98] K. Olive, et al., Review of particle physics, Chin. Phys. (2014) 090001.

[99] V. Avdeichikov, L. Bergholt, M. Guttormsen, et al., Light output and energy resolution of CsI , YAG , GSO , BGO and LSO scintillators for light ions, Nuclear Instruments and Methods in Physics Research A 349 (1994) 216–224.

[100] Generating uniformly distributed numbers on a sphere - Mathemathinking, http://www.centralcoating.com/wp-content/uploads/2014/11/93-500.pdf, accessed: 2016-01-06.

[101] Refractiveindex.info, Refractive index database (1996).
URL http://refractiveindex.info/?shelf=main&book=Bi4Ge3O12&page=Williams

[102] P. A. Williams, A. H. Rose, K. S. Lee, et al., Optical, thermo-optic, electro-optic, and photoelastic properties of bismuth germanate (Bi4Ge3O12), Appl. Opt. 35 (19) (1996) 3562–3569. doi:10.1364/AO.35.003562.
URL http://ao.osa.org/abstract.cfm?URI=ao-35-19-3562

[103] Omega Piezo, BGO, LYSO and GSO crystal scintillators (2015).
URL http://www.omegapiezo.com/crystal_scintillators.html

[104] A. J. Tylka, J. H. Adams, P. R. Boberg, et al., CREME96 - A Revision of the Cosmic Ray Effects on Micro Electronics Code, IEEE Transactions on Nuclear Science 44 (6) (1997) 2150–2160.

[105] J. H. Adams Jr., A. F. Barghouty, M. H. Mendenhall, et al., CREME: The 2011 Revision of the Cosmic Ray Effects on Micro-Electronics Code , http://ntrs.nasa.gov/archive/nasa/casi.ntrs.nasa.gov/20120015473.pdf.

[106] M. Moszynski, M. Balcerzyk, W. Czarnacki, et al., Intrinsic energy resolution and light yield nonproportionality of BGO, IEEE Transactions on Nuclear Science 51 (3) (2004) 1074–1079. doi:10.1109/TNS.2004.829491.
URL http://ieeexplore.ieee.org/lpdocs/epic03/wrapper.htm?arnumber=1312019

[107] J. Soerensen, Solar Orbiter Environmental Specification, Tech. Rep. 3 (2010).
URL https://www2.mps.mpg.de/homes/schuehle/documents/Bilder/SolarOrbiter/TEC-EES-03-034%20JS%20i3r0%20S-0%20radiation%20env_spec.pdf

[108] M. DeLaus, W. Combs, Total-dose and SEU results for the ADS001, a high-performance commercial op-amp fabricated in a dielectrically-isolated, complementary-bipolar process (2013).

[109] Microsemi, RTAX-S/SL and RTAX-DSP radiation-tolerant FPGAs (2013).

[110] M. Xapsos, G. Summers, J. Barth, E. Stassinopoulos, E. Burke, Probability model for cumulative solar proton event fluences, IEEE Transactions on Nuclear Science 47 (3) (2000) 486–490. doi:10.1109/23.856469.
URL http://ieeexplore.ieee.org/lpdocs/epic03/wrapper.htm?arnumber=856469

[111] J. Tammen, [SO-EPD-KIE-RP-0061] EPT/HET radiation analysis report - issue 1 revision 5 (2014).

[112] S. A. Payne, W. W. Moses, S. Sheets, et al., Nonproportionality of Scintillator Detectors: Theory and Experiment, IEEE Transactions on Nuclear Science 56 (4) (2009) 3392–3402. doi:10.1109/TNS.2011.2167687.

[113] W. W. Moses, G. a. Bizarri, R. T. Williams, et al., The origins of scintillator nonproportionality, IEEE Transactions on Nuclear Science 59 (5) (2012) 2038–2044. doi:10.1109/TNS.2012.2186463.

[114] J. B. Birks, Scintillations from Naphthalene-Anthracene Crystals, Proceedings of the Physical Society. Section A 63 (1950) 1044.

[115] J. B. Birks, Scintillation Efficiency of Anthracene Crystals, Proceedings of the Physical Society. Section A 63 (1950) 1294.

[116] J. B. Birks, Scintillations from Organic Crystals: Specific Fluorescence and Relative Response to Different Radiations, Proceedings of the Physical Society. Section A 64 (10) (1951) 874–877. doi:10.1088/0370-1298/64/10/303.
URL http://stacks.iop.org/0370-1298/64/i=10/a=303?key=crossref.f6127795b0efda6211aab9d5c1b9ae31

[117] A. Nassalski, M. Moszyn, T. Szcze, Non-Proportionality of Organic Scintillators and BGO, IEEE Transactions on Nuclear Science 55 (3) (2008) 1069–1072.

[118] B. Borderie, M. F. Rivet, A. Chbihi, et al., Response of CsI(Tl) scintillators over a large range in energy and atomic number of ions Part I: recombination and d -electrons #, Nucl. Instr. and Meth. A 482 (2002) 674–692.

[119] D. Horn, G. Ball, A. Galindo-Uribarri, E. Hagberg, R. Walker, The mass dependence of CsI(Tl) scintillation response to heavy ions, Nuclear Instruments and Methods in Physics Research Section A: Accelerators, Spectrometers, Detectors and Associated Equipment 320 (1-2) (1992) 273–276. doi:10.1016/0168-9002(92)90785-3.
URL http://linkinghub.elsevier.com/retrieve/pii/0168900292907853

[120] E. Valtonen, J. Peltonen, J. J. Torsti, Response of BGO and CsI(Tl) Scintillators to Heavy Ions, Nuclear Instruments and Methods in Physics Research A 286 (1990) 169–174.

[121] V. Avdeichikov, L. Bergholt, M. Guttormsen, et al., Light output and energy resolution of BGO and GSO scintillators for light ions, Nuclear Instruments and Methods in Physics Research Section A: Accelerators, Spectrometers, Detectors and Associated Equipment 336 (1-2) (1993) 381–384. doi:10.1016/0168-9002(93)91125-7.
URL http://linkinghub.elsevier.com/retrieve/pii/0168900293911257

[122] Z. Dlouhy, A. Kugler, L. Nosek, et al., The Response of BGO Scintillation Detectors to Light Charged Nuclei, Nuclear Instruments and Methods in Physics Research A 317 (317) (1992) 604–606.

[123] N. Matsufuji, T. Kanai, H. Komami, T. Kohno, The Response of a BGO scintillator to relativistic heavy ions, Nuclear Instruments and Methods in Physics Research, Section A: Accelerators, Spectrometers, Detectors and Associated Equipment 430 (1) (1999) 60–68. doi:10.1016/S0168-9002(99)00180-1.

[124] K. Sato, K. Endo, M. Endo, et al., Heavy Ion Medical Accelerator in Chiba (HIMAC), Particle Accelerators 33 (1990) 147–152.

[125] Creative Commons, Creative Commons Attribution-NonCommercial-NoDerivs 4.0 (2016). URL http://creativecommons.org/licenses/by-nc-nd/4.0/

[126] ELJEN Technology, EJ-212 plastic scintillator (2011). URL http://www.ggg-tech.co.jp/maker/eljen/ej-212.html

[127] M. Shea, D. Smart, K. McCracken, G. Dreschhoff, H. Spence, Solar proton events for 450 years: The Carrington event in perspective, Advances in Space Research 38 (2) (2006) 232 – 238, The Great Historical Geomagnetic Storm of 1859: A Modern Look. doi:http://dx.doi.org/10.1016/j.asr.2005.02.100.
URL http://www.sciencedirect.com/science/article/pii/S0273117705008434

[128] D. N. Baker, X. Li, A. Pulkkinen, et al., A major solar eruptive event in july 2012: Defining extreme space weather scenarios, Space Weather 11 (10) (2013) 585–591, 2013SW000963. doi:10.1002/swe.20097.
URL http://dx.doi.org/10.1002/swe.20097

[129] R. Elftmann, J. Tammen, S. Kulkarni, et al., Characterization of an LSO scintillator for space applications, J.Phys.Conf.Ser. 632 (2015) 012006.

A Appendix

A.1 Scientific work

The following sections gives an overview over the scientific work performed during this thesis. The work is separated in three parts of which the first (A.1.1) covers presentations at conferences, the second one (A.1.2) gives an overview over the most important internal Solar Orbiter documents omitting some minor ones, the third (A.1.3) of the publications and the last one (A.1.4) contains work not matching any of the above categories. The order of each individual item in those sections does not reflect any weighting.

A.1.1 Presentations

- Calibration of the HET-Demonstration Model 3 for Solar Orbiter (Sun 360, Kiel, 2011)
- Quenching in BGO scintillating crystal of the Solar Orbiter HET (Solar Orbiter Workshop, Brügge, 2012)
- A High-Energy Telescope for the Solar Orbiter Mission: Initial Results of the Prototype (DPG Conference, Stuttgart, 2012)
- Scintillation quenching in BGO crystal of the Solar Orbiter HET (DPG Spring Meeting, Jena, 2013)

A.1.2 Internal documents

- Prototype Development Report for HETDM 3 (crosstalk analysis)
- HET Detector Test Report
- EPT-HET Radiation Analysis Report

A.1.3 Publications

- ECRS Proceeding 2014 "*Characterization of an LSO Scintillator for Space Applications*" (Co-Author) [129]
- Nucl. Instr. and Meth. B "*Quenching comparison of BGO and BSO for heavy ions*"[53]

A.1.4 Other work (excerpt)

- Assembly of HETDM version 4 (with S. Kulkarni)
- VIRENA radiation susceptibility test at the UKSH cancer treatment facility (with S. Burmeister)
- Design assembly and test of PETDM (with R. Elftmann)
- HIMAC run with HETDM version 4 and PETDM (with R. Elftmann and S. Burmeister)
- HET PQM detector incoming inspection and test
- Assembly of HET PQM sensor head
- Maintenance of the extraterrestrial GEANT 4 installation (with C. Terasa and J. Köhler)
- Assembly of HET FM detectors
- HIMAC run with HET PQM (with S. Boden and S. Burmeister)
- Programming of HET level-3 trigger and data products (currently ongoing)

A.2 Solar Orbiter Radiation Analysis

The internal Solar Orbiter report "*EPT-HET Radiation Analysis Report*" follows on the next 34 pages. It has been pubished as ESA report and is available under ESA's Solar Orbiter document encoding scheme as *SO-EPD-KIE-RP-0061 issue 1 revision 5*.

Christian-Albrechts-Universität zu Kiel	**EPT-HET Radiation Analysis Report**	Reference: SO-EPD-KIE-RP-0061 Issue: 1 Rev.: 5 Date: 15/04/2014 Page 1 of 34

SOLAR ORBITER ENERGETIC PARTICLE DETECTOR

EPT-HET Radiation Analysis Report

Document ID: SO-EPD-KIE-RP-0061
Issue: 1
Revision: 5

Signature not needed if electronically approved by route

Written	Checked	Approved Configuration Control	Approved QA	Approved Experiment Manager	Approved Principal Investigator
J. Tammen Date and Signature	R. Wimmer-Schweingruber Date and Signature	C. Martin Date and Signature	Date and Signature	Date and Signature	Date and Signature

File: **SO-EPD-KIE-RP-0061_iss1_rev5_EPT-HET_radiation_analysis_report.pdf** **Pages: 34**

Distribution List

The following lists indicate the individuals and agencies in receipt of review copies of the present document:

Agency / Organization	Name and Title	Contact information
SRG-UAH	Javier Rodriguez-Pacheco EPD-Principal Investigator	javier.pacheco@uah.es
SRG-UAH	Manuel Prieto EPD Project Manager	manuel.prieto@uah.es
SENER	Giuseppe Pennestri EPD System Engineer	giuseppe.pennestri@sener.es
SENER	Mario Basile EPD Product Assurance Manager	mario.basile@sener.es
CAU	EPD-Solar Orbiter Kiel Team	solo_kiel@physik.uni-kiel.de
UT	Eino Valtonen EPD-LET Lead Co-I	eino.valtonen@utu.fi
APL/JHU	Glenn Mason EPD-SIS Lead Co-I	glenn.mason@jhuapl.edu
SRG-UAH	Sebastian Sánchez EPD-ICU Lead Co-I	sebastian.sanchez@uah.es

Changes Record

Issue	Revision	Date	Modified by	Section / Paragraph modified	Change implemented
1	0	18/09/2012	Jan Grunau	All	Initial release
1	1	08/11/2012	Jan Grunau	7.1, 7.2	Moved to 7.1.1 and 7.2.1, added 7.1.2 and 7.2.2 edited 5.1 edited 10
1	2	04/01/2013	Jan Grunau	7.1.3, 7.2.3	added 7.1.3 and 7.2.3
1	3	26/11/2013	Jan Tammen	5.4 7.2.1 7.2.2 8 9 10 7.1.3, 7.2.3	removed this section, see 8 now several changes added percentage value to text rewritten this section Rewritten this section minor changes in conclusion added passage for alpha particles
1	4	16/12/2013	Jan Tammen	8	corrected wrong SEE rates
1	5	15/04/2014	Jan Tammen	8 9	Added individual SEE levels for parts used in EPT/HET Added individual TID levels for parts used in EPT/HET

Contents

1 INTRODUCTION

1.1 Scope

This document aims at describing the radiation analysis for the High Energy Telescope (HET) and the Electron Proton Telescope (EPT) and their commonly used Electronics Box (EBox).

2 GLOSARY AND DEFINITIONS

2.1 Acronyms and Abbreviations

CREME96 Cosmic Ray Effects on Micro-Electronics Code

EBox Electronics Box

EPT Electron Proton Telescope

GCR Galactic Cosmic Rays

GEANT4 Geometry and Tracking 4

HET High Energy Telescope

LET Linear Energy Transfer

MLI Multilayer Insulation

PCB Printed Circuit Board

PTFE Polytetrafluoroethylene

SPE Solar Particle Event

SEE Single Event Effect

SV sensitive volume

TID Total Ionizing Dose

3 APPLICABLE AND REFERENCE DOCUMENTS

3.1 Applicable Documents

ID.	Title	Reference	Iss./Rev.	Date
1	SolO Experiment Interface Document – Part A			
2	SolO Experiment Interface Document – Part B	SO-EPD-PO-IF-0001	2.4	
3	SolO Environmental specification	TEC-EES-03-034/JS	1.3	

3.2 References

[1] ESA. Solar Orbiter Environmental Specification. Technical Report 3, 2010.

[2] R A Mewaldt, A J Davis, W R Binns, G A De Nolfo, J S George, M H Israel, and Goddard Space. The Cosmic Ray Radiation Dose in Interplanetary Space – Present Day and Worst-Case Evaluations. *Jet Propulsion*, pages 101–104, 2005.

[3] J.D. Sullivan. Geometrical Factor and Directional Response of Single and Multi-Element Particle Telescopes. *Nuclear Instruments and Methods*, 95(1):5–11, 1971.

[4] M.a. Xapsos, G.P. Summers, J.L. Barth, E.G. Stassinopoulos, and E.a. Burke. Probability model for cumulative solar proton event fluences. *IEEE Transactions on Nuclear Science*, 47(3):486–490, 2000.

4 INPUT SPECTRA FOR CALCULATION

For all ion calculations the spectra from the Cosmic Ray Effects on Micro-Electronics Code (CREME96) code are used. The received radiation dose is split into two main components:

- Galactic Cosmic Rays (GCR)
- Solar Particle Events (SPEs)

Both of these components is described in detail in the following sections.

4.1 Galactic Cosmic Rays (GCR)

To overestimate the effects of the GCR on the telescope electronics the CREME96 spectrum for the solar minimum cycle at a distance of 1 AU is chosen. Figure 1 shows the intensity spectra for selected ion types. The calculations for the GCR radiation effect analysis are based on these spectra.

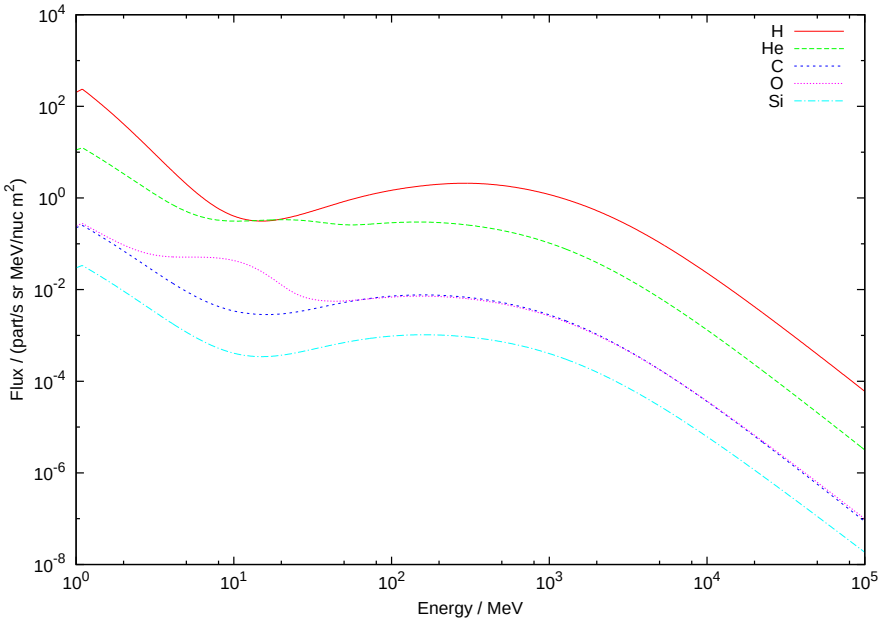

Figure 1: CREME96 flux spectrum for solar minimum cycle at 1 AU for specific ions.

4.2 Solar Particle Events (SPEs)

Figure 2 shows the intensity spectra for selected ion types for SPEs. The calculations for radiation effect analysis due to solar events are based on these spectra.

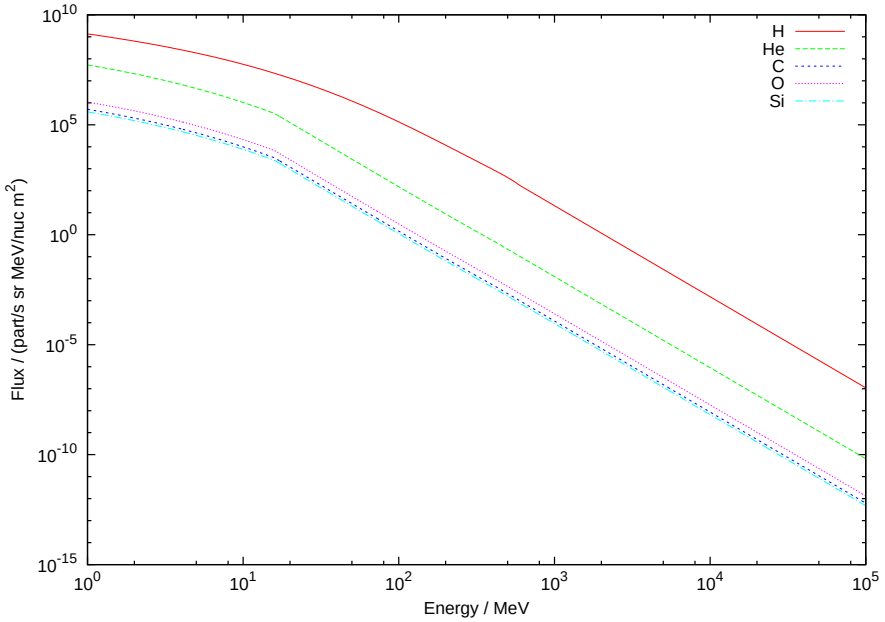

Figure 2: CREME96 flux spectrum for solar active cycle at 1 AU for specific ions, averaged 5 min peak fluxes.

4.3 Electrons

Electrons are simulated as described in [1]. The case for extreme solar events is chosen. In this case the electron spectrum can be described as a simple power law with the flux F:

$$F(E) = 3 \times 10^6 \cdot E^{-2} [\text{part/cm}^2\,\text{sr}\,\text{s}\,\text{keV}] \quad (1)$$

For electrons the energy range is 1 to 1×10^5 keV, divided into 100 logarithmic bins. The model describes the situation at 0.39 AU for solar electrons. Jovian electrons have fluxes which are 3 to 4 magnitudes lower than solar electrons.

5 SIMULATION SETUP

5.1 Geometry Setup

The EPT-HET consists of a complex geometry with large amounts of small surfaces. Geometry and Tracking 4 (GEANT4) calculation time largely depends on the complexity of the geometry. Calculations on geometries consisting of a few simple volumes as boxes and tubes are faster than calculations with particular complex designs. For this reason the real geometry is approximated by a simplified model which consists of the main parts of the telescope to save calculation time. The simple model consists of these main parts:

- EBox-housing with a defined equal thicknesses on each side
- Telescope housings with a defined equal thicknesses on each side and with colominators
- EPT magnets
- HET silicon detectors at the defined positions with some holder material (Al)
- HET calorimeter crystal with Polytetrafluoroethylene (PTFE) wrapping, crystal holder, and readout photodiodes
- 5 Printed Circuit Board (PCB) boards with 4 layers and a mean placement of electronic components

Figure 3 shows the simplified geometry. All components necessary to emulate the real shielding situation should be included in this model. The wall thicknesses are equally distributed among all sides of the housings and no extensions are taken into account. The real model has many of those housing extensions for mechanical reasons as can be seen in figure 4. The simple design should underestimate the shielding by the housing as there are also no supporting structures simulated within the telescope. Also some other structural elements as detector holders, cables, MLI and screws are not simulated, so that the calculations can be considered as "worst case shielding" analysis.

Figure 5 shows the simplified model from one side where one can see the position of the five PCBs. Each PCB consists of several layers to simulate a populated 4-layered board. Figure 6 shows the sequence of layers of one PCB. Starting from the top there is at first one layer of 300 µm Si embedded in two layers of Al_2O_3 with a thickness of 250 µm. These layers simulate an average population with electronic components inside a cereamic package. The silicon layer acts as the detector volume for our radiation analysis. Each PCB has one of these 3-segmented layers on top and one on the bottom. In between there is a stack of epoxy/copper as sketched in figure 6.

The radiation sensitive volumes are numbered from the bottom of the instrument to the top from 1 to 10 and are named as **SV (sensitive volume) #** in this document.

The dose inside the silicon detectors of the HET sensor is also measured. These detectors have the following dimensions:

- A-Detector (first detector)
  - Diameter 1.74 cm
  - Thickness 0.03 cm

- B-Detector (second detector in front of crystal)
  - Diameter 3.649 cm
  - Thickness 0.03 cm

Both detectors can be seen in figure 3 as light green circles surrounded by yellow supporting structures.

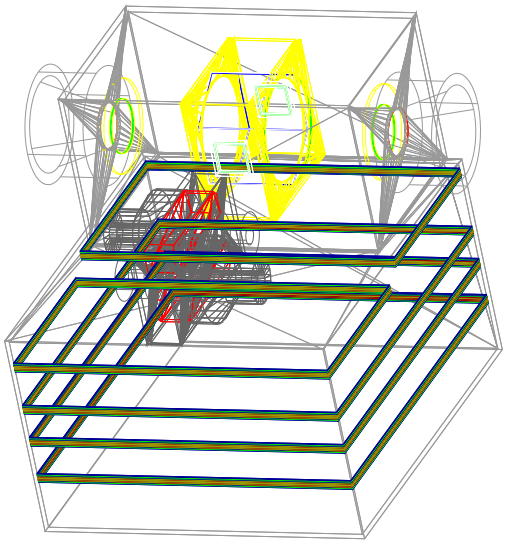

Figure 3: Geometry of the simplified EPT-HET and EBox model used for the simulations.

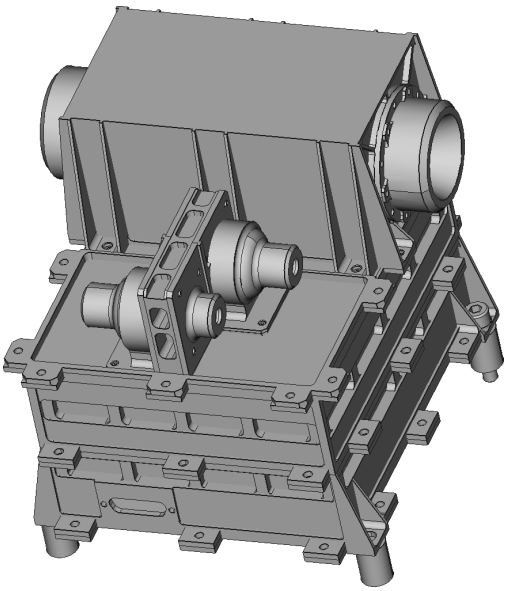

Figure 4: Geometry of the real EPT-HET with the EBox. The geometry is much more complex in comparision to the simple model in figure 3. Especially the outer additional structural elements can be seen here.

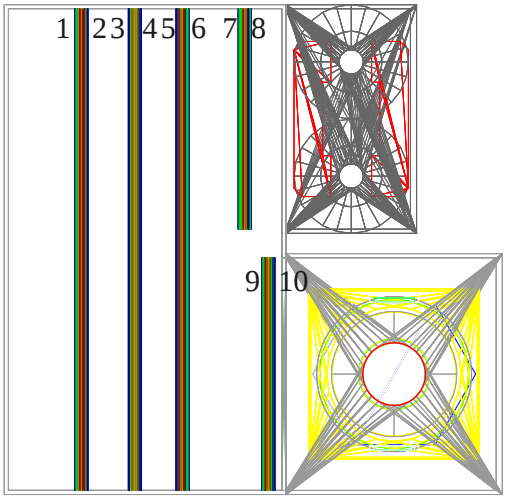

Figure 5: Geometry of the EPT-HET with the EBox used for the simulations (side view) and the numbering used for the ten sides of all PCBs.

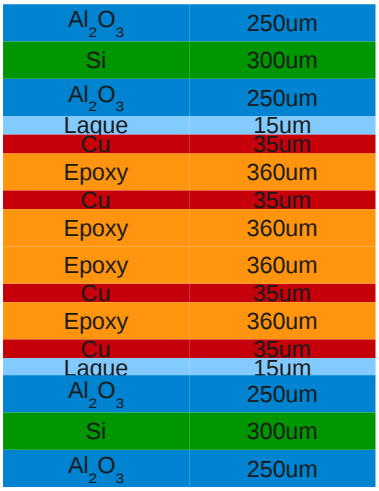

Figure 6: Sketch of the PCB layout design with the different layer types and thicknesses.

5.2 GEANT4 Physics list parameters

The choosen physics list is the "QGSP_BERT" reference physics list, recommended for high energy physics. It contains the standard EM processes and uses Bertini cascade and Quark-Gluon String Precompound Model. Fragmentation processes are also included in this physics list. It is used without any changes with the following code:

```
G4PhysListFactory *physListFactory = new G4PhysListFactory();
G4VUserPhysicsList *physicsList = physListFactory->GetReferencePhysList("QGSP_BERT");
runManager->SetUserInitialization(physicsList);
```

5.3 TID Simulation parameters

The simulations are performed using the energy binning of the previously defined spectra (see section 4). For each ion species ($Z = 1 \ldots 26$) and each of the 835 energy bins ($E_{\text{kin}} = 1$ to 1×10^5 MeV) a simulation is performed with 1000 particles coming from a box shaped source surface surrounding the telescope as described in section 5.1. The angular distribution was cosine distributed to simulate an isotropic field and the source cube had a side length of 15 cm. Dose deposition by ions heavier than helium is almost negliable because of the very low count rates so that the calculations above iron were not performed. The GEANT4 macro code for one of those bins (protons, 1.0023 to 1.016 23 MeV) was:

```
/gps/source/clear
/gps/source/add 1
/gps/particle ion
/gps/ion 1 1 1 0
/gps/ene/type Lin
/gps/ene/min 1.002300 MeV
/gps/ene/max 1.016230 MeV
/gps/ene/gradient 0.
/gps/ene/intercept 2.

/gps/ang/type cos

/gps/pos/type Surface
/gps/pos/shape Para
/gps/pos/centre 0. 0. 0. cm
/gps/pos/halfx 7.5 cm
/gps/pos/halfy 7.5 cm
/gps/pos/halfz 7.5 cm

/run/beamOn 1000
```

6 RESULTS OF THE SIMULATIONS

Figures 7 to 8 show the hit probability and the average energy distribution of the simulations for protons and different wall thicknesses (1.0 mm and 1.5 mm) for the sensitive volume (SV) 1,9 and 10. One can see the effect of different board sizes. SV 1 is approximately twice as large as 9 and 10. The effect of different shielding thicknesses can only be seen in the cut-off energy. For 1.5 mm Al the cut-off energy is just a few MeV higher than with 1.0 mm Al wall thickness.

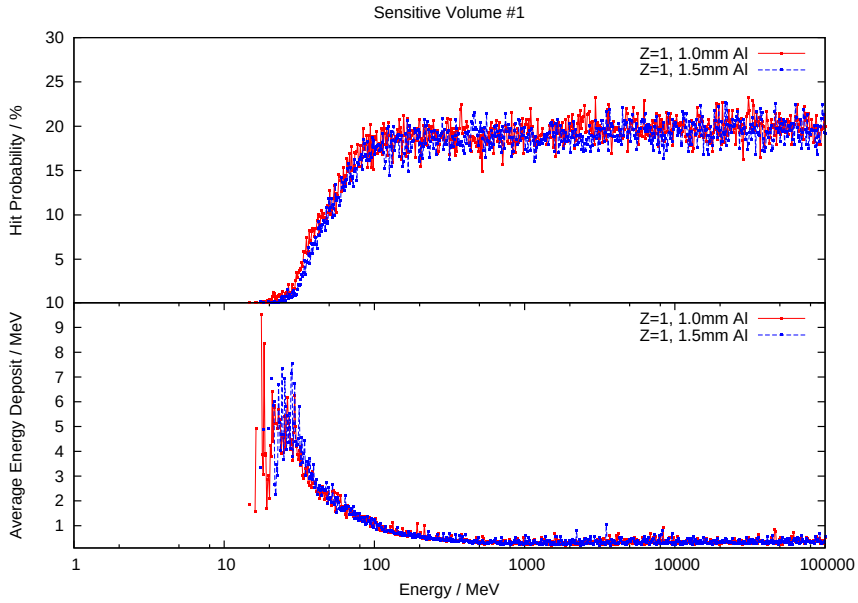

Figure 7: Average hit probability and average energy deposition for the silicon layer on the bottom of the PCB on the very bottom of the telescope (Board 1, Bottom, SV 1 in figure 3).

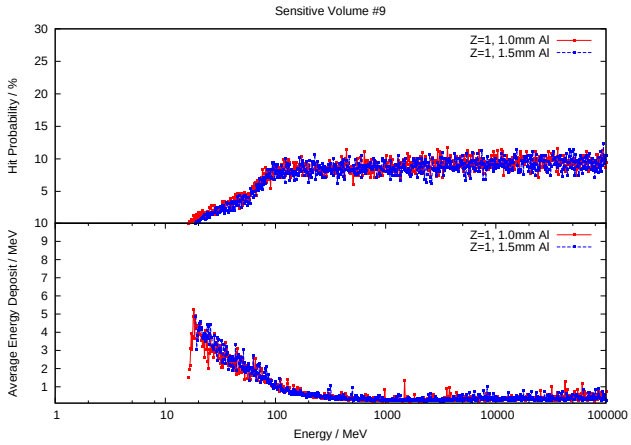

Figure 8: Average hit probability and average energy deposition for the silicon layer on the bottom of the PCB on the very top of the PCB stack (Board 5, Bottom, SV 9 in figure 3).

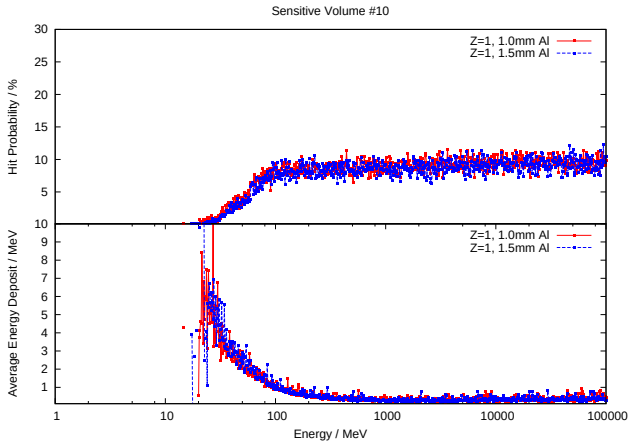

Figure 9: Average hit probability and average energy deposition for the silicon layer on the top of the PCB on the very top of the PCB stack (Board 5, Top, SV 10 in figure 3).

7 CALCULATION OF THE TOTAL IONIZING DOSE

The energy deposited per time T_i by particles within one energy bin can be described as:

$$T_i = H_i \cdot \bar{E}_i \cdot I_i \cdot G \cdot B_i \tag{2}$$

H_i : Hit probability of one particle
$\bar{E}_i$: Average energy deposition inside the detector for one hit
I_i : Flux (part./(m^2 sr s MeV/nuc)
G : Geometrical factor of the source box
B_i : Bin width in MeV/nuc

H_i and $\bar{E}_i$ are retrieved from the simulation results by using:

$$H_i = \frac{N_{\text{hits}}}{N_{\text{total}}} \tag{3}$$

$$\bar{E}_i = \frac{E_{\text{dep, total}}}{N_{\text{hits}}} \tag{4}$$

N_{hits} : Number of hits in the i-th bin
N_{total} : Number of particles simulated per bin
$E_{\text{dep, total}}$: Sum of all energy depositions in the detector in the current bin

I_i and B_i originate from the spectra datasets described in section 4 for both GCR and SPEs. The geometrical factor G for the source surface box can be calculated according to [3] for a telescope (with particles incident from one side) with:

$$G = \pi A \tag{5}$$

Where A is the area on which the particles are incident. In our case the source surface is a cube with a side length of 15 cm. Therefor the geometrical factor is $\pi \cdot 6 \cdot (15\,\text{cm})^2\text{sr} = \pi \cdot 1350\,\text{cm}^2\,\text{sr}$

7.1 Radiation dose due to Galactic Cosmic Rays (GCR)

7.1.1 Dose inside PCB and electronic components

The dose deposition per year D due to GCR can be calculated with equation 2:

$$D = \sum_i T_i \cdot 3600 \cdot 24 \cdot 365\,\mathrm{s/yr} \tag{6}$$

This is done for all ten PCBs in our model. The results are tabulated in tables 1 and 2. The doses differ only by small amounts from each other and the sum over all Z values lies at around 11 rad/a. The yearly dose rates are very similar to those reported in [2]. Figure 10 shows the dose distibution in SV 1 as a function of Z. Significant doses only come from H and He.

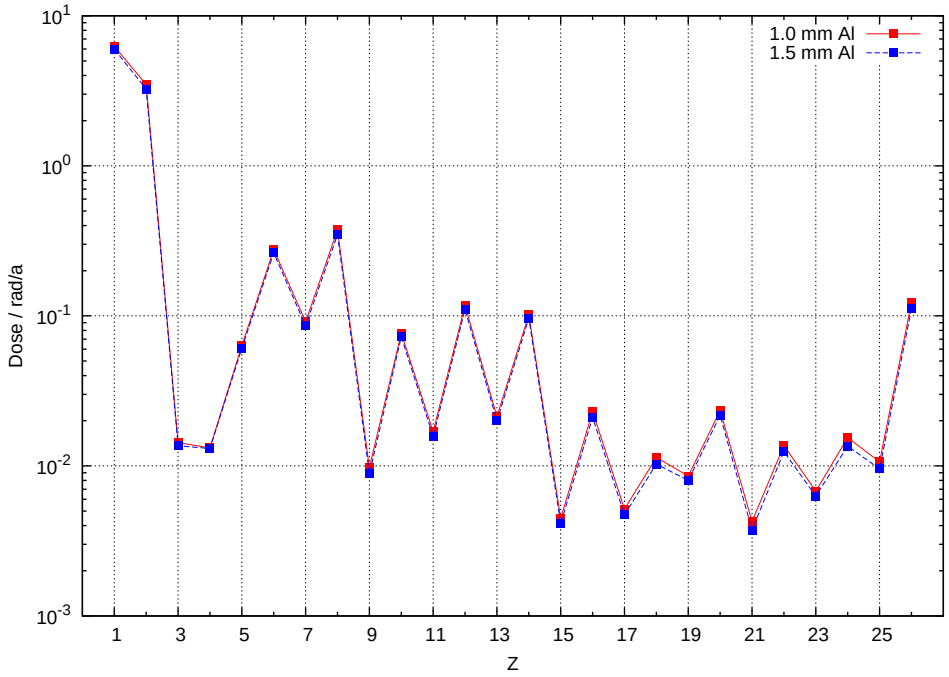

Figure 10: GCR induced dose distribution in the sensitive volume 1 for Z=1 to 26 for different thicknesses of Aluminium shielding.

	Dose in sensitive volume # / rad/a									
Z	1	2	3	4	5	6	7	8	9	10
1	6.3e+00	6.2e+00	6.6e+00	6.3e+00	6.4e+00	6.6e+00	6.5e+00	6.4e+00	6.2e+00	6.3e+00
2	3.5e+00	3.7e+00	3.5e+00	3.4e+00	3.4e+00	3.4e+00	3.5e+00	3.5e+00	3.5e+00	3.5e+00
3	1.5e-02	1.5e-02	1.4e-02	1.5e-02	1.4e-02	1.4e-02	1.4e-02	1.4e-02	1.4e-02	1.4e-02
4	1.4e-02	1.4e-02	1.3e-02	1.3e-02	1.3e-02	1.3e-02	1.4e-02	1.4e-02	1.3e-02	1.3e-02
5	6.5e-02	6.7e-02	6.3e-02	6.4e-02	6.3e-02	6.2e-02	6.4e-02	6.4e-02	6.4e-02	6.3e-02
6	2.8e-01	3.0e-01	2.7e-01	2.8e-01	2.7e-01	2.7e-01	2.8e-01	2.8e-01	2.8e-01	2.8e-01
7	9.4e-02	9.9e-02	9.0e-02	9.2e-02	9.0e-02	8.8e-02	9.6e-02	9.3e-02	9.4e-02	9.1e-02
8	3.9e-01	4.3e-01	3.6e-01	3.7e-01	3.7e-01	3.6e-01	3.9e-01	3.8e-01	3.9e-01	3.7e-01
9	1.0e-02	1.1e-02	9.5e-03	9.6e-03	9.7e-03	9.3e-03	1.0e-02	9.9e-03	9.9e-03	9.7e-03
10	8.1e-02	9.0e-02	7.5e-02	7.7e-02	7.8e-02	7.5e-02	8.2e-02	7.9e-02	8.1e-02	7.7e-02
11	1.8e-02	2.0e-02	1.6e-02	1.7e-02	1.7e-02	1.6e-02	1.8e-02	1.7e-02	1.8e-02	1.7e-02
12	1.3e-01	1.4e-01	1.1e-01	1.2e-01	1.2e-01	1.1e-01	1.3e-01	1.2e-01	1.2e-01	1.2e-01
13	2.3e-02	2.7e-02	2.1e-02	2.2e-02	2.2e-02	2.1e-02	2.3e-02	2.3e-02	2.3e-02	2.1e-02
14	1.1e-01	1.2e-01	9.6e-02	1.0e-01	9.9e-02	9.5e-02	1.1e-01	1.0e-01	1.0e-01	1.0e-01
15	4.8e-03	5.4e-03	4.3e-03	4.5e-03	4.5e-03	4.3e-03	4.8e-03	4.7e-03	4.7e-03	4.5e-03
16	2.4e-02	2.7e-02	2.2e-02	2.3e-02	2.3e-02	2.2e-02	2.4e-02	2.3e-02	2.3e-02	2.3e-02
17	5.5e-03	6.2e-03	4.9e-03	5.1e-03	5.0e-03	4.8e-03	5.4e-03	5.4e-03	5.4e-03	5.2e-03
18	1.2e-02	1.3e-02	1.1e-02	1.1e-02	1.1e-02	1.1e-02	1.2e-02	1.2e-02	1.1e-02	1.1e-02
19	9.4e-03	1.1e-02	8.2e-03	8.8e-03	8.6e-03	8.3e-03	9.1e-03	9.0e-03	9.0e-03	8.6e-03
20	2.5e-02	2.9e-02	2.2e-02	2.4e-02	2.4e-02	2.3e-02	2.6e-02	2.5e-02	2.5e-02	2.3e-02
21	4.5e-03	5.4e-03	4.0e-03	4.2e-03	4.2e-03	4.0e-03	4.7e-03	4.4e-03	4.4e-03	4.3e-03
22	1.5e-02	1.8e-02	1.3e-02	1.4e-02	1.4e-02	1.3e-02	1.5e-02	1.4e-02	1.5e-02	1.4e-02
23	7.6e-03	9.1e-03	6.6e-03	7.0e-03	7.0e-03	6.5e-03	7.6e-03	7.3e-03	7.5e-03	6.8e-03
24	1.7e-02	2.0e-02	1.4e-02	1.5e-02	1.5e-02	1.4e-02	1.6e-02	1.5e-02	1.6e-02	1.5e-02
25	1.1e-02	1.4e-02	1.0e-02	1.0e-02	1.0e-02	9.9e-03	1.1e-02	1.1e-02	1.1e-02	1.1e-02
26	1.3e-01	1.6e-01	1.2e-01	1.3e-01	1.2e-01	1.2e-01	1.3e-01	1.3e-01	1.3e-01	1.2e-01
Tot.	**1.1e+01**	**1.2e+01**	**1.1e+01**	**1.1e+01**	**1.1e+01**	**1.1e+01**	**1.1e+01**	**1.1e+01**	**1.1e+01**	**1.1e+01**

Table 1: GCR dose distribution in the different sensitive volumes for Z=1 to 26 for 1 mm Aluminium shielding.

	Dose in sensitive volume # / rad/a									
Z	1	2	3	4	5	6	7	8	9	10
1	6.4e+00	6.2e+00	6.2e+00	6.3e+00	6.3e+00	6.2e+00	6.2e+00	6.2e+00	6.1e+00	6.0e+00
2	3.4e+00	3.6e+00	3.3e+00	3.4e+00	3.3e+00	3.3e+00	3.3e+00	3.3e+00	3.3e+00	3.2e+00
3	1.4e-02	1.4e-02	1.4e-02	1.4e-02	1.4e-02	1.4e-02	1.4e-02	1.4e-02	1.4e-02	1.4e-02
4	1.3e-02	1.3e-02	1.3e-02	1.3e-02	1.3e-02	1.3e-02	1.3e-02	1.3e-02	1.3e-02	1.3e-02
5	6.2e-02	6.5e-02	6.0e-02	6.1e-02	6.1e-02	6.0e-02	6.0e-02	6.1e-02	6.2e-02	6.1e-02
6	2.7e-01	2.8e-01	2.6e-01	2.6e-01	2.6e-01	2.6e-01	2.7e-01	2.6e-01	2.7e-01	2.6e-01
7	9.2e-02	9.7e-02	8.6e-02	8.8e-02	8.7e-02	8.6e-02	9.0e-02	9.0e-02	8.8e-02	8.6e-02
8	3.7e-01	4.0e-01	3.5e-01	3.7e-01	3.6e-01	3.5e-01	3.7e-01	3.7e-01	3.6e-01	3.5e-01
9	9.5e-03	1.1e-02	8.8e-03	9.3e-03	9.1e-03	8.9e-03	9.5e-03	9.3e-03	9.2e-03	8.9e-03
10	7.6e-02	8.5e-02	7.1e-02	7.3e-02	7.3e-02	7.2e-02	7.7e-02	7.4e-02	7.5e-02	7.2e-02
11	1.7e-02	1.9e-02	1.5e-02	1.6e-02	1.6e-02	1.5e-02	1.6e-02	1.6e-02	1.6e-02	1.6e-02
12	1.2e-01	1.3e-01	1.1e-01	1.1e-01	1.1e-01	1.1e-01	1.2e-01	1.1e-01	1.2e-01	1.1e-01
13	2.2e-02	2.5e-02	2.0e-02	2.0e-02	2.0e-02	2.0e-02	2.2e-02	2.1e-02	2.1e-02	2.0e-02
14	1.0e-01	1.1e-01	9.0e-02	9.5e-02	9.4e-02	9.0e-02	9.8e-02	9.8e-02	9.9e-02	9.6e-02
15	4.5e-03	5.1e-03	4.0e-03	4.3e-03	4.1e-03	3.9e-03	4.5e-03	4.3e-03	4.2e-03	4.1e-03
16	2.3e-02	2.5e-02	2.0e-02	2.1e-02	2.1e-02	2.0e-02	2.2e-02	2.2e-02	2.1e-02	2.1e-02
17	5.2e-03	5.8e-03	4.6e-03	4.9e-03	4.7e-03	4.5e-03	5.1e-03	5.0e-03	4.8e-03	4.7e-03
18	1.1e-02	1.3e-02	1.0e-02	1.1e-02	1.1e-02	1.0e-02	1.1e-02	1.1e-02	1.1e-02	1.0e-02
19	8.9e-03	9.9e-03	7.8e-03	8.2e-03	8.0e-03	7.7e-03	8.4e-03	8.2e-03	8.1e-03	8.0e-03
20	2.4e-02	2.7e-02	2.1e-02	2.2e-02	2.2e-02	2.1e-02	2.3e-02	2.2e-02	2.2e-02	2.2e-02
21	4.2e-03	4.9e-03	3.7e-03	3.9e-03	3.8e-03	3.6e-03	4.1e-03	4.0e-03	3.9e-03	3.7e-03
22	1.4e-02	1.6e-02	1.2e-02	1.3e-02	1.3e-02	1.2e-02	1.4e-02	1.3e-02	1.3e-02	1.2e-02
23	7.0e-03	8.3e-03	6.0e-03	6.4e-03	6.4e-03	6.0e-03	6.9e-03	6.6e-03	6.6e-03	6.3e-03
24	1.5e-02	1.8e-02	1.3e-02	1.4e-02	1.4e-02	1.3e-02	1.5e-02	1.4e-02	1.4e-02	1.4e-02
25	1.1e-02	1.3e-02	9.3e-03	9.8e-03	9.6e-03	9.2e-03	1.0e-02	1.0e-02	1.0e-02	9.6e-03
26	1.2e-01	1.4e-01	1.1e-01	1.1e-01	1.1e-01	1.1e-01	1.2e-01	1.1e-01	1.2e-01	1.1e-01
Tot.	**1.1e+01**	**1.1e+01**	**1.1e+01**	**1.1e+01**	**1.1e+01**	**1.1e+01**	**1.1e+01**	**1.1e+01**	**1.1e+01**	**1.1e+01**

Table 2: GCR dose distribution in the different sensitive volumes for Z=1 to 26 for 1.5 mm Aluminium shielding.

7.1.2 Dose inside silicon detectors

The dose inside the silicon detectors is calculated as in section 7.1.1. The doses are shown in table 3. The doses are compareable to the doses in the PCBs. The second detector receives around 50 % of the dose of the front detector. this is due to the heavy crystal which shields one side of the detector completely.

	Dose in silicon detector / rad/a	
Z	Detector A	Detector B
1	7.005	7.103
2	2.442	2.464
3	0.014	0.014
4	0.013	0.014
5	0.070	0.074
6	0.380	0.371
7	0.140	0.132
8	0.634	0.642
9	0.017	0.017
10	0.155	0.158
11	0.042	0.040
12	0.288	0.288
13	0.061	0.060
14	0.276	0.282
15	0.013	0.014
16	0.077	0.071
17	0.018	0.018
18	0.041	0.042
19	0.037	0.039
20	0.106	0.102
21	0.021	0.021
22	0.075	0.074
23	0.042	0.042
24	0.093	0.093
25	0.064	0.064
26	0.732	0.732
Tot.	12.857	12.970

Table 3: GCR dose distribution in the different silicon detectors for Z=1 to 26 for 1.0 mm Aluminium shielding.

7.1.3 Non-ionizing Dose inside silicon detectors

The non-ionizing dose inside silicon detectors is calculated from the doses in section 7.1.1 in combination with a SRIM table for ionizing and non-ionizing energy loss. For protons the comparision of non-ionizing

and ionizing energy loss per year is listed in table 4. The non-ionizing dose for alpha particles is a factor of 10 higher than for protons but the abundancy is also approximately a factor of 10 lower. This means that the non-ionizing dose due to alphas will be in the same order as for protons.

	Det. A / rad/a	Det. B / rad/a
Total Dose	7.005	7.103
Non-ionizing Dose	0.002	0.002

Table 4: GCR non-ionizing dose for protons

7.2 Radiation dose due to Solar Particle Events (SPEs)

7.2.1 Dose inside PCB and electronic components

For the solar events a slightly different approach is chosen. Dose distribution is also described with formula 2 but I_i is chosen different:

- The relative intensity of one bin to another is taken from the solar spectra described in section 4
- The yearly average flux is taken from the model in [4].

The probability to not exceed an annual fluence of particles above 100 MeV by this model can be seen in figure 11. The values are taken as reference points to calibrate solar proton fluxes with the simulations. From the reference spectrum described in section 4 the value for particles with energies >100 MeV is calculated as:

$$\sum_{E=100\,\mathrm{MeV}}^{100\,\mathrm{GeV}} I_i \cdot B_i = 1.6799 \times 10^{10}\,\mathrm{part/(yr\,sr\,cm^2)} \tag{7}$$

To get the one sided, omnidirectional fluence of one has to multiply the value with 2π so that the value is now:

$$\sum_{E=100\,\mathrm{MeV}}^{100\,\mathrm{GeV}} I_i \cdot B_i \cdot 2\pi = 1.055\,525 \times 10^{11}\,\mathrm{part/(cm^2 yr)} \tag{8}$$

With this value one can now calculate a scaling factor S which scales the spectra from section 4 to the values expected with the model:

$$S(P) = \frac{F(P)}{1.055\,525 \times 10^{11}\,\mathrm{part/(cm^2 yr)}} \tag{9}$$

Where $F(P)$ is a fluence value corresponding to a probability P, taken from figure 11. The dose equation for SPEs then looks analoque to equation 2 like this:

$$T_i = H_i \cdot \bar{E}_i \cdot I_i \cdot G \cdot B_i \cdot S(P) \tag{10}$$

For SPEs the radial distance from the source has to be considered. The averaged radius during the science phase is 0.56 AU[1]. Assuming a r^{-2} dependency of the intensity one has to correct the doses

[1] calculated as $1/\sqrt{\langle R^{-2}\rangle}$

with a factor of $F_{sci} = 3.24$. For the cruise phase the averaged radius is 0.81 AU [1] with a scaling factor of $F_{cruise} = 1.54$. Results for all SVs are tabulated in tables 5 to 6, significant doses only come from H and He.

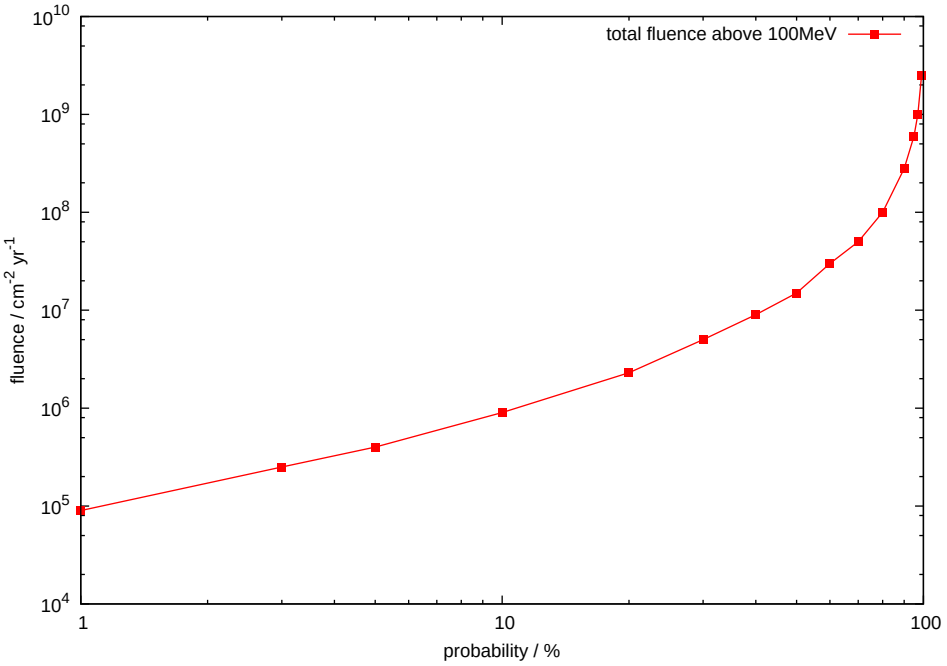

Figure 11: Probability to not exceed a fluence above 100 MeV in one year due to SPE at 1 AU from [4].

	Dose in sensitive volume # / rad/a									
Z	1	2	3	4	5	6	7	8	9	10
1	4.0e+3	9.3e+3	3.2e+3	3.7e+3	4.0e+3	3.1e+3	5.7e+3	4.0e+3	5.8e+3	4.0e+3
2	7.5e-1	2.8e+0	6.1e-1	7.2e-1	8.7e-1	5.6e-1	1.4e+0	8.9e-1	1.6e+0	8.3e-1
3	0.0e+0	0.0e+0	0.0e+0	0.0e+0	0.0e+0	0.0e+0	0.0e+0	0.0e+0	0.0e+0	0.0e+0
4	0.0e+0	0.0e+0	0.0e+0	0.0e+0	0.0e+0	0.0e+0	0.0e+0	0.0e+0	0.0e+0	0.0e+0
5	0.0e+0	0.0e+0	0.0e+0	0.0e+0	0.0e+0	0.0e+0	0.0e+0	0.0e+0	0.0e+0	0.0e+0
6	2.4e-3	9.1e-3	1.8e-3	2.0e-3	2.6e-3	1.8e-3	4.4e-3	2.8e-3	5.5e-3	2.5e-3
7	4.1e-4	1.7e-3	3.4e-4	4.0e-4	4.3e-4	3.2e-4	9.0e-4	5.2e-4	1.1e-3	4.3e-4
8	2.9e-3	1.1e-2	2.0e-3	2.4e-3	3.1e-3	2.1e-3	5.4e-3	3.1e-3	6.4e-3	3.0e-3
9	1.0e-7	4.2e-7	7.6e-8	9.0e-8	1.2e-7	7.9e-8	1.9e-7	1.3e-7	2.6e-7	1.1e-7
10	3.9e-4	1.7e-3	3.1e-4	3.8e-4	4.4e-4	3.1e-4	8.2e-4	5.2e-4	9.5e-4	4.6e-4
11	3.1e-5	1.3e-4	2.4e-5	2.9e-5	3.5e-5	2.2e-5	6.1e-5	3.7e-5	7.9e-5	3.2e-5
12	3.1e-4	1.6e-3	2.3e-4	3.0e-4	4.0e-4	2.5e-4	7.2e-4	3.9e-4	9.5e-4	3.4e-4
13	2.8e-5	1.3e-4	2.0e-5	2.3e-5	3.4e-5	2.1e-5	5.7e-5	3.5e-5	7.1e-5	3.0e-5
14	5.1e-4	2.1e-3	3.8e-4	4.4e-4	5.6e-4	3.4e-4	1.0e-3	6.6e-4	1.2e-3	4.8e-4
15	2.9e-7	1.2e-6	2.1e-7	2.4e-7	3.4e-7	2.1e-7	5.8e-7	3.6e-7	7.6e-7	3.1e-7
16	1.2e-4	4.8e-4	1.0e-4	1.0e-4	1.4e-4	8.9e-5	2.3e-4	1.5e-4	2.6e-4	1.4e-4
17	2.0e-7	7.6e-7	1.4e-7	1.6e-7	2.0e-7	1.4e-7	3.8e-7	2.3e-7	4.4e-7	2.1e-7
18	1.9e-6	7.2e-6	1.3e-6	1.7e-6	2.1e-6	1.3e-6	3.7e-6	2.3e-6	4.3e-6	1.9e-6
19	3.7e-7	1.4e-6	2.5e-7	3.1e-7	4.1e-7	2.5e-7	6.3e-7	4.2e-7	8.3e-7	3.5e-7
20	4.3e-5	1.7e-4	3.3e-5	3.6e-5	4.8e-5	3.0e-5	8.3e-5	5.2e-5	1.0e-4	4.5e-5
21	5.1e-8	2.2e-7	3.4e-8	4.6e-8	5.6e-8	3.7e-8	1.0e-7	6.0e-8	1.3e-7	4.8e-8
22	7.0e-7	3.1e-6	4.5e-7	5.4e-7	7.6e-7	4.7e-7	1.4e-6	7.6e-7	1.6e-6	7.2e-7
23	5.9e-8	2.7e-7	4.3e-8	4.7e-8	6.8e-8	4.4e-8	1.1e-7	7.7e-8	1.6e-7	6.1e-8
24	2.0e-6	1.0e-5	1.6e-6	1.7e-6	2.3e-6	1.5e-6	4.6e-6	2.7e-6	5.5e-6	2.2e-6
25	6.8e-7	3.0e-6	5.0e-7	5.4e-7	7.5e-7	4.9e-7	1.3e-6	7.5e-7	1.9e-6	7.1e-7
26	1.1e-4	5.4e-4	8.2e-5	9.0e-5	1.3e-4	8.4e-5	2.3e-4	1.2e-4	2.9e-4	1.1e-4
Tot.	4.0e+3	9.3e+3	3.2e+3	3.7e+3	4.0e+3	3.1e+3	5.7e+3	4.0e+3	5.8e+3	4.0e+3

Table 5: Dose distribution in the different sensitive volumes for Z=1 to 26 for 1.0 mm Aluminium shielding and 90 % confidence scaled to 0.56 AU.

	Dose in sensitive volume # / rad/a									
Z	1	2	3	4	5	6	7	8	9	10
1	3.3e+3	6.4e+3	2.5e+3	2.9e+3	3.0e+3	2.5e+3	3.9e+3	3.4e+3	4.3e+3	3.1e+3
2	5.2e-1	1.6e+0	3.9e-1	4.9e-1	5.1e-1	3.8e-1	7.8e-1	5.6e-1	9.2e-1	5.3e-1
3	0.0e+0	0.0e+0	0.0e+0	0.0e+0	0.0e+0	0.0e+0	0.0e+0	0.0e+0	0.0e+0	0.0e+0
4	0.0e+0	0.0e+0	0.0e+0	0.0e+0	0.0e+0	0.0e+0	0.0e+0	0.0e+0	0.0e+0	0.0e+0
5	0.0e+0	0.0e+0	0.0e+0	0.0e+0	0.0e+0	0.0e+0	0.0e+0	0.0e+0	0.0e+0	0.0e+0
6	1.6e-3	5.1e-3	1.2e-3	1.5e-3	1.7e-3	1.2e-3	2.4e-3	1.6e-3	2.9e-3	1.4e-3
7	2.9e-4	9.8e-4	2.2e-4	2.6e-4	2.9e-4	2.1e-4	4.8e-4	3.5e-4	5.5e-4	2.8e-4
8	1.8e-3	6.3e-3	1.4e-3	1.7e-3	2.0e-3	1.3e-3	3.1e-3	2.3e-3	3.9e-3	1.8e-3
9	7.0e-8	2.4e-7	4.7e-8	6.0e-8	7.3e-8	4.6e-8	1.1e-7	7.5e-8	1.3e-7	6.8e-8
10	2.6e-4	9.6e-4	1.9e-4	2.2e-4	2.7e-4	1.8e-4	4.7e-4	3.1e-4	5.9e-4	2.6e-4
11	2.0e-5	7.7e-5	1.4e-5	1.6e-5	2.2e-5	1.3e-5	3.5e-5	2.4e-5	4.1e-5	1.9e-5
12	2.0e-4	8.5e-4	1.5e-4	1.7e-4	2.2e-4	1.6e-4	4.0e-4	2.3e-4	5.0e-4	2.2e-4
13	2.0e-5	7.3e-5	1.3e-5	1.6e-5	2.1e-5	1.2e-5	3.5e-5	2.1e-5	4.2e-5	1.9e-5
14	3.2e-4	1.2e-3	2.4e-4	2.8e-4	3.7e-4	2.3e-4	5.8e-4	3.5e-4	7.3e-4	3.2e-4
15	1.9e-7	7.1e-7	1.4e-7	1.7e-7	2.1e-7	1.3e-7	3.4e-7	2.1e-7	3.9e-7	2.0e-7
16	8.3e-5	2.6e-4	5.0e-5	6.4e-5	8.2e-5	5.5e-5	1.2e-4	8.9e-5	1.5e-4	8.0e-5
17	1.3e-7	4.2e-7	8.9e-8	1.1e-7	1.2e-7	8.6e-8	2.1e-7	1.4e-7	2.3e-7	1.2e-7
18	1.2e-6	4.1e-6	8.6e-7	1.0e-6	1.2e-6	9.3e-7	1.9e-6	1.3e-6	2.4e-6	1.2e-6
19	2.3e-7	7.4e-7	1.7e-7	2.0e-7	2.2e-7	1.5e-7	3.6e-7	2.3e-7	4.6e-7	2.2e-7
20	2.7e-5	9.0e-5	1.9e-5	2.2e-5	2.8e-5	1.9e-5	4.3e-5	3.1e-5	5.0e-5	2.7e-5
21	2.7e-8	1.0e-7	2.0e-8	2.4e-8	2.8e-8	1.8e-8	5.3e-8	3.2e-8	6.1e-8	2.6e-8
22	3.9e-7	1.5e-6	2.7e-7	3.1e-7	4.1e-7	2.6e-7	7.1e-7	4.7e-7	8.4e-7	4.1e-7
23	3.2e-8	1.3e-7	2.3e-8	2.6e-8	3.4e-8	2.3e-8	6.3e-8	3.9e-8	7.4e-8	3.4e-8
24	1.1e-6	4.7e-6	9.0e-7	1.0e-6	1.2e-6	8.4e-7	2.1e-6	1.6e-6	2.7e-6	1.2e-6
25	3.6e-7	1.5e-6	2.5e-7	3.2e-7	4.0e-7	2.6e-7	6.5e-7	4.0e-7	7.9e-7	3.7e-7
26	6.3e-5	2.4e-4	3.9e-5	5.1e-5	6.7e-5	4.6e-5	1.0e-4	6.6e-5	1.5e-4	5.8e-5
Tot.	3.3e+3	6.4e+3	2.5e+3	2.9e+3	3.0e+3	2.5e+3	3.9e+3	3.4e+3	4.3e+3	3.1e+3

Table 6: Dose distribution in the different sensitive volumes for Z=1 to 26 for 1.5 mm Aluminium shielding and 90 % confidence scaled to 0.56 AU.

7.2.2 Dose inside silicon detectors

The dose inside the silicon detectors is calculated as in section 7.2.1 with a confidence of 90 %. The doses are shown in table 7. The doses are compareable to the doses in the PCBs during solar events. The second detector receives around 50 % of the dose of the front detector. this is due to the heavy crystal which shields one side of the detector almost completely.

	Dose in silicon detector / rad/a	
Z	Detector A	Detector B
1	10212.026	4714.737
2	702.198	193.996
3	0.000	0.000
4	0.000	0.000
5	0.000	0.000
6	18.557	8.208
7	5.431	2.497
8	59.305	25.076
9	0.003	0.001
10	16.751	6.150
11	1.415	0.680
12	19.500	8.162
13	2.024	0.785
14	28.045	18.594
15	0.027	0.012
16	11.006	5.527
17	0.022	0.010
18	0.253	0.135
19	0.047	0.027
20	6.833	3.491
21	0.019	0.012
22	0.360	0.167
23	0.033	0.017
24	1.050	0.729
25	0.465	0.257
26	92.090	53.248
Tot.	11 177.460	5042.519

Table 7: Dose distribution in the different silicon detectors for Z=1 to 26 for 1.0 mm Aluminium shielding and 90 % confidence scaled to 0.56 AU.

7.2.3 Non-ionizing Dose inside silicon detectors

The non-ionizing dose inside silicon detectors is calculated from the doses in section 7.2.1 in combination with a SRIM table for ionizing and non-ionizing energy loss. For protons the comparision of non-ionizing

and ionizing energy loss per year is listed in table 8. The non-ionizing dose for alpha particles is a factor of 10 higher than for protons but the abundancy is also approximately a factor of 10 lower. This means that the non-ionizing dose due to alphas will be in the same order as for protons.

	Det. A / rad/a	Det. B / rad/a
Total Dose	10212.026	4714.737
Non-ionizing Dose	5.854	2.497

Table 8: SPE non-ionizing dose for protons

7.3 Radiation Dose due to solar electrons

The dose deposition per time for solar electrons is calculated with equation 2. The simulation results are weighted with the corresponding electron spectrum in equation 1. If one assumes that the electron spectrum is valid at all times and that the radius is constant at 0.39 AU, the dose rate over one year can be calculated. The results are listed in table 9 for each SV. The assumptions that the spectrum is present all the time as well as the radius of 0.39 AU are completely overestimating the electron dose. More realistic assumptions (4 weeks of SPE per year and mean radius of 0.56 AU) would decrease the total dose due to electrons to 4 % of the value displayed in table 9 so that electron contribution to the dose can be completely neglected.

Dose in sensitive volume # / rad/a									
1	2	3	4	5	6	7	8	9	10
2638	4402	2225	2431	2601	2243	3219	2634	3152	2520

Table 9: Electron dose contribution in the different sensitive volumes for 1.0 mm Aluminium shielding. The values assume that the electron specrum is always SPE like and that radius is always at 0.39 AU

8 CALCULATION OF SINGLE EVENT EFFECTS

The Single Event Effect (SEE) rate is calculated using Spenvis[2] data with 1 mm of aluminium shielding. GCR SEE rate is calculated using the CREME96 GCR spectrum for solar minimum. SPE SEE rate is calculated using the same spectrum as for the Total Ionizing Dose (TID). The same scaling factors as in section 7.2.1 were applied for a confidence level of 90 %. Figures 12 and 13 show the expected rate for GCR and during a SPE.

Table 10 lists the thresholds for the Linear Energy Transfer (LET) values of critical parts in our Instrument. The values of 36 MeV cm^2 mg^{-1}, 86 MeV cm^2 mg^{-1} and 100 MeV cm^2 mg^{-1} are marked in figures 12 and 13.

The values have to be scaled down to the typical size of the active area of electronic components. Therefore we assume that the critical area for SEE effects is in the order of $\approx 1 \cdot 1\,\mu m^2$ which is the structural size of our FPGA.

The SEE rates calculated under this assumption are listed in table 10. As it can be seen the probability to get a SEE per area is very low. Assuming that the total area of one small device (like a MOSFET transistor) is in the order of a few thousands μm^2, the probability to receive one SEE will be $< 1 \times 10^{-3}$ %/year. For the larger devices like the FPGA the area to be taken into account will be in the order of a few mm^2 which leads to probabilities in the order of 1×10^{-5} %/year. These rates are considered to be not critical to the instrument behaviour.

[2] http://www.spenvis.oma.be/

Part Number	Description	SEL $MeV^{-1}\,cm^2\,mg^{-1}$	GCR rate /year µm^2	SPE rate /year µm^2	total rate /year µm^2
MSK5059	switching regulator	(36)[1]	5.9×10^{-12}	2.9×10^{-09}	2.9×10^{-09}
ISL78841ASRH	current mode PWM controller	86	4.0×10^{-13}	7.6×10^{-11}	7.6×10^{-11}
ADC128S102	ADC 8-CH 12-Bit 1MSPS	120	1.1×10^{-14}	3.7×10^{-14}	4.8×10^{-14}
54LVDS055	3V3 Dual LVDS driver/receiver	100	1.2×10^{-13}	2.0×10^{-11}	2.0×10^{-11}
RTAX2000SL-CQ256	FPGA	117	1.1×10^{-14}	3.7×10^{-14}	4.8×10^{-14}
UT8CR512K32	512kx32 SRAM	100	1.2×10^{-13}	2.0×10^{-11}	2.0×10^{-11}
28LV010	1Megabit (128K x 8Bit) EEPROM	184	1.1×10^{-14}	3.7×10^{-14}	4.8×10^{-14}
IS-1009	shunt regulator diode TO-206AB	(36)[1]	5.9×10^{-12}	2.9×10^{-09}	2.9×10^{-09}
RH1498	Op Amp	117	1.1×10^{-14}	3.7×10^{-14}	4.8×10^{-14}
RH1056	Op Amp	(36)[1]	5.9×10^{-12}	2.9×10^{-09}	2.9×10^{-09}
AD8005	Op Amp	(36)[1]	5.9×10^{-12}	2.9×10^{-09}	2.9×10^{-09}
CD4024	7-STAGE RIPPLE CARRY BINARY COUNTER / DIVIDER	72	9.0×10^{-13}	1.5×10^{-10}	1.5×10^{-10}
IRHLUB7970Z4	logic level power MOSFET	38	5.2×10^{-12}	2.2×10^{-09}	2.2×10^{-09}
IRHLUB770Z4	logic level power MOSFET	38	5.26×10^{-12}	2.2×10^{-09}	2.2×10^{-09}
IRHNJ57133SE	MOSFET	36	5.9×10^{-12}	2.9×10^{-09}	2.9×10^{-09}
2N2857	Silicon Ultra-High frequency NPN amplifier	(36)[1]	5.9×10^{-12}	2.9×10^{-09}	2.9×10^{-09}
2N4957	Silicon VHF-UHF PNP amplifier transistor	(36)[1]	5.9×10^{-12}	2.9×10^{-09}	2.9×10^{-09}
2N5551	Silicon NPN Transistor	(36)[1]	5.9×10^{-12}	2.9×10^{-09}	2.9×10^{-09}
BF862	JFET N-CH	(36)[1]	5.9×10^{-12}	2.9×10^{-09}	2.9×10^{-09}

Table 10: Rates for several LET-Threshold values for GCR and SPEs.

[1] SEE hardness not specified in the datasheet, but stated as rad-hard and useable for space environment, therefor a SEL level of 36 MeV cm^2 g^{-1} is assumed.

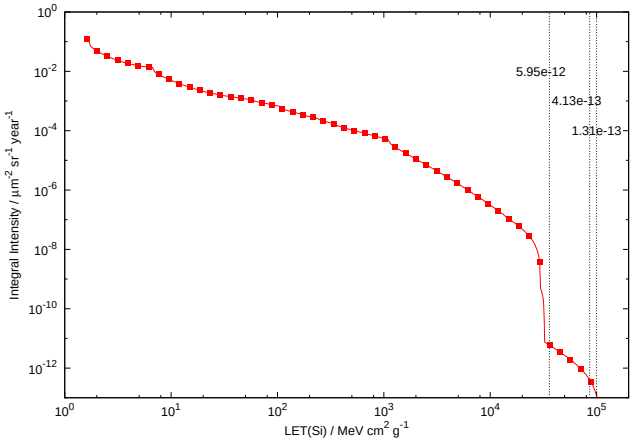

Figure 12: Integral GCR LET-spectrum for ions from H to U after 1 mm of aluminium shielding for the duration of 1 year. Marked are the LET values of 36, 86 and 100 MeV cm^2 g^{-1} with the corresponding rates.

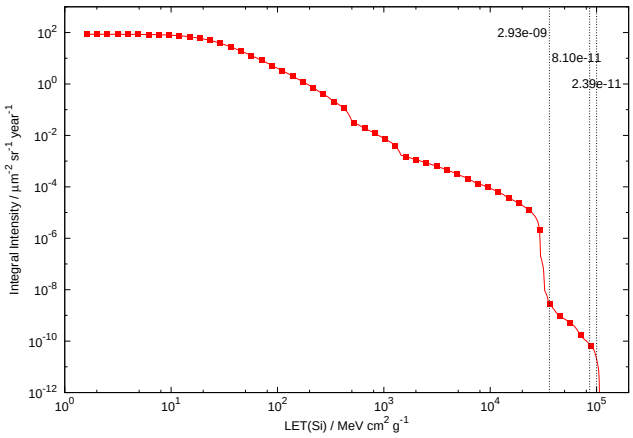

Figure 13: Integral SPE LET-spectrum for ions from H to U after 1 mm of aluminium shielding for solar events with the same spectrum as in section 7.2.1. Marked are the LET values of 36, 86 and 100 MeV cm^2 g^{-1} with the corresponding rates.

9 PROBABILITY ESTIMATION OF TOTAL DOSE

If one uses the values calculated in the previous sections and combines them with the according probabilities (see figure 11 for details) one can estimate the mission dose for EPTHET. The assumptions are:

- Cruise-Phase average radius is 0.81 AU, radial scaling factor $F_{sci} = 3.24$
- Science-Phase average radius is 0.56 AU, radial scaling factor $F_{cru} = 1.54$
- Worst case dose is taken as 9.3×10^3 kRad/year with a probability of 90 % at 0.56 AU
- other probabilities are calculated according to figure 11 and with formula 9

The results for a 3 years cruise phase and a science phase lasting 4 years are plotted in figures 14 and 15 for 1 mm aluminium and 1.5 mm aluminium. The probability that the total dose will not exceed 100 krad in the worst case assumption is 90.23 % for 1.0 mm aluminium (92.87 % for 1.5 mm). Please note that the median in this distribution is settled at 50 %. It is also important to mention that the highest probability plotted in this graph is at ≈93.2 % = 99 %[7]. Table 11 lists all the TIDs for all used parts, derived from their datasheets. The table also lists the probability that this part will not exceed its individual TID threshold by 50 % and 100 % within the complete mission (3 years cruise, 4 years of science).

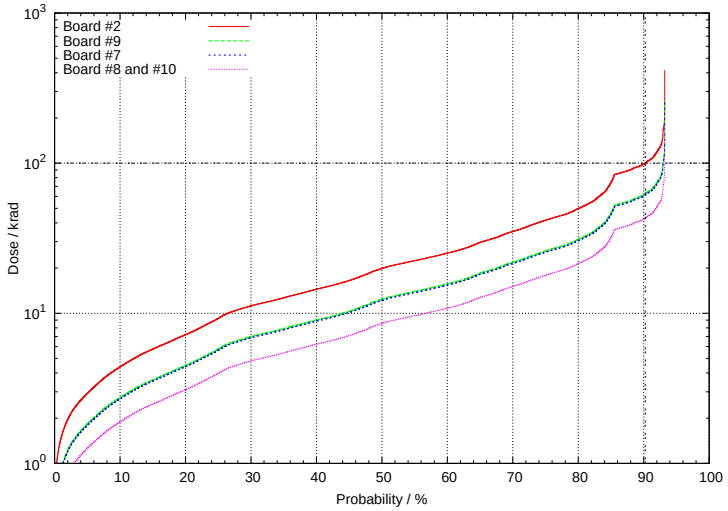

Figure 14: Dose probability for 1.0 mm Al shielding inside the PCBs. Board #2 receives the highest dose, boards 7 to 10 have the most sensitive electronic in respect to radiation hardness.

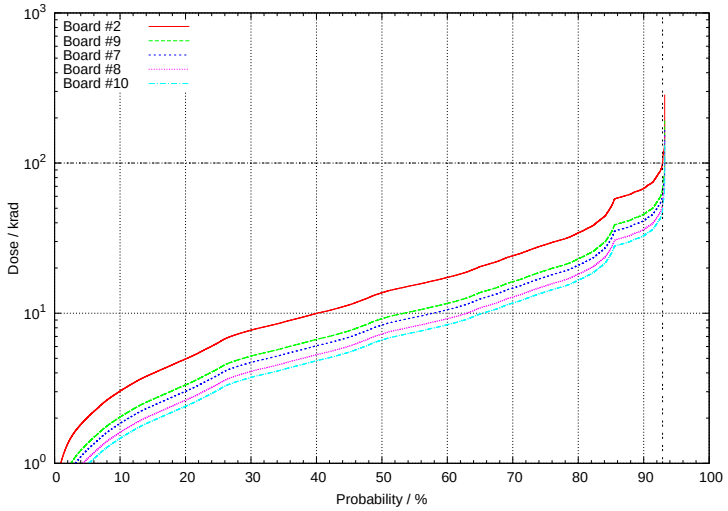

Figure 15: Dose probability for 1.5 mm Al shielding inside the PCBs. Board #2 receives the highest dose, boards 7 to 10 have the most sensitive electronic in respect to radiation hardness.

General Part Number	Description	TID level / krad	Ref. Board	P(D<50%TID) / %	P(D<100%TID) / %
MSK5059	step-down switching regulator	100	2	80.1	90.2
ISL78841ASRH	Single-Ended Current Mode PWM Controller	100	2	80.1	90.2
ADC128S102	ADC 8-CH 12-Bit 1MSPS	100	8	91.9	93.2
54LVDS055	3V3 Dual LVDS driver/receiver	100	8	91.9	93.2
RTAX2000SL-CQ256	FPGA	300	8	93.2	> 93.2
UT8CR512K32	512kx32 SRAM	300	8	93.2	> 93.2
28LV010	1Megabit (128K x 8Bit) EEPROM	100	8	91.9	93.2
IS-1009	2.5V shunt regulator diode TO-206AB	300	2	92.9	93.2
RH1498	Op Amp	200	2	90.2	93.2
RH1056	Op Amp	200	2	90.2	93.2
AD8005	Op Amp	100	8	91.9	93.2
CD4024	7-STAGE RIPPLE CARRY BINARY COUNTER / DIVIDER	100	2	80.1	90.2
IRHLUB7970Z4	logic level power MOSFET P-CH	100	2	80.1	90.2
IRHLUB770Z4	logic level power MOSFET N-CH	100	2	80.1	90.2
IRHNJ57133SE	MOSFET, N-CH	100	2	80.1	90.2
2N2857	Silicon Ultra-High frequency NPN amplifier	(100)[1]	9	85.4	93.0
2N4957	Silicon VHF-UHF PNP amplifier	(100)[1]	9	85.4	93.0
2N5551	Silicon NPN Transistor	100	2	80.1	90.2
BF862	JFET N-CH	(100)[1]	9	85.4	93.0

Table 11: TID-Levels for electronic parts. The column denoted with P(D< *xx*%TID) lists the probability that the part's TID level will **not be exceeded** within 7 years (3 years cruise, 4 years of science) by the percentage level indicated with *xx*.

[1] TID not specified in the datasheet, but stated as rad-hard and useable for space environment, therefor a TID level of 100 krad is assumed.

10 SUMMARY

In this document a detailed radiation analysis for the EPT-HET detector onboard Solar Orbiter was performed. All results are calculated using worst case estimates. Under these worst case assumptions the probability that the dose does not exceed 100 krad 90.23 % for 1 mm aluminium shielding. It should be mentioned that the worst case approximation is largely overestimating the total dose. The most important approximation is the absence of the spacecraft below the instrument. In reality there will be at least $\frac{1}{8}$ to $\frac{1}{4}$ of the solid angle covered by the spacecraft. This should have a huge effect on particles created due to solar events. As a first estimate one can say that this would reduce the doses by a factor similar to the coverage percentage (12.5 to 25 %) which means that the probability to not exceed 75 to 87.5 krad will be 90.23 %. This should leave enough margin for the TID.

Single event effects have to be considered during large solar events. During and after a solar event the configuration should be checked and/or refreshed. This should also be done from time to time to recover from GCR induced SEEs.

For the silicon detectors the doses of the front detectors are compareable to those of one of the PCBs. The inner silicon detector only sees 50 % of the dose of the front detector. This dose is considered not to be critical for the silicon detectors.

A.3 Nucl. Instr. and Meth. B 360 (2015) pp129-138

On the following pages the article "*Quenching comparison of BGO and BSO for heavy ions*" which was published in "*Nuclear Instruments and Methods in Physics Research Section B: Beam Interactions with Materials and Atoms*", volume 360 (2015) on pages 129-138 under the CC BY-NC-ND license (`http://creativecommons.org/licenses/by-nc-nd/4.0/`) is appended.

Nuclear Instruments and Methods in Physics Research B 360 (2015) 129–138

Contents lists available at ScienceDirect

Nuclear Instruments and Methods in Physics Research B

journal homepage: www.elsevier.com/locate/nimb

Quenching comparison of BGO and BSO for heavy ions

J. Tammen *, R. Elftmann, S.R. Kulkarni, S.I. Böttcher, R.F. Wimmer-Schweingruber

Institut für Experimentelle und Angewandte Physik, Universität Kiel, 24105 Kiel, Germany

ARTICLE INFO

Article history:
Received 3 June 2015
Received in revised form 24 July 2015
Accepted 27 July 2015

Keywords:
BGO
BSO
Scintillator non-linearity
Quenching

ABSTRACT

Scintillator non-linearity is an important parameter in calibration of scintillators, especially when measuring ions. Here we investigate the response of two scintillators, namely BGO ($Bi_4Ge_3O_{12}$) and BSO ($Bi_4Si_3O_{12}$), to different ions from helium to iron. We compare the scintillator output with the energy loss according to GEANT4 simulations and determine the quenching parameters for each ion species. BGO and BSO share the same crystalline structure but differ in one single component, therefore we also analyse differences in light output and non-linearity between the two scintillators caused by this similarity and present a model predicting these effects for heavy ions.

1. Introduction

Scintillators are commonly used to detect radiation. Quenching [1] introduces a non-linearity in the light output of scintillators which has to be considered during calibration of an instrument or detector. In the literature this phenomenon has often been investigated. There are measurements with electrons, X-rays and/or γ-rays [2–4] but only few publications for ions, and these focus on light ions [5] or lower energy ranges [6,7]. Nevertheless there is some data available for BGOs response to heavy ions [8]. All of those previously mentioned publications focus on stopping heavy ions while we also include penetrating ions in our study to extend the validity range of our model.

There are only few applications in which heavy ions are routinely measured. Consequently, there are only few measurements of the quenching of the light output of heavy ions. Nevertheless, in these applications, the knowledge of scintillation performance parameters is vital to achieve an accurate energy measurement with good resolution. With their high density scintillators provide high stopping power within a small volume, which can be further reduced when using a photodiode readout instead of photomultipliers. Small volume and the ensuring low packaging mass make scintillators very attractive for radiation measurements in space. For instance the Radiation Assessment Detector (RAD) [9] on NASA's Curiosity rover [10] uses a CsI scintillator.

In this paper we measure the response of Bismuth Germanate (BGO, $Bi_4Ge_3O_{12}$) and Bismuth Silicate (BSO, $Bi_4Si_3O_{12}$) to ions from helium to iron and compare those results with GEANT4 simulations of the expected energy deposition. BGO and BSO have the same crystal structure and differ only in one atom type which is Germanium for BGO and Silicon for BSO. This similarity becomes visible in the physical properties of both crystals where many parameters such as radiation length and peak emission/excitation are almost the same while the density differs by only 5% due to different atomic masses [11,12]. Considering this similarity we evaluate the effects it has on the scintillation parameters. We describe the experimental setup in Section 2, the simulations performed to estimate the quenching in Section 3 and the energy calibration in Section 4. Section 5 gives the experimental results which are discussed and interpreted in Section 7.

2. Experimental setup

The BSO crystal was bought from Molecular Technology (MolTech) GmbH and has a cubic shape with 2 cm edge length. The BGO crystal was bought from Eckhard Kruse Meechnik and has a hexagonal shape with 2 cm side length and 2 cm thickness. Both crystals were originally polished on all surfaces.

Two opposing sides of each crystal were roughened and a Hamamatsu photo diode S3590-19 was glued with Dow Corning DC93-500 space grade glue to each of these two sides. All other faces remained polished. After gluing the diodes both crystals were wrapped in two layers of nitrocellulose filter sheets (Millipore Corporation, 0.45 µm pore size, 140 µm thick) and two layers of PTFE (150 µm in total) to minimize light loss.

The experimental setup is illustrated in Fig. 1. For the BGO measurements two circular silicon passivated ion-implanted planar sil-

* Corresponding author.
E-mail address: tammen@physik.uni-kiel.de (J. Tammen).

http://dx.doi.org/10.1016/j.nimb.2015.07.127
0168-583X/

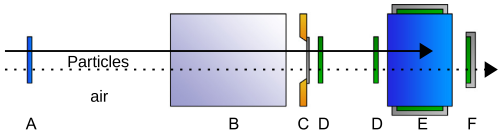

(a) BGO Setup with bare silicon detectors (D) as tracking detectors.

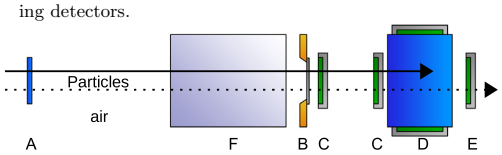

(b) BSO Setup with photodiodes with ceramic back (D) as tracking detectors.

Fig. 1. Experimental setup (not to scale). The main components are: (A) HIMAC beam monitor, (B) PET absorber, (C) entrance window covered with Al foil, (D) tracking detectors, (E) Crystal (blue) with two readout diodes (green) and (F) anticoincidence detector (photodiode). Stopping particles are marked with solid arrows and penetrating particles with dotted arrows. The gray areas around the photo diodes indicates their ceramic casings. (For interpretation of the references to color in this figure legend, the reader is referred to the web version of this article.)

icon detectors (Canberra, Belgium, ∅ 12 mm, 300 μm thickness) were placed in front of the crystal (shown in blue) at 5 mm and 45 mm distance from the crystal front. They serve as tracking detectors for the ion beam. In Fig. 1(a) they are indicated as green rectangles and labeled "D". One photo diode (Hamamatsu S3204) was placed behind the crystal acting as anticoincidence (labeled F). In the case of BSO (bottom label) two photodiodes (Hamamatsu S3590-19) were used as tracking detectors (D) and anticoincidence (F). In both configurations the scintillators were read out by photodiodes (labeled "E") and the detectors and crystals were put into light tight boxes with an entrance window covered by 50 μm thick aluminum foils (C). Each detector is connected to a charge sensitive preamplifier followed by two shapers (2.2 μs shaping time) with times 1 and times 16 gain, followed by two ADCs with FPGA readout at 3 MHz. From the ADC data the pulse-heights of all channels are reconstructed. A similar data-acquisition system is being developed for the Energetic Particle Detector (EPD) on the Solar Orbiter mission [13,14].

Heavy ion (He, C, O, Ne, Si and Fe) beams were provided by the Heavy Ion Medical Accelerator in Chiba (HIMAC) [15], Japan. We used the ions listed in Table 1 with a rate of 100–1000 ions/s for a duration of 15 minutes per datapoint. The energy of monoenergetic incident particles was reduced using polyethylene (PET) blocks with different thicknesses (Fig. 1B). All absorber thicknesses are listed in Table 1. A scintillator for controlling particle flux was positioned 5 cm behind the beam exit window with varying thicknesses of 50 μm (C, O, Si, Ne, Fe) and 3 mm (He) (Fig. 1A). The distance between beam exit and the instrument entrance window was 80 cm in air.

3. Simulation setup

We performed simulations of all combinations of ions, beam energies and absorber thicknesses listed in Table 1 using GEANT4 toolkit version 10.0.1 [16,17]. BSO and BGO densities were taken as 6.80 g cm^{-3} and 7.13 g cm^{-3} respectively [11]. The density of our absorber was set to 0.96 g cm^{-3} since the measured density of polyethylene in the experiment was 0.959 ± 0.003 g cm^{-3}. For the density of the ceramic backs of the BSO tracking diode we used a simple aluminum oxide based ceramic with a density of 3.9 g cm^{-3}. Consistency between simulations and experiment was checked using the anticoincidence detector signal with barely stopping and barely penetrating ions. Both showed a good agreement of simulations and experiment.

4. Energy calibration

Energy calibration was performed in an iterative way. In a first step we simulated the energy deposit of cosmic muons in the scintillators and assumed that quenching is negligible for these. This seems reasonable to us since electrons [18] and protons [5,19] are commonly used as references when calculating quenching parameters. Subsequently we verified that penetrating secondary protons from fragmentation inside the polyethylene absorber were in good agreement with this calibration after which they were added as additional calibration points. This procedure was repeated with penetrating helium ions without any absorber. As one can see in Fig. 2 this method leads to good calibration curves for both crystals confirming the assumption of negligible quenching for penetrating protons and helium. The silicon detectors were calibrated using the same procedure and the same datapoints.

5. Experimental results

Fig. 4 shows selected data points of simulated (left) and calibrated experimental data (right) for carbon ions in the BGO crystal. E_{Si} and $E_{Crystal}$ denote the calibrated energy deposit in the first tracking detector (Si) and in the Crystal. The simulated energy deposit in the tracking detector agrees very well with the experimental values while the energy measured in the scintillators is reduced by the quenching effect when compared to the simulated values. As the ion energy approaches the Bragg peak, the measured energy is approximately 45% lower than the simulated energy deposit. We fitted the position of each peak individually using a

Table 1
List of primary ions with their energies and thicknesses of polyethylene absorber.

Ion	Energy/MeV/nuc	Absorber thicknesses/mm	
		BGO	BSO
He	100	0, 30, 60	
	230	0, 151, 222, 234, 243, 244, 249, 252, 253, 264, 272, 283, 284, 304.5, 314, 314.5	0, 151, 202, 224, 243, 244, 247, 253, 263, 269, 283, 289, 303, 309.5, 314.5
C	400	0, 151, 171, 171.5, 181.5, 191.5, 196.5, 201, 211.5, 215, 224, 245, 249, 259	0, 101, 151.5, 214, 224, 244, 196.5
O	400	0, 40, 60, 80, 103, 117, 126, 130, 146, 150, 166, 180	0, 51, 81, 111, 121, 131, 152, 172
Ne	600	0, 151, 176, 214, 224, 229, 239, 250, 259, 270.5, 279	0, 151, 196.5, 214, 224, 229, 239, 259, 269, 279, 289, 292
Si	600	0, 40, 60, 120, 160, 180, 190	
	800	0, 121, 201.5, 249, 259, 269, 289, 304.5	0, 214, 254, 259, 279, 294.5, 304.5, 319.5
Fe	500	18, 28, 30, 35, 40, 45, 55, 65, 70	0, 5, 8, 13, 18, 28

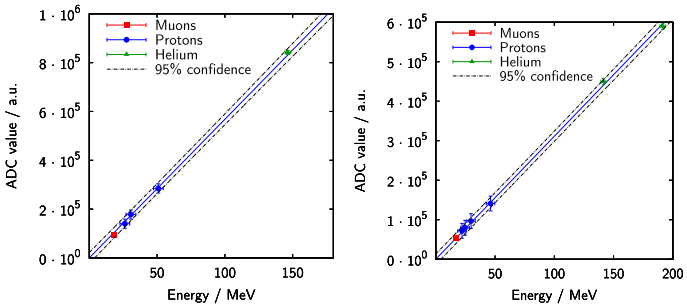

Fig. 2. Calibration for BGO (a) and BSO (b) crystals with 95% confidence interval calculated from the present datapoints.

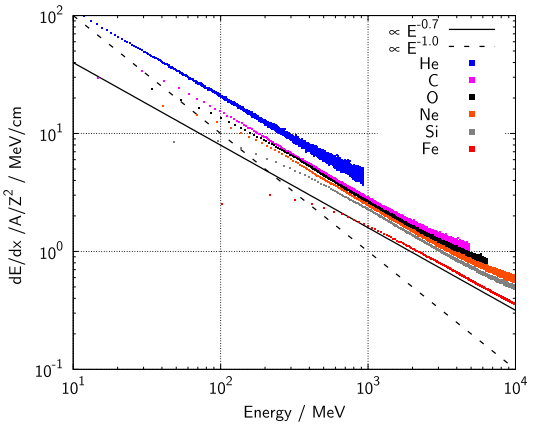

Fig. 3. Simulation of energy loss per path length versus total Energy of particle for different ion species (dots) in BGO. The solid line represents a function which is proportional to $E^{-0.7}$ and the dashed one a function which is proportional to E^{-1}.

rotated two-dimensional Gaussian function with two independent values for σ_{Silicon} and σ_{Crystal}. We compare the resulting peak positions for measurement and simulation in Fig. 5. These peak positions correspond to the measured (simulated) energy deposits in the two crystals, BGO and BSO. The measured energy deposits (in MeV/nuc) are plotted vs. simulated energy deposit in red symbols for BGO and blue for BSO. Ions having enough energy to penetrate through the crystals and trigger the anticoincidence are plotted as triangles while particles stopping in the crystals are plotted as squares.

A simple approximation for the curves of stopping particles can be derived assuming Birks-like quenching [1]. In this case the light output, dL, per unit length, dx, can be described as

$$\frac{dL}{dx} = \frac{S\frac{dE}{dx}}{1 + KB\frac{dE}{dx}} \tag{1}$$

where S describes the efficiency for converting the energy deposited per unit length into scintillation photons, $B \cdot \frac{dE}{dx}$ describes the probability to create defects along the particle's path and K is the trapping probability inside a defect compared to "normal" radiative

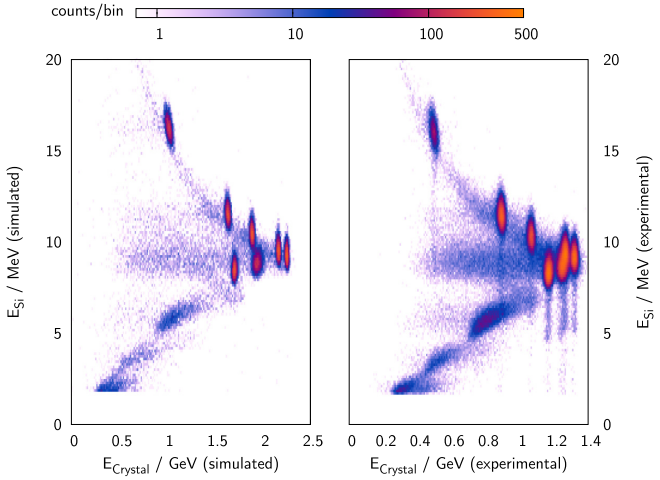

Fig. 4. E_{Si} vs. E_{Crystal} intensity map for simulation (left) and experiment (right) for BGO crystal and carbon ions. Counts are not normalized and experimental data includes electronics noise. Trigger levels for the experiment were set to ≈1.5 MeV for tracking detectors.

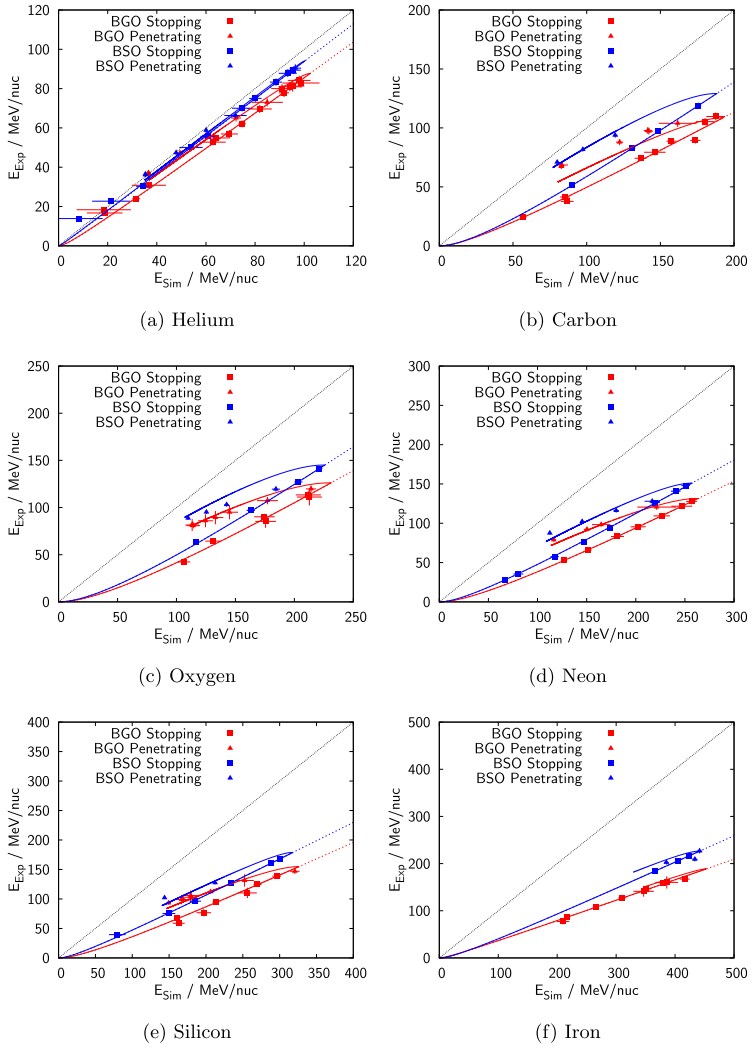

(a) Helium (b) Carbon

(c) Oxygen (d) Neon

(e) Silicon (f) Iron

Fig. 5. Light yields for all six ions with fits of analytical light curve Eq. (3) to stopping particles (dashed lines). Numerical solution of Eq. (3) including stopping particles in 2 cm of crystal material (solid line). Particles without any quenching are expected to lie on the diagonal black dotted line with a slope of 1.

recombination. For energies well below the minimally ionizing values, the energy loss $\frac{dE}{dx}$, is often approximated as [20]

$$\frac{dE}{dx} \approx \frac{C \cdot AZ^2}{E}, \tag{2}$$

which allows one to determine an analytical expression for the integral:

$$L(E,A,Z) = \int dL = \int_0^{x_{max}} dx \frac{S\frac{dE}{dx}}{1 + KB\frac{dE}{dx}}$$
$$= f_1 \cdot \left(E - f_2 \cdot AZ^2 \cdot \log\left(\frac{E + f_2 \cdot AZ^2}{f_2 \cdot AZ^2} \right) \right) \tag{3}$$

For ions stopping inside the scintillator [5] x_{max} is the range inside the crystal.

$$f_1 = S \tag{4}$$

is a measure of the energy to light conversion efficiency for a specific ion while

$$f_2 = C \cdot KB \tag{5}$$

describes the probability for quenching of charge carriers. Fitting Eq. (3) to the datapoints of stopping ions (squares in Fig. 5) leads to the dashed lines in Fig. 5. These lines are thus the calibration curves for BGO and BSO for the various ions indicated beneath.

Although Eq. (2) is a commonly used approximation which leads to an analytically solvable equation, we found that the energy loss in the particular energy range covered in this paper is better described by (see also Fig. 3):

Table 2
Fit results for the analytical solution (Eq. (3)) for stopping particles (left half) and for the numerical fit of Eq. (1) for the same datapoints (right half).

Ion	Crystal	Analytical solution		Numerical solution	
		$\frac{dE}{dX} \propto E^{-1}$		$\frac{dE}{dX} \propto E^{-1}$	
		f1/a.u.	f2/MeV	f1/a.u	f2/MeV
He	BGO	0.921 ± 0.022	0.434 ± 0.143	0.916 ± 0.025	0.397 ± 0.162
	BSO	0.957 ± 0.026	0.083 ± 0.112	0.952 ± 0.025	0.055 ± 0.099
C	BGO	0.700 ± 0.060	0.384 ± 0.168	0.698 ± 0.060	0.379 ± 0.167
	BSO	0.907 ± 0.007	0.535 ± 0.017	0.908 ± 0.007	0.539 ± 0.017
O	BGO	0.790 ± 0.119	0.551 ± 0.267	0.790 ± 0.119	0.551 ± 0.267
	BSO	0.913 ± 0.043	0.502 ± 0.094	0.914 ± 0.043	0.505 ± 0.094
Ne	BGO	0.663 ± 0.008	0.276 ± 0.014	0.662 ± 0.009	0.274 ± 0.015
	BSO	0.733 ± 0.009	0.191 ± 0.010	0.731 ± 0.010	0.188 ± 0.010
Si	BGO	0.589 ± 0.062	0.120 ± 0.062	0.590 ± 0.062	0.120 ± 0.062
	BSO	0.641 ± 0.017	0.059 ± 0.014	0.642 ± 0.017	0.060 ± 0.014
Fe	BGO	0.442 ± 0.020	0.009 ± 0.006	0.442 ± 0.020	0.009 ± 0.006
	BSO	0.578 ± 0.005	0.021 ± 0.002	0.578 ± 0.005	0.021 ± 0.002

Table 3
Fit results for the numerical solution of Eq. (3) in combination with Eq. (2) $\left(\frac{dE}{dX} \propto E^{-1}\right)$ and (6) $\left(\frac{dE}{dX} \propto E^{-0.7}\right)$ for stopping and penetrating particles.

Ion	Crystal	Numerical solution, added penetrating ions			
		$\frac{dE}{dX} \propto E^{-1}$		$\frac{dE}{dX} \propto E^{-0.7}$	
		f1/a.u.	f2/MeV	f1/a.u	f2/MeV
He	BGO	1.002 ± 0.013	1.052 ± 0.144	1.043 ± 0.014	0.372 ± 0.039
	BSO	1.007 ± 0.010	0.347 ± 0.083	1.024 ± 0.011	0.137 ± 0.026
C	BGO	0.868 ± 0.023	0.902 ± 0.103	0.995 ± 0.031	0.185 ± 0.018
	BSO	0.912 ± 0.016	0.555 ± 0.054	0.996 ± 0.017	0.113 ± 0.008
O	BGO	0.793 ± 0.015	0.600 ± 0.053	0.902 ± 0.021	0.104 ± 0.008
	BSO	0.833 ± 0.031	0.379 ± 0.099	0.914 ± 0.042	0.066 ± 0.014
Ne	BGO	0.699 ± 0.010	0.337 ± 0.022	0.774 ± 0.009	0.053 ± 0.002
	BSO	0.761 ± 0.018	0.225 ± 0.026	0.841 ± 0.019	0.041 ± 0.003
Si	BGO	0.626 ± 0.012	0.164 ± 0.018	0.679 ± 0.015	0.022 ± 0.002
	BSO	0.691 ± 0.025	0.107 ± 0.029	0.733 ± 0.029	0.015 ± 0.003
Fe	BGO	0.442 ± 0.020	0.009 ± 0.006	0.452 ± 0.027	0.001 ± 0.001
	BSO	0.507 ± 0.013	0.000 ± 0.001	0.514 ± 0.032	0.000 ± 0.001

$$\frac{dE}{dx} \approx \frac{C \cdot AZ^2}{E^{0.7}}. \tag{6}$$

Using this expression for $\frac{dE}{dx}$ in Eq. (1) leads to an integral (3) which cannot be solved analytically. Therefore, we solved (3) numerically. To check the validity of this treatment, we also numerically integrated (3) for $\frac{dE}{dx}$ given by Eq. (2). We then fitted the constants f_1 and f_2 to the data for the analytical and both numerical solutions. Tables 2 and 3 list the resulting fitting parameters which are also plotted in Figs. 6 and 7. Figs. 6(a) and 7(a) show the results listed in Table 2. There we compare our analytical solution (Eq. (3)) with the numerically integrated Eq. (2). The two should ideally be the same. One can see that both fits agree very well within their errorbars. This assures us that our numerical solution is accurate enough for our purposes. For this comparison we limited our dataset to stopping ions. Stopping means that the ion does not have enough energy to penetrate through the scintillating crystal and does not trigger the anticoincidence. The limitation to stopping ions has the advantage that we can set one limits of the integration (Eq. (3)) to zero. Otherwise we would need to use the calculated stopping energy as integration limit which would possibly decrease the accuracy of our result.

The results in Table 3 correspond to the curves in Figs. 6(b) and 7(b). These results are obtained by using all datapoints of stopping and penetrating particles and numerically integrating Eqs. (2) and (6). In the following Section 5.1 we describe in detail how our errors were estimated and thereafter we discuss our results in Section 7.

5.1. Error estimation

The two dominant sources of uncertainties are the energy calibration and the thickness and density of the PET energy absorbers. The first error can be directly calculated from the confidence interval of our calibration. The second uncertainty was estimated by varying the absorber thickness in the simulation and comparing the values of the energy depositions in the tracking detectors.

The absorber thickness, d, in our simulations was varied around the measured value of the absorber, d_0, until the simulated and experimental energy deposits in the tracking detectors were equal

$$E_{\mathrm{Si,sim}}(d) = E_{\mathrm{Si,exp}}(d_0). \tag{7}$$

The resulting simulated crystal energy at modified thickness $E_{\mathrm{Crystal,sim}}(d)$ was then compared to the simulated energy at measured thickness $E_{\mathrm{Crystal,sim}}(d_0)$. The difference between those two values should then be a measure for the uncertainty due to possible variations in effective material thickness. For the uppermost peak in Fig. 4 (at $E_{\mathrm{Crystal,exp}} = 500$ MeV and $E_{\mathrm{Si,exp}} = 16$ MeV) this leads to an error of 2%. This procedure also covers alignment errors for the absorber since a possible small tilt angle would result in a slightly thicker effective absorber.

The absorber thickness error yields greater uncertainties the lower the energy of the incident particle is because the high non-linearity of the energy loss near the Bragg-peak results in large differences due to small variations in the absorber thickness. This leads to larger error bars for stopping ions with low energies. The effect can especially been seen in Fig. 5(a) where the four data

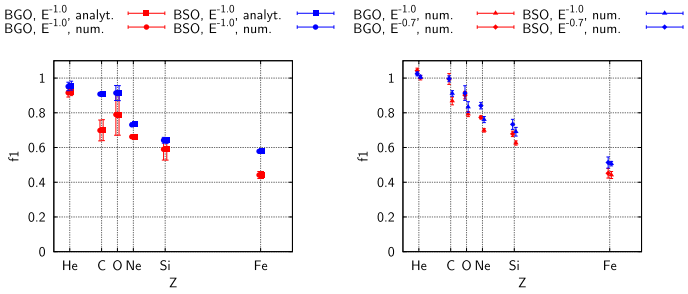

(a) f_1 parameter obtained through fits to all datapoints of only stopping ions for analytical (squares) and numerical (points) solution.

(b) f_1 parameter obtained through fits to all datapoints of stopping and penetrating ions for numerical evaluation with different exponents of -1 (equation (2)) and -0.7 (equation (6)).

Fig. 6. Fit results for f_1 parameter for BGO (red) and BSO (blue). (For interpretation of the references to color in this figure legend, the reader is referred to the web version of this article.)

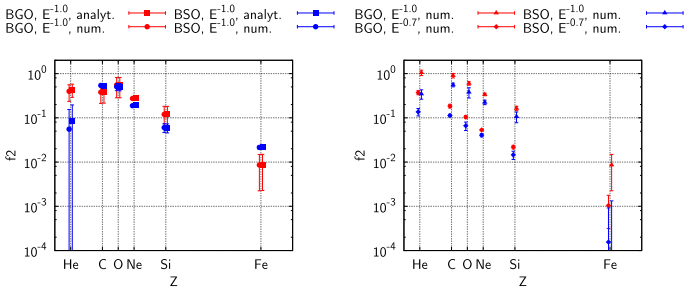

(a) f_2 parameter obtained through fits to all datapoints of only stopping ions for analytical (squares) and numerical (points) solution.

(b) f_2 parameter obtained through fits to all datapoints of stopping and penetrating ions for numerical evaluation with different exponents of -1 (equation (2)) and -0.7 (equation (6)).

Fig. 7. Fit results for f_2 parameter for BGO (red) and BSO (blue). (For interpretation of the references to color in this figure legend, the reader is referred to the web version of this article.)

points of helium with the lowest energy for both crystal types differ a lot from the calculated light yield curve and they partly lie above $f(E) = E$ which is unphysical. The estimated energy error for these points is 60%, assuming 2% uncertainty for the absorber thickness. Nevertheless this error non-linearity only affects very low energy stopping particles and is included in the error bars plotted in Fig. 5.

6. Model for parameterization of BGO and BSO quenching

We developed a simple model to describe the scintillation properties of BGO and BSO for heavy ions. It predicts the values for f_1 and f_2 for different heavy ion species using a limited number of parameters. We plan to verify this model by testing BGO with other heavy ion species in the future. The model uses the following two functions

$$f_1(Z) = \min(I_1, A_1 \cdot \exp(-\lambda_1 \cdot Z + O_1)) \quad (8)$$

and

$$f_2(Z) = I_2 \cdot \exp(-\lambda_2 \cdot Z) \quad (9)$$

to describe the dependence of f_1 and f_2 on Z. Both functions are fitted to the individual results of f_1 and f_2 as determined in the previous sections for the numerical solution with $\frac{dE}{dx} \propto E^{-0.7}$ (data with blue and red diamonds in Figs. 6(b) and 7(b)). The helium data was omitted for the f_2 parameter because the helium datapoints which determine the f_2 parameter have large uncertainties (see Fig. 5(a) in the low energy region below 30 MeV/nuc). The resulting parameter values for both crystal types (BGO, BSO) are listed in Table 4 and the corresponding functions are plotted in Fig. 8 as solid lines.

The quality of this remarkably simple model can be seen in Fig. 9 which shows the same data as in Fig. 5 but now with the

Table 4
Fit results for Eqs. (8) and (9) to the data of Figs. 6 and 7(b).

	BGO	BSO
I_1	1.043 ± 0.121	1.024 ± 0.052
A_1	1.109 ± 0.077	0.978 ± 0.014
λ_1	0.089 ± 0.021	0.062 ± 0.004
O_1	0.344 ± 0.071	0.321 ± 0.026
I_2	0.851 ± 0.203	0.543 ± 0.034
λ_2	0.272 ± 0.024	0.261 ± 0.008

addition of dashed curves which show the quenching curves predicted by our model using the values in Table 4. In contrast, the solid lines describe the best individual fit for each ion/crystal combination of the numerically solved Eq. (1) with the approximation of Eq. (6) using all datapoints (stopping and penetrating ions).

The energy-to-light curve described by our model follows those of the individual fits with almost no deviation for oxygen and heavier ions. Small deviations can be seen for carbon but the model still describes the measured data very well within the errors of the individual datapoints and might also be taken as good approximation for this ion species. For helium the larger deviations are caused by the fact that the helium data was excluded from our model for the f_2 parameter. Overall the model describes the energy-to-light conversion ratio for both BGO and BSO crystals in this particular energy range from a few MeV/nucto approximately 100 MeV/nuc very well within the errors of the experimental results.

6.1. Implications for the Birks constant, KB

Using our model for parameter f_2 from Eq. (9) and combining it with Eq. (5) leads to an expression for the Birks constant:

$$KB = \frac{f_2(Z)}{C(Z)} \tag{10}$$

where C originates from Eq. (6) and can be estimated from Fig. 3 for BGO and in the same way for BSO which is not shown here. Fig. 10 shows the quotient of the modeling function (9) and the C parameter as a function of particle Z value. This is the value for the Birks constant for different types of ions. Helium data is again excluded before fitting the exponential decay

$$KB(Z) = A \cdot \exp(-B \cdot Z) \tag{11}$$

to the data points since the it was shown in the previous section that the model fails in describing the helium behavior. Nevertheless the calculated data points for helium are plotted and the fit results are shown in Table 5. It can be seen that all data points except the ones of helium are well described by an exponential law, the helium data points follow the same trend, but differ from their expected values when compared to the other ion species.

7. Discussion and conclusions

Scintillators are used in many applications and an accurate knowledge of their light output is required for any quantitative analysis. In principle, one would need to calibrate every detector with all expected ion species, which is unrealistic. Here we presented a model which predicts the quenching properties of BGO and BSO which has been fitted to calibration data for He, C, O, Ne, Si, and Fe. It does not predict the absolute light yield of BGO and BSO which differs by approximately a factor of 5 [11], but the relative behavior of the two scintillators and various heavy ions. It is required to pass through zero light output for vanishing incident energy, and shows an asymptotically linear behavior which is superimposed by a non-linear one at low energies for stopping ions. The light output shows the opposite behavior for penetrating ions. We investigate the non-linear nature of the light output and have "calibrated out" this overall factor ~5 by using muons, protons, and one high-energy He data point for which a linear behavior and no quenching is expected. Thus, this factor ~5 is not reflected in our f_1 parameter which describes the energy to light conversion efficiency. With the use of calibrated data we also exclude any influence of the crystal geometry to affect our analysis. Therefore the observed difference in the linear regime (f_1), between BGO and BSO is real.

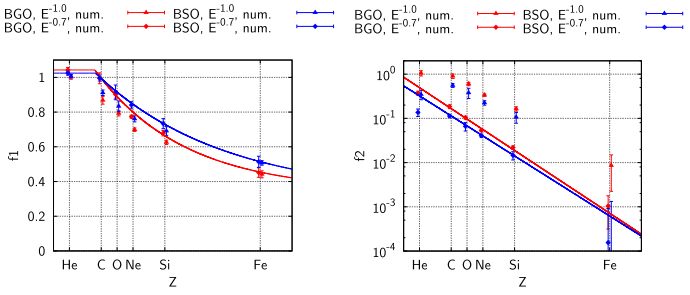

(a) f_1 parameter obtained through fits to all datapoints of stopping and penetrating ions for numerical evaluation with different exponents of -1 (triangles) and -0.7 (diamonds). Solid lines represent model function (8) with best fit to the individual points.

(b) f_2 parameter obtained through fits to all datapoints of stopping and penetrating ions for numerical evaluation with different exponents of -1 (triangles) and -0.7 (diamonds). Solid lines represent model function (9) with best fit to the individual points.

Fig. 8. Fit results for the model functions (8) and (9) to the individual parameters f_1 and f_2 for BGO (red) and BSO (blue). (For interpretation of the references to color in this figure legend, the reader is referred to the web version of this article.)

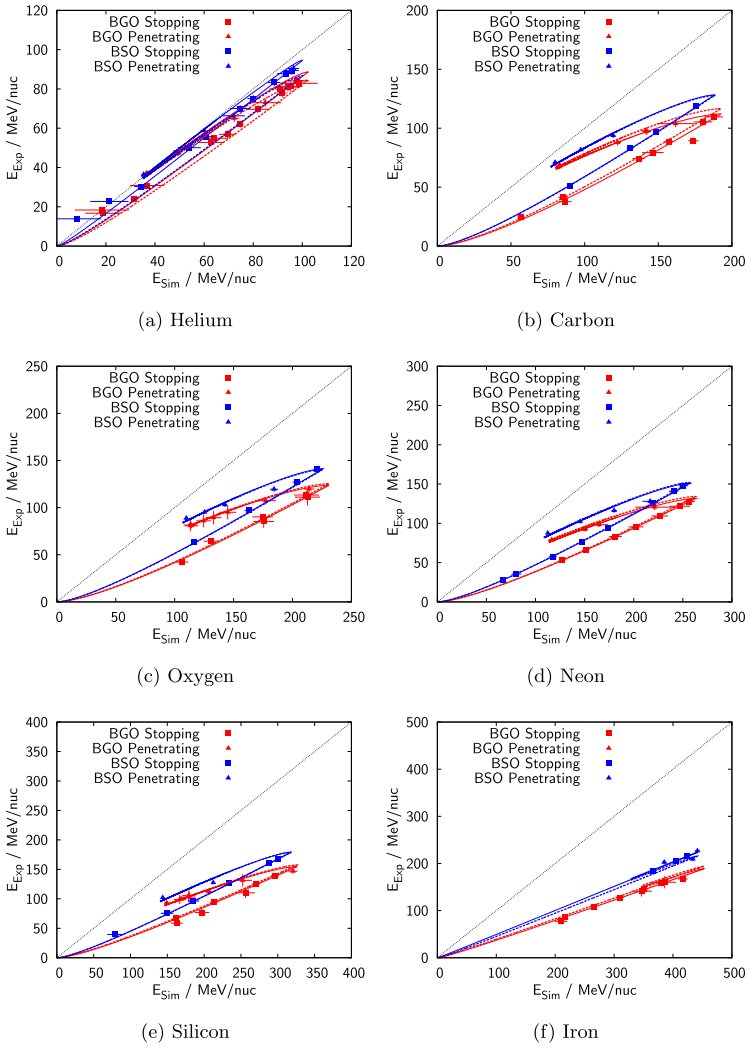

Fig. 9. Data from measurement (squares/triangles) for both BGO (red) and BSO (blue) together with the best individual fit for each ion species (solid lines) and the model described in Section 6 (dashed lines). (For interpretation of the references to color in this figure legend, the reader is referred to the web version of this article.)

A key finding is that the energy loss suffered by heavy ions in this energy range is better described by $E^{-0.7}$ than by the conventionally used $E^{-1.0}$. Using this expression for the energy loss, we find that both crystals qualitatively show the same behavior for f_1 and f_2. For f_1 it looks like a step function with a plateau up to carbon ($Z = 6$) which is followed by an exponential decrease towards heavier ions ($Z \gtrsim 14$). The f_2 parameter also shows an exponential behavior for BGO as well as BSO, but requires a separate treatment of He. The decay constant λ_2 is very similar for the two scintillators. The f_2 parameter is mainly responsible for the curvature of the light yield in the lower energy range, so its value may also be affected by the small number of data points and by larger uncertainties in this region which is particularly true for the helium datapoints (see Section 5.1) making it hard to derive the exact shape in this region. The large uncertainties for helium might also be a reason why our model describes the performance of other ions very precisely with one set of parameters while the helium data needs to be treated separately. Other (doped) scintillators [21] may be described with a single set of parameters, including helium, using also a Birks like approach. However, this might still be a scintillator specific property of BGO and BSO.

The f_1 parameter is comparable to the slope of the models used to describe the BGO behavior in other publications [8,7]. There the slope is found to be linear with $\log(AZ^2)$ for similar ions and energies. In the particular Z-range investigated here our curve for the f_1 parameter may also be described by a linear dependence with $\log(AZ^2)$ within the estimated errors, excluding our helium datapoints.

On the other hand, our f_2 parameter is not comparable to the intercept used in those models [8]. Especially in the low-energy

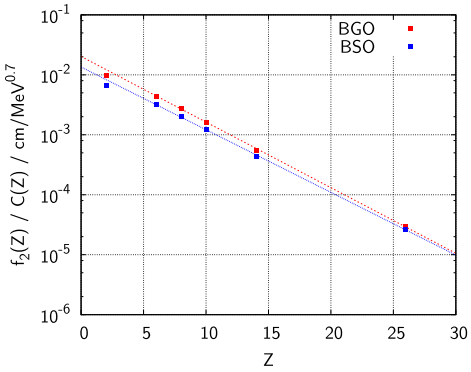

Fig. 10. Calculated values for Birks constant *KB* as a function of *Z* (squares).

range the intercept implies a cut-off energy below which the light output reaches zero. Low energy data [7] shows a steady decrease without a cut-off. Our model provides such a steady decrease and light output converges to zero when particle energy is diminished. It is for this reason that we believe that our model to describes the scintillator response better than others.

One can see that the fit parameters change slightly when adding additional data points from penetrating ions, but those changes can still be explained within their uncertainties. In contrast to that the choice of E^{-1} or $E^{-0.7}$ is affects the absolute values of f_2 considerably, as can be seen in Fig. 7(b).

It is noticeable that f_1 of BGO lies systematically below the one of BSO and vice versa for the f_2 parameter. This causes the linear portion of the BGO light curves (see Fig. 5) to be flatter than those of BSO. A perfect scintillator with linear energy-to-light conversion would follow the black dashed line in Fig. 5. BSO therefore, despite his lower absolute light output, is closer to the optimal linear light-to-energy relation than BGO.

8. Summary

We measured the response of BGO and BSO to He, C, O, Ne, Si and Fe ions in the energy range of several tens to hundreds MeV/nuc with a dual photodiode readout system designed for space applications and compared those measurements with GEANT4 simulations. We showed that the very simple Birks-like approach which describes quenching inside an inorganic crystal can be used as a first approximation to describe light yields of heavy ions in both scintillators. We also showed that the choice how to approximate the energy loss $\frac{dE}{dx} \propto E^{-1}$ or $\frac{dE}{dx} \propto E^{-0.7}$ has a strong impact on the calculated light yield parameters. We found that the latter choice ($E^{-0.7}$) better describes our data. The two different crystal types, BGO and BSO, behaved qualitatively in a very similar way as one would expect based on their identical crystalline structure. Nevertheless the nonlinearity in their light output differs quantitatively by a few percent up to a few ten percent depending on the incident ions. We presented a simple model which predicts the quenching properties of these scintillators with remarkable accuracy for heavy ions ($Z \leqq 6$). Future tests with additional ions species will allow us to verify and possibly refine the model.

Table 5
Fit results for Eq. (11) as seen in Fig. 10.

	BGO	BSO
A	0.022 ± 0.001	0.013 ± 0.001
B	0.252 ± 0.006	0.241 ± 0.006

Acknowledgments

We would thank the NIRS-HIMAC team, especially Yukio Uchihori and Hisashi Kitamura, for the opportunity to perform research with their accelerator, and their Accelerator Engineering Corporation (AEC) for smooth beam times. This work was supported by Grant 50 OT 1202 from the German Space Agency (DLR).

References

[1] J.B. Birks, Scintillations from organic crystals: specific fluorescence and relative response to different radiations, Proc. Phys. Soc. Sect. A 64 (10) (1951) 874–877, http://dx.doi.org/10.1088/0370-1298/64/10/303. <http://stacks.iop.org/0370-1298/64/i=10/a=303?key=crossref.f6127795b0efda6211aab9d5c1b9ae31>.
[2] A. Nassalski, M. Moszyn, T. Szcze, Non-proportionality of organic scintillators and BGO, IEEE Trans. Nucl. Sci. 55 (3) (2008) 1069–1072.
[3] M. Balcerzyk, M. Moszynski, M. Kapusta, D. Wolski, J. Pawelke, C.L. Melcher, YSO, LSO, GSO and LGSO. A Study of Energy Resolution and Nonproportionality, 47 (4) (2000) 1319–1323.
[4] G. Hull, W.S. Choong, W.W. Moses, G. Bizarri, J.D. Valentine, S.a. Payne, N.J. Cherepy, B.W. Reutter, Measurements of NaI(Tl) electron response: comparison of different samples, IEEE Trans. Nucl. Sci. 56 (1) (2009) 331–336, http://dx.doi.org/10.1109/TNS.2008.2009876.
[5] V. Avdeichikov, L. Bergholt, M. Guttormsen, J. Taylor, L. Westerberg, B. Jakobsson, W. Klamra, Y.A. Murin, Light output and energy resolution of CsI, YAG, GSO, BGO and LSO scintillators for light ions, Nucl. Inst. Meth. Phys. Res. A 349 (1994) 216–224.
[6] E. Valtonen, J. Peltonen, J.J. Torsti, Response of BGO and CsI(Tl) scintillators to heavy ions, Nucl. Inst. Meth. Phys. Res. A 286 (1990) 169–174.
[7] Z. Dlouhy, A. Kugler, L. Nosek, J. Svanda, V. Wagner, R. Anne, C. Borcea, A. Kordyasz, M. Lewitowicz, M. Saint-Laurent, R. Bimbot, V. Borrel, S. Dogny, D. Guillemaud-Mueller, A. Mueller, F. Pougheon, S. Lukyanov, Y. Penionzhkevich, The response of BGO scintillation detectors to light charged nuclei, Nucl. Inst. Meth. Phys. Res. A 317 (317) (1992) 604–606.
[8] N. Matsufuji, T. Kanai, H. Komami, T. Kohno, The response of a BGO scintillator to relativistic heavy ions, Nucl. Inst. Meth. Phys. Res., Sect. A: Accel., Spectrometers, Detectors Assoc. Equip. 430 (1) (1999) 60–68, http://dx.doi.org/10.1016/S0168-9002(99)00180-1.
[9] D.M. Hassler, C. Zeitlin, R.F. Wimmer-Schweingruber, S. Böttcher, C. Martin, J. Andrews, E. Böhm, D.E. Brinza, M.a. Bullock, S. Burmeister, B. Ehresmann, M. Epperly, D. Grinspoon, J. Köhler, O. Kortmann, K. Neal, J. Peterson, a. Posner, S. Rafkin, L. Seimetz, K.D. Smith, Y. Tyler, G. Weigle, G. Reitz, F.a. Cucinotta, The radiation assessment detector (RAD) investigation, in: Space Sci. Rev. 170 (1-4) (2012) 503–558, http://dx.doi.org/10.1007/s11214-012-9913-1.
[10] J.P. Grotzinger, J. Crisp, A.R. Vasavada, R.C. Anderson, C.J. Baker, R. Barry, D.F. Blake, P. Conrad, K.S. Edgett, B. Ferdowski, R. Gellert, J.B. Gilbert, M. Golombek, J. Gómez-Elvira, D.M. Hassler, L. Jandura, M. Litvak, P. Mahaffy, J. Maki, M. Meyer, M.C. Malin, I. Mitrofanov, J.J. Simmonds, D. Vaniman, R.V. Welch, R.C. Wiens, Mars science laboratory mission and science investigation, Space Sci. Rev. 170 (1–4) (2012) 5–56, http://dx.doi.org/10.1007/s11214-012-9892-2.
[11] M. Ishii, K. Harada, Y. Hirose, N. Senguttuvan, M. Kobayashi, I. Yamaga, H. Ueno, K. Miwa, F. Shiji, F. Yiting, M. Nikl, X. Feng, Development of BSO ($Bi_4Si_3O_{12}$) crystal for radiation detector, Opt. Mater. 19 (2002) 201–212.
[12] M. Lalic, S. Souza, The first-principles study of electronic and optical properties of BGO and BSO scintillators, Opt. Mater. 30 (7) (2008) 1189–1192, http://dx.doi.org/10.1016/j.optmat.2007.05.046. <http://linkinghub.elsevier.com/retrieve/pii/S0925346707001917>.
[13] E. Marsch, R. Marsden, R. Harrison, R. Wimmer-Schweingruber, B. Fleck, Solar orbitermission profile, main goals and present status, Adv. Space Res. 36 (8) (2005) 1360–1366, http://dx.doi.org/10.1016/j.asr.2004.11.012. <http://linkinghub.elsevier.com/retrieve/pii/S0273117704008701>.
[14] R. Marsden, B. Fleck, The solar orbiter mission, Adv. Space Res. 32 (12) (2003) 2699–2704, http://dx.doi.org/10.1016/j.asr.2003.01.003. <http://linkinghub.elsevier.com/retrieve/pii/S0273117703800868>.
[15] K. Sato, K. Endo, M. Endo, T. Hattori, A. Itano, T. Kanai, M. Kanazawa, K. Kawachi, T. Kohno, S. Matsumoto, Y. Miyazawa, A. Noda, K. Noda, H. Ogawa, Y. Sato, F. Soga, H. Suzuki, S.-I. Watanabe, S. Yamada, T. Yamada, Y. Hirao, Heavy ion medical accelerator in Chiba (HIMAC), Part. Accel. 33 (1990) 147–152.
[16] S. Agostinelli, J. Allison, K. Amako, J. Apostolakis, H. Araujo, P. Arce, M. Asai, D. Axen, S. Banerjee, G. Barrand, F. Behner, L. Bellagamba, J. Boudreau, L. Broglia, a. Brunengo, H. Burkhardt, S. Chauvie, J. Chuma, R. Chytracek, G. Cooperman, G. Cosmo, P. Degtyarenko, a. Dell'Acqua, G. Depaola, D. Dietrich, R. Enami, a. Feliciello, C. Ferguson, H. Fesefeldt, G. Folger, F. Foppiano, a. Forti, S. Garelli, S. Giani, R. Giannitrapani, D. Gibin, J. Gómez Cadenas, I. González, G. Gracia Abril, G. Greeniaus, W. Greiner, V. Grichine, a. Grossheim, S. Guatelli, P. Gumplinger, R. Hamatsu, K. Hashimoto, H. Hasui, a. Heikkinen, a. Howard, V. Ivanchenko, a. Johnson, F. Jones, J. Kallenbach, N. Kanaya, M. Kawabata, Y. Kawabata, M.

Kawaguti, S. Kelner, P. Kent, a. Kimura, T. Kodama, R. Kokoulin, M. Kossov, H. Kurashige, E. Lamanna, T. Lampén, V. Lara, V. Lefebure, F. Lei, M. Liendl, W. Lockman, F. Longo, S. Magni, M. Maire, E. Medernach, K. Minamimoto, P. Mora de Freitas, Y. Morita, K. Murakami, M. Nagamatu, R. Nartallo, P. Nieminen, T. Nishimura, K. Ohtsubo, M. Okamura, S. O'Neale, Y. Oohata, K. Paech, J. Perl, a. Pfeiffer, M. Pia, F. Ranjard, a. Rybin, S. Sadilov, E. Di Salvo, G. Santin, T. Sasaki, N. Savvas, Y. Sawada, S. Scherer, S. Sei, V. Sirotenko, D. Smith, N. Starkov, H. Stoecker, J. Sulkimo, M. Takahata, S. Tanaka, E. Tcherniaev, E. Safai Tehrani, M. Tropeano, P. Truscott, H. Uno, L. Urban, P. Urban, M. Verderi, a. Walkden, W. Wander, H. Weber, J. Wellisch, T. Wenaus, D. Williams, D. Wright, T. Yamada, H. Yoshida, D. Zschiesche, Geant4a simulation toolkit, Nucl. Inst. Meth. Phys. Res. Sect. A: Accel., Spectrometers, Detectors Assoc. Equip. 506(3), 2003, pp. 250–303. doi:10.1016/S0168-9002(03)01368-8. <http://linkinghub.elsevier.com/retrieve/pii/S0168900203013688>.

[17] J. Allison, K. Amako, J. Apostolakis, H. Araujo, P.A. Dubois, M. Asai, G. Barrand, R. Capra, S. Chauvie, R. Chytracek, G.A.P. Cirrone, G. Cooperman, G. Cosmo, G. Cuttone, G.G. Daquino, M. Donszelmann, M. Dressel, G. Folger, F. Foppiano, J. Generowicz, V. Grichine, S. Guatelli, P. Gumplinger, A. Heikkinen, I. Hrivnacova, A. Howard, S. Incerti, V. Ivanchenko, T. Johnson, F. Jones, T. Koi, R. Kokoulin, M. Kossov, H. Kurashige, V. Lara, S. Larsson, F. Lei, O. Link, F. Longo, M. Maire, A. Mantero, B. Mascialino, I. Mclaren, P.M. Lorenzo, K. Minamimoto, K. Murakami, P. Nieminen, L. Pandola, S. Parlati, L. Peralta, J. Perl, A. Pfeiffer, M.G. Pia, A. Ribon, P. Rodrigues, G. Russo, S. Sadilov, G. Santin, T. Sasaki, D. Smith, N. Starkov, S. Tanaka, E. Tcherniaev, B. Tomé, A. Trindade, P. Truscott, L. Urban, M. Verderi, A. Walkden, J.P. Wellisch, D.C. Williams, D. Wright, H. Yoshida, Geant4 developments and applications, IEEE Trans. Nucl. Sci. 53 (1) (2006) 270–278.

[18] I. Bavykina, P. Christ, P. Huff, J. Ninković, F. Proebst, W. Seidel, L. Stodolsky, Interpretation of light-quenching factor measurements, Astropart. Phys. 28 (4–5) (2007) 489–493, http://dx.doi.org/10.1016/j.astropartphys.2007.09.006. <http://linkinghub.elsevier.com/retrieve/pii/S092765050700134X>.

[19] A. Martinez-Davalos, E. Belmont-Moreno, K. Michaelian, A. Menchaca-Rocha, Light-output response of CsI(T1) detectors for low-energy ions, J. Lumin. 74 (1997) 769–771.

[20] D. Horn, G. Ball, A. Galindo-Uribarri, E. Hagberg, R. Walker, The mass dependence of CsI(Tl) scintillation response to heavy ions, Nucl. Inst. Meth. Phys. Res. Sect. A: Accel. Spectrometers, Detectors Assoc. Equip. 320 (1–2) (1992) 273–276, http://dx.doi.org/10.1016/0168-9002(92)90785-3. <http://linkinghub.elsevier.com/retrieve/pii/0168900292907853>.

[21] Y. Koba, H. Iwamoto, K. Kiyohara, T. Nagasaki, G. Wakabayashi, Y. Uozumi, N. Matsufuji, Scintillation efficiency of inorganic scintillators for intermediate-energy charged particles, Progr. Nucl. Sci. Technol. 1 (2011) 218–221. <http://www.aesj.or.jp/publication/pnst001/data/218.pdf>.

A.4 HIMAC data storage location

As already mentioned in section 4.1 currently (January 2016) all HIMAC data is stored on the workgroup server **etph** in this folder:

`/data/etph/solo/data/`

It is separated in folders according to the acquisition year. Filenames include date of acquisition, ion type and absorber thickness. Absorber is polyethylene unless otherwise noted in the filenames[1]. In cases where different crystal types than BGO were used, this is also indicated in the filenames. Possible other crystal types are GSO (very rare, only in early measurements), BSO and LSO. Beam energies are typically not mentioned in the filenames. They have to be taken from table 4.1 on page 85.

[1] For some early iron measurements aluminium plates were used as absorber.

Danksagung (Acknowledgments)

An dieser Stelle möchte ich allen Menschen danken, die mich während der Anfertigung dieser Arbeit unterstützt und begleitet haben. Einige, deren Anteil hieran besonders groß gewesen ist, möchte ich hier namentlich nennen. Insbesondere danke ich:

Robert Wimmer-Schweingruber für die freundlich Aufnahme in Deine Arbeitsgruppe und für die Möglichkeit, diese Arbeit bei Dir anzufertigen. Darüber hinaus danke ich Dir für die gute Betreuung, insbesondere, dass Du es trotz vollem Terminkalender immer schaffst, Zeit für ein Gesräch zu finden.

Stephan Böttcher dafür, dass ich die von Dir entwickelte Elektronik für diese Arbeit nutzen konnte.

Shrinivasrao Kulkarni für die gute Zusammenarbeit, insbesondere während der Montage der einzelnen Modelle und der Teile für die Flugmodelle.

Sönke Burmeister und **Hisashi Kitamura** für die Organisation der HIMAC Messkampagnen und die freundliche Unterstützung vor Ort.

Robert Elftmann und **Nina Dresing** dafür, dass Ihr mir als Korrekturleser/-in zur Verfügung gestanden habt und für die daraus resultierenden, sehr hilfreichen Fachgespräche.

Lauri Panitzsch und **Jan Steinhagen**, da ich mit Euch sehr gerne unser gemeinsames Büro geteilt habe und für die immer wieder interessanten und anregenden Diskussionen im Bereich der Physik und darüber hinaus, die wir dort führen konnten.

Meiner Frau **Annika** für all die Unterstützung und Hilfe, die Du mir außerhalb der Universität gegeben hast, auch wenn ich es Dir nicht immer einfach gemacht habe. Aus eigener Erfahrung weißt Du schließlich, was es bedeutet, eine solche Dissertation anzufertigen und Du warst mir damit meine größte Stütze.

Erklärung

Hiermit versichere ich an Eides statt, dass die vorliegende Dissertation – abgesehen von der Beratung durch meinen wissenschaftlichen Lehrer und der Verwendung der angegebenen Hilfsmittel – nach Inhalt und Form meine eigene ist. Sie hat weder ganz noch teilweise an einer anderen Stelle im Rahmen eines Prüfungsverfahrens vorgelegen. Teile dieser Arbeit (siehe Anhang A.2 und A.3) wurden bereits unter [53] und [111] veröffentlicht. Die Arbeit entstand unter Einhaltung der Regeln guter wissenschaftlicher Praxis der Deutschen Forschungsgemeinschaft.

Ort, Datum

Jan Tammen